Submillimeter diffusion-weighted magnetic resonance imaging of the human brain

Sajjad Feizollah

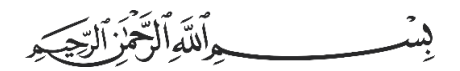
Integrated Program in Neuroscience

Department of Neurology and Neurosurgery

McGill University, Montreal

January 2025

A thesis submitted to McGill University
in partial fulfillment of the requirements of the degree of Doctor of Philosophy



In the Name of Allah, the Most Beneficent, the Most Merciful

To the noblest of souls, Imam Mahdi (peace be upon him), son of Imam Ali (peace be upon him) The beacon of hope and justice,

In whose awaited return, the world shall find peace and purpose...

To my beloved parents,

Whose love and sacrifice have shaped my journey.

May my success be a reflection of their endless devotion...

تقدیم به پدرو مادر غزیزم، که عثق و از خودکذشتی شان راه زندگیم راساخته است. امیدوارم موفقیتم باز بابی از عثق بی پایانشان باشد...

Abstract

Diffusion magnetic resonance imaging (dMRI) is a leading imaging modality for obtaining in-vivo information about brain connectivity and microstructure. In recent years, there has been increasing interest in using dMRI to investigate small brain structures, such as the cortex and hippocampus, driven by advancements in microstructure models and imaging technologies. However, achieving high and ultra-high effective resolutions with current diffusion imaging methods remains challenging, especially within reasonable scan times on clinical scanners. This PhD project 1) characterizes the effective resolution of dMRI that can be achieved using 2D sequences at 7 Tesla (T), and 2) introduces a novel SNR-efficient 3D sequence at 3 T that balances the trade-off between scan time and resolution.

The first objective of this thesis was to evaluate the effective resolutions that can be achieved using an efficient single-shot spiral readout trajectory at 7 T to maximize the SNR. The difference between nominal and effective resolution of dMRI, due to T_2^* decay during readout, has not been extensively studied at 7 T. First, I explored the effective resolution of dMRI through extensive sequence simulations and point spread function (PSF) characterization. A 2D single-shot spiral trajectory was implemented, and field monitoring probe measurements were integrated into the image reconstruction pipeline to correct distortions and artifacts caused by unwanted fields. Simulation results showed that the effective resolution of a spiral trajectory is ~25% lower than the nominal resolution at 3 T and ~45% lower at 7 T. However, in-vivo comparisons to a typical echo planar imaging (EPI) trajectory demonstrated that spirals provide ~40% higher SNR than EPI at a matching effective resolution of 1.5 mm at 7 T.

These results further indicated that even though using spirals at 7 T improves the SNR efficiency significantly, submillimeter effective resolutions require higher SNRs than can be achieved with a 2D single-shot spiral. To address these limitations and further increase SNR efficiency, the second objective of this thesis was to design a novel 3D Multishot Enhanced Recovery Motion Artifact Insensitive Diffusion (MERMAID) sequence. This sequence significantly enhances signal recovery by incorporating an additional inversion pulse immediately before the excitation pulse in a typical spin-echo sequence. Trajectory using radially batched internal navigator echoes (TURBINE) readout was employed to correct phase errors between shots caused by macroscopic motion. Phantom and in-vivo scans demonstrated that this new sequence improves SNR efficiency by 30-80% compared to typical multi-slice 2D spin-echo sequences. This improvement allowed for the acquisition of scans with nominal and effective resolutions of 0.74 mm and ~0.9 mm, respectively, at 3 T, with a maximum b-value of 2000 s/mm² in 112 directions, all within 37 minutes. This is a significant improvement to most recent high-resolution dMRI works that acquire a similar diffusion protocol in 100 minutes at 3 T.

The results of this PhD research show that 2D single-shot spiral imaging is more SNR efficient than typical 2D techniques for high-resolution (~1.5-1.2 mm effective resolution) imaging at 7 T. For submillimeter resolutions, the SNR efficiency of the 3D MERMAID sequence is required. This sequence holds great potential for investigating the microstructure of small brain structures within feasible scan times on clinical scanners. There is also potential to further improve SNR by implementing 3D MERMAID at 7 T, which would also address the challenges of B₁⁺ nonuniformity at ultra-high fields.

Résumé

L'imagerie par résonance magnétique de diffusion (IRMd) est l'une des principales modalités d'imagerie permettant d'obtenir des informations in vivo sur la connectivité et la microstructure du cerveau. Ces dernières années, l'IRMd a suscité un intérêt croissant pour l'étude des petites structures cérébrales, telles que le cortex et l'hippocampe, grâce aux progrès réalisés dans les modèles de microstructure et les technologies d'imagerie. Cependant, l'obtention de résolutions effectives élevées et ultra-élevées avec les méthodes actuelles d'IRMd demeure un défi, surtout pour des temps de balayage raisonnables sur les scanners cliniques. Ce projet de doctorat 1) caractérise la résolution effective de l'IRMd qui peut être atteinte en utilisant des séquences 2D à 7 Tesla (T), et 2) introduit une nouvelle séquence 3D efficace en terme de rapport signal/bruit (RSB) à 3 T avec un compromis optimal entre le temps de balayage et la résolution.

Le premier objectif de cette thèse était d'évaluer les résolutions effectives qui peuvent être atteintes en utilisant une trajectoire de lecture en spirale à 7 T pour maximiser le RSB. La différence entre la résolution nominale et effective de l'IRMd, due à la décroissance pondérée T2* du signal pendant la lecture, n'a pas fait l'objet d'études approfondies à 7 T. Tout d'abord, j'ai exploré la résolution effective de l'IRMd grâce à des simulations approfondies de séquences et à la caractérisation de la fonction d'étalement du point (PSF). Une trajectoire en spirale 2D à balayage unique a été mise en œuvre, et les mesures de variations du champs par des sondes additionnelles ont été intégrées dans le pipeline de reconstruction d'image pour corriger les distorsions et les artefacts causés par les champs indésirables. Les résultats de la simulation ont montré que la résolution effective d'une trajectoire en spirale est inférieure d'environ 25 % à la résolution nominale à 3 T et d'environ 45 % à 7 T. Cependant, des comparaisons in vivo avec une trajectoire

typique d'imagerie écho planaire (EPI) ont démontré que les spirales fournissent un RSB environ 40% plus élevé que l'EPI à une résolution effective correspondante de 1,5 mm à 7 T.

Ces résultats ont également montré que, bien que l'utilisation de spirales à 7 T améliore considérablement l'efficacité du RSB, les résolutions effectives submillimétriques nécessitent des RSB plus élevés que ceux que l'on peut obtenir avec une spirale 2D à balayage unique. Afin de remédier à ces limitations et d'augmenter l'efficacité du RSB, le deuxième objectif de cette thèse était de développer une nouvelle séquence 3D de diffusion insensible aux artefacts de mouvement (MERMAID). Cette séquence améliore considérablement la récupération du signal en incorporant une impulsion d'inversion supplémentaire immédiatement avant l'impulsion d'excitation dans une séquence de type écho de spin. La trajectoire de balayage TURBINE a permis de corriger les erreurs de phase entre les acquisitions causées par le mouvement macroscopique. Des scans sur fantôme et in vivo ont démontré que cette nouvelle séquence améliorait l'efficacité du RSB de 30 à 80 % par rapport aux séquences 2D à écho de spin typiques. Cette amélioration a permis l'acquisition de scans avec des résolutions nominales et effectives de 0,74 mm et ~0,9 mm respectivement à 3 T, avec une valeur b maximale de 2000 s/mm² et 112 directions, le tout en 37 minutes. Il s'agit donc d'une amélioration significative par rapport à des travaux qui permettent d'acquérir un protocole de diffusion similaire en 100 minutes à 3 T.

Les résultats de cette recherche doctorale montrent que l'imagerie en spirale en un seul balayage améliore significativement le RSB pour l'imagerie 2D à 7 T. Cependant, pour des résolutions submillimétriques, l'efficacité RSB de la séquence 3D MERMAID est nécessaire. Cette séquence présente un grand potentiel pour l'étude de la microstructure des petites structures cérébrales dans des temps de scan réalisables sur des scanners cliniques. Il est également possible d'améliorer davantage le RSB lorsqu'elle est mise en œuvre à 7 T, ce qui peut également permettre

de relever les défis de la non-uniformité du champs de radio-fréquence B1 ⁺ aux des champs ultra-
élevés.

Acknowledgments

I would like to extend my deepest gratitude to all those who have supported me throughout my PhD journey. First and foremost, I am profoundly grateful to my supervisor, Prof. Christine Tardif, for her trust and confidence in me, which has been incredibly invaluable. Her decision to welcome me into her group has been pivotal, and I owe much of my future career to her mentorship. Without her expert guidance and remarkable patience, completing this PhD would not have been possible.

My heartfelt thanks go to my parents, whose unconditional support and encouragement have been my backbone during this journey. They endured the challenges of this path alongside me, and words cannot fully express my appreciation for all they have done.

I would like to thank Prof. Ives Levesque and Prof. David Rudko, my committee members, for their valuable comments and discussions throughout my PhD. Their insights provided me with new perspectives on my project, which were incredibly helpful.

I am deeply grateful to the staff at the McConnell Brain Imaging Center (BIC) for their consistent support over these years. Ilana Leppert shared her deep knowledge of MRI with me and cared for me both personally and professionally, for which I am incredibly thankful. Jennifer Campbell impressed me with her keen insights and thoughtful suggestions during our many discussions. Marcus Couch patiently guided me through sequence programming and helped with IDEA, even when my ideas seemed unconventional. Mike Ferreira was always there to assist me with any technical challenges, whether related to computers or experimenting with phantoms. I would also like to express my gratitude to Dr. Pedram Yazdanbakhsh for his constant support. He

was always there for me, offering guidance and standing by my side whenever I needed help. I also appreciate the unwavering help of David Costa, Ronaldo Lopez, Soheil Mollamohseni, and Carollyn Hurst, who supported me during scans without hesitation. Their sense of humor and the time we shared will remain fond memories of my time at BIC. Special thanks to Judith Barany and Stacey Peixoto for their assistance with scan scheduling.

I am fortunate to have been surrounded by many talented individuals in the Shark Tank. I am especially thankful to Dr. Christopher Rowley for the many insightful discussions we shared, which greatly contributed to my work. Risa Thevakumaran, my oldest friend in the lab, made my time there more enjoyable, and I will always cherish our friendship. Mark Nelson, although not physically in the Shark Tank, he was a great friend and source of support. Wen Da Lu often offered his expert opinion on my imaging work and generously volunteered for my scans. Jana Strizak shared many conversations with me and frequently volunteered as well. Hande Halilibrahimoglu brought warmth and kindness to the lab environment, and Vladimir Grouza offered thoughtful discussions and contributions as a volunteer. Lastly, I extend my thanks to Sneha Senthil, Heather Hansen, Michelle Lam, Benjamin Beggs, Daniel O'Sullivan, and Nan-Hao Chen for their valuable input, which helped me improve my work. I also would like to thank others for their support; Forest Liu, Hannah Bernstein, Mona Dlikan, Grace Shi.

Contents

Abstract		i
Résumé .		iii
Acknow	ledgments	vi
List of fi	gures	xii
List of ta	ables	xix
List of A	bbreviations	xx
Contribu	ution of authors	xxiv
Original	contributions	xxvii
Chapter	1 Introduction	1
1.1.	Motivation	1
1.2.	Rationale and objectives	2
1.3.	Thesis outline	3
Chapter	2 Background	4
2.1.	Principles of nuclear magnetic resonance	4
2.1.1.	Magnetization and precession	4
2.1.2.	Nuclear magnetic resonance phenomenon	6
2.1.3.	Free induction decay	7
2.2.	Spatial encoding and image reconstruction	9
2.2.1.	Spatial encoding	9
2.2.2.	Forward model representation	11
2.2.3.	Parallel imaging	13
2.2.3	3.1. Sensitivity encoding (SENSE)	14
2.2.3	3.2. Generalized autocalibrating partially parallel acquisitions (GRAPPA)	14

2.2.4.	Magnetic field monitoring	15
2.2.5.	Solving the forward model	17
2.3.	Gradient echo and spin echo pulse sequences	17
2.4.	Diffusion imaging basics	18
2.4.1.	Encoding diffusion in MR signal	18
2.4.2.	Characterizing diffusion in tissues	20
2.4.3.	Microstructure modelling	23
2.5.	Literature review of diffusion image acquisition techniques	26
2.5.1.	Diffusion-weighted sequences	26
2.5.2.	Single-shot acquisition techniques	28
2.5.3.	Multi-shot acquisition techniques	32
2.5.4.	Volumetric acquisition techniques	37
2.5.5.	Other acquisition techniques	40
Chapter	3 High-resolution diffusion-weighted imaging at 7 Tesla: single-shot reado	ut
trajector	ies and their impact on signal-to-noise ratio, spatial resolution and accura	cy 43
Preface		43
Abstra	et	45
Abstraction 3.1.	Introduction	
		46
3.1.	Introduction	46 50
3.1. 3.2.	Introduction	46 50
3.1. 3.2. 3.2.1.	Introduction Methods	
3.1. 3.2. 3.2.1. 3.2.2.	Introduction	
3.1. 3.2. 3.2.1. 3.2.2. 3.3.	Introduction	
3.1. 3.2. 3.2.1. 3.2.2. 3.3. 3.3.1.	Introduction Methods Artifact and blurring correction due to imperfections in spatial encoding Image reconstruction using the expanded signal model Simulations Sequence simulations	
3.1. 3.2. 3.2.1. 3.2.2. 3.3. 3.3.1. 3.3.2.	Introduction Methods Artifact and blurring correction due to imperfections in spatial encoding Image reconstruction using the expanded signal model Simulations Sequence simulations Point spread function characterisation	
3.1. 3.2.1. 3.2.2. 3.3. 3.3.1. 3.3.2. 3.4.	Introduction Methods Artifact and blurring correction due to imperfections in spatial encoding Image reconstruction using the expanded signal model Simulations Sequence simulations Point spread function characterisation Experiments	
3.1. 3.2.1. 3.2.2. 3.3. 3.3.1. 3.3.2. 3.4.	Introduction Methods Artifact and blurring correction due to imperfections in spatial encoding Image reconstruction using the expanded signal model Simulations Sequence simulations Point spread function characterisation Experiments In-vivo scans to validate simulation results	
3.1. 3.2.1. 3.2.2. 3.3. 3.3.1. 3.3.2. 3.4. 3.4.1. 3.4.2.	Introduction	
3.1. 3.2.1. 3.2.2. 3.3. 3.3.1. 3.3.2. 3.4. 3.4.1. 3.4.2.	Introduction Methods	
3.1. 3.2. 3.2.1. 3.2.2. 3.3. 3.3.1. 3.3.2. 3.4. 3.4.1. 3.4.2. 3.4.3.	Introduction Methods Artifact and blurring correction due to imperfections in spatial encoding Image reconstruction using the expanded signal model Simulations Sequence simulations Point spread function characterisation Experiments In-vivo scans to validate simulation results	

3.5.	Results	60
3.5.1.	Simulation results	60
3.5.1	.1. Sequence timing	60
3.5.1	.2. Point spread function	61
3.5.2.	In-vivo scan results	65
3.5.2	2.1. EPI has the highest effective resolution	65
3.5.2	2.2. Spirals provide the highest SNR	68
3.5.2	2.3. Spirals provide highest SNR for matching effective resolution	69
3.6.	Discussion	71
3.6.1.	Spirals are the optimal k-space readout trajectory for single-shot dMRI at 7 T	71
3.6.2.	Spatial specificity and sharpening factor	71
3.6.3.	Simulation results of the effective resolution are consistent with in-vivo scans	72
3.6.4.	Trade-off between SNR and effective resolution.	72
3.6.5.	Diffusion-encoding effects	73
3.6.6.	Limitations	74
3.7.	Conclusion	76
Code a	nd data availability	76
Acknow	wledgments	76
3.8.	Supplementary materials	78
Digita	l brain phantom simulations	85
Metl	nods	85
Resu	ılts	85
Referen	1ces	88
Chapter	4 3D MERMAID: 3D Multishot Enhanced Recovery Motion Artifact Insensiti	ve
Diffusion	n for sub-millimeter, multi-shell, and SNR efficient diffusion imaging	98
Preface	2	98
Abstra	ct	100
4.1.	Introduction	101
4.2.	Methods	105
4.2.1.	3D steady-state SE dMRI with enhanced longitudinal magnetization recovery	105
4.2.2.	Image reconstruction and motion correction	106

4.2.3.	Bloch Simulations to optimize the 3D MERMAID sequence	110
4.2.4.	Phantom scans to compare relative SNR of 3D MERMAID with 2D SE-EPI	
seque	nce 111	
4.2.5.	Removal of motion artifacts in reconstruction of 3D images	112
4.2.6.	2D SE-EPI and 3D MERMAID comparison at sub-millimetre resolution	113
4.2.7.	Pushing the spatial resolution of 3D MERMAID	114
4.3.	Results	116
4.3.1.	Bloch simulations to evaluate the performance of the 3D MERMAID sequence	116
4.3.2.	Phantom scans show improved SNR for 3D MERMAID compared to 2D SE-E	PI
sequei	nce 117	
4.3.3.	Removal of motion artifacts in reconstructed 3D images	120
4.3.4.	2D SE-EPI and 3D MERMAID comparison at sub-millimetre resolution	124
4.3.5.	Pushing the spatial resolution of 3D MERMAID	126
4.4.	Discussion	128
4.4.1.	SNR advantage of 3D MERMAID sequence over other 2D and 3D sequences	128
4.4.2.	Effective resolution of 3D MERMAID	128
4.4.3.	Microstructure modeling using 3D MERMAID	129
4.4.4.	Limitations	129
4.5.	Conclusion	131
4.6.	Acknowledgments	131
4.7.	Data and Code Availability Statement	132
4.8.	Supplementary materials	133
Postfac	e	146
Referei	ices	148
Chapter	5 Discussion	160
5.1.	Practical considerations	161
5.2.	Potential improvements to the sequences and reconstruction pipelines	162
5.3.	Future research directions	164
Chapter	6 Conclusion	165
Reference	es	167
Conveig	ht	102

List of figures

Figure 2.1. A: magnetization at the steady state (M ₀) along Z, and generated transverse
magnetization (Mxy) after applying B ₁ ⁺ . B: the path at which magnetization is recovered
back along Z, rotating at the Larmour frequency around Z
Figure 2.2. FID acquisition. The sequence diagram is shown at the top, and the transverse
magnetization is plotted at the bottom (TR $>> 5T_1$)
Figure 2.3. Spherical harmonic functions at the isocenter x-y plane of a scanner's bore 10
Figure 2.4. K-space and different readout trajectories. A: acquired data of a k-space plane. B: 2D
Cartesian (top- Echo Planar Imaging (EPI)) and non-Cartesian (bottom-spiral) readout
trajectories. C: a 3D non-Cartesian readout trajectory (TURBINE)11
Figure 2.5. Individual images of 8 coils around the FOV (adapted from (Deshmane et al., 2012)).
Figure 2.6. Schematic of GRAPPA kernel estimation and reconstruction. a: undersampled k-space
with every other line missing. b: fully sampled ACS lines. c: calculating GRAPPA weights.
d: fill the missing k-space lines using the weights to reconstruct the image in e. (adapted
from (Deshmane et al., 2012))
Figure 2.7. NMR field probe consisting of a sample droplet and solenoid coils for excitation and
receiving the NMR signal (adapted from De Zanche et al., 2008)
Figure 2.8. Spin-echo acquisition. The sequence diagram for one TR is shown at the top, and the
transverse magnetization is plotted at the bottom
Figure 2.9. Pulse gradient spin-echo (PGSE) experiment is a SE sequence that includes two
gradient pulses to encode diffusion. The phase evolution for diffusing and stationary spins
are plotted at the bottom
Figure 2.10. From left to right: different configurations of fibers, resulting diffusion scattering
pattern, diffusion tensor, principal diffusion direction, and fiber orientation distribution
function. (adapted from (Seunarine & Alexander, 2009))
Figure 2.11. FODFs calculated using spherical deconvolution method show different fiber
orientations in each voxel

Figure	2.12. Schematic of a white matter fiber showing intracellular, extracellular, parallel and
	perpendicular diffusivities in mm ² /s (adapted from (Jelescu et al., 2015))
Figure	2.13. Different dMRI sequences: A: PGSE, B: twice refocused, C: FSE, D: STEAM, and
	E: DW-SSFP. 28
Figure	2.14. Color FA maps of the same subject at 3 T (1.25 mm) and 7 T (1.05 mm) on the first
	row. Comparison of DTI maps overlaid on FA maps of the same dataset at 3 T and 7 T
	(adapted from (A. Vu et al., 2015))
Figure	2.15. Comparison of using nominal trajectory and using measured trajectory and correcting
	for B_0 nonuniformities (Feizollah & Tardif, 2021)
Figure	2.16. Different types of EPI trajectory. A: single shot. B: interleaved. C: RS-EPI, and D:
	SAP-EPI. 32
Figure	2.17. Comparison of MUSE and AMUSE in reconstructing interleaved EPI. 0.86×0.86×5
	mm, b-value of 800 s/mm² in 15 directions (adapted from (Guhaniyogi et al., 2016a)) 34
Figure	2.18. FA maps from 15 diffusion directions with a b-value of 1000 s/mm² and in-plane
	resolution of 0.5 mm acquired using RS-EPI in 35 minutes (adapted from (Holdsworth et
	al., 2019))
Figure	2.19. Comparison of three different image reconstructions: a: uncorrected, b: direct phase
	subtraction, c: magnitude averaging over shots, d: iterative phase correction (adapted from
	(Truong & Guidon, 2014b))
Figure	2.20. 3D multi-slab acquisition and approaches to correct slab boundary artifacts (adapted
	from (Wu, Poser, et al., 2016a))
Figure	2.21. Isotopic 0.6 mm scan with a b-value of 1000 s/mm ² in 64 directions using gSlider
	acquisition in 117 minutes (adapted from (Liao et al., 2021))
Figure	2.22. Comparison of 2D EPI sequence and 3D DW-SSFP sequence acquired using
	TURBINE readout (adapted from (McNab et al., 2010))
Figure	2.23. White matter fibers entering the grey matter using ZOOPPA method (adapted from
	(Heidemann et al., 2012))
Figure	2.24. High-resolution diffusion scans and color FA maps with a resolution of
	0.7×0.7×2.8 mm, b-value of 1000 s/mm ² in 12 directions using PSF mapping imaging in
	30 minutes (adapted from (In et al., 2017))
Figure	3.1. Timing properties of trajectories. A: Readout duration as a function of nominal

	resolution. Spiral trajectories have shorter readout durations due to more efficient way of
	sampling k-space for the same acceleration factor. B: Echo time (TE) as a function of
	nominal resolution for a b-value = 2000 s/mm2. The echo time remains at 44 ms for spiral
	trajectories, while it increases with resolution for EPI and PF-EPI
Figure	3.2. MTF along the PE direction and corresponding PSF. A and B, and their corresponding
	PSFs in C and D for the WM and GM at 7 T. There is more broadening of the PSF for the
	WM in comparison to the GM. The dashed portion of the PF-EPI MTFs was generated
	using the Hermitian conjugate property of the k-space
Figure	3.3. PSF analysis. A, B: Spiral has similar ringing in all directions while ringing is
	constrained along the PE and FE axes for EPI. C, D: There is greater variability in the
	effective resolution of WM compared to GM due to its shorter T ₂ *. E, F: The specificity of
	EPI is higher due to its narrower main lobe compared to PF-EPI and spiral. EPI and PF-
	EPI have a constant sharpening effect, while the sharpness of spirals reduces significantly
	at high resolutions due to the signal decay causing suppression of the side lobes 64
Figure	3.4. FA maps calculated using different trajectories at 1.5 mm isotropic nominal resolution.
	DEC maps in the axial plane are shown in the first row, and FA maps in axial, sagittal and
	coronal planes with magnified regions for better examination are shown below. EPI-based
	scans show a minimal blurring in the coronal direction, and maximal blurring in the sagittal
	plane, while blurring in the spiral trajectory occurs in all directions. The sharpest FA map
	is acquired using EPI with $R = 4$, and the map with the lowest effective resolution is
	generated using PF-EPI with R = 2
Figure	3.5. Line plots of FA values in PE and FE directions at a nominal isotropic resolution of 1.5
	mm. A and B: line plots of FA values along the FE direction. C and D: line plots of FA
	values along PE direction. FA values show more variations in EPI and PF-EPI trajectories
	in the PE direction compared to the FE direction. The blue arrow shows more variability
	of the FA values calculated using spirals in the FE direction. The red arrow shows a drop
	in FA for PF-EPI with $R = 2$ and 3 in contrast to other trajectories
Figure	3.6. SNR calculated from in-vivo scans. The SNR was calculated within a brain tissue mask
	in b=0 s/mm ² scans at three resolutions of 1, 1.2, and 1.5 mm isotropic
Figure	3.7. FA map of scans with a matching effective resolution of 1.5 mm. Similar structures in
	FA maps can be seen in all maps due to the matching effective resolution. Effect of higher

SNR of the spiral scan is clear in ICVF maps
Figure 3.8. MTF along the PE direction and corresponding PSF. A and B, and their corresponding
PSFs in C and D for the WM and GM at 3 T. There is more broadening of the PSF for the
WM in comparison to the GM. The dashed portion of the PF-EPI MTFs was generated
using the Hermitian conjugate property of the k-space
Figure 3.9. Effective resolution as a function of nominal resolution. The effective resolution of
WM and GM is shown in A and B. WM has a lower effective resolution due to its shorter
T ₂ * relaxation time
Figure 3.10. Diffusion-weighted images using different readout trajectories at a nominal resolution
of 1.5 mm isotropic at 7 T. Images for b-values of 0, 300, 1000, and 2000 s/mm ² acquired
by different trajectories are shown. Images in the same rows are shown with the same scale
adjusted for better visibility
Figure 3.11. Reconstructed images at matching effective resolution of 1.5-mm. Diffusion images
with b-values of 0, 300, 1000, and 2000 s/mm ² using different trajectories are shown 81
Figure 3.12. different slices of b=0 s/mm ² and FA maps at matching resolution of 1.5 mm. Effects
of B1 nonuniformity are clear in the last two columns which causes loss of SNR 82
Figure 3.13. ICVF maps generated from different trajectories with the same effective resolution.
Low SNR of EPI and PF-EPI leads to inaccurate estimation of ICVF. B ₁ nonuniformity
causes SNR loss in some areas which are clear in the last column
Figure 3.14. The echo time and effective resolution as a function of nominal resolution for b-values
of 500 and 1000 s/mm ² . TEs are shorter in $b = 500$ s/mm ² , but effective resolution is not
affected since the blurring mostly caused by T2* decay after the echo in a spin-echo
sequence84
Figure 3.15. Digital phantom imaging results. EPI and PF-EPI have higher ringing artifact and
blurring in the PE direction, while in spirals they appear in all directions. Blurrier images
and more ringing artifacts cause lower specificity and effective resolution
Figure 3.16. Line plots from the digital brain phantom images in the phase- and frequency-encode
directions. The line plots correspond to the red lines in the digital brain image to the left.
Spiral and PF-EPI smooth details of the phantom in the anterior-posterior direction. EPI
and PF-EPI show similar structural details of the phantom in the left-right direction, while
spiral performs similarly to the anterior-posterior direction, losing fine structures 87

A: sequence diagram shows the new components added to/modified in a conventional SE sequence in blue: an inversion pulse, spoilers, and non-selective pulses. B: shows one TR of a 3D SE sequence at the steady state. C: shows Bloch simulation of the 3D MERMAID sequence at the steady state. D: TURBINE readout (undersampled due to better visualization) constructed from a 2D EPI plane rotating around anterior-posterior axis. Each color shows a shot, and projections specified by dotted line are skipped to accelerate the scan in the radial direction	_	4.1. Sequence diagram, Bloch simulations, and the readout of the 3D MERMAID sequence.
of a 3D SE sequence at the steady state. C: shows Bloch simulation of the 3D MERMAID sequence at the steady state. D: TURBINE readout (undersampled due to better visualization) constructed from a 2D EPI plane rotating around anterior-posterior axis Each color shows a shot, and projections specified by dotted line are skipped to accelerate the scan in the radial direction		A: sequence diagram shows the new components added to/modified in a conventional SE
sequence at the steady state. D: TURBINE readout (undersampled due to better visualization) constructed from a 2D EPI plane rotating around anterior-posterior axis. Each color shows a shot, and projections specified by dotted line are skipped to accelerate the scan in the radial direction		sequence in blue: an inversion pulse, spoilers, and non-selective pulses. B: shows one TR
visualization) constructed from a 2D EPI plane rotating around anterior-posterior axis Each color shows a shot, and projections specified by dotted line are skipped to accelerate the scan in the radial direction		of a 3D SE sequence at the steady state. C: shows Bloch simulation of the 3D MERMAID
Each color shows a shot, and projections specified by dotted line are skipped to accelerate the scan in the radial direction		sequence at the steady state. D: TURBINE readout (undersampled due to better
the scan in the radial direction		visualization) constructed from a 2D EPI plane rotating around anterior-posterior axis
Figure 4.2. Image reconstruction pipeline. A: method used to calculate in-plane GRAPPA kernels and coil sensitivity of each PE plane. B: pipeline used to reconstruct each volume with motion correction		Each color shows a shot, and projections specified by dotted line are skipped to accelerate
and coil sensitivity of each PE plane. B: pipeline used to reconstruct each volume with motion correction		the scan in the radial direction
motion correction	Figure	4.2. Image reconstruction pipeline. A: method used to calculate in-plane GRAPPA kernels
Figure 4.3. Bloch simulations to determine the performance of the 3D MERMAID sequence. As ratio of the available transverse magnetization of the 3D MERMAID sequence and a 3D SE sequence at different TEs/TRs corresponding to b-values of 1000, 2000, and 3000 s/mm2. B: sensitivity of the 3D MERMAID sequence to B1+ nonuniformity compared to a 3D SE sequence. C: the transverse magnetization at steady state as a function of TR for three tissues. D: changes in transverse magnetization of GM, WM, and CSF with flip angle (FA)		and coil sensitivity of each PE plane. B: pipeline used to reconstruct each volume with
ratio of the available transverse magnetization of the 3D MERMAID sequence and a 3D SE sequence at different TEs/TRs corresponding to b-values of 1000, 2000, and 3000 s/mm2. B: sensitivity of the 3D MERMAID sequence to B1+ nonuniformity compared to a 3D SE sequence. C: the transverse magnetization at steady state as a function of TR for three tissues. D: changes in transverse magnetization of GM, WM, and CSF with flip angle (FA)		motion correction. 109
SE sequence at different TEs/TRs corresponding to b-values of 1000, 2000, and 3000 s/mm2. B: sensitivity of the 3D MERMAID sequence to B1+ nonuniformity compared to a 3D SE sequence. C: the transverse magnetization at steady state as a function of TR for three tissues. D: changes in transverse magnetization of GM, WM, and CSF with flip angle (FA)	Figure	4.3. Bloch simulations to determine the performance of the 3D MERMAID sequence. As
s/mm2. B: sensitivity of the 3D MERMAID sequence to B1+ nonuniformity compared to a 3D SE sequence. C: the transverse magnetization at steady state as a function of TR for three tissues. D: changes in transverse magnetization of GM, WM, and CSF with flip angle (FA)		ratio of the available transverse magnetization of the 3D MERMAID sequence and a 3D
a 3D SE sequence. C: the transverse magnetization at steady state as a function of TR for three tissues. D: changes in transverse magnetization of GM, WM, and CSF with flip angle (FA)		SE sequence at different TEs/TRs corresponding to b-values of 1000, 2000, and 3000
three tissues. D: changes in transverse magnetization of GM, WM, and CSF with flip angle (FA)		s/mm2. B: sensitivity of the 3D MERMAID sequence to B1+ nonuniformity compared to
(FA)		a 3D SE sequence. C: the transverse magnetization at steady state as a function of TR for
Figure 4.4. SNR map and relative SNR of the 3D MERMAID sequence compared to 2D SE-EPI sequence at different TEs/TRs. A: SNR maps of a 2D SE-EPI and 3D MERMAID sequence at nominal isotropic resolution of 1 mm. The scan times for both scans are matched to show the SNR efficiency of the 3D MERMAID sequence. The area at the center of the phantom used to calculate the relative SNR is specified as dotted line. B, C, D, and E are the SNR of the 3D MERMAID sequence relative to the 2D SE-EPI sequence at the center of the phantom for different timings corresponding to b-values of 0, 1000, 2000, and 3000 s/mm2 respectively		three tissues. D: changes in transverse magnetization of GM, WM, and CSF with flip angle
sequence at different TEs/TRs. A: SNR maps of a 2D SE-EPI and 3D MERMAID sequence at nominal isotropic resolution of 1 mm. The scan times for both scans are matched to show the SNR efficiency of the 3D MERMAID sequence. The area at the center of the phantom used to calculate the relative SNR is specified as dotted line. B, C, D, and E are the SNR of the 3D MERMAID sequence relative to the 2D SE-EPI sequence at the center of the phantom for different timings corresponding to b-values of 0, 1000, 2000, and 3000 s/mm2 respectively		(FA)117
at nominal isotropic resolution of 1 mm. The scan times for both scans are matched to show the SNR efficiency of the 3D MERMAID sequence. The area at the center of the phantom used to calculate the relative SNR is specified as dotted line. B, C, D, and E are the SNR of the 3D MERMAID sequence relative to the 2D SE-EPI sequence at the center of the phantom for different timings corresponding to b-values of 0, 1000, 2000, and 3000 s/mm2, respectively	Figure	4.4. SNR map and relative SNR of the 3D MERMAID sequence compared to 2D SE-EPI
the SNR efficiency of the 3D MERMAID sequence. The area at the center of the phantom used to calculate the relative SNR is specified as dotted line. B, C, D, and E are the SNR of the 3D MERMAID sequence relative to the 2D SE-EPI sequence at the center of the phantom for different timings corresponding to b-values of 0, 1000, 2000, and 3000 s/mm2 respectively. Figure 4.5. Raw projections acquired at b-values of 0, 1000, and 2000 s/mm2 in 0-, 45-, and 90-degrees angles. Each projection is independently reconstructed showing the brain overlaying on a single image. Blue and yellow arrows show artifacts due to ΔB0 nonuniformities. 120		sequence at different TEs/TRs. A: SNR mans of a 2D SE_EPI and 2D MERMAID sequence
used to calculate the relative SNR is specified as dotted line. B, C, D, and E are the SNR of the 3D MERMAID sequence relative to the 2D SE-EPI sequence at the center of the phantom for different timings corresponding to b-values of 0, 1000, 2000, and 3000 s/mm2 respectively. 119 Figure 4.5. Raw projections acquired at b-values of 0, 1000, and 2000 s/mm2 in 0-, 45-, and 90-degrees angles. Each projection is independently reconstructed showing the brain overlaying on a single image. Blue and yellow arrows show artifacts due to ΔB0 nonuniformities. 120		sequence at different TEs/TKs. A. STAR maps of a 2D SE-E1 Tand 3D WERWAID sequence
of the 3D MERMAID sequence relative to the 2D SE-EPI sequence at the center of the phantom for different timings corresponding to b-values of 0, 1000, 2000, and 3000 s/mm2 respectively. Figure 4.5. Raw projections acquired at b-values of 0, 1000, and 2000 s/mm2 in 0-, 45-, and 90-degrees angles. Each projection is independently reconstructed showing the brain overlaying on a single image. Blue and yellow arrows show artifacts due to ΔB0 nonuniformities.		
phantom for different timings corresponding to b-values of 0, 1000, 2000, and 3000 s/mm2 respectively. Figure 4.5. Raw projections acquired at b-values of 0, 1000, and 2000 s/mm2 in 0-, 45-, and 90-degrees angles. Each projection is independently reconstructed showing the brain overlaying on a single image. Blue and yellow arrows show artifacts due to ΔB0 nonuniformities.		at nominal isotropic resolution of 1 mm. The scan times for both scans are matched to show
respectively		at nominal isotropic resolution of 1 mm. The scan times for both scans are matched to show the SNR efficiency of the 3D MERMAID sequence. The area at the center of the phantom
Figure 4.5. Raw projections acquired at b-values of 0, 1000, and 2000 s/mm2 in 0-, 45-, and 90-degrees angles. Each projection is independently reconstructed showing the brain overlaying on a single image. Blue and yellow arrows show artifacts due to ΔB0 nonuniformities.		at nominal isotropic resolution of 1 mm. The scan times for both scans are matched to show the SNR efficiency of the 3D MERMAID sequence. The area at the center of the phantom used to calculate the relative SNR is specified as dotted line. B, C, D, and E are the SNR
degrees angles. Each projection is independently reconstructed showing the brain overlaying on a single image. Blue and yellow arrows show artifacts due to $\Delta B0$ nonuniformities.		at nominal isotropic resolution of 1 mm. The scan times for both scans are matched to show the SNR efficiency of the 3D MERMAID sequence. The area at the center of the phantom used to calculate the relative SNR is specified as dotted line. B, C, D, and E are the SNR of the 3D MERMAID sequence relative to the 2D SE-EPI sequence at the center of the
overlaying on a single image. Blue and yellow arrows show artifacts due to $\Delta B0$ nonuniformities.		at nominal isotropic resolution of 1 mm. The scan times for both scans are matched to show the SNR efficiency of the 3D MERMAID sequence. The area at the center of the phantom used to calculate the relative SNR is specified as dotted line. B, C, D, and E are the SNR of the 3D MERMAID sequence relative to the 2D SE-EPI sequence at the center of the phantom for different timings corresponding to b-values of 0, 1000, 2000, and 3000 s/mm2
nonuniformities		at nominal isotropic resolution of 1 mm. The scan times for both scans are matched to show the SNR efficiency of the 3D MERMAID sequence. The area at the center of the phantom used to calculate the relative SNR is specified as dotted line. B, C, D, and E are the SNR of the 3D MERMAID sequence relative to the 2D SE-EPI sequence at the center of the phantom for different timings corresponding to b-values of 0, 1000, 2000, and 3000 s/mm2 respectively.
		at nominal isotropic resolution of 1 mm. The scan times for both scans are matched to show the SNR efficiency of the 3D MERMAID sequence. The area at the center of the phantom used to calculate the relative SNR is specified as dotted line. B, C, D, and E are the SNR of the 3D MERMAID sequence relative to the 2D SE-EPI sequence at the center of the phantom for different timings corresponding to b-values of 0, 1000, 2000, and 3000 s/mm2 respectively. 119 4.5. Raw projections acquired at b-values of 0, 1000, and 2000 s/mm2 in 0-, 45-, and 90-
Figure 4.6. Effects of the cardiac cycle on the magnitude images of the projections and		at nominal isotropic resolution of 1 mm. The scan times for both scans are matched to show the SNR efficiency of the 3D MERMAID sequence. The area at the center of the phantom used to calculate the relative SNR is specified as dotted line. B, C, D, and E are the SNR of the 3D MERMAID sequence relative to the 2D SE-EPI sequence at the center of the phantom for different timings corresponding to b-values of 0, 1000, 2000, and 3000 s/mm2 respectively. 119 4.5. Raw projections acquired at b-values of 0, 1000, and 2000 s/mm2 in 0-, 45-, and 90-degrees angles. Each projection is independently reconstructed showing the brain
	Figure	at nominal isotropic resolution of 1 mm. The scan times for both scans are matched to show the SNR efficiency of the 3D MERMAID sequence. The area at the center of the phantom used to calculate the relative SNR is specified as dotted line. B, C, D, and E are the SNR of the 3D MERMAID sequence relative to the 2D SE-EPI sequence at the center of the phantom for different timings corresponding to b-values of 0, 1000, 2000, and 3000 s/mm2, respectively. 119 4.5. Raw projections acquired at b-values of 0, 1000, and 2000 s/mm2 in 0-, 45-, and 90-degrees angles. Each projection is independently reconstructed showing the brain overlaying on a single image. Blue and yellow arrows show artifacts due to ΔB0

performance of the motion correction method. A. she	ows 10 consecutive sagittal projections
for two cardiac cycles. Colors of the pulse signal cor	respond to a phase in the cardiac cycle
a projection is acquired. Signal drop at the center	of the brain is obvious in the third
projection of each cycle. B: performance of the	motion correction when there is no
correction, only phase correction (PC), phase and r	nagnitude correction (PC + MC), and
the difference map between PC, and PC+MC image	s overlayed to the image 122
Figure 4.7. Comparison between diffusion measures cal	culated from a 2D SE-EPI and 3D
MERMAID sequence with a matching scan time.	A: shows different contrast between
tissues in scans with no diffusion weighting. B: show	s calculated diffusion parameters from
12 diffusion directions using the 3D MERMAID sec	quence compared to a standard 2D SE-
EPI sequence.	
Figure 4.8. Comparison between high spatial- and angular-	resolution scans of the 2D SE-EPI and
3D MERMAID sequences- SNR, MDWI, DEC, and	d ADC maps are shown in the top two
rows. fODFs overlayed on the anatomical scan an	d their zoomed-in images are shown
below.	
Figure 4.9. High-resolution diffusion maps and fODFs ca	alculated from the nominal 0.74 mm
isotropic scan acquired using the 3D MERMAID sec	quence- diffusion maps in the first row,
and fODFs overlayed on the MPRAGE scan in di	ifferent orientations are shown in the
second row. Zoomed-in areas, delineated by different	ent box colors, reveal exquisite details
of the intra-cortical fibers, WM crossing fibers, and	the curvature of the hippocampus. 127
Figure 4.10. Output of each image reconstruction step des	scribed in Section 4.2.2. A and B are
triangle and semi-Hanning filters, respectively	
Figure 4.11. 3D MERMAID image reconstruction pip	eline including denoising. First all
projections of all volumes are reconstructed, then d	lenoising (NORDIC) is performed for
each coil channel individually. In the next step, denote	ised projections are used to reconstruct
every volume as in the pipeline described in Figure	4.2
Figure 4.12. SNR maps of 3D MERMAID and 2D SE-EPI	at nominal resolution of 0.9 mm 135
Figure 4.13. MDWI of 3D MERMAID and 2D SE-EPI at n	ominal resolution of 0.9 mm 136
Figure 4.14. DEC maps of 3D MERMAID and 2D SE-EPI	at nominal resolution of 0.9 mm 137
Figure 4.15. ADC maps of 3D MERMAID and 2D SE-EPI	at nominal resolution of 0.9 mm 138
Figure 4.16. Axial fODFs of 3D MERMAID and 2D SE-I	EPI overlayed on the MPRAGE scan

	139
Figure 4.17. coronal fODFs of 3D MERMAID and 2D SE-EPI overlayed on the MP	RAGE scan.
	140
Figure 4.18. Sagittal fODFs of 3D MERMAID and 2D SE-EPI overlayed on the MP	RAGE scan.
	141
Figure 4.19. MDWI of nominal isotropic 0.74 scan.	142
Figure 4.20. DEC maps of nominal isotropic 0.74 mm scan.	143
Figure 4.21. ADC map of nominal isotropic 0.74 mm scan.	144
Figure 4.22. FA map of nominal isotropic 0.74 mm scan	145

List of tables

Table 2.1- Spherical harmonics basis functions up to 3 rd order
Table 3.1: In-vivo scan parameters at 7 T for three experiments to validate simulation results,
calculate SNR, and investigate SNR and efficiency of trajectories with a matching
resolution
Table 4.1- Parameters of phantom and human scans. Phantom and human scans acquired to
compare the 3D MERMAID and 2D SE-EPI sequences, and optimize 3D MERMAID
sequence

List of Abbreviations

ACS: autocalibration signal

ADC: apparent diffusion coefficient

ALS: amyotrophic lateral sclerosis

AMUSE: augmented multiplexed sensitivity encoding

BOLD: blood oxygenation level dependent

CAIPIRINHA: controlled aliasing in parallel imaging results in higher acceleration

CG: conjugate gradient

CS: compressed sensitivity encoding

CSF: cerebrospinal fluid

DEC: diffusion encoded color

dMRI: diffusion magnetic resonance imaging

DTI: diffusion tensor imaging

DW-SSFP: diffusion-weighted steady state free precession

ECC: eddy current compensation

EPI: echo-planar imaging

EPTI: echo planar time-resolved imaging

ESPIRiT: eigenvector-based self-consistent parallel imaging reconstruction

FA: fractional anisotropy

FE: frequency encode

FFT: fast Fourier transform

FID: free induction decay

fMRI: functional magnetic resonance imaging

fODF: fiber orientation distribution function

FOV: field of view

FSE: fast spin echo

FWHM: full width at half maximum

GM: gray matter

GRAPPA: generalized autocalibrating partially parallel acquisitions

GRASE: gradient and spin echo

GRE: gradient echo

HCP: human connectome project

ICVF: intracellular volume fraction

IDEA: integrated development environment for applications

ISMRMRD: international society for magnetic resonance in medicine raw data format

IVI: inner volume imaging

LORAKS: low-rank modeling of local k-space neighborhoods

MC: magnitude correction

MDWI: mean diffusion-weighted image

MERMAID: multishot enhanced recovery motion artifact insensitive diffusion

MP2RAGE: magnetization prepared 2 rapid acquisition gradient echoes

MPRAGE: magnetization prepared rapid acquisition gradient echoes

MRI: magnetic resonance imaging

MTF: modulation transfer function

MUSE: multiplexed sensitivity-encoding

MUSSELS: Multi-shot sensitivity-encoded diffusion data recovery using structured low-rank matrix completion

NMR: nuclear magnetic resonance

NODDI: neurite orientation dispersion and density imaging

NORDIC: noise reduction with distribution corrected

NPEN: nonlinear inversion for slab profile encoding

OVS: outer volume suppression

PC: phase correction

PE: phase encode

PF-EPI: partial Fourier echo-planar imaging

PGSE: pulsed gradient spin echo

PNS: peripheral nerve stimulation

POCS: projections onto convex sets

PROPELLER: periodically rotated overlapping parallel lines with enhanced reconstruction

PSF: point spread function

RF: radio frequency

ROI: region of interest

ROMER: rotating-view motion-robust super-resolution

RS-EPI: readout segmented echo-planar imaging

SAP-EPI: short-axis periodically rotated overlapping parallel lines with enhanced reconstruction echo-planar imaging

SAR: specific absorption rate

SD: standard deviation

SE: spin echo

SENSE: sensitivity encoding

SMASH: simultaneous acquisition of spatial harmonics

SMS: simultaneous multi slice

SNR: signal to noise ratio

SPIRiT: eigenvector-based self-consistent parallel imaging reconstruction

STEAM: stimulated echo acquisition mode

TE: echo time

TI: inversion time

TR: repetition time

TURBINE: trajectory using radially batched internal navigator echoes

UHF: ultra-high field

WM: white matter

ZOOM-EPI: zonally magnified oblique multislice echo-planar imaging

ZOOPPA: zoomed generalized autocalibrating partially parallel acquisitions

Contribution of authors

The original contributions in this thesis are presented in Chapter 3 and Chapter 4. For both manuscripts, I took the lead in conceptualizing ideas, designing experiments, performing simulations, implementing pulse sequences, developing image reconstruction pipelines, troubleshooting, interpreting results, and conducting post-reconstruction analysis. The tools that were not developed are mentioned in the relevant sections. I drafted the first versions of both manuscripts and incorporated feedback and revisions from Prof. Christine Tardif and journal reviewers.

Prof. Christine Tardif supervised the work for both manuscripts, providing guidance in conceptualization, experiment design, troubleshooting, result interpretation, and funding for scans and research. She also contributed to manuscript writing and revision.

Chapter 3: High-resolution diffusion-weighted imaging at 7 Tesla: single-shot readout trajectories and their impact on signal-to-noise ratio, spatial resolution and accuracy. Sajjad Feizollah, Christine L Tardif (2023). Neuroimage 274: 120159.

Chapter 4: 3D MERMAID: 3D Multishot Enhanced Recovery Motion Artifact Insensitive Diffusion for sub-millimeter, multi-shell, and SNR efficient diffusion imaging. Sajjad Feizollah, Christine L Tardif (2024). The manuscript submitted to Magnetic Resonance in Medicine in October 2024 is included in this thesis. A revised version of this manuscript is now accepted by the journal.

Abstracts

Chapter 3:

Toward high-resolution mapping of microscopic anisotropy in the cortex using b-tensor diffusion imaging with a spiral readout at 7 Tesla. Sajjad Feizollah, Christine L. Tardif, ISMRM, 2021

Effects of T2*-blurring on effective resolution of diffusion MRI with spiral and EPI readout trajectories at 7 T. Sajjad Feizollah, Christine L. Tardif, Diffusion Study Group, 2022 Effects of T2*-blurring on effective resolution of diffusion MRI with spiral and EPI readout

trajectories at 7 T. Sajjad Feizollah, Christine L. Tardif, ISMRM, 2023

Chapter 4:

Multi-shot 3D diffusion MRI sequence for a fast and high-resolution imaging at 3 T- Sajjad Feizollah, Christine L. Tardif, ISMRM, 2024

Co-authored papers

During my PhD, I also contributed to other projects that led to publications. My specific contribution to each paper and abstract is described below.

A size-adaptive radiofrequency coil with integrated NMR field probes for magnetic resonance imaging of the pediatric human brain at 7 T. Pedram Yazdanbakhsh, Christian Sprang, Marcus J. Couch, Kyle M. Gilbert, **Sajjad Feizollah**, Christine L. Tardif, David A. Rudko (2024). Submitted to Magnetic Resonance in Medicine- under review

Contribution: Provided support for field monitoring probe placement and conducted field measurements using integrated probes.

The possible influence of third-order shim coils on gradient-magnet interactions: an inter-field and inter-site study. Nicolas Boulant, Caroline Le Ster, Alexis Amadon, Guy Aubert, Alexander

Beckett, Jean Belorgey, Cédric Bonnelye, Dario Bosch, David Otto Brunner, Guillaume Dilasser, Olivier Dubois, Philipp Ehses, David Feinberg, **Sajjad Feizollah**, Vincent Gras, Simon Gross, Quentin Guihard, Hervé Lannou, Denis Le Bihan, Franck Mauconduit, Frédéric Molinié, François Nunio, Klaas Pruessmann, Lionel Quettier, Klaus Scheffler, Tony Stöcker, Christine Tardif, Kamil Ugurbil, Alexandre Vignaud, An Vu, Xiaoping Wu. (2024). Magnetic Resonance Materials in Physics, Biology and Medicine, 37(2), 169-183.

Contribution: Conducted experiments using provided protocol to measure the gradient response function and investigate the interactions of third-order shim coils.

Abstracts

Workflow and performance measures for integrating magnetic field monitoring with an 8-channel pediatric head coil for 7 T MRI. Christian Sprang, Pedram Yazdanbakhsh, Marcus Couch, Sajjad Feizollah, Christine L. Tardif, and David A Rudko, ISMRM, 2023

A size-adaptive RF coil with integrated NMR field probes for pediatric brain imaging at 7 T. Pedram Yazdanbakhsh, Christian Sprang, Marcus Couch, **Sajjad Feizollah**, Christine L. Tardif, and David A. Rudko, ISMRM, 2024

3D diffusion MRI at 7 T with Universal Pulses for improved image uniformity- Sajjad Feizollah, Daniel Löwen, Marcus J. Couch, Eberhard D. Pracht, Tony Stöcker, and Christine L. Tardif, ISMRM, 2024

Original contributions

Chapter 3

The original contributions to methodology and knowledge of Chapter 3 are listed below.

Three parameters were defined from point spread function (PSF) analysis to characterize image quality: specificity, sharpness and effective resolution. Sequence simulations were performed for echo planar imaging (EPI), partial Fourier EPI (PF-EPI) and spiral trajectories, and these parameters were calculated.

At a matching nominal resolution, EPI has the highest specificity, sharpness and effective resolution compared to PF-EPI and spirals.

Effective resolutions are \sim 45% and \sim 25% lower than nominal resolution at 3 T and 7 T, respectively.

Effective resolutions of spiral trajectory are \sim 10% and \sim 20% lower than EPI trajectories at 3 T and 7 T, respectively.

At a matching effective resolution, spirals offer \sim 50% higher SNR efficiency than EPI and PF-EPI trajectories at 7 T.

A framework was developed for simulating and characterizing dMRI scans acquired with EPI, PF-EPI, and spiral trajectories which is available on GitHub and re-used by another group (https://github.com/TardifLab/dMRI sequence simulations).

dMRI sequences using EPI and spiral trajectories were implemented on a 7 T scanner, optimized for the use of field monitoring probes. A multi-echo GRE sequence, adapted for field

monitoring probes, was also implemented to enhance ΔB_0 field mapping. These sequences can be shared with other sites through sharing websites.

Field measurements described using spherical harmonic terms were incorporated into an image reconstruction pipeline. This pipeline uses a forward model to correct the effects of B₀ field nonuniformities and other gradient imperfections, resulting in scans with minimal artifacts and distortions. It is available on GitHub (https://github.com/TardifLab/ESM image reconstruction).

Chapter 4

The original contributions to methodology and knowledge of Chapter 4 are listed below.

The novel 3D MERMAID sequence was developed to improve the SNR efficiency of dMRI and address most limitations of 2D, 3D, and multi-slab acquisitions. The sequence is available to share with other sites.

Several techniques were incorporated into the developed sequence at 3 T to overcome practical challenges: a single-shot-projection TURBINE trajectory to correct phase errors between shots, double gradient and RF spoiling to eliminate stimulated echoes, the simultaneous use of fat suppression pulses and water excitation to remove strong fat signals, and the use of adiabatic inversion and refocusing pulses to achieve a uniform excitation profile.

The SNR of 3D MERMAID sequence increases exponentially as a function of TR, which shows a significant SNR efficiency compared to other 2D and 3D sequences with increased SNR as a function of $\sqrt{N_{averages}}$.

Phantom and human scans using 3D MERMAID showed SNR efficiency improvements of 30-80% compared to 2D multi-slice sequences at different resolutions and b-values.

Scans using 3D MERMAID with isotropic resolutions of 0.74 mm and maximum b-value of 2000 s/mm² were demonstrated that have an effective TR of 19 s, compared to similar scans using gSlider method with a minimum effective TR of \sim 45 s.

A complete image reconstruction pipeline was developed for the 3D MERMAID sequence, which includes GRAPPA reconstruction of individual TURBINE projections, motion correction through phase removal and rejection of magnitude-affected projections, and compressed sensing reconstruction to enable high radial undersampling factors. The pipeline is available on GitHub at (https://github.com/TardifLab/diffusion_mermaid).

Chapter 1

Introduction

1.1. Motivation

MRI is a unique and versatile tool for imaging human anatomy and measuring physiological mechanisms. Diffusion, which refers to the random motion of particles due to thermal energy, is a phenomenon that can be detected using diffusion MRI (dMRI). In biological tissues, the diffusion of water molecules is constrained by the local microstructure of the tissue. dMRI is thus a non-invasive method to probe the diffusion of hydrogen atoms in water molecules, providing insights into tissue microstructure in vivo.

The signal-to-noise ratio (SNR) of dMRI is inherently low due to the method used to encode diffusion in the MR signal. As a result, image resolution on clinical scanners is limited, particularly for studying tissue microstructure in vivo (typically ~2.5-1.5 mm at 3 Tesla (T)), compared to other imaging contrasts where resolutions of ~0.8-1.0 mm are more commonly acquired.

Ex-vivo dMRI studies of healthy human brains have been performed at isotropic resolutions of ~100-650 μm and validated using histology (Budde & Annese, 2013; Roebroeck et al., 2019; A. Seehaus et al., 2015; A. K. Seehaus et al., 2013). These studies have captured the complex geometry and microstructure of crossing fibers in the white matter, the layered intracortical myeloarchitecture showing radial and tangential cortical projections, as well as short-range U-fibers (Aggarwal et al., 2015; Leuze et al., 2014; Ly et al., 2020). High-resolution post-mortem dMRI has also revealed microstructural alterations of cortical grey matter and small structures in patients such as the hippocampus in Alzheimer's (Zhao et al., 2023), seizures (Ke et al., 2020), and hippocampal sclerosis (Coras et al., 2014), the substantia nigra in Parkinson's (Knossalla et al., 2018), and the corpus callosum in Amyotrophic lateral sclerosis (ALS) (Cardenas et al., 2017). These high-resolution ex-vivo dMRI studies have motivated the development of MRI techniques to enhance SNR efficiency of dMRI to achieve higher resolutions in vivo.

1.2. Rationale and objectives

Current techniques to acquire high-resolution dMRI scans in vivo will be reviewed in Chapter 2. While these methods improve the SNR of dMRI and, consequently, the resolution, a common drawback of most of these techniques is the long scan times, which limits their applicability in clinical settings. Specifically, dMRI experiments designed for microstructure mapping require significant amounts of data, resulting in scan times ranging from ~60 to 100 minutes for resolutions of ~0.75-0.85 mm. Therefore, there remains a need to develop pulse sequences and techniques that are more SNR-efficient and capable of high-resolution diffusion imaging within shorter scan times for studying brain microstructure in vivo.

The specific objectives of this thesis are the following:

Chapter 1- Introduction

- To investigate the effective resolution that can be achieved using efficient, 2D single-shot readout trajectories at ultra-high field.
- To improve SNR efficiency of dMRI further by developing a 3D pulse sequence to achieve submillimeter effective resolutions suitable for investigating microstructure in a feasible scan time on clinical scanners.

1.3. Thesis outline

Chapter 2 provides background on the principles of NMR, as well as the processes of image acquisition and reconstruction, followed by a literature review of existing dMRI sequences and acquisition methods. Chapter 3 and Chapter 4 present a published peer-reviewed journal article and a manuscript submitted for peer-review corresponding to the first and second objectives, respectively. Chapter 3 details the methods used to characterize image quality, the implementation of spiral trajectories at 7 T, and includes extensive SNR measurements along with comparisons between nominal and effective resolutions. Chapter 4 introduces a novel 3D dMRI pulse sequence with high SNR efficiency. The article presents simulation and phantom results, and comparisons with standard 2D dMRI sequences and demonstrates the sequence's ability to acquire high-resolution scans within a feasible scan time. The significance of this research, practical considerations of techniques used, and future work to further improve and apply the findings are discussed in Chapter 5. Finally, Chapter 6 concludes by summarizing the main contributions of this thesis.

Chapter 2

Background

This chapter will briefly explain the basics of nuclear magnetic resonance (NMR) phenomena, the process of image acquisition and image reconstruction, and the fundamentals of diffusion encoding and microstructure modeling.

2.1. Principles of nuclear magnetic resonance

2.1.1. Magnetization and precession

A brief explanation of NMR is provided here, with more detailed descriptions available in Haacke et al. (1999), Nishimura (1996) and Bernstein (2004). Although NMR operates on a quantum mechanical scale, it can be explained using classical physics. Atomic nuclei with an odd number of protons and/or neutrons, such as ¹H, ²³Na, and ³¹P, exhibit spin angular momentum, or spin, due to their charge (Gerlach & Stern, 1922). When these atoms are exposed to a static magnetic field (B₀), two phenomena occur: the formation of a macroscopic magnetization and

precession.

In an ensemble of spins, and in the absence of a static magnetic field, spins are randomly oriented such that no macroscopic magnetization is observed. However, when placed in a static magnetic field, the individual magnetic moments align with or against B_0 and sum up to form a macroscopic magnetization along the z-axis referred to as the equilibrium magnetization M_0 calculated using Equation (1) (Bloch, 1946a) and illustrated in Figure 2.1A.

$$M_0 = \frac{\rho \gamma^2 \hbar^2 I_z (I_z + 1) B_0}{3kT} \tag{1}$$

 ρ represents the number of nuclear spins per unit volume, I_z is the spin operator in quantum mechanics, k is Boltzmann's constant, T is the temperature in Kelvin, \hbar is Planck's constant, and γ is the gyromagnetic ratio, which is unique to different nuclei.

The other phenomenon is precession, typically described as the rotation of individual spins around an axis aligned with the static magnetic field B_0 . The rate (ω_0) at which the spins rotate is known as the Larmor frequency, which can be calculated using Equation (2) (Larmor, 1897).

$$\omega_0 = \gamma B_0 \tag{2}$$

This demonstrates the dependence of the Larmor frequency on the specific nuclei and the magnetic field it experiences. Hydrogen is the most abundant atom in the body and the primary focus for imaging. The gyromagnetic ratio of the hydrogen proton is 42.577478461 MHz/T. In clinical whole-body scanners, the static magnetic field typically ranges from 0.5 to 3 T and is generated by magnets constructed from niobium-titanium, a superconducting material cooled by helium to -269 °C, near absolute zero. Accordingly, the Larmor frequency for hydrogen is 128 MHz at 3 T, and 298 MHz at 7 T.

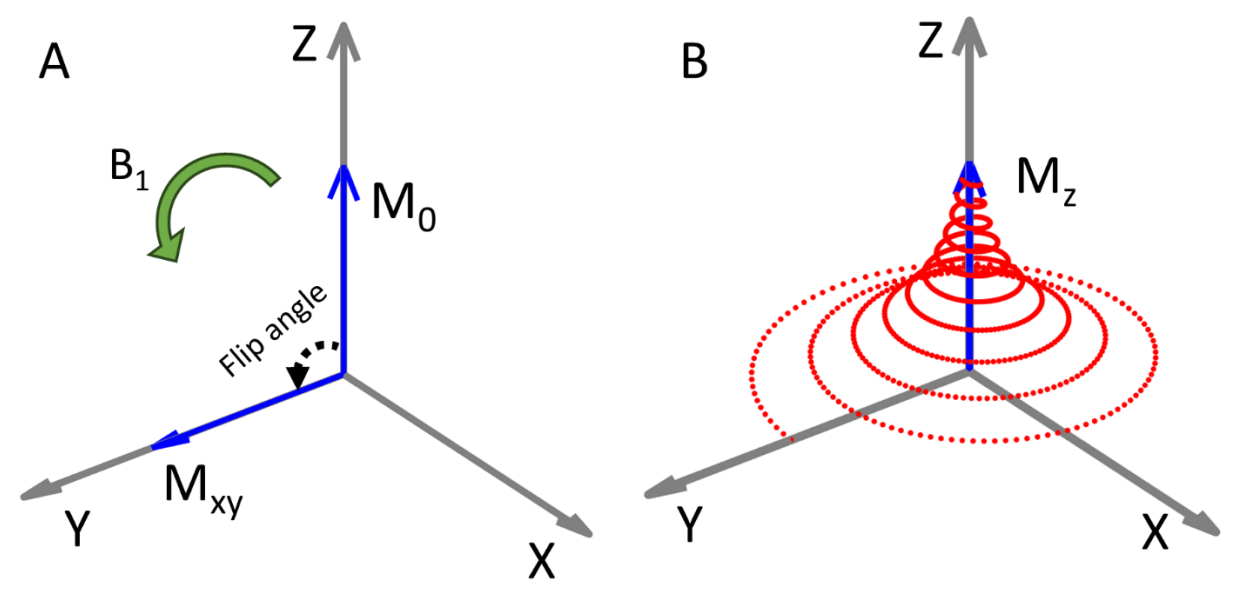


Figure 2.1. A: magnetization at the equilibrium (M_0) along Z, and generated transverse magnetization (Mxy) after applying B_1^+ . B: the path at which magnetization is recovered back along Z, rotating at the Larmour frequency around Z.

2.1.2. Nuclear magnetic resonance phenomenon

When an RF field (B_1^+) at the Larmor frequency is applied perpendicular to B_0 , it interacts with the spins and a resonance phenomenon occurs (Bloch, 1946a; Purcell et al., 1946). The B_1^+ field is generated by RF coils, such as the body coil inserted into the bore of the magnet or a local coil close to the organ to be imaged. The energy of the B_1^+ field with the same frequency as the spins' precession frequency is efficiently transferred to the spins, causing them to transition into an *excited* state resulting in rotation of the macroscopic magnetization vector M towards the transverse x-y plane (perpendicular to the z-axis) (Figure 2.1A). The axis of B_1^+ and amount of energy deposited by B_1^+ determines the axis of rotation and flip angle; a 90-degree flip angle rotates the magnetization M into the transverse plane. The resulting transverse magnetization Mxy formed in the x-y plane rotates about the z-axis at the Larmor frequency.

After the RF pulse is applied, the longitudinal magnetization Mz relaxes back to its

Chapter 2- Background

equilibrium state M_0 . Simultaneously, the transverse magnetization Mxy, in the XY plane, decays over time, but at a different rate (Figure 2.1B). This return to equilibrium is characterized by two MR parameters: the T_1 and T_2 relaxation time constants.

The behaviour of the NMR signal after excitation along three axes was formulated by Bloch in (1946a) as shown in Equations (3).

$$M_{x}(t) = M_{0}e^{-\frac{t}{T_{2}}}\sin\omega_{0}t$$

$$M_{y}(t) = M_{0}e^{-\frac{t}{T_{2}}}\cos\omega_{0}t$$

$$M_{z}(t) = M_{0}(1 - e^{-\frac{t}{T_{1}}})$$
(3)

These equations describe the effects of relaxation and procession on the magnetization as a function of time.

2.1.3. Free induction decay

The longitudinal magnetization Mz is not directly measurable. It is the transverse magnetization Mxy precessing about the z-axis that is measured using a receiver coil due to Faraday's law of induction (Equation (4)).

$$\vec{\epsilon} = -\frac{\partial \vec{\Phi}}{\partial t} \tag{4}$$

The induced electromotive force ϵ is calculated using the changing flux Φ in the coil over time t. The same RF coil used to generate the B_1^+ can be used to detect Mxy, although more commonly, a separate RF receive coil with multiple channels and placed closer to the body is used. The signal induced in the receive coil is demodulated at the Larmor frequency.

The simplest way to acquire a signal from a spin ensemble is by applying an excitation RF

pulse and recording the induced signal in the receive coils corresponding to the transverse magnetization during readout at a specific time called the echo time (TE). This process is repeated at regular intervals known as the repetition time (TR). The signal acquired this way is called the free induction decay (FID). Figure 2.2 shows the evolution of the transverse magnetization, along with a diagram of the different elements, referred to as the sequence diagram.

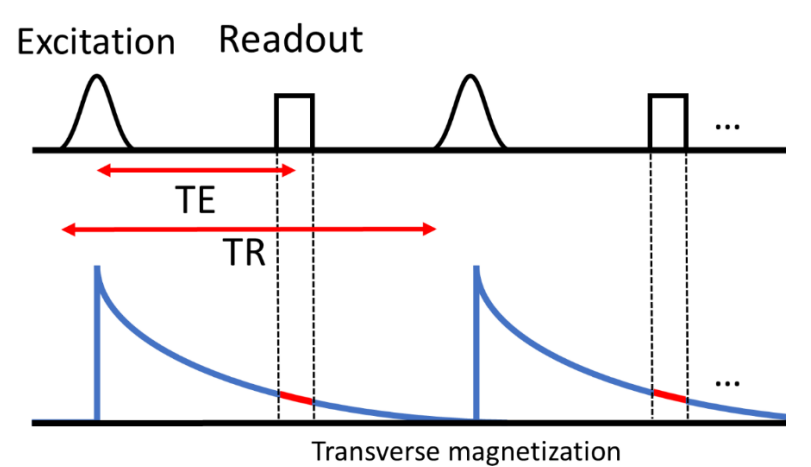


Figure 2.2. FID acquisition. The sequence diagram is shown at the top, and the transverse magnetization is plotted at the bottom $(TR >> 5T_1)$.

In practice, the signal acquired from an ensemble of spins decays faster than T_2 . This is due to magnetic susceptibility effects and main magnetic field inhomogeneities, which slightly alter local precession frequencies resulting in enhanced dephasing of the spins and therefore a more rapid decay of the transverse magnetization. This phenomenon is characterized by the time constants T_2^* and T_2 , as shown in Equation (5).

$$\frac{1}{T_2^*} = \frac{1}{T_2} + \frac{1}{T_2'} \tag{5}$$

2.2. Spatial encoding and image reconstruction

2.2.1. Spatial encoding

The transverse magnetization of an ensemble of spins measured at time TE can be expressed as in Equation (6).

$$M_{xy} = \sum_{n=1}^{N} m_n e^{i\theta_n} \tag{6}$$

m is the magnitude of an isochromat at the TE, θ is the accumulated phase of a spin at TE, and N is the number of spins of an ensemble. This aggregate signal does not include any information about the spatial location of the individual spins. To encode spatial information, gradient coils are used, generating linearly varying magnetic fields along the x, y, and z axes, typically in the range of several mT/m. The addition of these gradient fields to the main magnetic field creates unique magnetic fields at different spatial locations, leading to specific precession frequencies based on the positions of the spins. This variation in precession frequencies causes the spins to accumulate different phases as a function of their location, as formulated in Equation (7), which is described in a frame of reference that rotates at the Larmour frequency.

$$\theta(x, y, z, t) = \gamma \int_0^t B(x, y, z, \tau) d\tau \tag{7}$$

B is the total magnetic field at a specific time and location in space that can be decomposed into linear and non-linear components as described using spherical harmonics in Equation (8) (Haacke et al., 1999).

$$B(x, y, z, t) = \sum_{l=0}^{N_l} k_l(t) h_l(x, y, z)$$
 (8)

 h_l denotes the l-th spherical harmonic basis function, and k_l the corresponding expansion coefficient. Table 2.1 presents the spherical harmonic basis functions up to the 3rd order, and Figure 2.3 shows the corresponding functions plotted at the center x-y plane of the scanner's bore, known as the isocenter.

<i>Table 2.1- S</i>	Spherical	harmonics	basis	<i>functions</i>	un to .	3 rd order
---------------------	-----------	-----------	-------	------------------	---------	-----------------------

0 th order	1st order	2 nd order	3 rd order
			$h_9 = 3yx^2 - y^3$
		$h_4 = xy$	$h_{10} = xyz$
	$\mathbf{h}_1 = \mathbf{x}$	$h_5 = zy$	$h_{11} = (5z^2 - (x^2 + y^2 + z^2)) y$
$h_0 = 1$	$h_2 = y$	$h_6 = 3z^2 - (x^2 + y^2 + z^2)$	$h_{12} = 5z^3 - 3z(x^2 + y^2 + z^2)$
	$h_3 = z$	$h_7 = xz$	$h_{13} = (5z^2 - (x^2 + y^2 + z^2)) x$
		$h_8 = x^2 - y^2$	$h_{14} = x^2 z - y^2 z$
			$h_{15} = x^3 - 3xy^2$

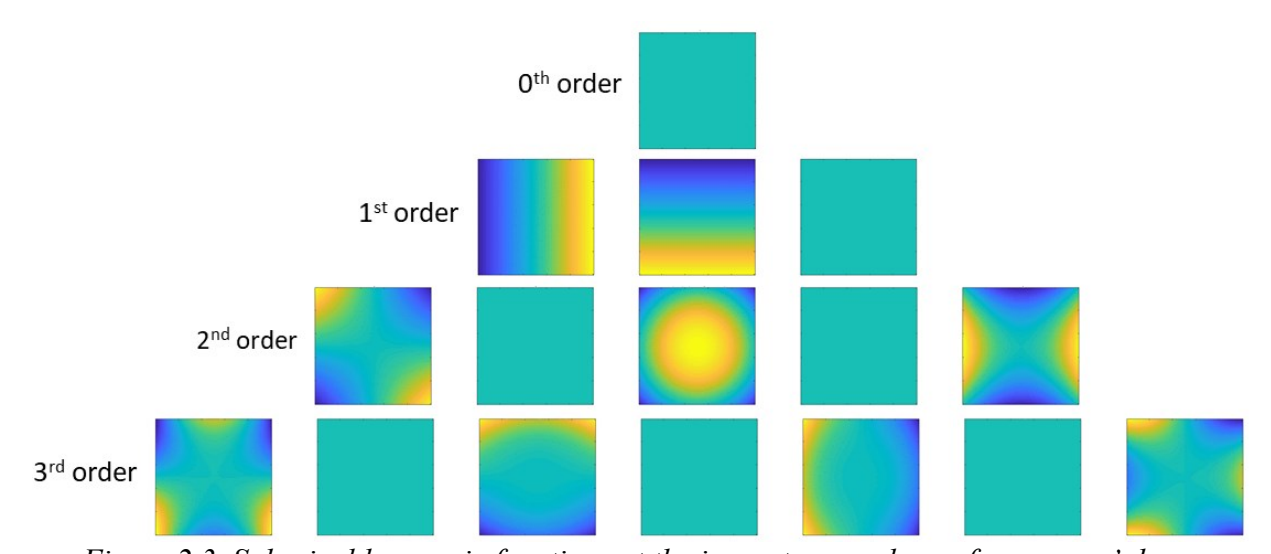


Figure 2.3. Spherical harmonic functions at the isocenter x-y plane of a scanner's bore.

The gradient coils are designed to generate linear magnetic fields, corresponding to the 1st order of spherical harmonics. By varying the magnitude of these gradient fields over time, unique phase terms are generated as the spins accumulate phase, which encodes their spatial information. The phase terms, usually displayed as a waveform as a function of time and referred to as the readout trajectory, encode the location in 3 dimensions from which the MR signal is originating.

When only linear field terms are considered, the 3-dimensional space through which the readout trajectory traverses is known as k-space, as illustrated in Figure 2.4A. K-space, as defined in Equation (7), corresponds to the Fourier space that represents an image in the spatial frequency domain.

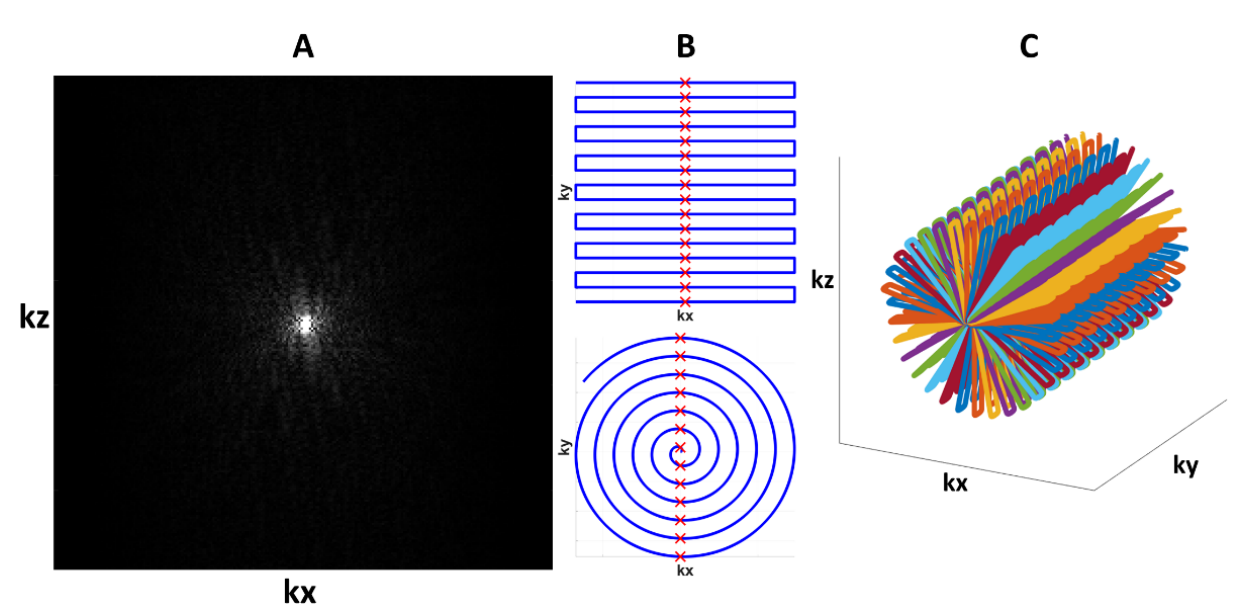


Figure 2.4. K-space and different readout trajectories. A: acquired data of a k-space plane. B: 2D Cartesian (top- Echo Planar Imaging (EPI)) and non-Cartesian (bottom-spiral) readout trajectories. C: a 3D non-Cartesian readout trajectory (TURBINE).

2.2.2. Forward model representation

The signal in Equation (7) is continuously measured along the k-space readout trajectory for each location over time. By using the known phase terms generated by the readout trajectory and the corresponding measured signals, the image can be reconstructed using the forward model (Haacke et al., 1999; Wilm et al., 2011). The matrix form of the forward model is presented in Equation (9).

$$s = Em \tag{9}$$

s is the measured signal at different time points, E is the encoding matrix that includes the

phase information generated by the gradient fields, and m is the magnetization to be determined. This matrix format discretizes the spins in space, and the acquired signal in time. Each discretization step in space represents an ensemble of spins referred to as an isochromat, and the signal is acquired at different time points representing a measured value corresponding to a phase term generated by the readout trajectory. Combining (6), (7), and (8) leads to the encoding matrix in (10).

$$E(x, y, z, t) = e^{i[\gamma \sum_{l=0}^{N_l} k_l(t) b_l(x, y, z)]}$$
(10)

A special case of the forward model occurs when the readout trajectory used to encode spatial information follows a Cartesian path, resulting in a Cartesian k-space (such as rectilinear readout and echo planar imaging trajectories, shown in Figure 2.4B-top). In this case, the encoding matrix takes the form of a Fast Fourier Transform (FFT), which significantly reduces computational complexity. The magnetization *m* can be calculated by directly applying the inverse FFT to the measured signal matrix. This is the most common approach for spatial encoding and image reconstruction in MRI. Alternatively, a non-Cartesian readout trajectory (such as a 2D spiral or 3D TURBINE readout trajectory, displayed in Figure 2.4) can be used. In such cases, the acquired data can be projected onto a Cartesian grid using a technique known as gridding, followed by the application of an inverse FFT to reconstruct the image (Schomberg & Timmer, 1995; Baron et al., 2018).

A powerful aspect of the forward model is its versatility in accounting for various events during acquisition. Any deviations from the nominal encoding matrix, such as imperfect gradient performance, unwanted magnetic fields (Ahn & Cho, 1991), subject motion (Atkinson et al., 1997), or non-uniformity of the main magnetic field, can be modeled and corrected using the forward model (Wald, 2019).

2.2.3. Parallel imaging

A minimum number of spatial encodings in the encoding matrix *E* is required to reconstruct an image. In the Cartesian case, the minimum values are described as 1/FOV for the minimum distance between two adjacent samples in each direction of k-space, and 1/resolution for the minimal extent of k-space coverage. Acquiring fewer data points than these minimums results in undersampling artifacts, which appear as multiple replicas of the FOV for Cartesian images, or as specific aliasing patterns for non-Cartesian images, depending on the trajectory shape.

Modern receive coils consist of multiple channels arranged at different locations in space to cover the full FOV, as shown in Figure 2.5. It is possible to undersample k-space and use parallel imaging techniques to estimate the missing samples by leveraging the spatial information encoded using the different sensitivity profiles of the coil channels. Among the various proposed techniques, SENSE (Pruessmann et al., 1999) and GRAPPA (Griswold et al., 2002), which are used in this work, are the most common and will be briefly described.

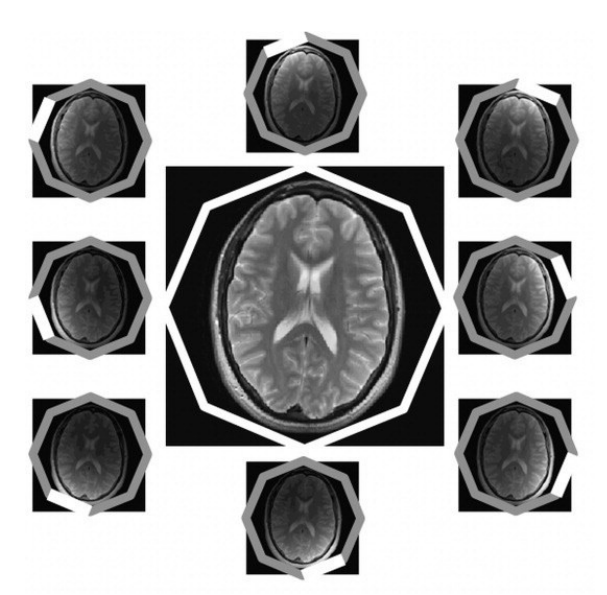


Figure 2.5. Individual images of 8 coils around the FOV (adapted from (Deshmane et al., 2012)).

2.2.3.1. Sensitivity encoding (SENSE)

This technique operates in the image domain, using the undersampled images from each coil channel to reconstruct the final combined image. It relies on solving an equation generated by pixel-wise multiplication of the desired final image and the coil sensitivity profile. Conceptually, each pixel in the final image is a weighted combination of the corresponding pixels from each coil channel, with the weights determined by the coil sensitivity profile. This equation is integrated into the forward model, and the encoding matrix in Equation (10) is modified in Equation (11) to incorporate the coil sensitivity profile.

$$E(x, y, z, t) = \begin{bmatrix} c_1(x, y, z) e^{i\left[\sum_{l=0}^{N_l} k_l(t)b_l(x, y, z)\right]} \\ c_2(x, y, z) e^{i\left[\sum_{l=0}^{N_l} k_l(t)b_l(x, y, z)\right]} \\ \vdots \\ c_n(x, y, z) e^{i\left[\sum_{l=0}^{N_l} k_l(t)b_l(x, y, z)\right]} \end{bmatrix}$$
(11)

Where c_n is the value of the coil sensitivity map of the n^{th} channel at x, y, and z, and E includes all coil channels. S in Equation (9) also includes the measurements of all coil channels. Solving for M results in a single combined image without undersampling artifacts.

2.2.3.2. Generalized autocalibrating partially parallel acquisitions (GRAPPA)

Unlike SENSE, GRAPPA is applied in k-space within the Cartesian grid (Griswold et al., 2002). In this method, a set of weights is calculated from autocalibration signal (ACS) lines, which are fully sampled reference scans (Figure 2.6b) around the k-space centre. These weights serve as coefficients that establish the relationship between a missing k-space sample and its neighboring samples (within the GRAPPA kernel window) across all coil channels (Figure 2.6c). The calculated weights are then used to fill in the missing data of k-space using the acquired samples, as shown in Figure 2.6d. The resulting image, displayed in Figure 2.6e, is free of undersampling artifacts.

K-space undersampling reduces the scan time significantly, however it comes at the cost of SNR loss due to sampling less data and a g-factor penalty that is related to the coupling between coil channels as a result of coil design. Coil sensitivity estimation and GRAPPA weights are not perfect, which may cause residual artifacts in the reconstructed images as well.

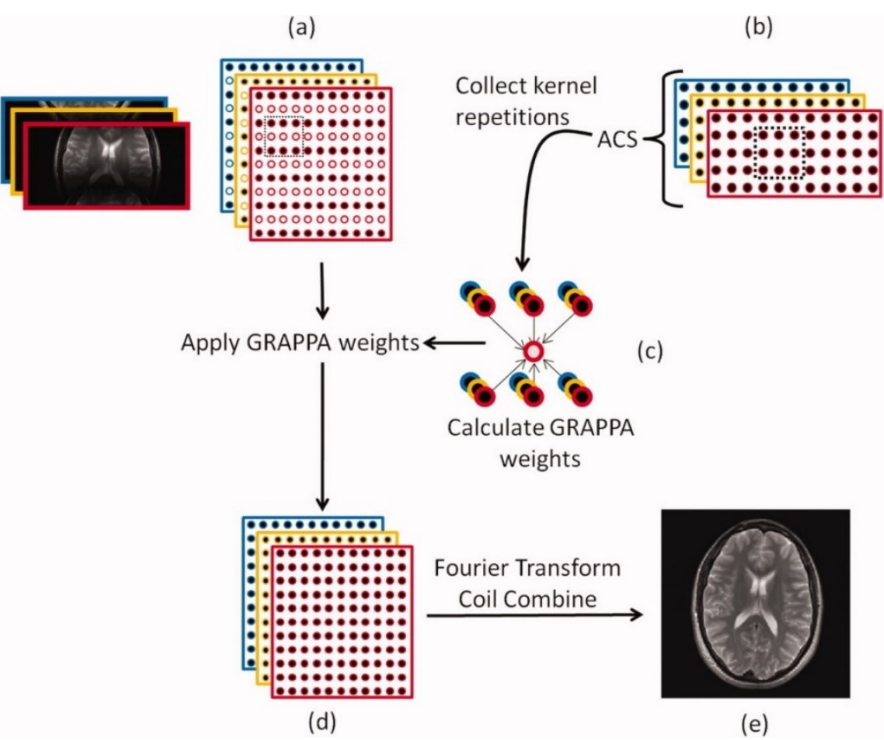


Figure 2.6. Schematic of GRAPPA kernel estimation and reconstruction. a: undersampled k-space with every other line missing. b: fully sampled ACS lines. c: calculating GRAPPA weights. d: fill the missing k-space lines using the weights to reconstruct the image in e. (adapted from (Deshmane et al., 2012)).

2.2.4. Magnetic field monitoring

Imperfections in gradient coils, eddy currents, and concomitant fields induce unwanted linear and non-linear magnetic fields, which adversely affect spatial encoding. This results in a readout trajectory that deviates from the prescribed one. The actual field experienced during the scan can be measured using NMR field probes (De Zanche et al., 2008; Wilm et al., 2015, 2017). These probes consist of a capillary containing an NMR-active sample, such as water or fluorine

Chapter 2- Background

(¹⁹F), to generate the NMR signal, and a solenoid for excitation and signal reception as shown in Figure 2.7.

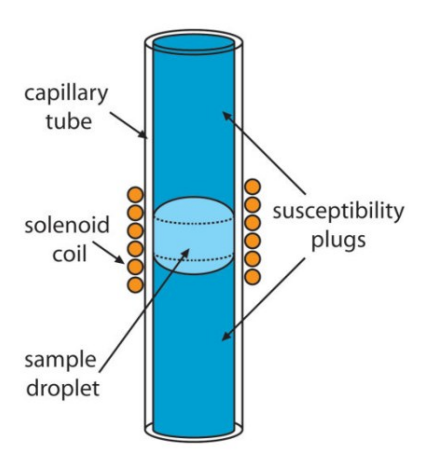


Figure 2.7. NMR field probe consisting of a sample droplet and solenoid coils for excitation and receiving the NMR signal (adapted from De Zanche et al., 2008).

Probes are placed at multiple locations in space to estimate the local magnetic field by measuring the deviation of the precession frequency from the Larmor frequency. Spherical harmonic coefficients are then fitted to the field measurements of the probes using Equation (8). The number of probes required depends on the number of spherical harmonic coefficients needed; for instance, measuring the field up to the 3rd order requires 16 probes that are uniformly distributed on a sphere. The measurement can be performed simultaneously, during the imaging scan, using probes integrated into a receive coil, or in a separate scan session using the same acquisition protocol on a phantom. In this thesis, the Skope system (Skope MRT, Zurich, Switzerland¹) was used to measure the field up to the 3rd order spherical harmonics. The measured field is then used to construct the encoding matrix of the forward model, replacing the nominal readout trajectory with the actual measured trajectory.

.

¹ https://skope.swiss

2.2.5. Solving the forward model

In most cases, the forward model cannot be solved directly by inverting the encoding matrix E. This occurs when the number of spatial encoding samples is lower than the image matrix size in an accelerated scan, or when using non-Cartesian trajectories, where the encoding matrix is not square or is poorly conditioned. In such situations, data from multiple receive channels are used with a fitting method, such as least squares or conjugate gradient, rather than directly inverting the encoding matrix E, as in Equation (12).

$$\boldsymbol{m}^* = \operatorname{argmin}_{\widehat{\boldsymbol{m}}} ||\boldsymbol{E}\widehat{\boldsymbol{m}} - \boldsymbol{s}||_2^2 \tag{12}$$

As with any optimization problem, various regularization techniques can be added to the equation to enforce specific properties of the solution. One such property is sparsity of the image, which is commonly applied in compressed sensing (Lustig et al., 2007), as shown in Equation (13).

$$\boldsymbol{m}^* = \operatorname{argmin}_{\widehat{m}} ||\boldsymbol{E}\widehat{\boldsymbol{m}} - \boldsymbol{s}||_2^2 + \lambda_1 ||P(\widehat{\boldsymbol{m}})||_1$$
 (13)

 λ_I is a regularization parameter that controls the balance between the data fidelity term and the regularization term, and $||P(\hat{m})||_1$ is the L₁ norm of the regularization operator, in this case the wavelet transforms, applied to the image. This sparsity constraint enables the reconstruction of an image from highly undersampled k-space data with little image quality degradation.

2.3. Gradient echo and spin echo pulse sequences

If the FID acquisition includes any spatial encoding as described above, the sequence is called a gradient echo sequence or GRE that produces a T_2^* -weighted image. The TRs generally used in GRE sequences (in the range of a few milliseconds) are much shorter than the T_1 relaxation times of biological tissues (which are in the range of seconds). This leads to the saturation of the available longitudinal magnetization, as there is insufficient time for full recovery. To maximize

the transverse magnetization in steady state, the Ernst flip angle defined in Equation (14) is used.

$$\alpha_{Ernst} = \arccos(e^{\left(-\frac{TR}{T_1}\right)})$$
 (14)

In (1950), Hahn introduced the nuclear magnetic resonance spin-echo. After the initial excitation, a 180° RF pulse, known as the refocusing pulse, is applied to flip the transverse and longitudinal magnetizations. This pulse compensates for effects of local precession frequency differences and rephase the spins, thereby recovering the signal that was lost due to T2' effects. This recovery manifests as a temporary increase in the received signal, with a maximum occurring along the T2 decay curve at the TE. The refocusing pulse is positioned midway between the excitation and the echo, as shown in Figure 2.8.

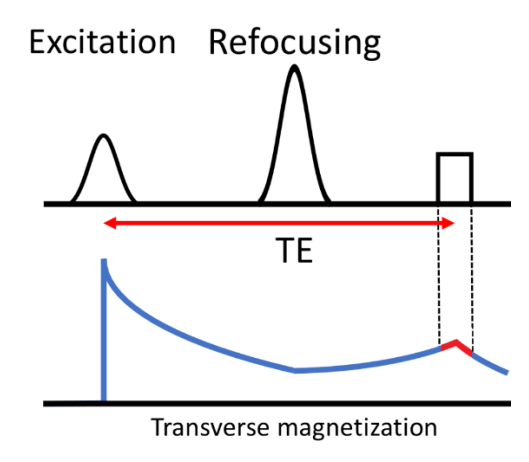


Figure 2.8. Spin-echo acquisition. The sequence diagram for one TR is shown at the top, and the transverse magnetization is plotted at the bottom.

2.4. Diffusion imaging basics

2.4.1. Encoding diffusion in MR signal

An introductory explanation of diffusion imaging is provided here, but more detailed descriptions can be found in (Jones, 2010). Diffusion is a macroscopic phenomenon linked to the microscopic random Brownian motion of particles, driven by thermal energy. This connection was

well established by Einstein in 1905, where he described it using a random walk model, which is formulated in Equation (15).

$$\langle r^2 \rangle = 6Dt \tag{15}$$

r is the displacement of a particle in 3 dimensions, D is the diffusion coefficient, and t is the time of diffusion. The diffusion coefficient of water at body temperature is 0.003 mm²/s corresponding to microscopic displacements on the time scale of an MR experiment.

The effect of diffusion on the MR signal was discovered as an attenuation in the signal in early days by Carr and Purcell (1954), and Stejskal and Tanner (1965a). The attenuation of the transverse magnetization is due to phase dispersion of the spins due to their movement during an NMR experiment. Stejskal and Tanner (1965a) proposed a spin-echo sequence with two additional gradient pulses applied before and after the refocusing pulse as shown in Figure 2.9 to sensitized the MR signal to diffusion in a specific direction. The first diffusion-encoding gradient causes an accumulation of phase in spins, similar to spatial encoding explained in Section 2.4.1 and depicted in Figure 2.9. After the refocusing pulse, the same diffusion-encoding gradient is played out to invert the accumulated phase. Stationary spins experience the same magnetic field before and after the refocusing pulse leading to complete rephasing. Whereas the spins that diffuse along the diffusion encoded direction, experience different magnetic fields before and after the refocusing pulse due to their changed location, therefore, the spins are only partially rephased. This phase discrepancy causes a detectable attenuation in the MR signal. The experiment is repeated to sensitize the signal to diffusion in different directions using a combination of gradients along the x, y, and z axes.

The signal attenuation caused by diffusion gradients depends on the diffusivity of water molecules in the tissue and is characterized by Equation (16) (Le Bihan et al., 1986).

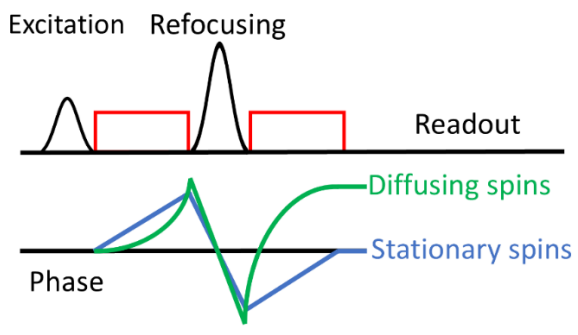


Figure 2.9. Pulse gradient spin-echo (PGSE) experiment is a SE sequence that includes two gradient pulses to encode diffusion. The phase evolution for diffusing and stationary spins are plotted at the bottom.

$$s = s_0 e^{-bD} ag{16}$$

In this equation, s is the measured signal in the presence of a diffusion-encoding gradient, s_0 is the signal measured without the diffusion-encoding gradient, D is the diffusion coefficient, and b is the b-value, which controls the degree of diffusion weighting in the image calculated for rectangular pulses as in Equation (17).

$$b = \gamma^2 G^2 \delta^2 (\Delta - \frac{\delta}{3}) \tag{17}$$

Where G is the amplitude of the gradient, δ is the duration of the gradient, and Δ is the time between the start of the first and second pulses.

2.4.2. Characterizing diffusion in tissues

In biological tissues, the diffusion of water molecules is hindered or restricted by the microstructure of the tissue (e.g., cell membranes), causing the diffusion coefficient to appear lower than that of free water. The diffusivity estimated using MRI, D, is referred to as the apparent diffusion coefficient (ADC) (Le Bihan et al., 1986).

In structured biological tissues, the diffusion of water can preferentially occur in specific directions, known as diffusion anisotropy. For instance, in the case of a bundle of co-aligned axons,

the diffusion coefficient can be high along the bundle, and very low perpendicular to it. In this case, the diffusion coefficient can be represented as a tensor, rather than a single value, as shown in Equation (18) (Basser et al., 1994b).

$$\mathbf{D} = \begin{bmatrix} D_{xx} & D_{xy} & D_{xz} \\ D_{xy} & D_{yy} & D_{yz} \\ D_{xz} & D_{yz} & D_{zz} \end{bmatrix}$$
(18)

The diagonal elements of the diffusion tensor represent the diffusion coefficients along the spatial x, y, and z axes, while the off-diagonal elements indicate the correlation between diffusion in two different directions. This matrix is often described by its eigenvalues, where the off-diagonal elements are zero. The three main eigenvalues, λ_I , λ_2 , and λ_3 correspond to the diffusivities along the three principal axes of the diffusion tensor. From these eigenvalues, the fractional anisotropy (FA) index is calculated, as shown in Equation (19), which quantifies the degree of anisotropic diffusion (Basser & Pierpaoli, 1996).

$$FA = \frac{\sqrt{\frac{3}{2}}\sqrt{(\lambda_1 - \langle \lambda \rangle)^2 + (\lambda_2 - \langle \lambda \rangle)^2 + (\lambda_3 - \langle \lambda \rangle)^2)}}{\sqrt{\lambda_1^2 + \lambda_2^2 + \lambda_3^2}}$$
(19)

Where $\langle \lambda \rangle$ is one third of the trace of the tensor, and FA in a range between 0 and 1 with closer values to 1 showing more anisotropic diffusions.

The displacement probability of free water molecules follows a Gaussian distribution in three dimensions. Therefore, the shape of diffusion of free water is spherical, while in highly anisotropic conditions, it becomes ellipsoidal, with other shapes possible depending on the type of diffusion in the microstructure. A single voxel in diffusion MRI can contain axon fibers with different orientations, as shown in the first column of Figure 2.10. Different fiber orientations can produce similar diffusion distributions, which may lead to ambiguous interpretation of results in

DTI, as seen in the third column of Figure 2.10, where distinct fiber orientations yield the same diffusion tensor. Additionally, diffusion can exhibit non-Gaussian behavior, particularly when water molecules are restricted within a given compartment, such as the intra-axonal compartment in white matter. This behavior is typically observed with b-values higher than 1000 s/mm². In such cases, more advanced methods are required to resolve the fiber orientations within a voxel.

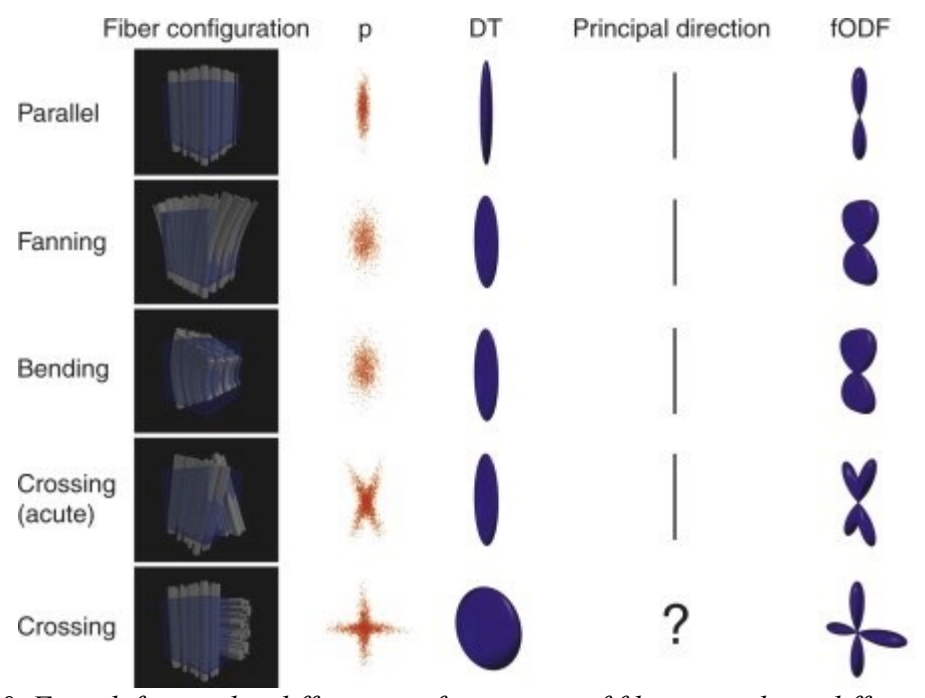


Figure 2.10. From left to right: different configurations of fibers, resulting diffusion scattering pattern, diffusion tensor, principal diffusion direction, and fiber orientation distribution function. (adapted from (Seunarine & Alexander, 2009))

One method to better resolve complex fiber geometries is to calculate the fiber orientation distribution function (fODF), which reveals different diffusion orientations within a voxel (rightmost column in Figure 2.10). One approach for calculating fODF is spherical deconvolution, as proposed by Tournier et al. (2004). In this method, the measured diffusion signal from a voxel is modeled as the convolution of a response function, representing the diffusion signal of a single fiber, and the orientation distribution function of the voxel, as written in Equation (20).

$$S = F \otimes R \tag{20}$$

In this context, S represents the measured signal from a voxel, F is the orientation distribution function of the voxel, R is the single fiber response function, and \otimes is the convolution operator. To calculate F, the response function is deconvolved from the measured diffusion signal. The resulting fODFs are typically visualized using glyphs at each voxel of an image, representing the likelihood of diffusion in various directions, as shown in Figure 2.11.

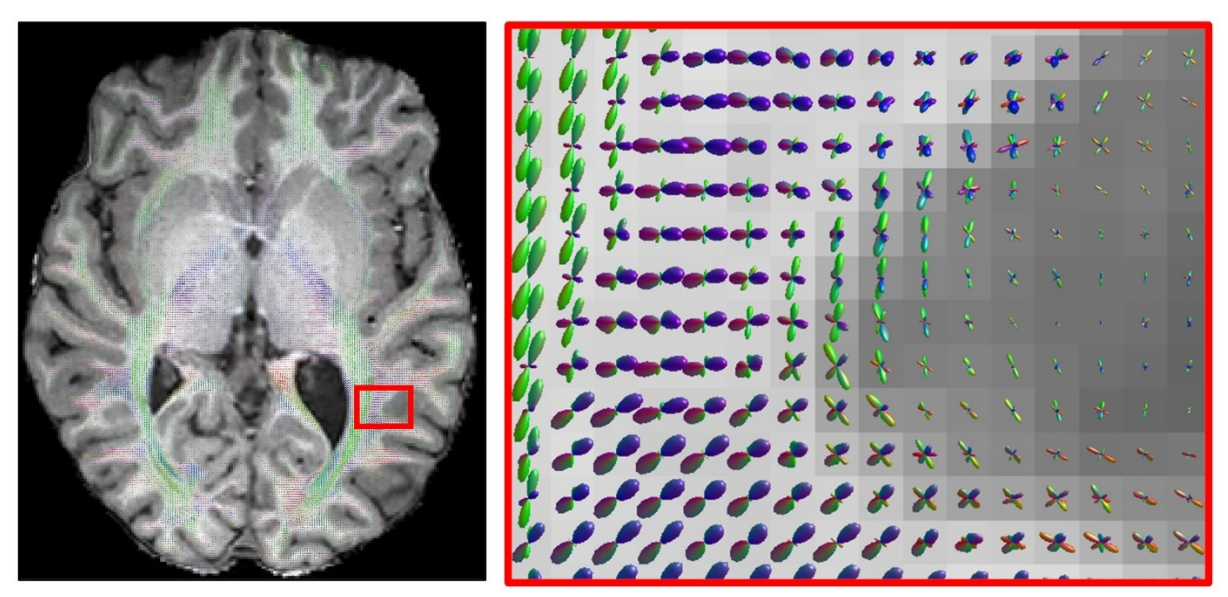


Figure 2.11. FODFs calculated using spherical deconvolution method show different fiber orientations in each voxel.

2.4.3. Microstructure modelling

dMRI has the potential to go beyond the voxel resolution and quantify the microstructure properties of the tissue within the voxel. This is based on biophysical modeling of the cellular compartment contributions to the measured MR signal. Intracellular, extracellular, and free water compartments are the most frequent compartments modeled. They are characterized by specific diffusion distributions in the radial (D_{\perp}) and parallel (D_{\parallel}) directions as shown in Figure 2.12. For example, a stick is used to model diffusion from the intracellular (neurite) compartment (D_a) and

has an almost zero radial diffusivity and high parallel diffusivity. A zeppelin is used to model the extracellular compartment (D_e) with less constrained radial and parallel diffusivities, and a ball for free water compartment describing isotropic diffusion with the same radial and parallel diffusivities.

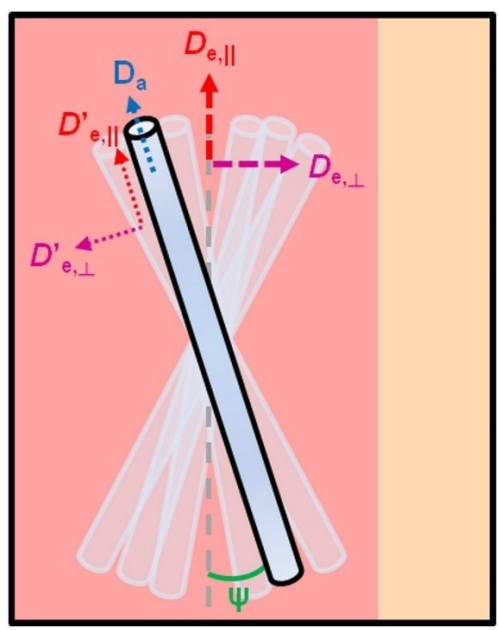


Figure 2.12. Schematic of a white matter fiber showing intracellular, extracellular, parallel and perpendicular diffusivities in mm²/s (adapted from (Jelescu et al., 2015)).

Most of these models incorporate compartments with non-Gaussian diffusion distributions which are observed at high b-values. A high number of diffusion-encoding directions provides the angular resolution needed in the diffusion-encoding space (q-space) to resolve complex fiber geometries. Also, to properly fit a model, different b-values are needed, which are referred to as shells in q-space. Therefore, diffusion protocols used for biophysical modeling typically include multiple b-values and several diffusion-encoding directions, known as multi-shell and multiple direction protocols.

Several multi-compartment diffusion models have been proposed for microstructure

mapping (Kärger, 1985; Fieremans et al., 2010; Novikov, Veraart, et al., 2018; Bai et al., 2020; Palombo et al., 2020a). Neurite orientation dispersion and density imaging (NODDI) (H. Zhang et al., 2012), used in this work, is one of the models that quantifies intracellular, extracellular and isotropic signal fractions using the relationship in Equation (21).

$$A = (1 - v_{iso})(v_{ic}A_{ic} + (1 - v_{ic})A_{ec}) + v_{iso}A_{iso}$$
(21)

Where A is the normalized signal, A_{ic} and v_{ic} are the normalized signal and volume fraction (T₂-weighted signal fraction) of the intracellular compartment, A_{ec} is the normalized signal of the extracellular compartment, and A_{iso} and v_{iso} are the normalized signal and volume fraction (T₂-weighted signal fraction) of the CSF compartment. To limit the number of free parameters when fitting the measurements to model parameters, NODDI fixes parallel diffusivity to 1.7×10^{-3} mm²/s, and isotropic diffusivity to 3.0×10^{-3} mm²/s, as in (Alexander et al., 2010; H. Zhang et al., 2011) and estimates other parameters in Equation (21).

Microstructure models have been developed over time to incorporate different cellular structures in different tissues such as grey matter (e.g., Jelescu et al., 2022; Palombo et al., 2020). A detailed review of multi-compartment diffusion models can be found in Novikov et al. (2018).

2.5. Literature review of diffusion image acquisition techniques

dMRI acquisition methods and diffusion-encoding schemes have been a prominent area of research. Acquisition techniques have focused on enhancing image SNR and geometric fidelity, and spatial resolution while minimizing artifacts. Advanced diffusion-encoding techniques improve accuracy of diffusion measurements and encode various structural information. The focus of this section is reviewing diffusion acquisition techniques that have been used. Recent advancements in this field have been reviewed by Wu & Miller (2017), Gallichan (2018), and Holdsworth (2019). In this section, an overview of dMRI acquisition methods will be presented, categorized into five areas: diffusion-weighted sequences, single-shot, multi-shot, volumetric acquisition techniques, and other acquisition techniques.

2.5.1. Diffusion-weighted sequences

While all dMRI sequences rely on the principle of diffusion sensitization using gradient pulses, as outlined in Section 2.4.1, various implementations have been developed to address the challenges associated with dMRI. The most common dMRI sequence, the pulsed gradient spin echo (PGSE), was proposed by Stejskal and Tanner in (1965b). This method, described in Section 2.4.1 and illustrated in Figure 2.13A, remains the foundation of dMRI techniques to date.

One of the challenges in dMRI is that large diffusion-encoding gradients can induce eddy currents, leading to image artifacts and distortions. A highly effective method for mitigating eddy currents is the twice-refocused sequence (Figure 2.13B) (Feinberg & Jakab, 1990; Wider et al., 1994; Reese et al., 2003; Finsterbusch, 2010). This sequence uses an additional refocusing pulse and two sets of bipolar diffusion gradients, which significantly reduce eddy currents before the readout. The drawback of this technique is the increased echo time and therefore lower SNR.

To shorten scan time, most diffusion sequences use a long readout trajectory such as EPI to acquire the entire 2D k-space in a single TR. This results in geometrical artifacts caused by ΔB_0 . Fast spin echo (FSE) is insensitive to these static field non-uniformities and produces images with high geometric fidelity and minimal susceptibility artifacts (Figure 2.13C) (G. Liu et al., 1996a). This is achieved by incorporating a series of 180° refocussing pulses between short rectilinear readouts instead of a long EPI trajectory. Issues with this method are high SAR at high fields, and the phase errors between readout shots, typically caused by motion. The Gradient And Spin Echo (GRASE) sequence combines FSE and GRE by replacing the rectilinear readout with a very short bipolar GRE (or EPI) readout train (Oshio & Feinberg, 1991; G. Liu et al., 1996b).

Stimulated echo acquisition mode (STEAM), introduced by Merboldt et al. (1985), has also been used for dMRI acquisition mainly for long diffusion-encoding times. This sequence splits the traditional 180° refocusing pulse into two 90° pulses, as shown in Figure 2.13D. Although this approach results in a loss of half the signal, it has been shown to be more effective for long diffusion times, especially at ultra-high field strengths (Tanner, 1972; Reischauer et al., 2012; Lundell et al., 2014).

Most of the sequences reviewed so far are suitable for 2D acquisition techniques. The diffusion-weighted steady-state free precession (DW-SSFP) sequence shown in Figure 2.13E has been proposed as a whole-brain 3D sequence (Le Bihan et al., 1989; Bosak & Harvey, 2001; E.-K. Jeong et al., 2003a; Jung et al., 2009; McNab et al., 2009; McNab & Miller, 2010; McNab et al., 2010; Lu et al., 2012; O'Halloran et al., 2013). Despite its superior SNR efficiency, the DW-SSFP sequence has a complex T₁/T₂ and diffusion contrast, and is highly sensitive to motion, which limits its application for in-vivo imaging. This sequence has been most successful in ex-vivo imaging where there are no motion artifacts (Miller et al., 2012).

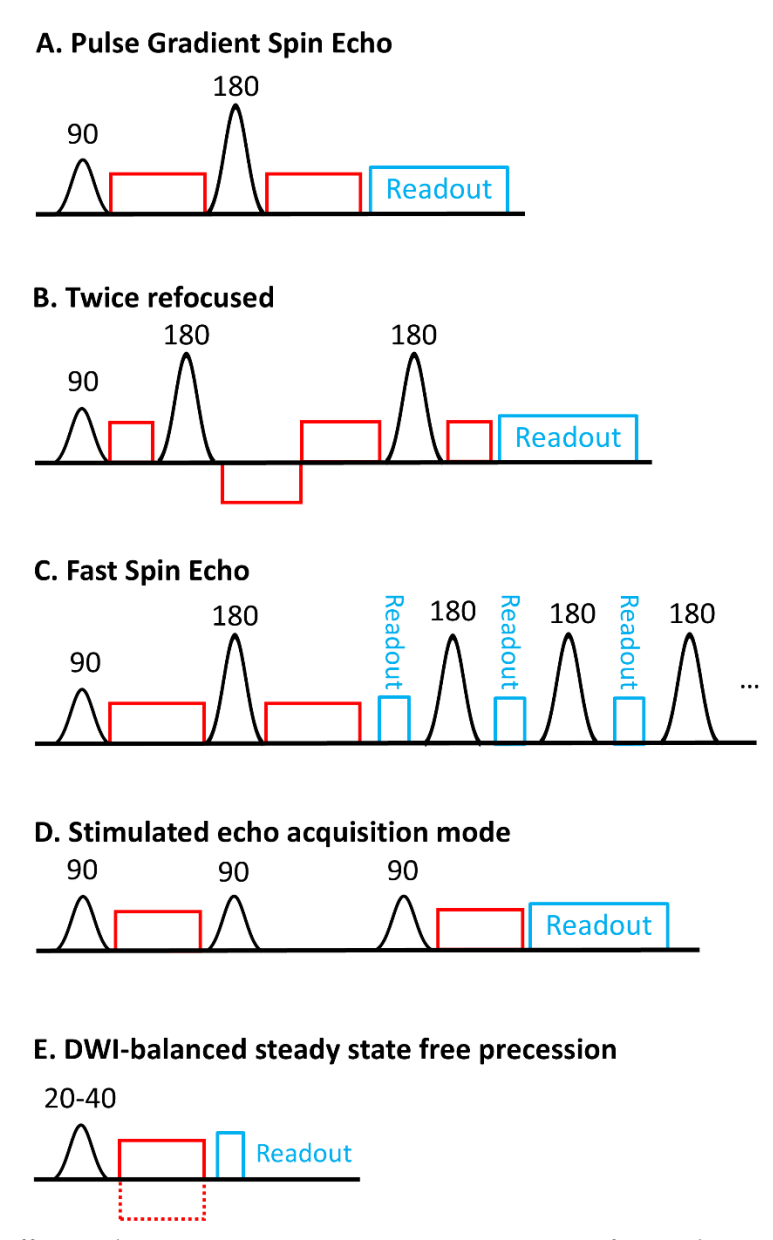


Figure 2.13. Different dMRI sequences: A: PGSE, B: twice refocused, C: FSE, D: STEAM, and E: DW-SSFP.

2.5.2. Single-shot acquisition techniques

Among the reviewed sequences, the PGSE, twice-refocused, and STEAM sequences are most often combined with a single-shot EPI readout. Despite susceptibility and eddy current-related artifacts associated with EPI, this readout method is efficient and robust against motion

artifacts, more specifically when combined with parallel imaging, partial Fourier and multi-slice acquisition. There are also methods to correct these artifacts in post processing (Andersson et al., 2003; Smith et al., 2004).

Several methods have been proposed to reduce the readout time and TE of EPI to minimize the susceptibility artifacts and distortions, as well as scan time by reducing the number of TRs per volume to increase the efficiency. Parallel imaging, discussed in Section 2.2.3, is widely used for reducing scan time and improving image quality by minimizing the effective echo spacing. Common 2D in-plane parallel imaging techniques include SENSE (Pruessmann et al., 1999), GRAPPA (Griswold et al., 2002), simultaneous acquisition of spatial harmonics (SMASH) (Sodickson & Manning, 1997), iterative self-consistent parallel imaging reconstruction (SPIRiT) (Lustig & Pauly, 2010), and Eigenvector-based SPIRiT (ESPIRiT) (Uecker et al., 2014a).

Partial Fourier acquisition is a method used to reduce the echo time, which leverages the symmetry property of k-space in real images. Since MR images contain an imaginary component, various methods have been proposed to reconstruct images. The homodyne approach uses k-space filtering and a low-resolution phase image for reconstruction (Noll et al., 1991), while the projection onto convex sets (POCS) method utilizes a low-resolution phase image and data consistency for reconstruction (Willig-Onwuachi et al., 2005). A more recent method, the virtual coil concept, treats the phase component of the image as a virtual coil and reconstructs it similarly to SENSE (Blaimer et al., 2009).

A major breakthrough was the introduction of the simultaneous multi-slice (SMS) acquisition technique that shortens scan time without compromising the SNR (Larkman et al., 2001; Nunes et al., 2006; Feinberg et al., 2010). SMS acquires multiple slices simultaneously without significant SNR loss, allowing for a significant reduction in the TR and therefor scan time.

Chapter 2- Background

The development of the CAIPIRINHA technique (Controlled Aliasing in Parallel Imaging Results in Higher Acceleration) (Fa et al., 2005; K et al., 2012) further advanced SMS by reducing the g-factor penalty and enabling higher acceleration factors.

These acceleration methods have led to significant reductions in scan time allowing more comprehensive sampling of the q-space with multiple b-values and high angular resolution for microstructure modeling and tractography. Notable contributions from the Human Connectome Project have demonstrated high-resolution dMRI using the 2D PGSE EPI sequence with SMS and GRAPPA acceleration (S et al., 2010; McNab et al., 2013; Setsompop et al., 2013; Uğurbil et al., 2013a; A. T. Vu et al., 2015a). These studies have achieved isotropic resolutions of 1.05 mm at 7 T and 1.25 mm at 3 T, with b-values of 1000 and 2000 s/mm² in total 128 diffusion directions. Figure 2.14 compares scans of the same subject at 3 T and 7 T using the HCP sequence and protocol.

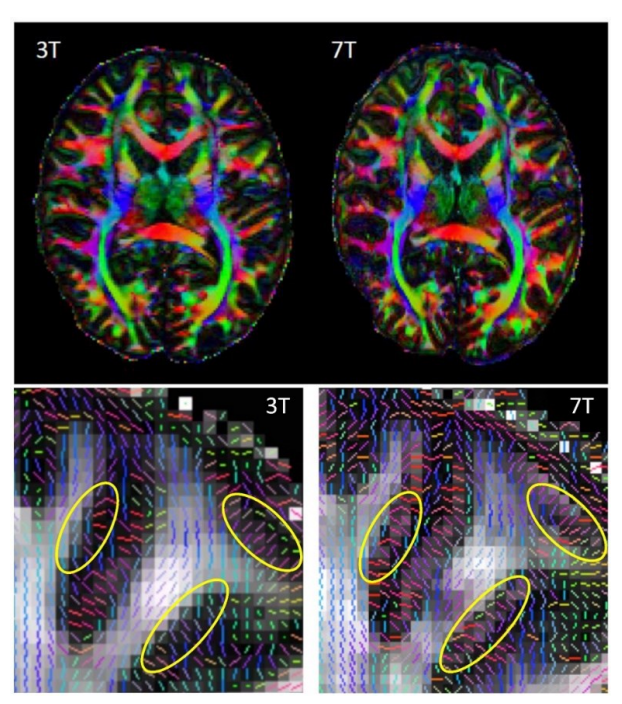


Figure 2.14. Color FA maps of the same subject at 3 T (1.25 mm) and 7 T (1.05 mm) on the first row. Comparison of DTI maps overlaid on FA maps of the same dataset at 3 T and 7 T (adapted from (A. Vu et al., 2015)).

Chapter 2- Background

Spiral readouts were introduced as an alternative to EPI in dMRI due to their efficiency and reduced echo time (Ahn et al., 1986; Meyer et al., 1992). In an EPI readout, the center of k-space is acquired midway through the readout, which necessitates adding idle time before the refocusing pulse to maintain symmetry in the spin echo sequence. In contrast, a spiral readout begins at the center of k-space, eliminating this idle time and thereby reducing the echo time, which improves the SNR. A drawback of spiral readouts is their sensitivity to susceptibility artifacts and gradient imperfections, especially during long readout periods. This limitation has constrained the use of single-shot spiral imaging. In recent years, field monitoring systems (discussed in Section 2.2.4) have been employed to correct these artifacts (Wilm et al., 2015, 2017; Lee et al., 2021a; Feizollah & Tardif, 2023; Varela-Mattatall et al., 2023; Dubovan et al., 2023), as demonstrated in Figure 2.15.

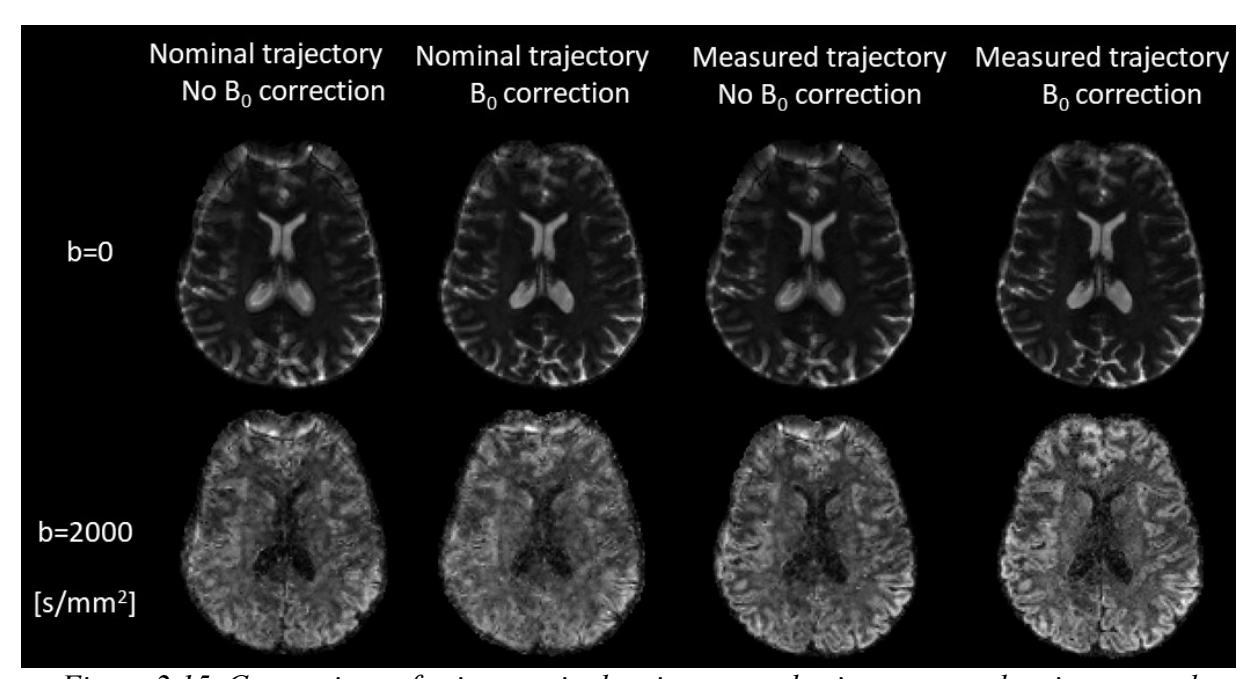


Figure 2.15. Comparison of using nominal trajectory and using measured trajectory and correcting for B_0 nonuniformities (Feizollah & Tardif, 2021).

2.5.3. Multi-shot acquisition techniques

Achieving submillimeter resolution in dMRI requires advanced techniques that offer higher SNR and reduce image artifacts caused by long readout times. Multi-shot methods, which acquire different portions of k-space over multiple acquisitions, have been the primary strategy to achieving these goals (Figure 2.16). The greatest challenge with multi-shot techniques is minimizing artifacts due to motion between shots.

Diffusion-encoding gradients sensitize the MR signal to both microscopic and macroscopic motion, meaning that bulk movement and displacements due to cardiac cycles can cause significant linear and nonlinear phase changes in the MR signal (Feinberg & Mark, 1987; L. Chen et al., 2015; Terem et al., 2021). In this section, multi-shot methods developed to address these phase differences between shots will be reviewed.

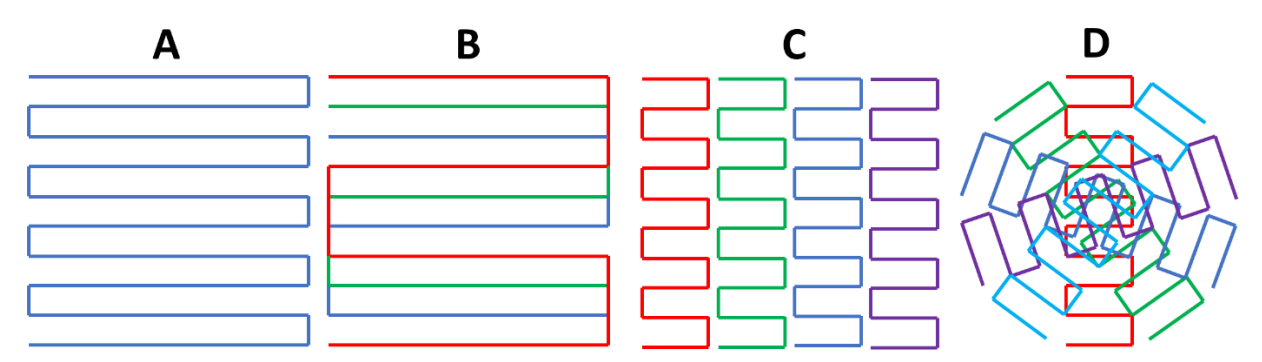


Figure 2.16. Different types of EPI trajectory. A: single shot. B: interleaved. C: RS-EPI, and D: SAP-EPI.

FSE sequences were one of the first sequences that achieved high-resolution images with minimal artifacts. A radial implementation of this sequence helps reduce phase errors between shots (Trouard et al., 1999; Sarlls et al., 2005; Sarlls & Pierpaoli, 2008). The combination of Periodically Rotated Overlapping ParallEL Lines with Enhanced Reconstruction (PROPELLER) and FSE by Pipe (1999a) further minimized phase errors, resulting in robust, high-quality dMRI

images. PROPELLER is a self-navigated acquisition technique where each shot acquires enough lines through the central region of k-space to reconstruct an image, allowing for phase correction between shots before they are combined. Modified versions of this method have been proposed to reduce the number of 180° pulses, which increase the SAR and scan time (Cheryauka et al., 2004; Pipe & Zwart, 2006a; Aboussouan & Pipe, 2009; Z. Li et al., 2011a; Skare et al., 2013; Srinivasan et al., 2018).

Interleaved EPI is a method that acquires k-space using multiple interleaved shots where the spacing between lines in each shot is increased, as illustrated in Figure 2.16B. Phase errors between shots can be corrected using both navigator-based and navigator-free approaches. In navigator-based methods, navigator echoes are acquired either by adding an additional 180-degree pulse after the EPI train followed by a short readout train for the navigator echo, or using a selfnavigating trajectory in which the navigator is acquired at the same time as the imaging data. These navigators provide a low-resolution phase image for each shot, which is used in the image reconstruction process (Anderson & Gore, 1994; Bammer et al., 1999; Dietrich et al., 2000; Atkinson et al., 2006; H.-K. Jeong et al., 2013). More recent approaches omit navigators and rely on image reconstruction techniques to correct phase errors. MUSE (Bruce et al., 2017a; N.-K. Chen et al., 2013; Guhaniyogi et al., 2016b; Truong et al., 2012a; Truong & Guidon, 2014a) and AMUSE (Guhaniyogi et al., 2016a) use SENSE to estimate the slowly varying phase errors for each shot and simultaneously compute magnitude images from all interleaves. However, these methods struggle to accurately estimate phase images in highly segmented acquisitions. Low-rank matrix completion techniques, such as MUSSELS (Mani et al., 2017a; Mani, Aggarwal, et al., 2020; Mani, Jacob, et al., 2020; Hu et al., 2019) have been developed based on the assumption of consistent contrast across all interleaves with slowly varying phase. This approach has enabled the

acquisition of images with high in-plane resolution of 0.375 mm and slice thickness of 8 mm (Figure 2.17) (N.-K. Chen et al., 2013). The main drawback of these techniques is increased scan times (i.e., scan time is proportional to the number of shots).

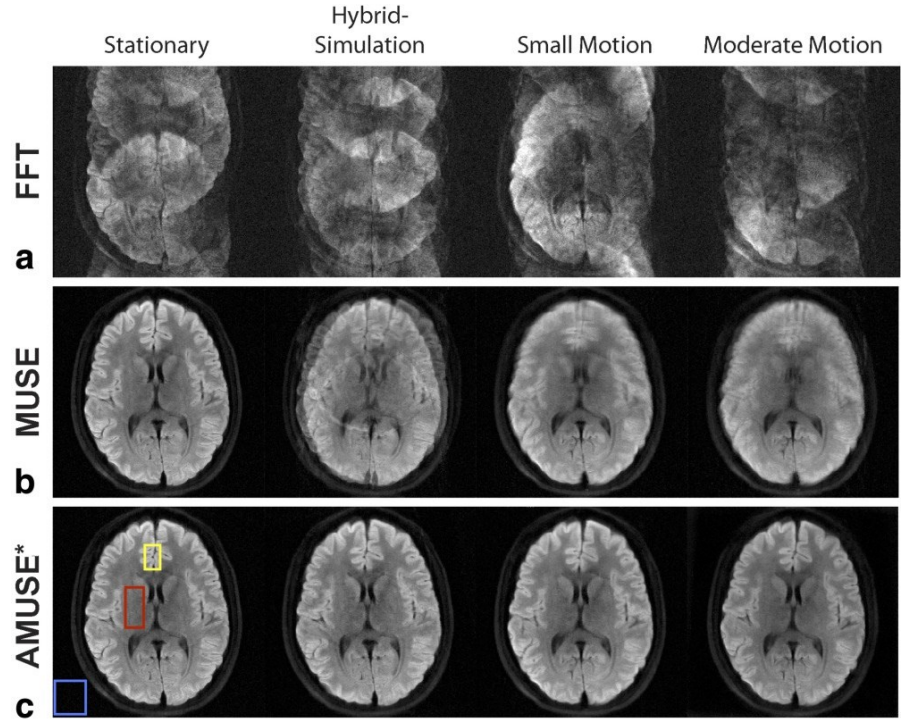


Figure 2.17. Comparison of MUSE and AMUSE in reconstructing interleaved EPI. $0.86 \times 0.86 \times 5$ mm, b-value of 800 s/mm² in 15 directions (adapted from (Guhaniyogi et al., 2016a)).

Readout-segmented EPI (rs-EPI), illustrated in Figure 2.16C, is an alternative approach to high-resolution imaging that also reduces B₀ nonuniformity artifacts by increasing the effective bandwidth along the phase-encoding direction (Holdsworth et al., 2008a, 2009; Porter & Heidemann, 2009a; Heidemann et al., 2010a; Frost et al., 2015). A navigator echo is required in rs-EPI to correct phase errors between shots. A similar technique, short-axis PROPELLER EPI (SAP-EPI), shown in Figure 2.16D eliminates the need for navigator scans (Engström et al., 2008; Skare et al., 2006, 2008; Wen et al., 2018). Similarly to interleaved EPI, rs-EPI and short-axis PROPELLER EPI have much longer scan times. Their main advantage is the reduction of image

Chapter 2- Background

distortions. High in-plane resolution of 0.5 mm for a b-value of 1000 s/mm² in 15 diffusion directions with slice thickness of 3 mm has been achieved with rs-EPI in 35 minutes (Figure 2.18) (Holdsworth et al., 2019).

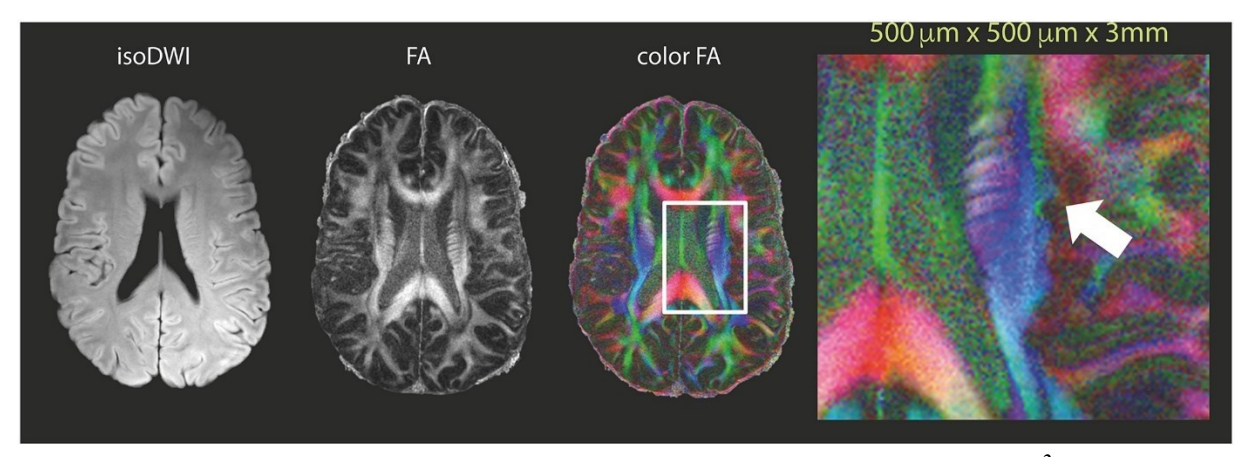


Figure 2.18. FA maps from 15 diffusion directions with a b-value of 1000 s/mm² and in-plane resolution of 0.5 mm acquired using RS-EPI in 35 minutes (adapted from (Holdsworth et al., 2019)).

A specific type of spiral readout, in which the sampling density varies across k-space, has been employed in multi-shot acquisitions (Van et al., 2009; C. Liu et al., 2004a; T.-Q. Li et al., 2005; Avram et al., 2014). In this approach, the central portion of k-space is sampled more densely and serves as a navigator to correct phase errors. This trajectory retains the advantages of the spiral readout, such as minimizing echo time, without the need for an additional navigator acquisition. Alternatively, a spiral-in trajectory has been use to acquire a navigator, followed immediately by a spiral-out acquisition for imaging (Aksoy et al., 2008). Non-navigated approaches have also been proposed, utilizing SENSE similar to MUSE and AMUSE, to iteratively estimate and correct the phase of each shot as shown in Figure 2.19 (Truong et al., 2012b; Truong & Guidon, 2014b; Guo et al., 2016; Jiang et al., 2024).

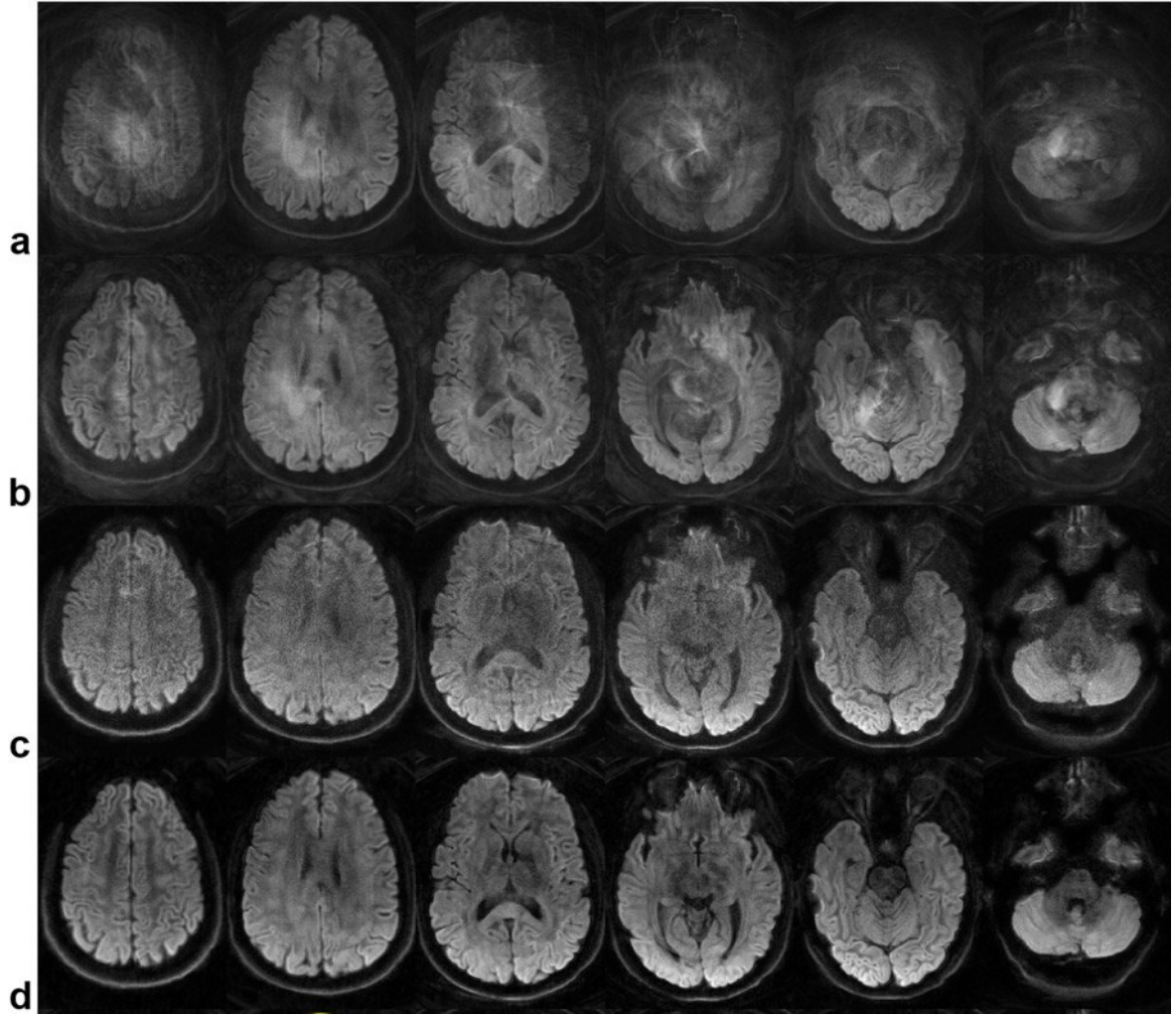


Figure 2.19. Comparison of three different image reconstructions: a: uncorrected, b: direct phase subtraction, c: magnitude averaging over shots, d: iterative phase correction (adapted from (Truong & Guidon, 2014b)).

Instead of correcting phase errors, their source can be eliminated by designing motion-compensated diffusion-encoding gradients. This technique is commonly used in cardiac and body imaging where extreme motion is a significant issue (Geng et al., 2021; Nguyen et al., 2014; Ozaki et al., 2013; Stoeck et al., 2016a; Xie et al., 2014), but is less frequently applied in brain imaging (Prasad & Nalcioglu, 1991; Brockstedt et al., 1995; Clark et al., 2000; Szczepankiewicz et al., 2021). The main limitation of these diffusion-encoding gradients is that they require substantially longer durations, which increases the echo time and leads to SNR loss. However, with recent

advances in high-performance gradients, these motion-compensated gradients can now be designed to have similar duration as normal gradients on a typical gradient systems (Michael et al., 2024a).

2.5.4. Volumetric acquisition techniques

The diffusion imaging techniques described in the previous section are all 2D multi-slice techniques. It is also possible to acquire volumetric data, where a slab or the whole brain is excited rather than individual slices. Volumetric methods typically employ multi-shot techniques to encode the partition dimension. The primary advantage of 3D imaging is the higher SNR it provides, facilitating the acquisition of isotropic, high-resolution images.

A volumetric FOV can be acquired as a single or multiple 3D slabs using multi-shot acquisitions, with additional phase encoding to resolve the third dimension within the slab (Golay et al., 2002; E.-K. Jeong et al., 2006; Frank et al., 2010; Engström & Skare, 2013a, 2013b; Chang et al., 2015; Wu, Poser, et al., 2016a; Bruce et al., 2017b; Dai et al., 2021; S. Liu et al., 2023; Z. Li et al., 2024b). Various types of multi-shot EPI and spiral acquisitions, as reviewed earlier, can be employed. Navigator-based methods from 2D acquisition techniques are often applied here, under the assumption that phase variations within a slab of \leq 2 mm thickness are minimal (Engström & Skare, 2013a; Frost et al., 2014). In this case, SNR is increased compared with 2D acquisition by a factor of $\sqrt{N_{partitions}}$, where $N_{partitions}$ is the number of phase-encoded partitions.

A key challenge with 3D slab-selective techniques is the extended scan time inherent to multi-shot approaches, as well as slab boundary artifacts, which have been partially mitigated by recent advancements such as nonlinear inversion for slab profile encoding (NPEN) in Figure 2.20

(Van et al., 2015; Wu, Koopmans, et al., 2016).

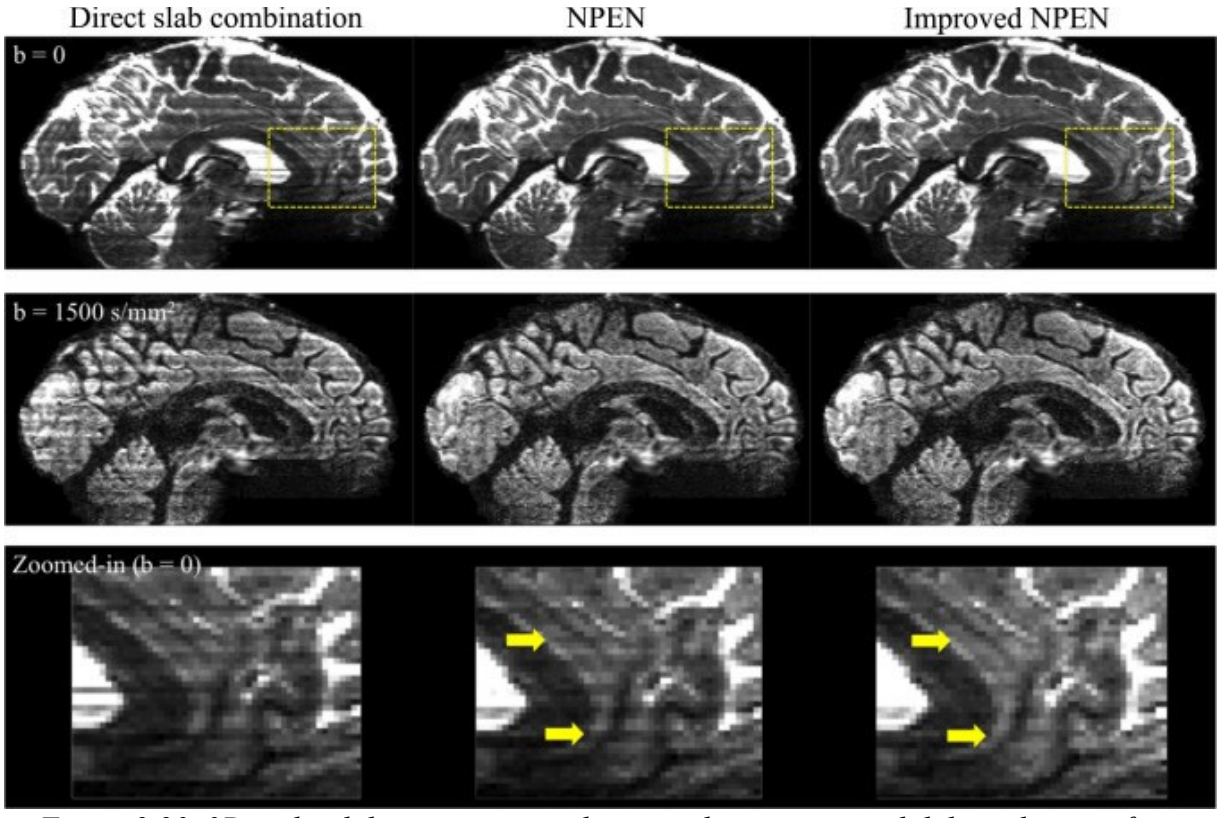


Figure 2.20. 3D multi-slab acquisition and approaches to correct slab boundary artifacts (adapted from (Wu, Poser, et al., 2016a)).

An alternative method for spatial encoding within a slab is by varying RF pulse profiles, as employed in gSlider (Ramos-Llordén et al., 2020; Setsompop et al., 2018; Liao et al., 2021). In this approach, the acquisition is repeated $N_{partition}$ times with different RF pulse profile shapes that selectively omit a different partition at each repetition. The low-resolution slabs are then used to reconstruct partitions by solving a system of equations. This technique eliminates the need to acquire a navigator and has a better robustness to motion. While this method offers a different approach to spatial encoding in the partition direction using gradients, it shares the same disadvantages as the previous method, including longer scan times and slab boundary artifacts. Using this technique, images with an isotropic resolution of 0.6 mm and a b-value of 1000 s/mm²

in 64 directions was achieved in 117 minutes (Figure 2.21).

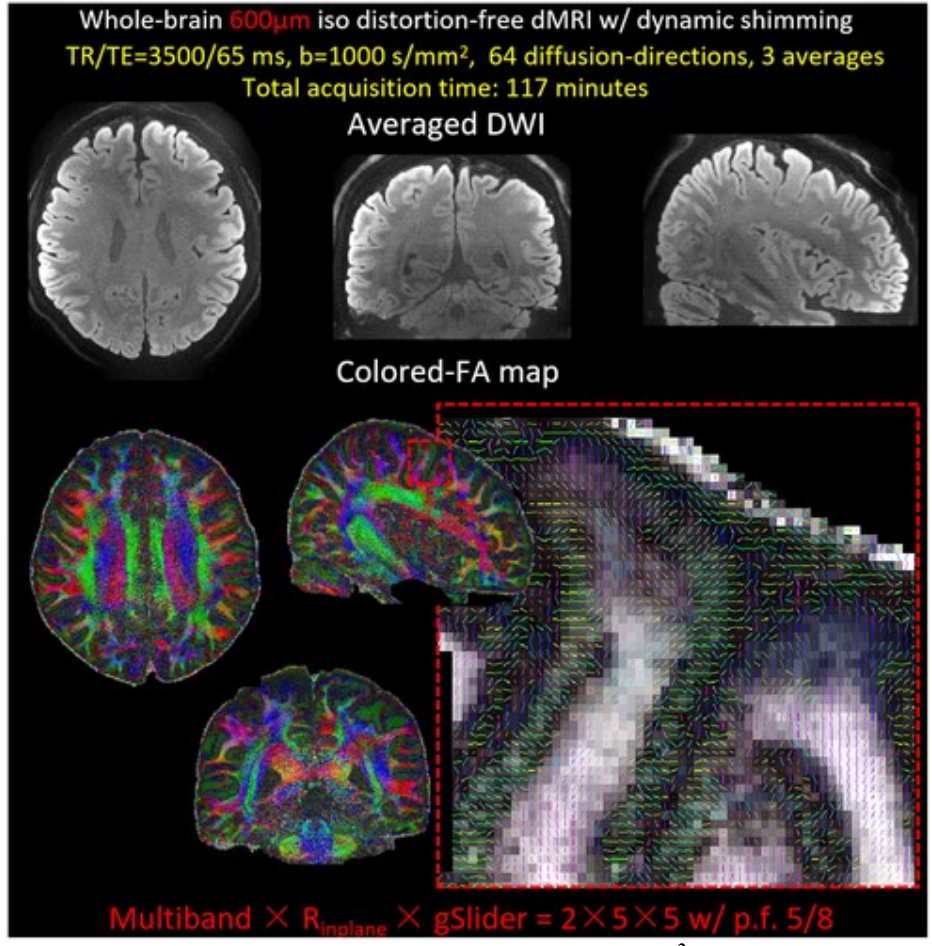


Figure 2.21. Isotopic 0.6 mm scan with a b-value of 1000 s/mm² in 64 directions using gSlider acquisition in 117 minutes (adapted from (Liao et al., 2021)).

There are few 3D acquisition techniques for dMRI that use whole-brain excitation, as opposed to a multi-slab approach. Similar to anatomical imaging, these 3D techniques often employ steady-state sequences with a short TR. One such technique is DW-SSFP mentioned in Section 2.5.1, which is acquired using a navigated trajectory, the Radially Batched Internal Navigator Echoes (TURBINE) readout (McNab et al., 2010) (Figure 2.22). Another recent development is the 3D GRASE sequence, which uses a 3D navigator to correct phase errors (H. Li et al., 2023). However, these sequences have a high sensitivity to motion, and complex T₁/T₂

and diffusion contrast.

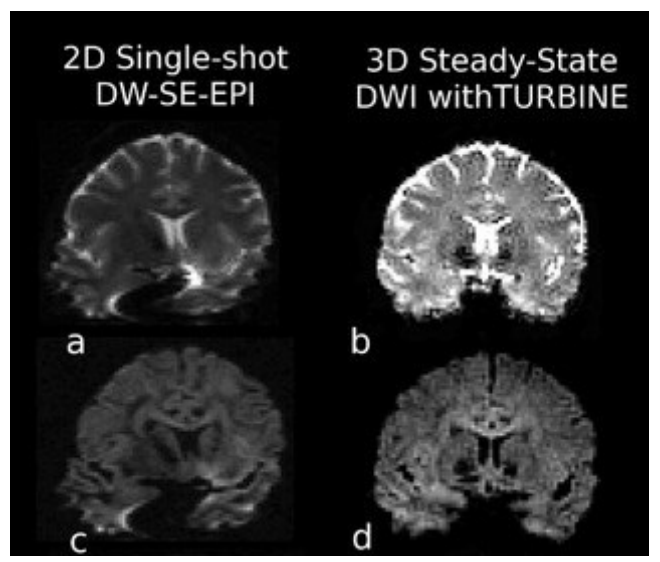


Figure 2.22. Comparison of 2D EPI sequence and 3D DW-SSFP sequence acquired using TURBINE readout (adapted from (McNab et al., 2010)).

2.5.5. Other acquisition techniques

Several additional acquisition techniques can be combined with the methods introduced above. One such technique is reduced field of view (rFOV) imaging, where a smaller region is excited. This can be achieved using methods like inner volume imaging (IVI) (Feinberg et al., 1985; E.-K. Jeong et al., 2005; Wheeler-Kingshott et al., 2002), outer volume suppression (OVS) such as ZOOPPA and ZOOM-EPI (Karampinos et al., 2009; von Morze et al., 2010), or spatially selective RF pulses (Finsterbusch, 2009; Rieseberg et al., 2002; Saritas et al., 2014; Schneider et al., 2013). The main disadvantages of this technique are partial brain coverage and lower SNR due to the excitation of a smaller volume. However, using this approach, isotropic resolutions of ~0.8 mm with a b-value of 1000 s/mm² in 60 directions at 7 T in 60 minutes have been achieved (Figure 2.23) (Heidemann et al., 2012).

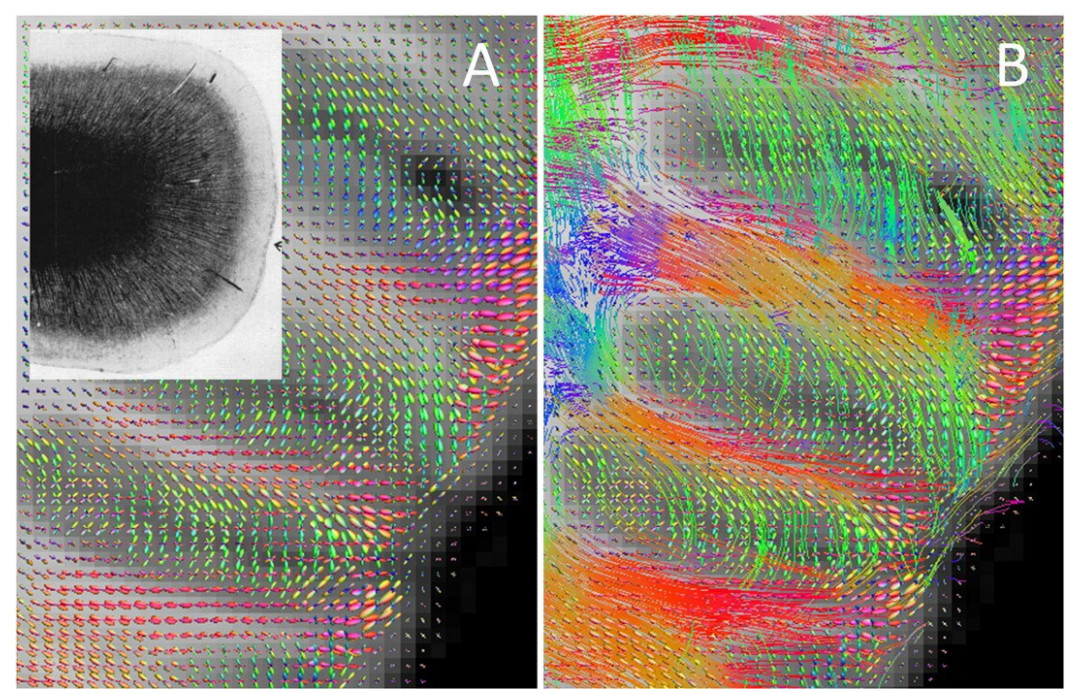


Figure 2.23. White matter fibers entering the grey matter using ZOOPPA method (adapted from (Heidemann et al., 2012)).

Super-resolution techniques are another category of methods that reconstruct high-resolution images from a series of lower-resolution scans with translation or rotation (Scherrer et al., 2011; Vis et al., 2021). Most recently, rotating-view motion-robust super-resolution (ROMER) has been combined with Echo Planar Time-resolved Imaging (EPTI) to achieve images with an isotropic resolution of 0.5 mm at 3 T in 80 minutes (Dong et al., 2024).

PSF mapping technique is an approach that produces artifact-free images (M. D. Robson, Gore, et al., 1997; Zeng & Constable, 2002). This intensive spatial encoding method introduces an additional phase-encoding dimension by shifting the phase-encode lines in small steps. The technique creates a voxel-wise distortion map, resulting in images that are free from susceptibility artifacts, eddy currents, and T₂* blurring (In et al., 2017; Dong et al., 2019).

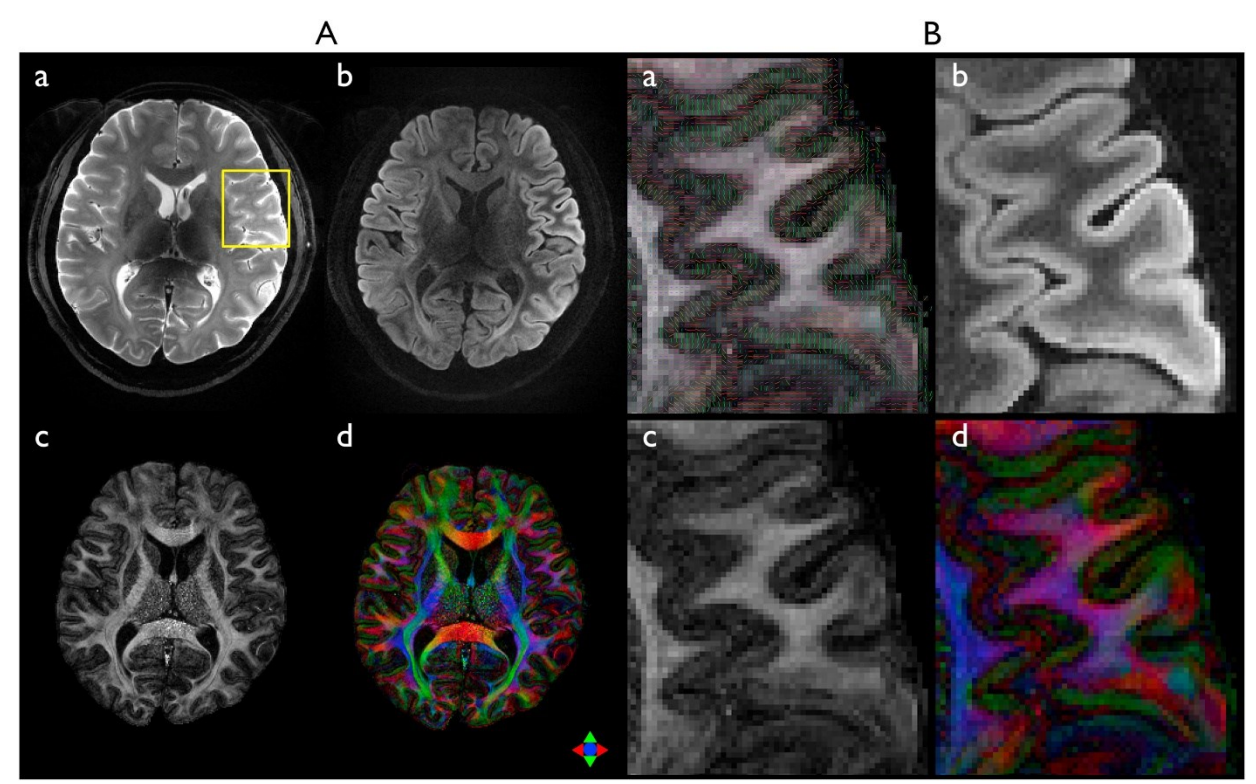


Figure 2.24. High-resolution diffusion scans and color FA maps with a resolution of $0.7 \times 0.7 \times 2.8$ mm, b-value of 1000 s/mm² in 12 directions using PSF mapping imaging in 30 minutes (adapted from (In et al., 2017)).

The methods reviewed here have been developed to enhance the resolution of dMRI and/or address specific limitations, such as susceptibility artifacts. Each technique has its own set of advantages and disadvantages, making it suitable for specific applications. They tend to focus on high-resolution scans, long diffusion-encoding times (to achieve high b-values or non-linear encoding), or dense q-space sampling, and rarely achieve all three due to trade-offs in terms of scan time and SNR. There are thus on-going efforts to develop an SNR efficient sequence to enable high-resolution imaging with prolonged diffusion-encoding time and large number of diffusion encodings within reasonable scan times.

Chapter 3

High-resolution diffusion-weighted imaging at 7 Tesla: single-shot readout trajectories and their impact on signal-to-noise ratio, spatial resolution and accuracy

Sajjad Feizollah, Christine L Tardif

Published in the Neuroimage, July 2023, Volume 274, Page 120159,

https://doi.org/10.1016/j.neuroimage.2023.120159

Preface

As a part of the first objective of this PhD thesis, the effective resolutions were investigated that were achievable in a short scan time. In order to maximize the SNR efficiency, optimal single-shot trajectories were studied, and experiments were performed at 7 T due to the SNR gain provided. The spiral k-space trajectory is one of the most efficient readout trajectories for dMRI.

Furthermore, it enables a shorter echo time than an EPI readout, thus increasing the SNR.

The effective resolution of an MR image differs from the nominal resolution entered at the scanner console due to T2* decay during the readout, and thus depends on the readout trajectory used. This chapter focuses on investigating the SNR improvement and the achievable effective resolution of dMRI at 7 T using a single-shot spiral trajectory in comparison to EPI. This work builds on a recent study performed at 3 T (Lee et al., 2021a) that showed significant SNR improvement using spirals at a matching effective resolution. The trade-off between SNR and effective resolution will differ at 7 T due to the shorter T2* relaxation times. The manuscript outlines the implementation of the spiral readout trajectory for dMRI at 7 T, the integration of a field monitoring system into the image reconstruction pipeline to obtain high-quality scans with minimal artifacts and isolate the effects of T2* decay. The effective resolutions obtained using EPI, partial Fourier EPI, and spiral trajectories are evaluated through image acquisition simulations and PSF characterization. Finally, the SNR of dMRI using EPI, PF-EPI, and spiral trajectories is measured across different nominal resolutions, and compared at a matching effective isotropic resolution of 1.5 mm.

Thought this thesis and based on the terminology that is usually used in MRI, the nominal resolution is the desired in-plane resolution, i.e. the minimum structure size that is resolvable, that is set as a scan parameter and most often determines the dimensions of the image voxel. The effective resolution is the true resolution achieved after considering any external sources that affect the image quality and is quantified in this work by the Full Width at Half Maximum (FWHM) of the PSF.

Abstract

Diffusion MRI (dMRI) is a valuable imaging technique to study the connectivity and microstructure of the brain in vivo. However, the resolution of dMRI is limited by the low signal-to-noise ratio (SNR) of this technique. Various multi-shot acquisition strategies have been developed to achieve sub-millimeter resolution, but they require long scan times which can be restricting for patient scans. Alternatively, the SNR of single-shot acquisitions can be increased by using a spiral readout trajectory to minimize the sequence echo time. Imaging at ultra-high fields (UHF) could further increase the SNR of single-shot dMRI; however, the shorter T_2^* of brain tissue and the greater field non-uniformities at UHFs will degrade image quality, causing image blurring, distortions, and signal loss.

In this study, we investigated the trade-off between the SNR and resolution of different k-space trajectories, including echo planar imaging (EPI), partial Fourier EPI, and spiral trajectories, over a range of dMRI resolutions at 7 T. The effective resolution, spatial specificity and sharpening effect were measured from the point spread function (PSF) of the simulated diffusion sequences for a nominal resolution range of 0.6-1.8 mm. In-vivo partial brain scans at a nominal resolution of 1.5 mm isotropic were acquired using the three readout trajectories to validate the simulation results. Field probes were used to measure dynamic magnetic fields offline up to the 3rd order of spherical harmonics. Image reconstruction was performed using static ΔB0 field maps and the measured trajectories to correct image distortions and artifacts, leaving T2* effects as the primary source of blurring. The effective resolution was examined in fractional anisotropy (FA) maps calculated from a multi-shell dataset with b-values of 300, 1000, and 2000 s/mm2 in 5, 16, and 48 directions, respectively. In-vivo scans at nominal resolutions of 1, 1.2, and 1.5 mm were acquired and the SNR of the different trajectories calculated using the multiple replica method to investigate

the SNR. Finally, in-vivo whole brain scans with an effective resolution of 1.5 mm isotropic were acquired to explore the SNR and efficiency of different trajectories at a matching effective resolution. FA and intra-cellular volume fraction (ICVF) maps calculated using neurite orientation dispersion and density imaging (NODDI) were used for the comparison. The simulations and in vivo imaging results showed that for matching nominal resolutions, EPI trajectories had the highest specificity and effective resolution with maximum image sharpening effect. However, spirals have a significantly higher SNR, in particular at higher resolutions and even when the effective image resolutions are matched. Overall, this work shows that the higher SNR of single-shot spiral trajectories at 7 T allows us to achieve higher effective resolutions compared to EPI and PF-EPI to map the microstructure and connectivity of small brain structures.

3.1. Introduction

Diffusion MRI (dMRI) is sensitive to the motion of water molecules in tissue and thus provides insight into its microstructure (Afzali et al., 2021; Basser et al., 1994c; Jones, 2010). As gradient pulses are employed to encode diffusion in a specific direction, the loss of phase coherence due to motion along that direction results in attenuation of the MR signal (Jones, 2010; Tanner, 1979). This signal attenuation together with long diffusion-encoding times significantly reduces the signal-to-noise ratio (SNR) of dMRI and thus limits the spatial resolution that can be achieved (Polders et al., 2011; Polzehl & Tabelow, 2016). 2-D fast imaging approaches typically used for diffusion imaging further reduce the SNR compared to 3D acquisitions normally performed for anatomical scans. Several imaging techniques have been implemented in dMRI to reduce the echo time (TE) in order to minimize the signal loss due to T₂ decay without sacrificing scan time, including accelerated parallel imaging (Griswold et al., 2002; Pruessmann et al., 1999, 2001), partial Fourier echo-planar imaging (PF-EPI) (e.g., Noll et al., 1991; Blaimer et al., 2009),

non-Cartesian trajectories such as spirals (Block & Frahm, 2005; Assländer et al., 2013), and high performance gradients (Foo et al., 2020; Setsompop et al., 2013; F. Wang et al., 2021).

Complementary techniques have also been developed to increase image resolution that are based on acquiring k-space in multiple shots. These techniques include acquiring multiple interleaves in the phase encode direction (e.g., Butts et al., 1996), multiple segments in the readout direction (e.g., Robson et al., 1997; Porter & Heidemann, 2009; Heidemann et al., 2010), using multi-shot non-Cartesian trajectories (e.g., Liu et al., 2004; Wang et al., 2005; Pipe & Zwart, 2006; Truong & Guidon, 2014), and 3-D multi-slab acquisitions (Dai et al., 2021; Engström & Skare, 2013a; Moeller et al., 2020; Wu, Poser, et al., 2016b). These multi-shot techniques are sensitive to phase differences between shots due to motion and artifacts caused by physiological motion such as breathing, which must be corrected (e.g., Chen et al., 2013; Guhaniyogi et al., 2016; Mani et al., 2017). The above techniques can be combined with g-slider, a multi-shot technique to increase resolution along the slice direction. g-Slider uses a tailored RF pulse profile to excite a slab that modulates single slice information. The acquisition is repeated the same number of times as the slice number each with different RF pulses, and then individual slices are unaliased using the acquired scans (Setsompop et al., 2018; Ramos-Llordén et al., 2020; F. Wang et al., 2021; Ramos-Llordén et al., 2022). Using this method, resolutions as high as 500 µm have recently been achieved (Liao et al., 2022). In addition to these techniques, reduced field-of-view (rFOV) imaging has been also proposed in which reduction in the FOV results in an increased distance between two adjacent k-space lines allowing shorter readout duration to minimize T₂* signal decay (e.g., Feinberg et al., 1985; Karampinos et al., 2009; Saritas et al., 2014). Although this method covers a small region, it can be used repetitively for a whole-brain acquisition which increases the scan time similar to other techniques. Using these techniques, a typical diffusion-weighted sequence

with 64 directions can take \sim 45-60 minutes, which limits the application of high-resolution dMRI in clinical research. This has motivated the development and optimization of single-shot readout approaches to improve dMRI SNR and resolution.

One way to boost the SNR is to scan at ultra-high magnetic field (UHF), which offers an increase in the intrinsic sensitivity and thus the opportunity to acquire high-resolution scans. The SNR has a supralinear ($\sim B_0^{1.95}$) relationship with the main magnetic field (B₀) over a range of about 3 to 7 T (Pohmann et al., 2016). However, due to shorter T₂ and T₂* relaxation times at UHFs leading to a faster signal decay, the benefit of UHF imaging for dMRI depends on the echo time (Gallichan, 2018; Uğurbil et al., 2013b). Efficient readout trajectories that reduce TE can maximize the SNR increase provided by UHF imaging.

Single-shot spiral acquisitions are among the most efficient trajectories (Assländer et al., 2013; Engel et al., 2018; Lee et al., 2021a; Wilm et al., 2017). Center-out spiral trajectories minimize the echo time by starting acquisition from the k-space center, resulting in a significant SNR advantage (Lee et al., 2021a). Furthermore, acquiring with a spiral pattern avoids sharp changes in the trajectory direction that decrease speed due to limitations in gradient slew rates and peripheral nerve stimulation (PNS). Additionally, spiral trajectories inherently have zero gradient moments at the k-space center which make them robust to flow artifacts (Nishimura et al., 1995). The disadvantage of this type of k-space sampling is increased sensitivity to gradient imperfections and B₀ field non-uniformities that cause image blurring and ring-shaped artifacts (Block & Frahm, 2005).

The development of field monitoring probes allows us to measure dynamic field imperfections and use this information during image reconstruction to minimize image artifacts.

Application of these field probes has significantly improved dMRI image quality for EPI and spiral

trajectories at 3 T at a nominal in-plane resolution of 1.3 mm (Lee et al., 2021a; Wilm et al., 2015, 2017), and at 0.69 mm using high-performance gradients (Wilm et al., 2020). Ma and colleagues (2020) used field monitoring probes to correct artifacts caused by gradient imperfections in the Human Connectome Project with an isotropic resolution of 1.05 mm diffusion EPI protocol at 7 T. To the best of our knowledge, the advantages of single-shot spirals for dMRI at 7 T has not been investigated.

Although the SNR is an important factor in limiting image resolution, it is not the only contributing factor. The T_2^* signal decay during the readout will cause a blurring artifact that depends on the k-space sampling pattern, such that the effective resolution is lower than the nominal resolution of the scan. This blurring effect is enhanced at UHFs due to the shorter T_2^* relaxation times of brain tissue: T_2 and T_2^* is nearly halved at 7 T compared to 3 T (Cox & Gowland, 2010; Peters et al., 2007). This lower effective resolution reduces the benefit of moving to UHF for high-resolution dMRI. Reischauer and colleagues (2012) showed that a lower effective resolution is achieved for dMRI at 7 T in comparison to 3 T using an EPI readout with the same acceleration factor. Engel and colleagues (2018) showed that effective resolution of a single-shot T_2^* -weighted GRE spiral acquisition at 7 T is approximately 1.4 times higher than the nominal resolution. The impact of EPI and spiral readout trajectories with different acquisition parameters on image quality has not been thoroughly investigated at 7 T.

The aim of this study is to determine the optimal single-shot readout trajectory for high-resolution dMRI at 7 T by investigating the trade-off between SNR and effective resolution of various k-space trajectories. We use simulations to characterize the sole impact of T_2^* decay on spatial resolution and accuracy of dMRI using a PSF analysis for EPI, PF-EPI and spiral readout trajectories. In-vivo scans corrected for eddy currents and static field nonuniformities are used to

validate the simulation results, and compare the SNR of the different trajectories at matching nominal resolutions. Finally, scans with matching effective resolution were acquired to investigate the SNR and efficiency of the different trajectories.

3.2. Methods

3.2.1. Artifact and blurring correction due to imperfections in spatial encoding

There are spatio-temporal deviations from prescribed magnetic field gradients during the readout, mainly due to eddy currents and concomitant fields. Furthermore, there are subject-specific static field non-uniformities (ΔB_0), and dynamic field perturbations related to subject motion and physiology such as breathing. These field deviations result in the accumulation of additional phase terms during the readout as a function of spin location in space, which causes inaccuracies in spatial encoding. These inaccuracies result in ghosting artifacts, blurring, and the appearance of unwanted signal patterns that depend on the readout trajectory used (Bernstein, 2004). In order to investigate the sole effect of T_2^* signal decay during the readout on the PSF, image artifacts caused by these sources must first be corrected. We measured the spatio-temporal dynamics of the magnetic field using 16 field monitoring probes (Skope MRT, Zurich, Switzerland) and acquired a static ΔB_0 field map. This information was included in the image reconstruction pipeline using the expanded signal encoding model described below to minimize image artifacts. The differences in image quality between the reconstructed images acquired using different k-space trajectories are therefore primarily due to T_2^* signal decay during the readout.

3.2.2. Image reconstruction using the expanded signal model

The expanded signal model is a generalized form of the Fourier transform which is typically used for image reconstruction. Unlike the Fourier transform, the power of this method is that it can model the image acquisition using any basis function for spatial encoding, and thus can include terms to describe deviations from the prescribed linear field (Wilm et al., 2011). This approach can minimize image artifacts for cartesian and non-cartesian imaging, however its application has been limited by its significant computational requirements leading to long image reconstruction times. With recent advancements in computing hardware, it is gradually finding its way into image reconstruction pipelines.

A discretized form of the expanded signal model in time and space that accounts for gradient imperfections and B₀ spatial non-uniformity was implemented to reconstruct images using (22),

$$s = Em \tag{22}$$

where s is a matrix of samples of the measured MR signal over time, m is a matrix of the magnetization in space, and E is the encoding matrix of which elements are calculated as in (23).

$$\boldsymbol{E}_{\gamma,r,t} = c_{\gamma}(r).\,e^{-i\varphi(r,t)} \tag{23}$$

 $c_{\gamma}(r)$ is the sensitivity of coil γ at position r, and $\varphi(r,t)$ is the accumulated phase of a spin at position r and time t according to (24).

$$\varphi(r,t) = k_0(t) + \sum_{b=1}^{L} k_b(t) h_b(r) + \Delta B_0(r).t$$
(24)

 $k_0(t)$ is the measured zero-th order spherical harmonic term or dynamic ΔB_0 over time, $k_b(t)$ is the coefficient of the spherical harmonic basis function b that is calculated from the dynamic field probes measurements during the readout, and $h_b(r)$ is the spherical harmonic basis function b. L is the number of spherical harmonics coefficients, and $\Delta B_0(r)$ is the inhomogeneity of the main magnetic field (B₀) at position r. Images are reconstructed by solving for m in (22) using the Conjugate-Gradient (CG) method.

CG is an iterative reconstruction method that requires a termination criterion that is typically determined empirically. In every iteration, CG adds a small amount of noise to the solution; therefore, finding the optimal stopping point to achieve a high-quality reconstruction while avoiding excessive addition of noise is important. We used the same approach to stop the reconstruction as used by Lee and colleagues (2021b). Iteration was stopped when the difference images of two consecutive iterations had no visible structures. A minimum of 6 iterations was used. In general, higher resolutions and under-sampling factors required more iterations (up to 16). Spirals usually converged faster than EPI and PF-EPI for a given resolution.

In-house MATLAB code optimized for GPU processing was developed for image reconstruction on a workstation with Intel 11700F CPU, 64 GB of RAM, and an NVIDIA GeForce RTX 3090 graphics card with a reconstruction time of 1.8-0.3 seconds per slice, depending on the matrix size and trajectory duration.

3.3. Simulations

3.3.1. Sequence simulations

Diffusion-weighted spin-echo sequences with EPI, PF-EPI, and spiral readout trajectories were simulated in MATLAB. The excitation and refocusing pulse durations used in the simulations and in-vivo scans were set to 2.56 and 6.40 ms respectively to suppress the fat signal using the method by Ivanov et al. (2010) as used in the Human Connectome Project (A. T. Vu et al., 2015b). The diffusion-encoding duration was calculated based on trajectory specifications for a b-value of 2000 s/mm² with a maximum gradient amplitude and slew rate of 73 mT/m and 200 T/m/s respectively, as used on the Siemens Terra 7 T scanner.

Readout trajectories were simulated for resolutions of 0.6 to 1.8 mm isotropic with 0.1-mm

increments. Fixed parameters for all trajectories include: field-of-view (FOV) = 256×256 mm², repetition time (TR) = 5000 ms, and sampling rate of 1 MHz. EPI trajectories were generated with the same gradient limitations used for the diffusion-encoding, and the following parameters: acceleration factors (R) along phase encode (PE) direction = 2, 3, and 4, bandwidth-per-pixel = 1384 Hz, PF factor = 0.75, and spatial encoding in the anterior-posterior direction. Spiral trajectories were generated using the method in (Hargreaves, 2001) with a maximum gradient amplitude of 27 mT/m and slew rate of 160 T/m/s to avoid PNS and critical acoustic resonance frequencies of the gradient system. Three spiral trajectories were generated corresponding to acceleration factors R of 4, 5, and 6 respectively.

3.3.2. Point spread function characterisation

For the PSF analysis, a single point in the center of the image domain was simulated with T₁, T₂, and T₂* relaxation times of the GM/WM set to 1300/800, 72/79, 66/46 ms at 3 T, and 2000/1200, 47/47, 33/26 ms at 7 T respectively (Cox & Gowland, 2010; Peters et al., 2007; Rooney et al., 2007; Wansapura et al., 1999). The simulated signal decay was sampled at the time points along the different trajectories to fill k-space. For PF-EPI, the missing part of k-space was filled based on the conjugate symmetry feature of k-space.

In EPI-based trajectories, considerable signal decay occurs in the PE spatial encoding direction compared to the frequency-encode (FE) direction due to the longer time difference between adjacent k-space points along the PE direction in comparison to the FE direction. Consequently, T2* blurring will be more significant along the PE direction. For spiral trajectories, the signal decays uniformly in all radial directions. The effective resolution of each protocol was determined in PE direction using the full width at half maximum (FWHM) of the PSFs for the GM and WM.

Two-dimensional PSFs of the simulated k-space data for the WM were calculated on a 4096×4096 grid image using the image reconstruction method described in Section 3.2.2. Shape and magnitude of the main lobe and side lobes affect the contribution of other voxels to the final value of the central voxel, and its contrast with respect to neighbouring voxels. To characterise these effects, we define below the specificity, sharpness, and effective resolution of the PSF adapted from previous works (Chaimow et al., 2018; Engel et al., 2022). The specificity is defined as the integral of the main lobe within the nominal voxel size in both PE and FE directions normalized by the integral of the rest of the PSF outside the nominal voxel.

$$Specificity = \frac{\sum main\ lobe}{|\sum side\ lobes + residual\ main\ lobe|}$$
(25)

While positive side lobes have an overall blurring effect, negative lobes cause sharpening of the resulting image. Sharpness is defined as in Equation (26), of which higher values indicate a greater sharpening effect of the PSF.

$$Sharpness = \frac{|\sum negative \ side \ lobes |}{|\sum positive \ side \ lobes + residual \ main \ lobe|}$$
(26)

3.4. Experiments

3.4.1. In-vivo scans to validate simulation results

To validate the simulation results, a volunteer (female, 24 years old) was scanned on a 7 T Terra scanner running VE12U-SP01 (Siemens, Erlangen, Germany) using a single channel transmit and 32-channel receive coil (Nova, Wilmington, USA). All scans were approved by the Research Ethics Board of the Montreal Neurological Institute, and informed consent was obtained from all subjects.

Most scan parameters were similar to the Human Connectome Project 7 T protocol (A. T.

Vu et al., 2015b). The subject was scanned at a nominal isotropic resolution of 1.5 mm. While only a few (40) slices were acquired to reduce the reconstruction time, the TR of the protocols was set to 5 seconds to avoid signal saturation. All scan parameters are listed in Table 3.1. Coil sensitivity and ΔB_0 field maps were estimated using a bipolar GRE scan with 6 echos, $TE_1 = 3.81$ ms, and $\Delta TE = 1.07$ ms, in-plane resolution = 1.5 mm covering the same field view as the diffusion scans. A multi-shell diffusion-weighted spin echo protocol was acquired with b-values = 0, 300, 1000, and 2000 s/mm² in 5, 5, 16, and 48 directions respectively. The TE of all sequences was adjusted for a b-value of 2000 s/mm².

All scans, including the GRE sequences, were monitored using field monitoring probes in a separate session and the field measurements were used for offline image reconstruction as described in Section 3.2.2 to correct for B₀ non-uniformity and gradient imperfections. For PF-EPI, we included only the acquired part of k-space in the image reconstruction, which results in similar quality to the k-space zero-filling approach implemented on the scanner. However, there are several techniques available to reconstruct PF-EPI scans that improves the quality and reduces the blurring, such as projection onto convex sets (POCS) (Haacke et al., 1991) and the *virtual coil* concept (Blaimer et al., 2009).

Motion correction was performed on all images of the partial brain scans with nominal isotropic resolution of 1.5 mm and effective resolution of 1.5 mm using the Multidimensional diffusion MRI (MD-dMRI) (Nilsson et al., 2018) toolbox in MATLAB. No further pre-processing that could impact image resolution (e.g., denoising or Gibbs ringing correction) was performed. Fractional anisotropy (FA) maps were generated from the motion corrected images including all acquired b-values using MRtrix3 (Tournier et al., 2019). We compared the calculated FA maps as opposed to the raw diffusion-weighted images, since differences in the TEs results in differences

in the T₂-weighted image contrast.

3.4.2. In-vivo scans to investigate SNR

Twenty-seven images without diffusion encoding (b-value = 0) were acquired in a volunteer (male, 31 years old) to calculate the SNR of the different readout trajectories at three isotropic nominal resolutions of 1, 1.2, and 1.5 mm with parameters in Table 3.1. The TR for all scans was matched to the longest TR of the protocols, and the TE was adjusted for a b-value of 2000 s/mm².

SNR maps were generated using the pseudo multiple replica method (P. M. Robson et al., 2008). Briefly, the noise covariance matrix across the receive coil channels was calculated using noise scans added to the onset of the sequences, amounting to 11000 samples in total. One hundred sets of correlated complex-valued Gaussian white noise were generated for each scan with the same dimension as the raw k-space data. To obtain 100 image replicas per scan, the synthesized noise sets were added to the raw k-space data followed by image reconstruction. Images without added noise were also reconstructed to use as *original* scans. A standard deviation (SD) map of the noise for each scan was generated by calculating pixel-wise SD over the stack of replicas. The real part of image replicas was used in calculating the noise SD maps. SNR maps were then estimated as the magnitude of the *original* images divided by the corresponding noise SD map. The final calculated SNR was the average over a WM and GM mask extracted from the b = 0 s/mm² images.

3.4.3. In-vivo scans with matching effective resolution to investigate SNR and efficiency

In order to investigate the SNR and efficiency of different trajectories with a matching effective resolution, whole brain scans of a third volunteer (female, 26 years old) were acquired. The nominal resolution for each scan was chosen using the simulation results for a matching 1.5

Chapter 3- High-resolution diffusion-weighted imaging at 7 T

mm isotropic effective resolution. TR for every protocol was chosen to minimize the scan time. The other scan parameters are listed in Table 3.1. In addition to FA maps, intra-cellular volume fraction (ICVF) maps were calculated using neurite orientation dispersion and density imaging (NODDI) (H. Zhang et al., 2012) to investigate the effect of SNR on microstructural models that require shells with high b-values. Motion corrected diffusion images were denoised using MRTrix3 (Tournier et al., 2019) then ICVF maps were generated using AMICO (Daducci et al., 2015).

Chapter 3- High-resolution diffusion-weighted imaging at 7 T

Table 3.1: In-vivo scan parameters at 7 T for three experiments to validate simulation results, calculate SNR, and investigate SNR and efficiency of trajectories with a matching resolution

Scan	Nominal resolution			SNR measurement									Effective resolution		
Nominal resolution (mm)	1.5 1.5 1.5			1.5			1.2			1			1.2	1	1
Trajectory	EPI	PF-EPI	Spiral	EPI	PF-EPI	Spiral	EPI	PF-EPI	Spiral	EPI	PF-EPI	Spiral	EPI	PF-EPI	Spiral
TE (ms)	82,73	72,63	46	102,82,73	72,63,59	46	118,92,80	81,67,63	46	101,87	86,72,66	46	86	71	46
TR (ms)	5000			6700			6700			6700			11100	10300	8300
FOV (mm³)	256×256×60			256×256×36			256×256×36			256×256×36			256×256×144		
Slice thickness (mm)	1.5			1.5			1.2			1			1.5		
R	3,4	2,3	4,5	2,3,4	2,3,4	4,5,6	2,3,4	2,3,4	4,5,6	3,4	2,3,4	4,5,6	3	4	5
PF factor	-	0.75	-	-	0.75	-	-	0.75	-	-	0.75	-	-	0.75	-
Bandwidth- per-pixel (Hz)*	1384	1384	2906	1384	1384	2906	1374	1374	2336	1396	1396	1953	1798	1776	1953
Number of slices	40			24			30			36			96		
Scan time (min)	~7			~1			~1			~1			~15	~13	~10

^{*} The bandwidth for the spiral trajectory was calculated by dividing the sampling time by the matrix size.

3.4.4. Coil sensitivity and ΔB_0 field map estimation, and image reconstruction

Individual coil images from the GRE scan were first reconstructed by explicit multiplication of the Hermitian conjugate of the encoding matrix in (23) excluding the ΔB_0 term. Coil sensitivity maps were estimated from the first echo using ESPiRIT (Uecker et al., 2014c). To map the B_0 non-uniformity, pixel-wise unwrapping of the phase image of each channel across all echoes was performed, followed by averaging ΔB_0 maps obtained for every coil and smoothing the final map using a $7\times7\times7$ -pixel spatial median filter.

Measured trajectories up to the 3^{rd} order of spherical harmonics, coil sensitivity maps, and ΔB_0 maps were used in the expanded signal model in (22) to reconstruct the diffusion-weighted images.

3.4.5. Eddy current compensation

The Siemens scanner data acquisition pipeline includes online eddy current compensation (ECC) that adjusts the system's central frequency f_0 during the signal demodulation, which adds a phase term to the raw data. This correction needs to be disabled since these f_0 variations are also measured by the field probes, otherwise eddy current effects will be corrected twice during image reconstruction. Since this feature cannot be disabled on the 7 T Terra scanner, we must invert the scanner's ECC. The same protocols were simulated in the IDEA environment to obtain gradient waveforms, which were converted to ISMRMRD format² to calculate the ECC applied by the scanner to the raw data in the form of a k_0 phase terms. The scanner ECC correction is inverted by multiplying the raw data by the conjugate values of ECC phase terms. The measured k_0 terms obtained by field probe measurements, which are more accurate than scanner's simulated eddy

² https://github.com/SkopeMagneticResonanceTechnologies/siemens to ismrmrd

currents, are applied instead during the image reconstruction.

3.5. Results

3.5.1. Simulation results

3.5.1.1. Sequence timing

Figure 3.1A and B show the readout duration and echo time of the simulated trajectories as a function of nominal resolution, respectively. The readout duration of the spiral trajectory with R = 4 is shorter compared to EPI with the same acceleration factor for almost all resolutions, and it is shorter than PF-EPI for resolutions lower than 1 mm. The rate at which the readout duration increases at high-resolutions is greater for spirals than for PF-EPI and EPI due to the radial pattern of k-space acquisition in spiral trajectories.

Echo times in Figure 3.1B were calculated for sequences with a b-value of 2000 s/mm². In spiral trajectories, the TE is independent from the resolution and remains at 44 ms over the entire range. The echo time of EPI and PF-EPI increases with resolution as expected. Results show a significant advantage of spiral trajectories over EPI-based trajectories due to the shorter TE resulting in a higher SNR, particularly at high resolutions.

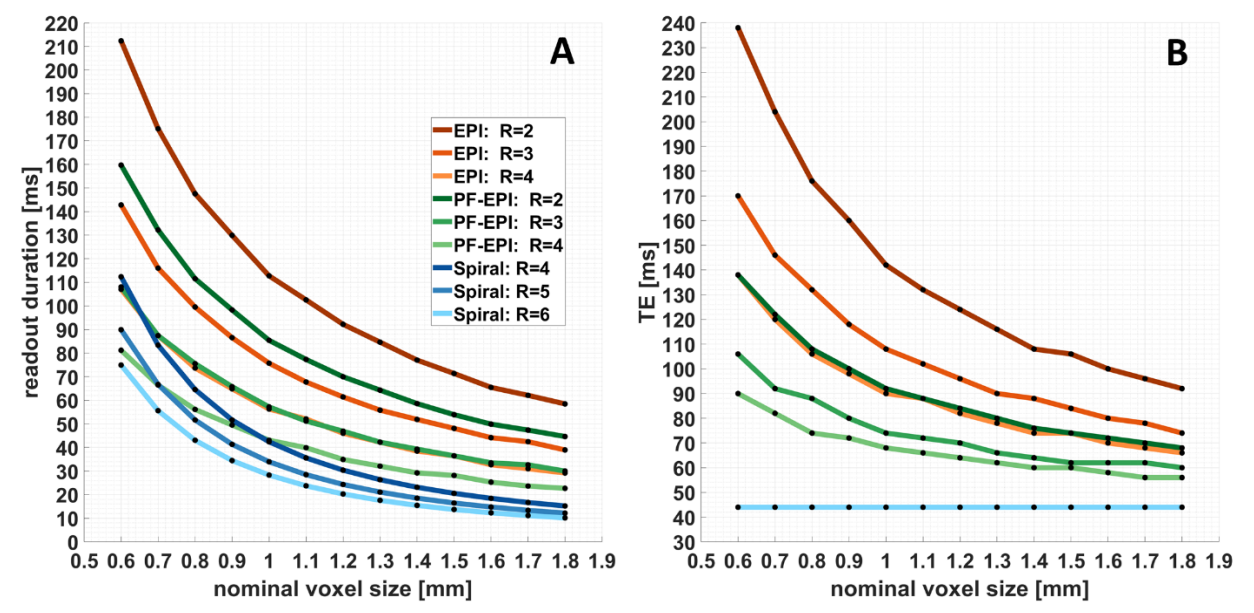


Figure 3.1. Timing properties of trajectories. A: Readout duration as a function of nominal resolution. Spiral trajectories have shorter readout durations due to more efficient way of sampling k-space for the same acceleration factor. B: Echo time (TE) as a function of nominal resolution for a b-value = 2000 s/mm2. The echo time remains at 44 ms for spiral trajectories, while it increases with resolution for EPI and PF-EPI.

3.5.1.2. Point spread function

The modulation transfer function (MTF) along the PE axis, reflecting the T_2 and T_2^* signal decay along the readout trajectory, and the corresponding PSFs for EPI, PF-EPI, and spiral trajectories are shown in Figure 3.2 for WM and GM. Equivalent simulation results at 3 T are included in Figure 3.8 of Supplementary materials for comparison. MTF signal amplitude was normalized so that the value at $k_y = 0$ is one. The right column of Figure 3.2 shows one-sided PSFs calculated from Fourier transformation of the corresponding MTFs. There are large variations in PSFs between the readout trajectories. Due to the shorter T_2^* time of the WM in comparison to the GM, PSFs are wider for the WM. This broadening of PSFs indicates more blurring, which results in a lower effective resolution. On the other hand, as the PSF gets sharper, the amplitude of

associated side lobes becomes larger, which affects specificity and sharpness.

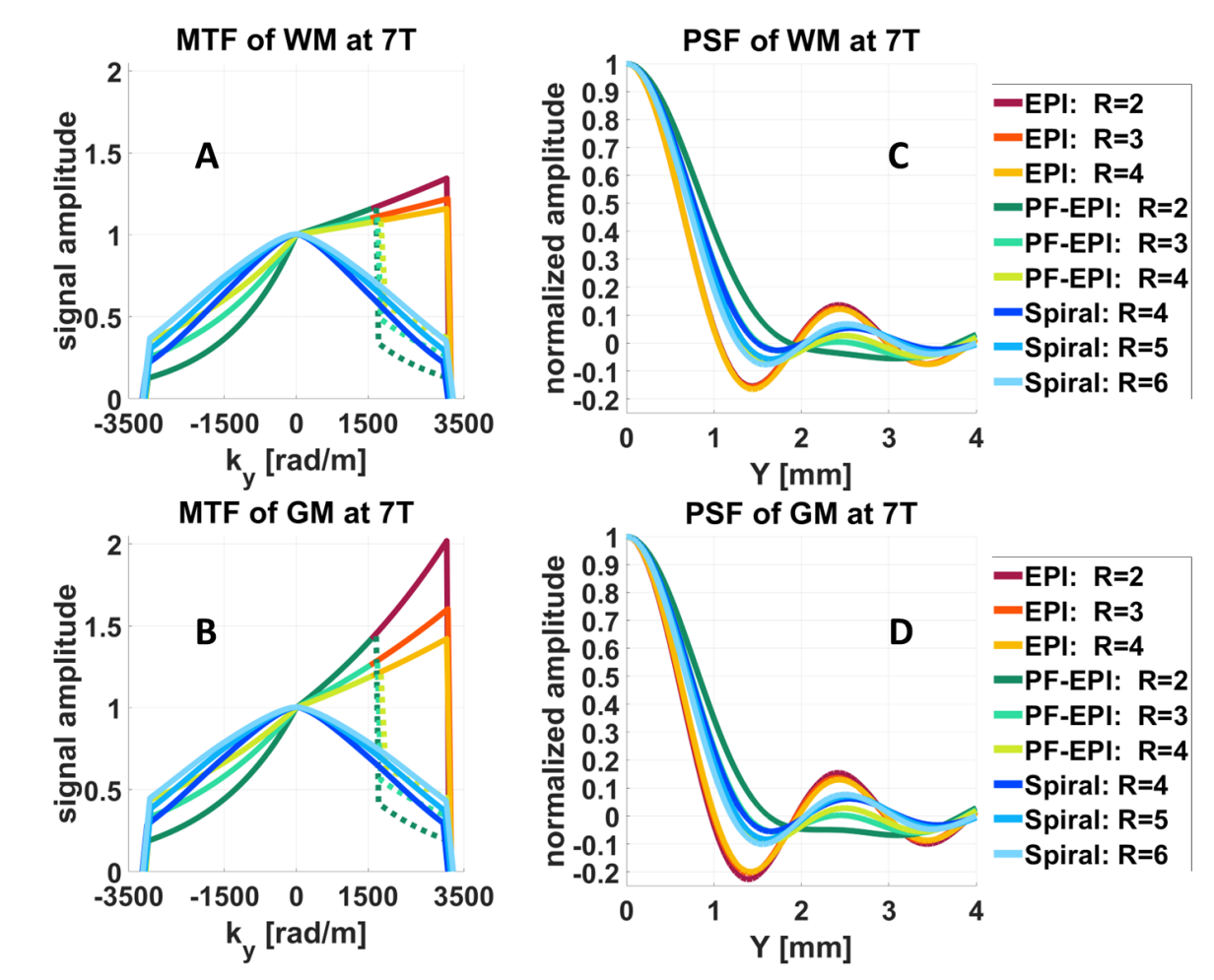


Figure 3.2. MTF along the PE direction and corresponding PSF. A and B, and their corresponding PSFs in C and D for the WM and GM at 7 T. There is more broadening of the PSF for the WM in comparison to the GM. The dashed portion of the PF-EPI MTFs was generated using the Hermitian conjugate property of the k-space.

The real part of the 2-D PSFs of the WM for a nominal resolution of 1 mm at 7 T are shown in Figure 3.3A and B for spiral and EPI trajectories, respectively. For EPI, ringing amplitudes are greater along the PE and FE axes while spiral has circular ringing that uniformly spreads in all radial directions. The effective resolution is compared to the nominal resolution at 7 T in Figure 3.3C and D, and at 3 T in Figure 3.9 of the Supplementary materials. There are large variations in the effective resolution between the trajectories at 7 T. As expected, the WM has a lower effective

resolution than the GM due to its shorter T₂* time. EPI and PF-EPI trajectories follow a linear trend over the range of resolutions considered, while spiral trajectories show a deviation from linearity for resolutions higher than 0.9 mm due to the extensive signal loss caused by long readout durations. This results in the suppression of high frequency components and thus a lower effective resolution. The specificity for all 2-D PSFs, defined in Section 3.3.2, are shown in Figure 3.3E. The specificity decreases at higher resolutions for all protocols. EPI has the highest specificity, which is expected due to its sharper peak, as shown in 1-D PSFs in Figure 3.2. The decrease in specificity at higher resolutions is most significant for spiral trajectories due to excessive suppression of high frequencies by the T₂* signal decay. The sharpening effects of EPI and PF-EPI remain almost constant over different resolutions, while this effect is significantly reduced at high resolutions for spirals as shown in Figure 3.3F. This is due to the signal decay which causes suppression of higher frequencies leading to decreasing side lobe amplitudes, while the residual main lobe remains at a high positive value. This sharpening effect in EPI and PF-EPI causes Gibbs ringing artifacts in the image, while spirals inherently reduce them, specifically at high resolutions.

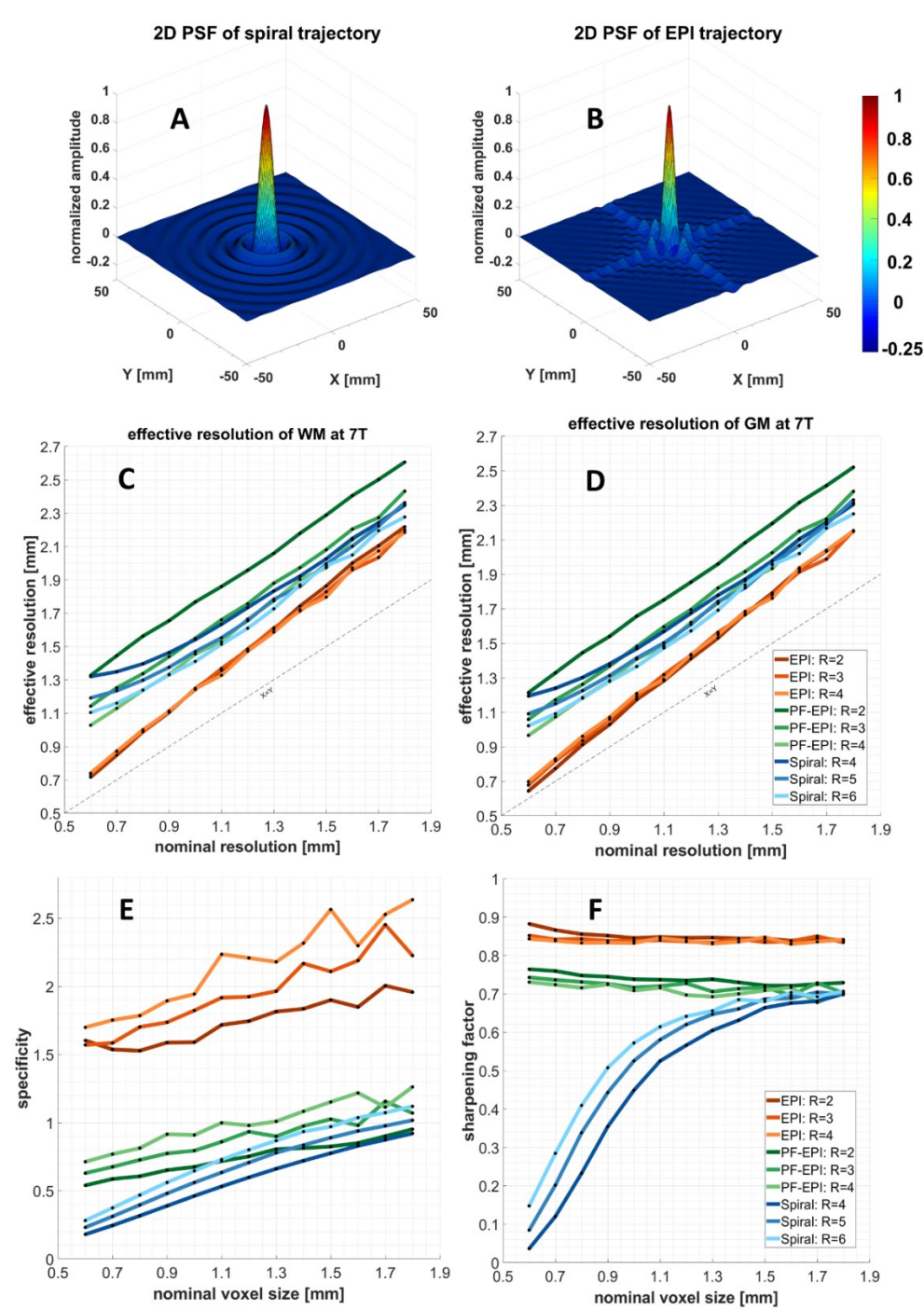


Figure 3.3. PSF analysis. A, B: Spiral has similar ringing in all directions while ringing is constrained along the PE and FE axes for EPI. C, D: There is greater variability in the effective resolution of WM compared to GM due to its shorter T_2^* . E, F: The specificity of EPI is higher due to its narrower main lobe compared to PF-EPI and spiral. EPI and PF-EPI have a constant sharpening effect, while the sharpness of spirals reduces significantly at high resolutions due to the signal decay causing suppression of the side lobes.

In addition to PSF simulations, a digital brain phantom was simulated to study effects of CG image reconstruction on image quality. Methods and results can be found in Supplementary materials. The results are similar to the PSF analysis results described above.

3.5.2. In-vivo scan results

3.5.2.1. EPI has the highest effective resolution

Figure 3.4 shows FA maps derived from the 1.5-mm scans shown in Figure 3.10 of Supplementary materials in the axial, sagittal, and coronal planes. The SNR advantage of spirals over EPI-based trajectories is clearly visible in the mean DWI images. The direction encoded color (DEC) maps of the PF-EPI scans clearly show blurring of fine structures in comparison to EPI and spirals along the anterior-posterior direction. In contrast with spiral trajectories characterized by uniform blurring in all directions in-plane, the majority of blurring due to T₂* decay in EPI-based trajectories appears along the phase-encoding (PE) direction, here the anterior-posterior direction. It is therefore expected to see a maximal blurring in the sagittal and axial planes, and minimal blurring in the coronal plane. A clear example of this in the axial and sagittal planes is the corticospinal fibers that form a striping pattern in the PE direction and are affected the most by the blurring.

EPI trajectories provide the sharpest FA maps in the sagittal and axial planes, in particular for R=4 due to the shorter readout and thus less T_2^* decay. The spiral with R=5 shows slightly sharper FA maps compared to the spiral with R=4 and PF-EPI with R=3. The blurriest FA map is obtained by using PF-EPI scans with R=2, mainly due to its longer readout duration.

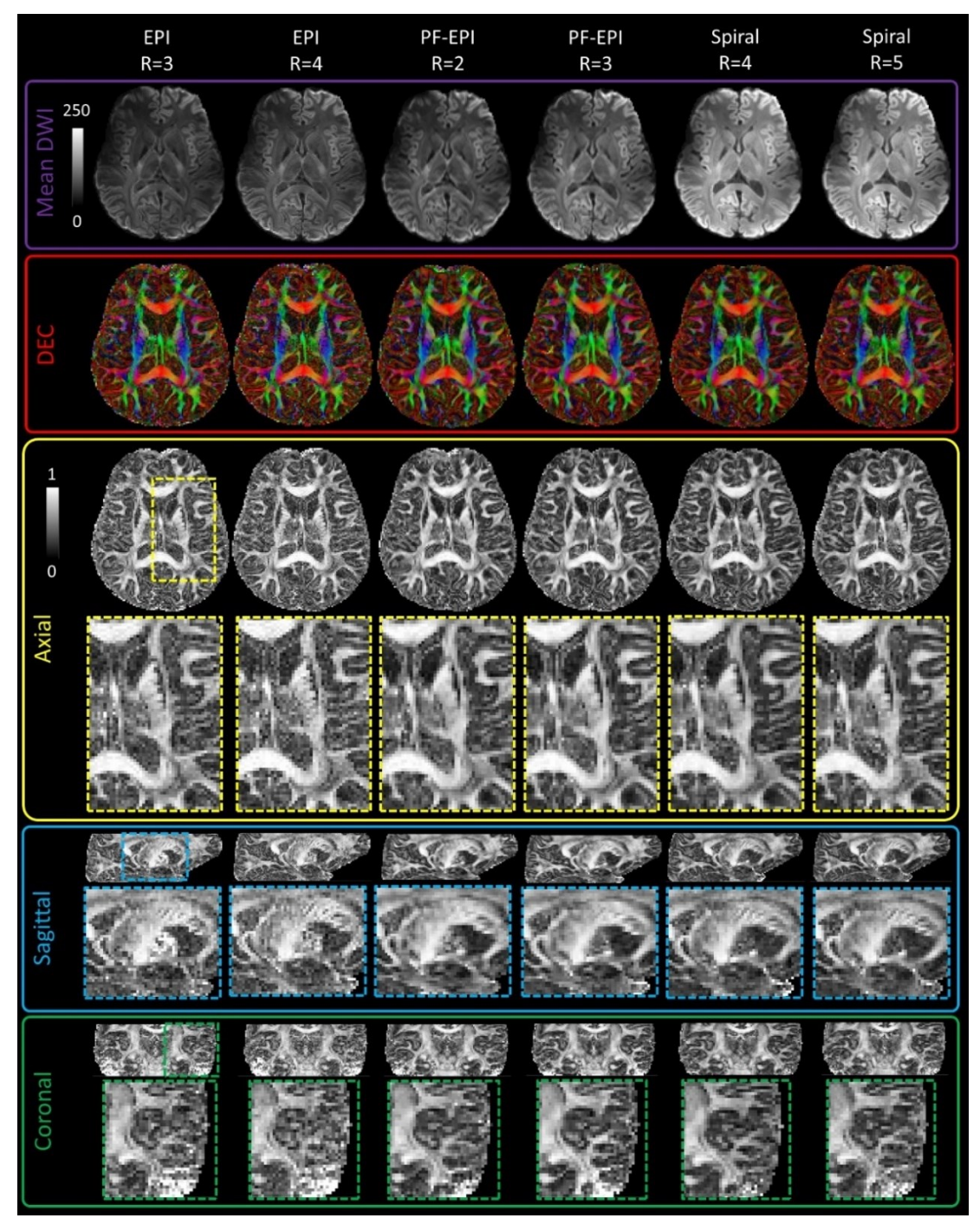


Figure 3.4. FA maps calculated using different trajectories at 1.5 mm isotropic nominal resolution. DEC maps in the axial plane are shown in the first row, and FA maps in axial, sagittal and coronal planes with magnified regions for better examination are shown below. EPI-based scans show a minimal blurring in the coronal direction, and maximal blurring in the sagittal plane, while blurring in the spiral trajectory occurs in all directions. The sharpest FA map is acquired using EPI with R=4, and the map with the lowest effective resolution is generated using PF-EPI with R=2.

To investigate the blurring effects on the calculated maps, FA values and smoothness of structures in specific regions of interest selected along the FE (Figure 3.5A, B) and PE (Figure 3.5C, D) axes in the 1.5-mm isotropic and 1-mm anisotropic scans were investigated more closely using line plots. These regions were selected to include fibers oriented perpendicular to the ROI. In Figure 3.5A and B, FA values obtained using EPI and PF-EPI trajectories are consistent within a range of ~0.1. Spirals show smoother FA profiles and larger differences compared to EPI and PF-EPI, as highlighted by the blue arrow in Figure 3.5A. In Figure 3.5C and D corresponding to the PE direction, the difference in FA values between EPI and PF-EPI trajectories is more significant than in the FE direction. These plots show sharper changes in FA for EPI trajectories and smoother variations for PF-EPI and spiral trajectories.

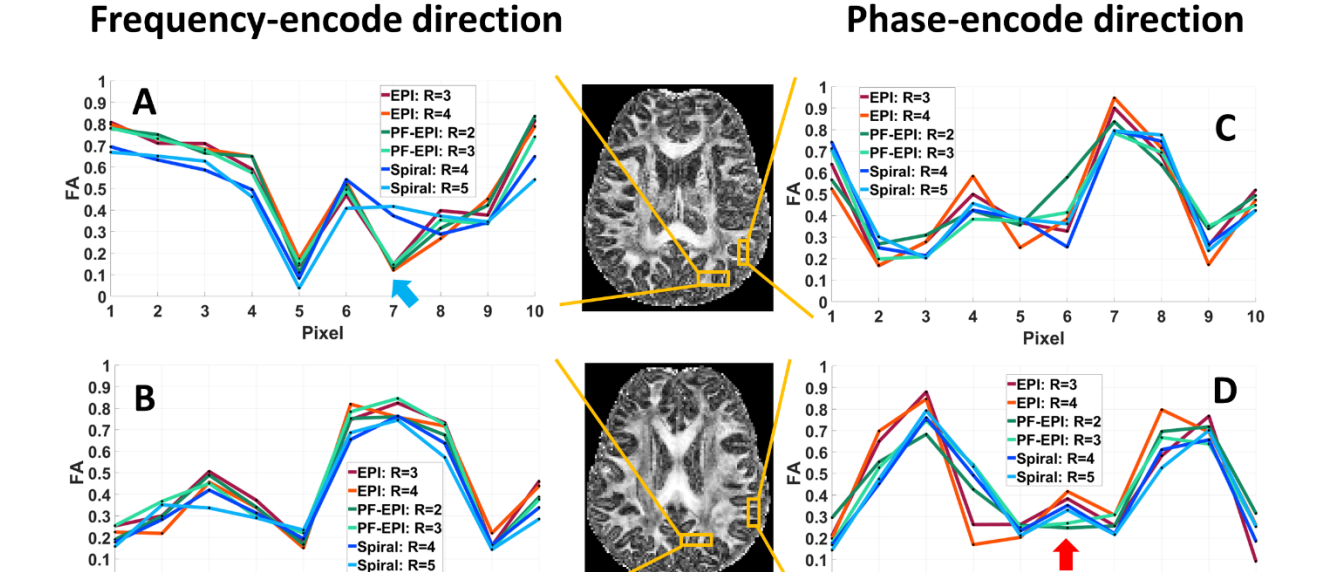


Figure 3.5. Line plots of FA values in PE and FE directions at a nominal isotropic resolution of 1.5 mm. A and B: line plots of FA values along the FE direction. C and D: line plots of FA values along PE direction. FA values show more variations in EPI and PF-EPI trajectories in the PE direction compared to the FE direction. The blue arrow shows more variability of the FA values calculated using spirals in the FE direction. The red arrow shows a drop in FA for PF-EPI with R=2 and 3 in contrast to other trajectories.

3.5.2.2. Spirals provide the highest SNR

The SNR values calculated from the in-vivo scans using different trajectories and parameters at three isotropic resolutions of 1, 1.2, and 1.5 mm are plotted in Figure 3.6. EPI with R = 2 at 1 mm was excluded due to low signal amplitude of the field monitoring probes towards the end of the readout. For a given acceleration factor R, EPI has the lowest SNR, mainly due to its longer echo time. The SNR of spiral trajectories varies the most as a function of R due to changes in the under-sampling rate in two dimensions compared to EPI and PF-EPI. Furthermore, the echo time of EPI and PF-EPI is shortened at higher acceleration factors which partially compensates for the SNR loss due to the increased undersampling. This figure clearly shows the advantage of spirals in preserving a high SNR at high resolutions.

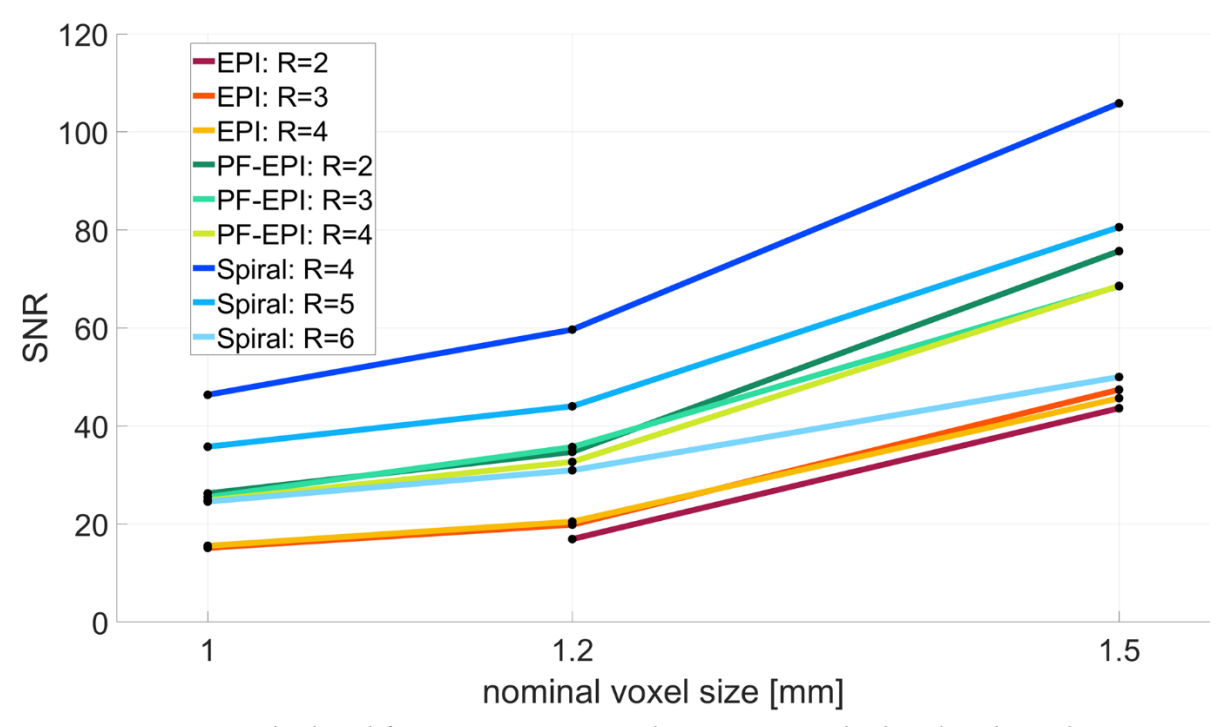


Figure 3.6. SNR calculated from in-vivo scans. The SNR was calculated within a brain tissue mask in b=0 s/mm² scans at three resolutions of 1, 1.2, and 1.5 mm isotropic.

3.5.2.3. Spirals provide highest SNR for matching effective resolution

FA and ICVF maps calculated from whole brain scans (Figure 3.11 of Supplementary materials) with a matching effective resolution of 1.5 mm are shown in Figure 3.7. The SNR of the b=0 s/mm² images for EPI, PF-EPI, and spiral were 23.7, 18.8, and 32.4, respectively. Despite the higher nominal resolution of the spiral trajectory to match the effective resolution of the other images, the SNR of spirals is still higher than for EPI. Although all scans provide FA maps of similar quality, ICVF maps clearly show the advantage of the higher SNR of the spirals for the shells with high b-values of 2000 s/mm². Furthermore, the spirals shorten the scan time by about 33% and 23% compared to EPI and PF-EPI, respectively. FA and ICVF maps of different slices are available in Figure 3.12 and Figure 3.13 of Supplementary materials, respectively.

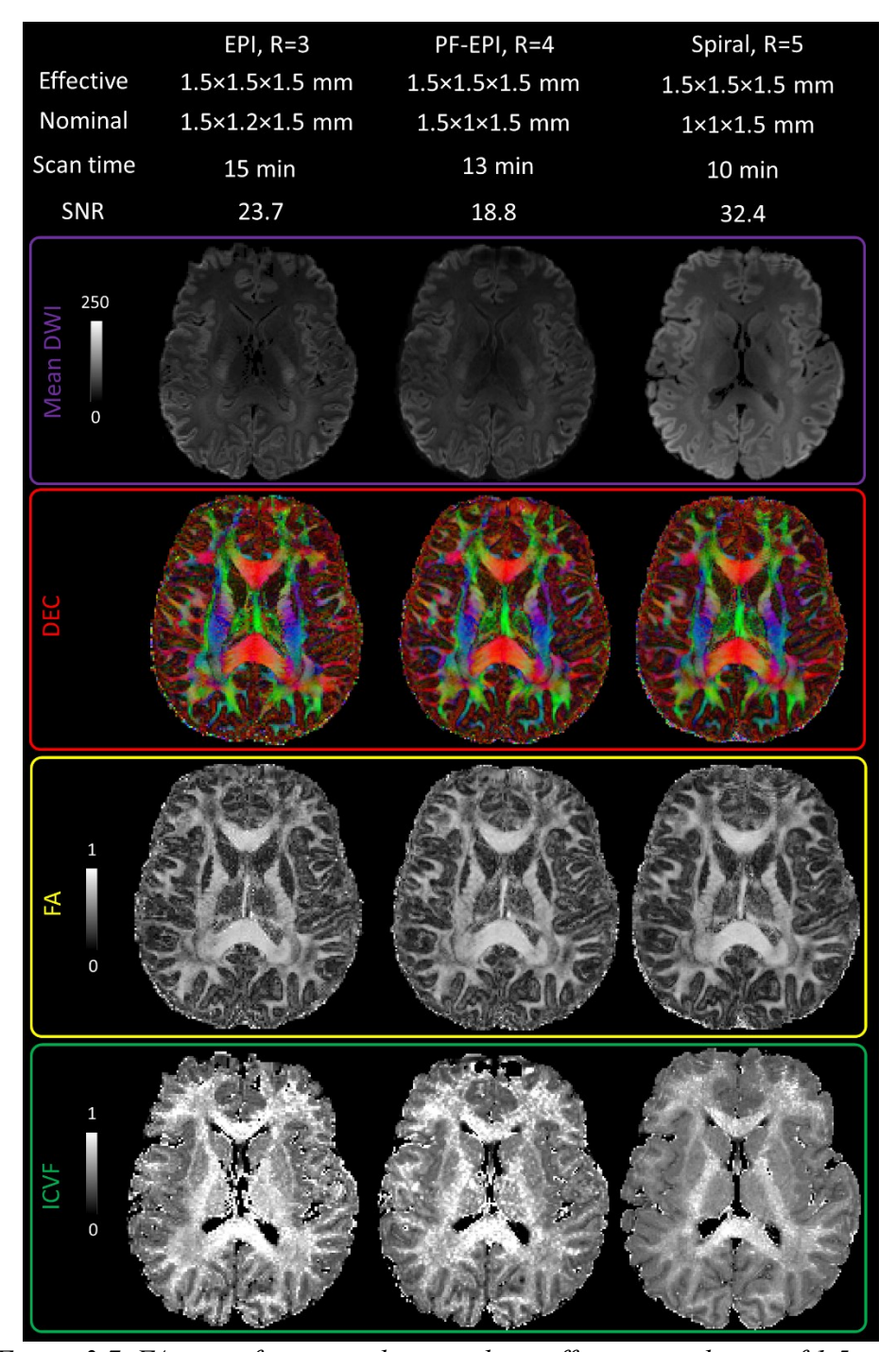


Figure 3.7. FA map of scans with a matching effective resolution of 1.5 mm. Similar structures in FA maps can be seen in all maps due to the matching effective resolution. Effect of higher SNR of the spiral scan is clear in ICVF maps.

3.6. Discussion

3.6.1. Spirals are the optimal k-space readout trajectory for single-shot dMRI at 7 T

The aim of this study was to characterise the effects of T_2^* decay on spatial resolution and quality of dMRI at 7 T and to find an optimal single-shot readout trajectory that balances the trade-off between SNR and image resolution. We characterised the PSF of dMRI with EPI, PF-EPI, and spiral trajectories using sequence simulations. Three measures were proposed for comparison of the trajectory PSFs: specificity, sharpness, and effective resolution. In vivo scans were acquired at 7 T to investigate consistency with simulation results, as well as to measure SNR. Field monitoring probes were used to eliminate distortions and artifacts caused by field imperfections. We showed that spirals generally have lower effective resolution and specificity compared to EPI at matching nominal resolutions. However, the SNR advantage of spiral enables the acquisition of single-shot spiral dMRI scans at an effective resolution of \sim 1.5 mm for a b-value of 2000 s/mm² at a higher SNR and in a shorter scan time than EPI and PF-EPI.

3.6.2. Spatial specificity and sharpening factor

The PSF is typically characterised using the FWHM. Engel et el. (2022) have recently used specificity and sensitivity in addition to FWHM to characterize the PSF and determine the optimal TE for BOLD fMRI contrast using spiral and EPI trajectories. They defined specificity as the ratio between the integral over the main lobe and the L²-norm of the side lobes. Here we used a different definition for specificity: the ratio between the main lobe within the nominal voxel boundaries to the integral of the side lobes. This definition was used to better reflect the contribution of spins within the nominal voxel. This specificity measure is affected by the residual main lobe, where a sharper peak in the PSF leads to a reduction of the area under the residual main lobe. This is the main reason that EPI has the greatest specificity, even though its side lobes have higher amplitude

than the other trajectories. Spirals have more variable specificity over the range of resolutions studied; higher suppression of side lobes leads to lowering side lobe amplitudes significantly. Side lobe suppression is expected to increase specificity; however, the greater area of the residual main lobe of spirals dominates and reduces the specificity.

The sharpness quantifies the effects of negative side lobes on image quality. A greater sharpening effect is not necessarily advantageous since it increases Gibbs ringing and intensifies edges. Due to suppression of high-frequency components using spirals, it has an inherent benefit of removing Gibbs ringing, especially at high resolutions.

3.6.3. Simulation results of the effective resolution are consistent with in-vivo scans

Simulation results in Figure 3.3 clearly show differences in the effective resolution between different trajectories, which are enhanced at higher resolutions. At 1.5-mm nominal resolution, the effective resolution can be nearly divided into three different groups where EPI trajectories perform best, and PF-EPI with R=2 have the lowest effective resolution, and other trajectories in between. In vivo FA maps in Figure 3.4 and line plots of Figure 3.5 confirm these considerable differences observed in the simulations, more specifically perpendicular to structures oriented along the FE direction, such as the corticospinal tract.

3.6.4. Trade-off between SNR and effective resolution

Several groups have investigated the gain in SNR at higher field strengths for diffusion MRI (Choi et al., 2011; Reischauer et al., 2012). In a recent study at 3 T, Lee et al. (2021b) used field monitoring probes and measured the SNR benefit of spiral over EPI trajectories. They performed a PSF analysis for trajectories with an equivalent effective resolution of 1 mm. Reported SNR values are lower than what we calculated in this study by a factor of ~6 for b=0 s/mm² at

similar TE values. This SNR difference is due to imaging at 7 T which is expected to provide ~5.21 $(SNR \propto \sim B_0^{1.95})$ times higher SNR than 3 T according to (Pohmann et al., 2016).

As mentioned above, T_2 and T_2^* are approximately halved at 7 T compared to 3 T. Although we did not perform in-vivo experiments at 3 T to compare them to our 7 T results, simulations shown in Figure 3.3 and Figure 3.9 of Supplementary materials suggest increased blurring at 7 T and greater differences between the different trajectories. Effective resolution of PF-EPI and spiral are decreased ~20% compared to 3 T, and differences in the effective resolution among trajectories was increased from ~13% at 3 T to ~27% at 7 T. Given the greater effect of T_2^* blurring at 7 T, nominal resolutions presented in dMRI studies at 7 T should be interpreted with caution, in particular for studies that investigate fine structures of the brain such as the cortical gray matter.

Future work could focus on minimizing the effect of T_2^* blurring by demodulating the k-space data before image reconstruction using a T_2^* map, at the cost of enhancing high-frequency noise. The PSF analysis can also be integrated into trajectory optimization methods to find a readout trajectory that minimizes blurring while preserving the SNR (e.g., Weiss et al., 2021).

3.6.5. Diffusion-encoding effects

Different diffusion-encoding strengths (b-values) and schemes (linear, b-tensor (Westin et al., 2016)) affect TE and therefore potentially the effective image resolution and the SNR. We calculated the effective resolution for various echo times in the PSF analysis and obtained the same results as shown in Figure 3.13 of the Supplementary materials. T2* decay after the echo in a spin-echo sequence remains the same regardless of the echo time. However, in a gradient-echo sequence, changes in TE affect the T2* decay modulation and therefore the effective resolution of the scans (Engel et al., 2018)

As shown in Figure 3.14 of Supplementary materials, the differences in echo time for b-values of 500 and 1000 s/mm^s is very small for EPI and PF-EPI readouts compared to spirals. This is due to the added idle time in EPI-based dMRI sequences which in addition to diffusion gradient duration, affects calculation of the b-value, whereas in spirals there is no idle time between diffusion gradients and the refocusing pulse, therefore changes in the b-value depend only on the diffusion gradient duration.

The b-values selected for this study are frequently employed in dMRI studies for tractography and microstructural modelling. However, to increase the specificity to the intra-axonal compartment higher b-values (4000-7000 s/mm²) are often used (e.g., Barakovic et al., 2021; McKinnon and Jensen, 2019; Veraart et al., 2020, 2018). The enhanced SNR efficiency of spiral trajectories would benefit such protocols and can be combined with other approaches to enhance SNR, such as the stimulated echo acquisition mode (STEAM) sequence (Reischauer et al. (2012) and high-performance gradients (e.g., Foo et al., 2020).

3.6.6. Limitations

The objective of this study was to evaluate the image quality of dMRI at 7 T using various trajectories in order to identify the ideal protocol. The PSF analysis and digital phantom simulations aim to quantify the effects of the different trajectories on the effective resolution and spatial accuracy. An aspect that is not taken into account in the simulations is the variability in tissue properties, such as proton density and relaxation times, across the brain. Despite these limitations, the simulation results at both high- and low- resolutions are consistent with the in-vivo scan results.

A limited number of subjects were scanned in this study. While we expect inter-individual

variations in T_2 and T_2^* times in healthy brain tissue to have small effects on our results (i.e. within the range of variation observed across a single brain), larger variations could occur in the case of pathology. Shorter T_2 and T_2^* times due to iron accumulation for instance will enhance the differences between the trajectories, whereas longer relaxation times due to oedema would reduce these differences.

Our results show that PF-EPI has poor spatial resolution and accuracy. More advanced image reconstruction techniques such as LORAKS (Haldar, 2014) can be employed for higher PF factors to reduce the blurring significantly at the cost of increased reconstruction time.

To minimize image artifacts and blurring due to field imperfections in the in-vivo scans, we used off-line field measurements. Motion and breathing can cause changes in the zeroth order fields. These effects are negligible for single-shot imaging due to the short readout duration for each slice (~ 100 ms). However, subject motion could lead to changes in the static ΔB_0 map that is used for image reconstruction. To minimize the discrepancy between the ΔB_0 map used for the image reconstruction and actual B_0 non-uniformity, GRE scans were repeated about every 15 minutes.

Figure 3.7 shows a bias between the ICVF maps from the three different trajectories at matching effective resolution. These differences may result from the differences in TE between the three protocols, 86, 71, and 46 ms for EPI, PF-EPI and spiral, respectively. The intra-cellular compartment has a longer T₂ time than the extra-cellular compartment (Lampinen et al., 2020; McKinnon & Jensen, 2019; Veraart et al., 2018a). ICVF maps calculated from data at longer TEs will thus have higher values than those at shorter TEs since the NODDI ICVF maps are actually intra-cellular T₂-weighted signal fraction maps.

Lastly, the scan time of the protocols implemented in this study can be further decreased by incorporating SMS. Combining spiral trajectories with SMS will make high spatial and angular resolution diffusion imaging of the whole-brain more efficient and feasible in clinical populations.

3.7. Conclusion

The effective resolution achieved using a specific k-space trajectory should be considered as it is significantly lower than the nominal resolution entered at the scanner and typically reported in the literature, in particular at UHFs due to the shorter T_2^* times of brain tissue. If time is not a limiting factor, multi-shot diffusion imaging acquisitions may be preferable as they provide higher SNR, better effective resolution, and specificity. In this work, we investigated fast, single-shot protocols that can be used in clinical research. We show that diffusion imaging with spiral trajectories reconstructed using field monitoring probes to minimize distortions and blurring due to eddy currents, provide sufficient signal to achieve higher effective resolutions than EPI overall and within a shorter scan time.

Code and data availability

The MATLAB code used for sequence simulation are available at (https://github.com/TardifLab/dMRI_sequence_simulations). The image reconstruction pipeline described in section 3.2.2 is available at

(https://github.com/TardifLab/ESM_image_reconstruction). Raw reconstructed diffusion images and calculated maps are available at (https://doi.org/10.5683/SP3/V7ITEH).

Acknowledgments

The authors would like to thank Ronaldo Lopez and David Costa at the McConnell Brain Imaging Centre for helping with the human scans, and Marcus Couch (Siemens Collaboration

Chapter 3- High-resolution diffusion-weighted imaging at 7 T

Scientist) for his technical support. We would like to thank Cameron Cushing and Paul Weavers (Skope MR Inc, WI, USA), and Christian Mirkes (Skope Magnetic Resonance Technologies AG, Zurich) for their technical support for the field monitoring probes.

Funding: This project was funded by the Natural Sciences and Engineering Research Council of Canada, the Fonds de recherche du Québec – Santé, and Healthy Brains for Healthy Lives. The data was acquired at the McConnell Brain Imaging Centre, which is supported by the Canadian Foundation for Innovation, Brain Canada, and Healthy Brains for Health Lives.

3.8. Supplementary materials

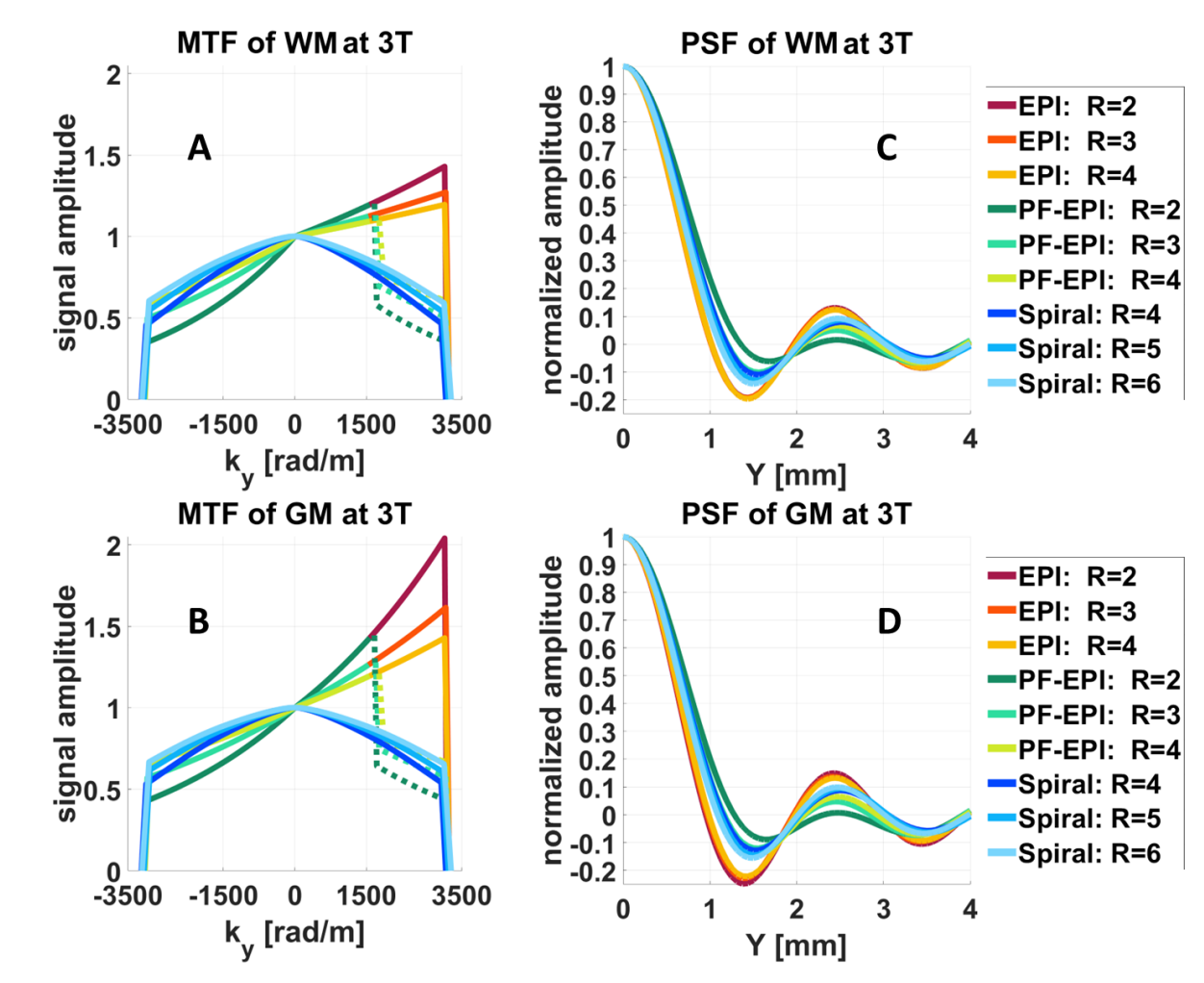


Figure 3.8. MTF along the PE direction and corresponding PSF. A and B, and their corresponding PSFs in C and D for the WM and GM at 3 T. There is more broadening of the PSF for the WM in comparison to the GM. The dashed portion of the PF-EPI MTFs was generated using the Hermitian conjugate property of the k-space.

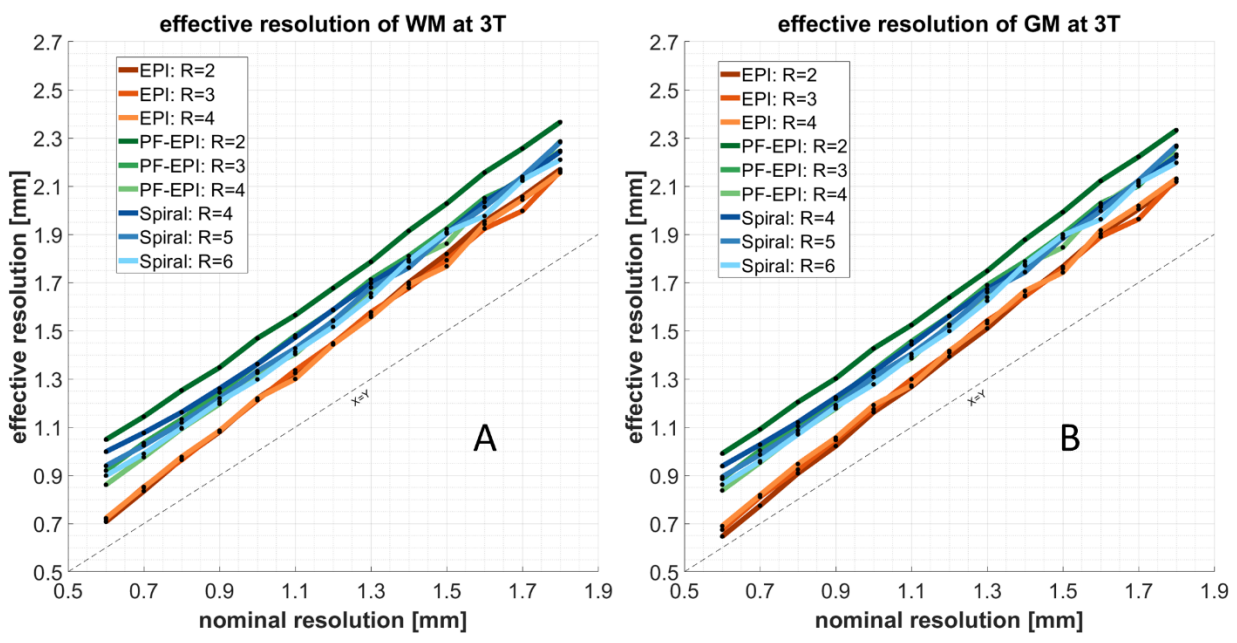


Figure 3.9. Effective resolution as a function of nominal resolution. The effective resolution of WM and GM is shown in A and B. WM has a lower effective resolution due to its shorter T_2^* relaxation time.

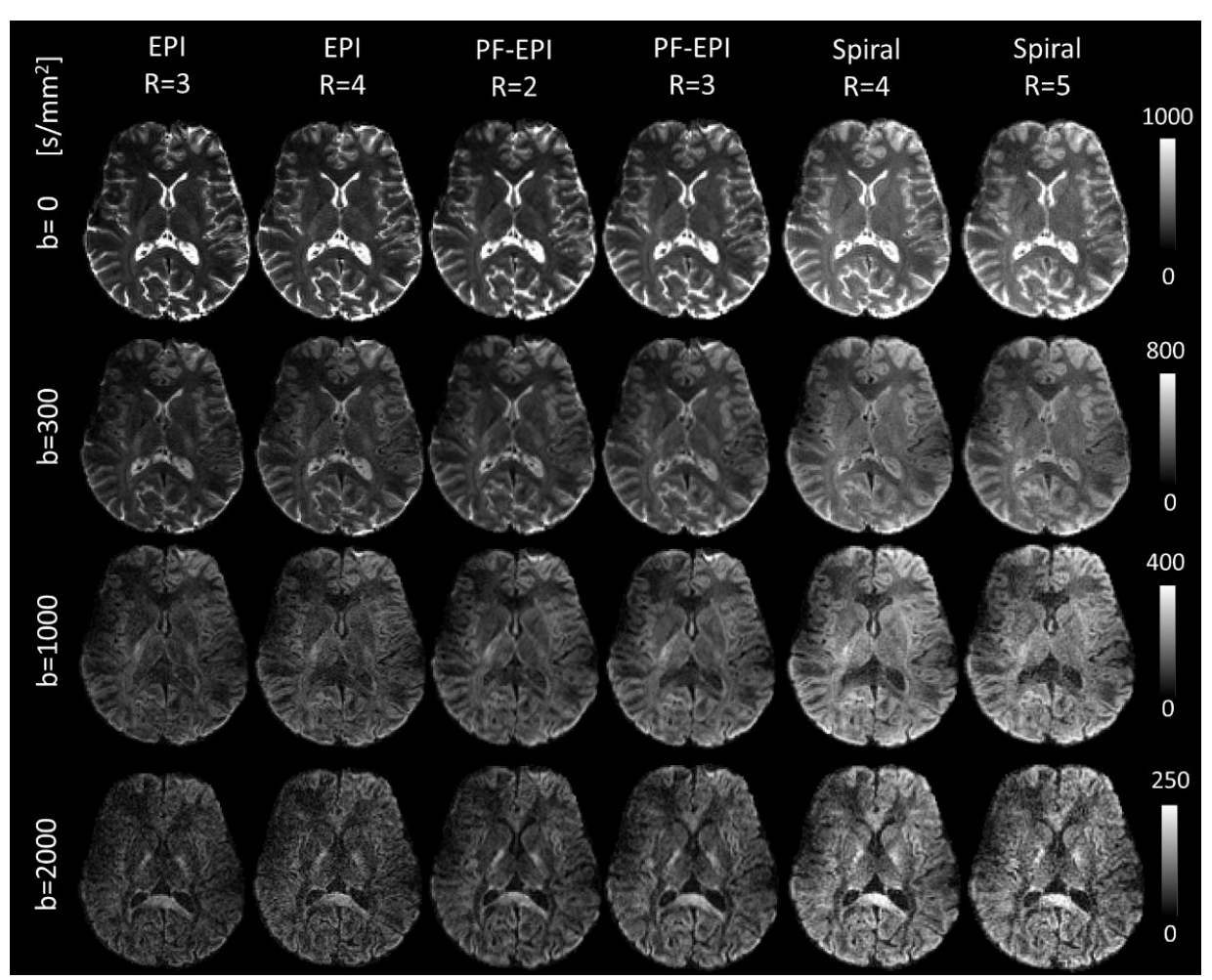


Figure 3.10. Diffusion-weighted images using different readout trajectories at a nominal resolution of 1.5 mm isotropic at 7 T. Images for b-values of 0, 300, 1000, and 2000 s/mm² acquired by different trajectories are shown. Images in the same rows are shown with the same scale adjusted for better visibility.

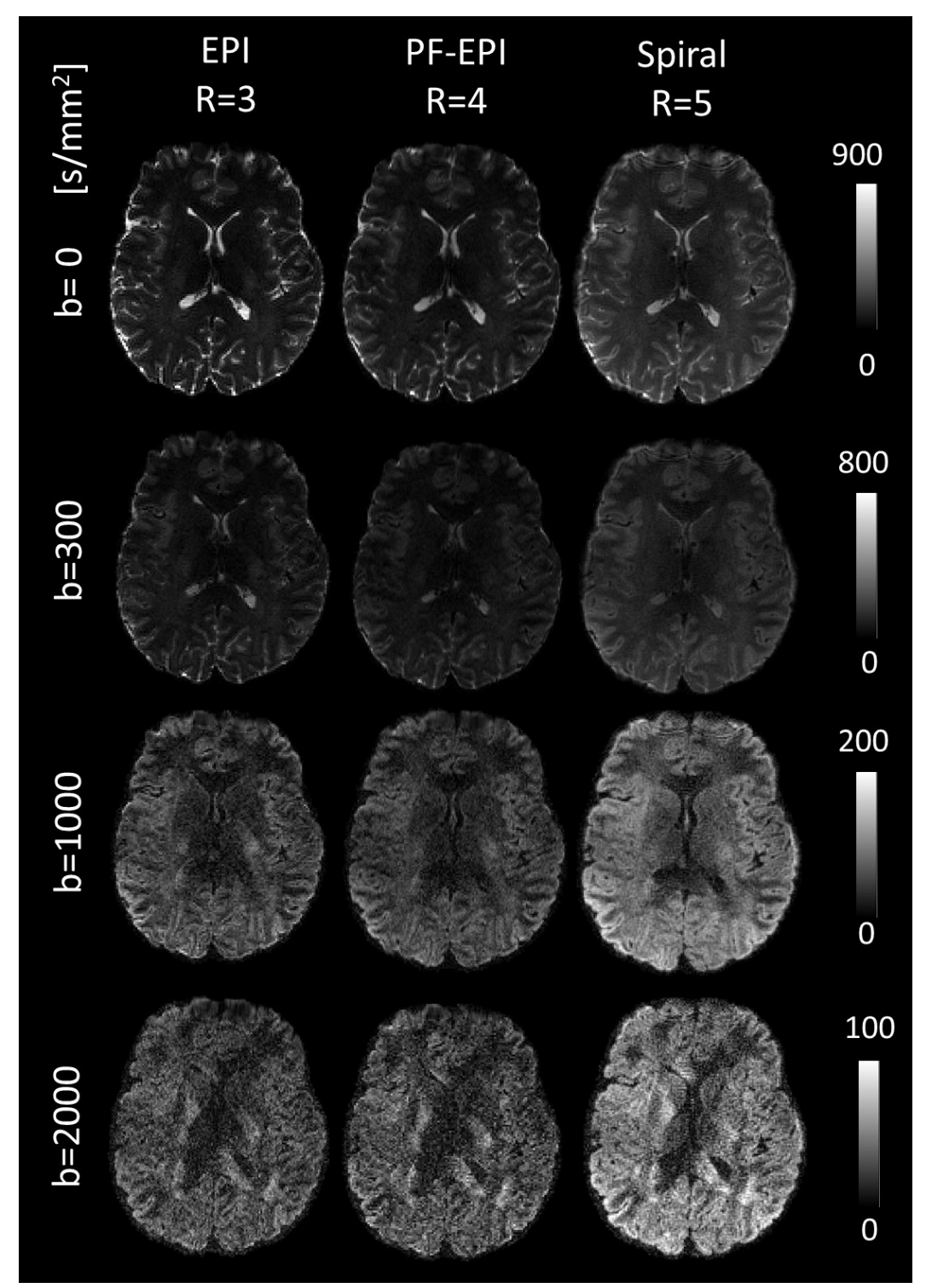


Figure 3.11. Reconstructed images at matching effective resolution of 1.5-mm. Diffusion images with b-values of 0, 300, 1000, and 2000 s/mm² using different trajectories are shown.

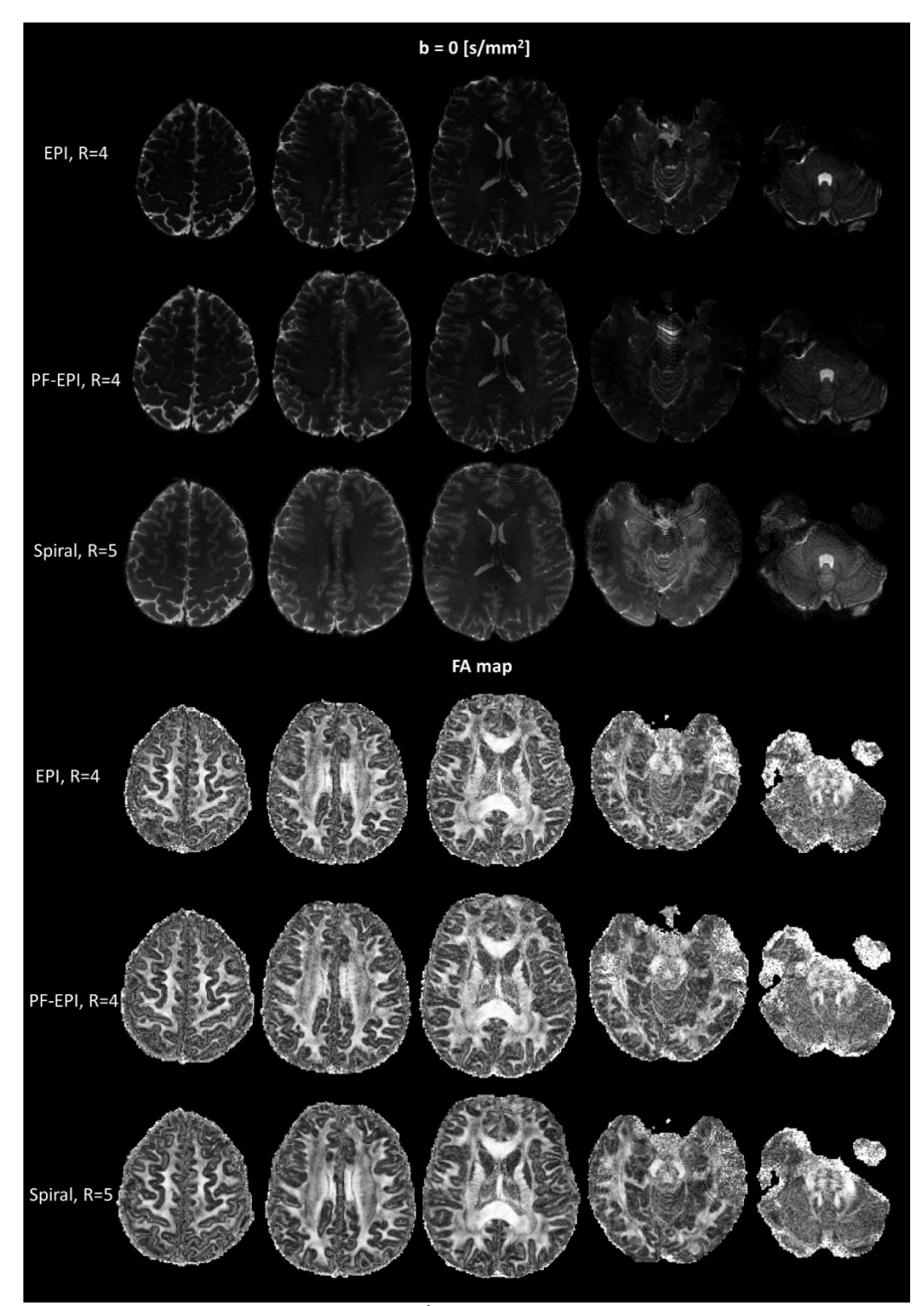


Figure 3.12. different slices of b=0 s/mm² and FA maps at matching resolution of 1.5 mm. Effects of B1 nonuniformity are clear in the last two columns which causes loss of SNR.

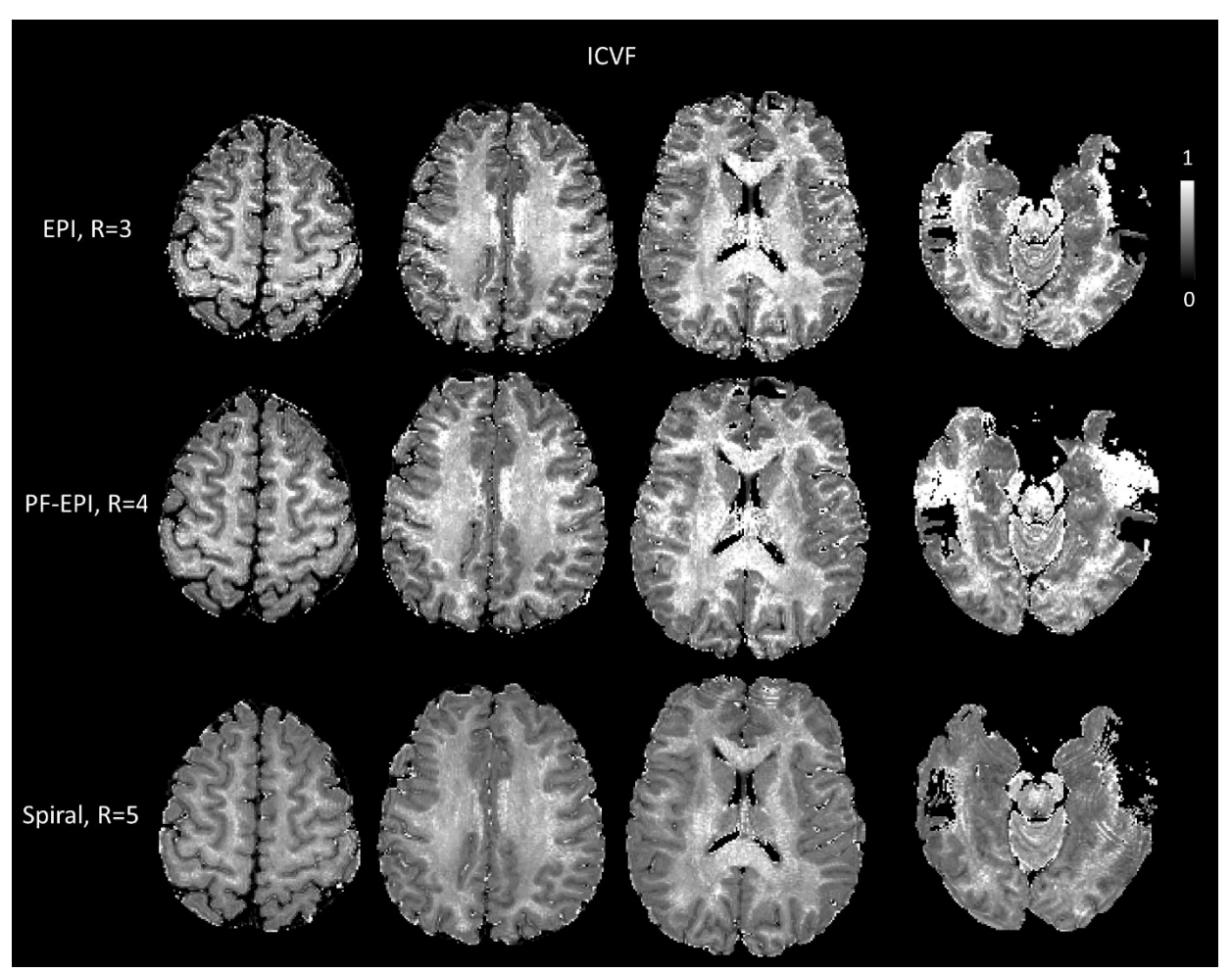


Figure 3.13. ICVF maps generated from different trajectories with the same effective resolution. Low SNR of EPI and PF-EPI leads to inaccurate estimation of ICVF. B₁ nonuniformity causes SNR loss in some areas which are clear in the last column.

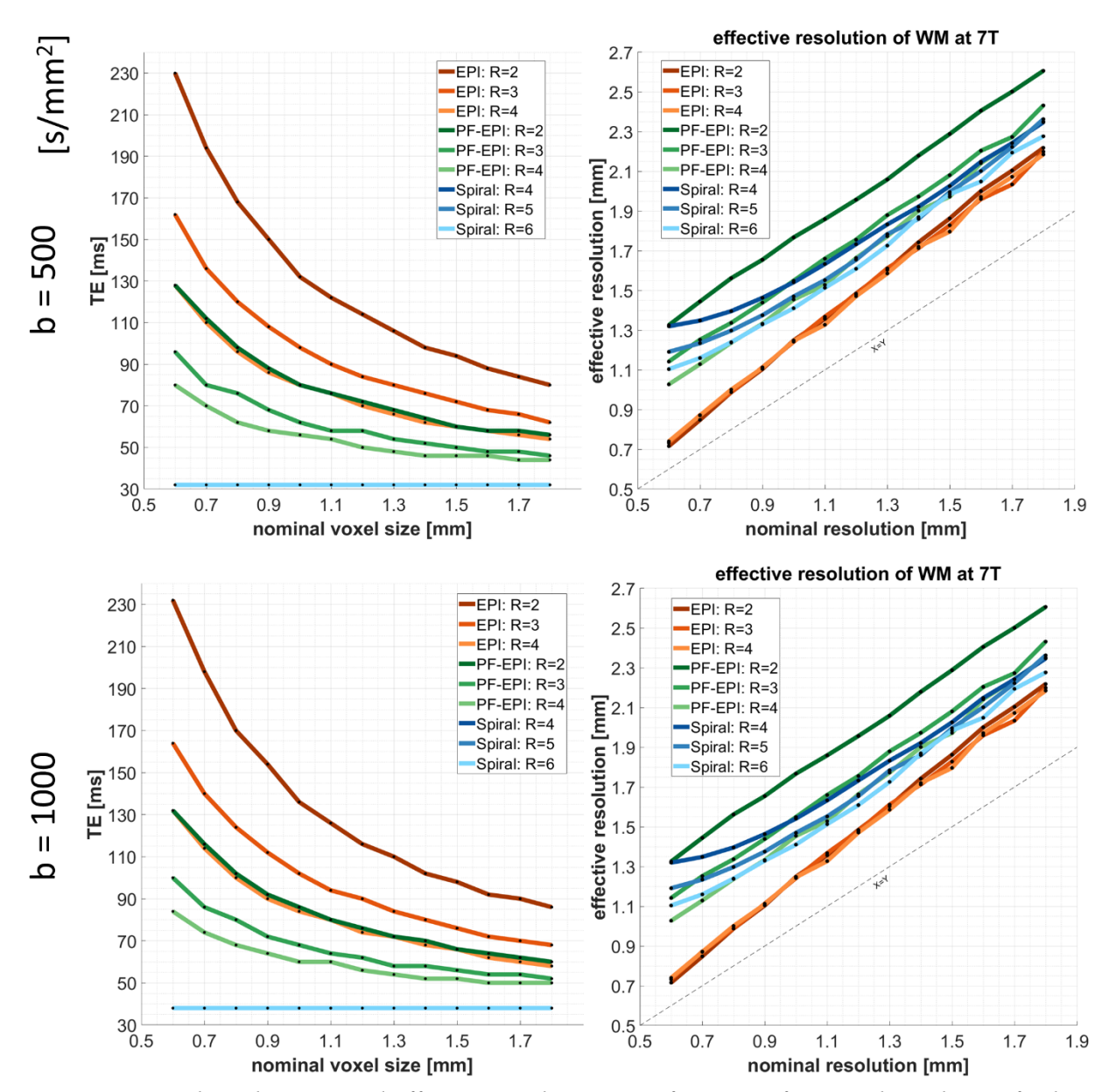


Figure 3.14. The echo time and effective resolution as a function of nominal resolution for b-values of 500 and 1000 s/mm². TEs are shorter in b = 500 s/mm², but effective resolution is not affected since the blurring mostly caused by T_2^* decay after the echo in a spin-echo sequence.

Digital brain phantom simulations

Methods

The PSF analysis above does not include the effects of CG image reconstruction on the image quality. We therefore performed simulations using a digital brain phantom as well. The digital phantom was generated from a segmented T1-weighted image acquired using the MP2RAGE sequence at 7 T (Marques et al., 2010) with an isotropic resolution of 1 mm. The WM, GM and cerebrospinal fluid (CSF) compartments were assigned the same relaxation times as for the single-point PSF simulations, and a proton density of 0.55, 0.85 and 1.0 respectively.

The digital phantom was multiplied by the sensitivity maps of the individual channels of the 32-channel Nova coil estimated from a gradient-echo (GRE) scan of the same participant using ESPiRIT (Uecker et al., 2014c). T₂*-modulated images of the phantom were generated at the time points of the EPI, PF-EPI and spiral trajectories generated for a resolution of 1.5 mm with the same parameters used in the PSF analysis. Points of the k-space were calculated by applying the Fourier transform to the modulated images at the corresponding time points of the trajectories. The undersampled k-space, coil sensitivity maps and nominal trajectories were then used to reconstruct images using the reconstruction method described in Section 3.2.2. To eliminate differences in image contrast due to echo times, TE was set to 50 ms for all trajectories. This will affect the SNR but will not have any effect on the effective resolution that is investigated. The effects of different trajectories on the resolution were then investigated by qualitatively comparing structural features and line plots.

Results

Figure 3.15 shows simulated spin-echo images created by applying the full image acquisition and reconstruction pipeline on a digital brain phantom. Blurring is visible in the images

created using a PF-EPI and spiral trajectory compared to EPI with minimum blurring. By closely looking at magnified regions, the blurring mainly appears along the PE direction in the EPI and PF-EPI images, whereas in images generated using spiral trajectories blurring is spread in all radial directions. Similarly, ringing artifacts in EPI and PF-EPI are mainly affecting voxels in the PE direction, whereas in spirals, voxels in all directions are affected.

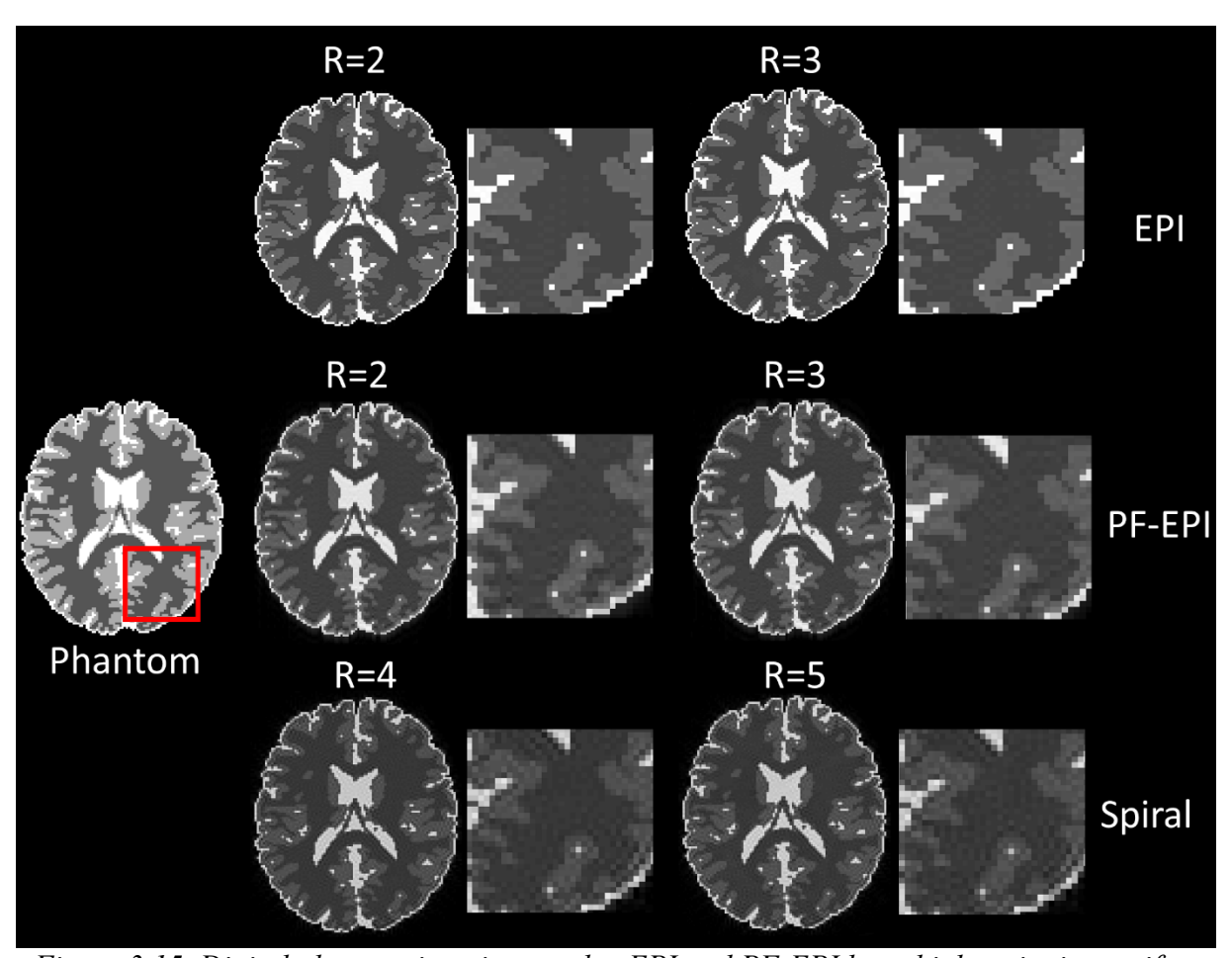


Figure 3.15. Digital phantom imaging results. EPI and PF-EPI have higher ringing artifact and blurring in the PE direction, while in spirals they appear in all directions. Blurrier images and more ringing artifacts cause lower specificity and effective resolution.

Line plots of the reconstructed images in Figure 3.16 for EPI and PF-EPI with R=2, and spiral R=4 along the anterior-posterior and left-right directions are shown in Figure 3.16. In the anterior-posterior direction, EPI follows sharp changes clearly, while PF-EPI and spiral smooth

out structural details. In the left-right direction, spiral trajectory performs the same as in the other direction, while PF-EPI line plots are similar to EPI due to less blurring in the FE direction.

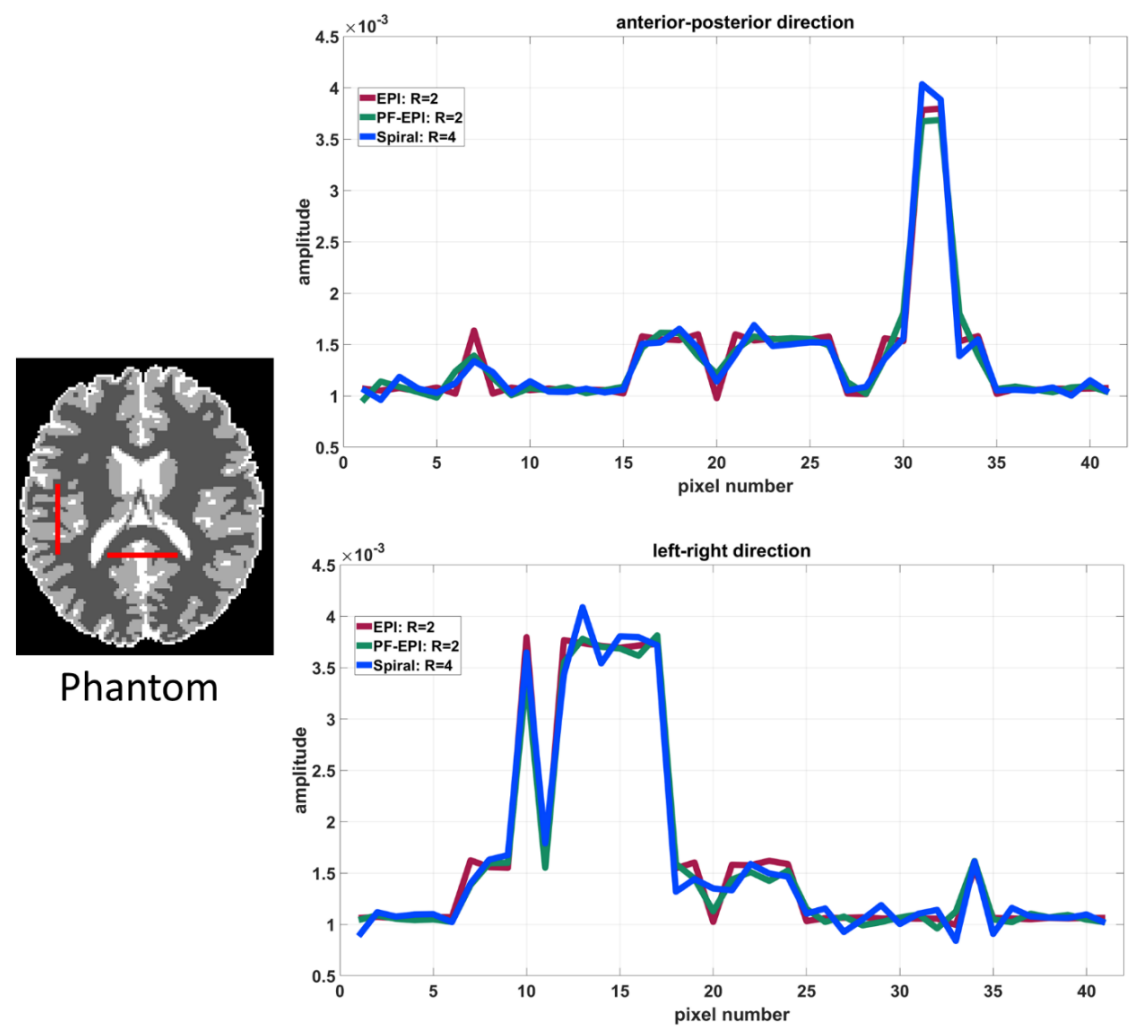


Figure 3.16. Line plots from the digital brain phantom images in the phase- and frequency-encode directions. The line plots correspond to the red lines in the digital brain image to the left. Spiral and PF-EPI smooth details of the phantom in the anterior-posterior direction. EPI and PF-EPI show similar structural details of the phantom in the left-right direction, while spiral performs similarly to the anterior-posterior direction, losing fine structures.

References

Afzali, M., Pieciak, T., Newman, S., Garyfallidis, E., Özarslan, E., Cheng, H., & Jones, D. K. (2021). The sensitivity of diffusion MRI to microstructural properties and experimental factors. Journal of Neuroscience Methods, 347, 108951. https://doi.org/10.1016/j.jneumeth.2020.108951

Assländer, J., Zahneisen, B., Hugger, T., Reisert, M., Lee, H.-L., LeVan, P., & Hennig, J. (2013). Single shot whole brain imaging using spherical stack of spirals trajectories. NeuroImage, 73, 59–70. https://doi.org/10.1016/j.neuroimage.2013.01.065

Barakovic, M., Tax, C. M. W., Rudrapatna, U., Chamberland, M., Rafael-Patino, J., Granziera, C., Thiran, J.-P., Daducci, A., Canales-Rodríguez, E. J., & Jones, D. K. (2021). Resolving bundle-specific intra-axonal T2 values within a voxel using diffusion-relaxation tract-based estimation. NeuroImage, 227, 117617. https://doi.org/10.1016/j.neuroimage.2020.117617

Basser, P. J., Mattiello, J., & LeBihan, D. (1994). MR diffusion tensor spectroscopy and imaging. Biophysical Journal, 66(1), 259–267. https://doi.org/10.1016/S0006-3495(94)80775-1

Bernstein, M. A. (with King, K. F., & Zhou, X. J.). (2004). Handbook of MRI pulse sequences. Academic Press.

Blaimer, M., Gutberlet, M., Kellman, P., Breuer, F. A., Köstler, H., & Griswold, M. A. (2009). Virtual coil concept for improved parallel MRI employing conjugate symmetric signals. Magnetic Resonance in Medicine, 61(1), 93–102. https://doi.org/10.1002/mrm.21652

Block, K. T., & Frahm, J. (2005). Spiral imaging: A critical appraisal. Journal of Magnetic Resonance Imaging, 21(6), 657–668. https://doi.org/10.1002/jmri.20320

Butts, K., de Crespigny, A., Pauly, J. M., & Moseley, M. (1996). Diffusion-weighted interleaved echo-planar imaging with a pair of orthogonal navigator echoes. Magnetic Resonance in Medicine, 35(5), 763–770. https://doi.org/10.1002/mrm.1910350518

Chaimow, D., Yacoub, E., Uğurbil, K., & Shmuel, A. (2018). Spatial specificity of the functional MRI blood oxygenation response relative to neuronal activity. NeuroImage, 164, 32–47. https://doi.org/10.1016/j.neuroimage.2017.08.077 Chen, N.-K., Guidon, A., Chang, H.-C., & Song, A. W. (2013). A robust multi-shot scan strategy for high-resolution diffusion weighted MRI enabled by multiplexed sensitivity-encoding (MUSE). NeuroImage, 72, 41–47. https://doi.org/10.1016/j.neuroimage.2013.01.038

Choi, S., Cunningham, D. T., Aguila, F., Corrigan, J. D., Bogner, J., Mysiw, W. J., Knopp, M. V., & Schmalbrock, P. (2011). DTI at 7 and 3 T: Systematic comparison of SNR and its influence on quantitative metrics. Magnetic Resonance Imaging, 29(6), 739–751. https://doi.org/10.1016/j.mri.2011.02.009

Cox, E. F., & Gowland, P. A. (2010). Simultaneous quantification of T2 and T'2 using a combined gradient echo-spin echo sequence at ultrahigh field. Magnetic Resonance in Medicine, 64(5), 1440–1445. https://doi.org/10.1002/mrm.22522

Daducci, A., Canales-Rodríguez, E. J., Zhang, H., Dyrby, T. B., Alexander, D. C., & Thiran, J.-P. (2015). Accelerated Microstructure Imaging via Convex Optimization (AMICO) from diffusion MRI data. NeuroImage, 105, 32–44. https://doi.org/10.1016/j.neuroimage.2014.10.026

Dai, E., Liu, S., & Guo, H. (2021). High-Resolution Whole-Brain Diffusion MRI at 3 T Using Simultaneous Multi-slab (SMSlab) Acquisition. NeuroImage, 118099. https://doi.org/10.1016/j.neuroimage.2021.118099

Engel, M., Kasper, L., Barmet, C., Schmid, T., Vionnet, L., Wilm, B., & Pruessmann, K. P. (2018). Single-shot spiral imaging at 7 T. Magnetic Resonance in Medicine, 80(5), 1836–1846. https://doi.org/10.1002/mrm.27176

Engel, M., Kasper, L., & Pruessmann, K. P. (2022). BOLD PSF: Impact of k-space sampling on T2* contrast [Proceedings]. ISMRM, London.

Engström, M., & Skare, S. (2013). Diffusion-weighted 3D multislab echo planar imaging for high signal-to-noise ratio efficiency and isotropic image resolution. Magnetic Resonance in Medicine, 70(6), 1507–1514. https://doi.org/10.1002/mrm.24594

Feinberg, D. A., Hoenninger, J. C., Crooks, L. E., Kaufman, L., Watts, J. C., & Arakawa, M. (1985). Inner volume MR imaging: Technical concepts and their application. Radiology, 156(3), 743–747. https://doi.org/10.1148/radiology.156.3.4023236

Foo, T. K. F., Tan, E. T., Vermilyea, M. E., Hua, Y., Fiveland, E. W., Piel, J. E., Park, K., Ricci, J., Thompson, P. S., Graziani, D., Conte, G., Kagan, A., Bai, Y., Vasil, C., Tarasek, M., Yeo, D. T. B., Snell, F., Lee, D., Dean, A., ... Ho, V. B. (2020). Highly efficient head-only magnetic field insert gradient coil for achieving simultaneous high gradient amplitude and slew rate at 3.0T (MAGNUS) for brain microstructure imaging. Magnetic Resonance in Medicine, 83(6), 2356–2369. https://doi.org/10.1002/mrm.28087

Gallichan, D. (2018). Diffusion MRI of the human brain at ultra-high field (UHF): A review. NeuroImage, 168, 172–180. https://doi.org/10.1016/j.neuroimage.2017.04.037

Griswold, M. A., Jakob, P. M., Heidemann, R. M., Nittka, M., Jellus, V., Wang, J., Kiefer, B., & Haase, A. (2002). Generalized autocalibrating partially parallel acquisitions (GRAPPA).

Magnetic Resonance in Medicine, 47(6), 1202–1210. https://doi.org/10.1002/mrm.10171

Guhaniyogi, S., Chu, M.-L., Chang, H.-C., Song, A. W., & Chen, N.-K. (2016). Motion immune diffusion imaging using augmented MUSE for high-resolution multi-shot EPI. Magnetic Resonance in Medicine, 75(2), 639–652. https://doi.org/10.1002/mrm.25624

Haacke, E. M., Lindskogj, E. D., & Lin, W. (1991). A fast, iterative, partial-fourier technique capable of local phase recovery. Journal of Magnetic Resonance (1969), 92(1), 126–145. https://doi.org/10.1016/0022-2364(91)90253-P

Haldar, J. P. (2014). Low-rank modeling of local k-space neighborhoods (LORAKS) for constrained MRI. IEEE Transactions on Medical Imaging, 33(3), 668–681. https://doi.org/10.1109/TMI.2013.2293974

Hargreaves, B. A. (2001). Spin-manipulation methods for efficient magnetic resonance imaging / (D. G. Nishimura, Ed.).

Heidemann, R. M., Porter, D. A., Anwander, A., Feiweier, T., Heberlein, K., Knösche, T. R., & Turner, R. (2010). Diffusion imaging in humans at 7 T using readout-segmented EPI and GRAPPA. Magnetic Resonance in Medicine, 64(1), 9–14. https://doi.org/10.1002/mrm.22480

Ivanov, D., Schäfer, A., Streicher, M. N., Heidemann, R. M., Trampel, R., & Turner, R. (2010). A simple low-SAR technique for chemical-shift selection with high-field spin-echo imaging. Magnetic Resonance in Medicine, 64(2), 319–326. https://doi.org/10.1002/mrm.22518

Jones, D. K. (2010). Diffusion MRI: Theory, Methods, and Applications. In Diffusion MRI. Oxford University Press.

http://oxfordmedicine.com/view/10.1093/med/9780195369779.001.0001/med-9780195369779

Karampinos, D. C., Van, A. T., Olivero, W. C., Georgiadis, J. G., & Sutton, B. P. (2009). High-resolution diffusion tensor imaging of the human pons with a reduced field-of-view, multishot, variable-density, spiral acquisition at 3 T. Magnetic Resonance in Medicine, 62(4), 1007–1016. https://doi.org/10.1002/mrm.22105

Lampinen, B., Szczepankiewicz, F., Mårtensson, J., van Westen, D., Hansson, O., Westin, C.-F., & Nilsson, M. (2020). Towards unconstrained compartment modeling in white matter using diffusion-relaxation MRI with tensor-valued diffusion encoding. Magnetic Resonance in Medicine, 84(3), 1605–1623. Scopus. https://doi.org/10.1002/mrm.28216

Lee, Y., Wilm, B. J., Brunner, D. O., Gross, S., Schmid, T., Nagy, Z., & Pruessmann, K. P. (2021a). On the signal-to-noise ratio benefit of spiral acquisition in diffusion MRI. Magnetic Resonance in Medicine, 85(4), 1924–1937. https://doi.org/10.1002/mrm.28554

Lee, Y., Wilm, B. J., Brunner, D. O., Gross, S., Schmid, T., Nagy, Z., & Pruessmann, K. P. (2021b). On the signal-to-noise ratio benefit of spiral acquisition in diffusion MRI. Magnetic Resonance in Medicine, 85(4), 1924–1937. https://doi.org/10.1002/mrm.28554

Liao, C., Yarach, U., Cao, X., Srinivasan Iyer, S., Wang, N., Kim, T. H., Bilgic, B., Kerr, A., & Setsompop, K. (2022). High-fidelity submillimeter-isotropic-resolution diffusion MRI through gSlider-BUDA and circular EPI with S-LORAKS reconstruction. ISMRM, London.

Liu, C., Bammer, R., Kim, D.-H., & Moseley, M. E. (2004). Self-navigated interleaved spiral (SNAILS): Application to high-resolution diffusion tensor imaging. Magnetic Resonance in Medicine, 52(6), 1388–1396. https://doi.org/10.1002/mrm.20288

Ma, R., Akçakaya, M., Moeller, S., Auerbach, E., Uğurbil, K., & Van de Moortele, P.-F. (2020). A field-monitoring-based approach for correcting eddy-current-induced artifacts of up to the 2nd spatial order in human-connectome-project-style multiband diffusion MRI experiment at 7 T: A pilot study. NeuroImage, 216, 116861. https://doi.org/10.1016/j.neuroimage.2020.116861

Mani, M., Jacob, M., Kelley, D., & Magnotta, V. (2017). Multi-shot sensitivity-encoded diffusion data recovery using structured low-rank matrix completion (MUSSELS). Magnetic Resonance in Medicine, 78(2), 494–507. https://doi.org/10.1002/mrm.26382

Marques, J. P., Kober, T., Krueger, G., van der Zwaag, W., Van de Moortele, P.-F., & Gruetter, R. (2010). MP2RAGE, a self bias-field corrected sequence for improved segmentation and T1-mapping at high field. NeuroImage, 49(2), 1271–1281. https://doi.org/10.1016/j.neuroimage.2009.10.002

McKinnon, E. T., & Jensen, J. H. (2019). Measuring intra-axonal T2 in white matter with direction-averaged diffusion MRI. Magnetic Resonance in Medicine, 81(5), 2985–2994. https://doi.org/10.1002/mrm.27617

Moeller, S., Ramanna, S., Lenglet, C., Pisharady, P. K., Auerbach, E. J., Delabarre, L., Wu, X., Akcakaya, M., & Ugurbil, K. (2020). Self-navigation for 3D multishot EPI with data-reference. Magnetic Resonance in Medicine, 84(4), 1747–1762. https://doi.org/10.1002/mrm.28231

Nilsson, M., Szczepankiewicz, F., Lampinen, B., Ahlgren, A., Martins, J., Lasič, S., Westin, C.-F., & Daniel, T. (2018). An open-source framework for analysis of multidimensional diffusion MRI data implemented in MATLAB.

Nishimura, D. G., Irarrazabal, P., & Meyer, C. H. (1995). A Velocity k-Space Analysis of Flow Effects in Echo-Planar and Spiral Imaging. Magnetic Resonance in Medicine, 33(4), 549–556. https://doi.org/10.1002/mrm.1910330414

Noll, D. C., Nishimura, D. G., & Macovski, A. (1991). Homodyne detection in magnetic resonance imaging. IEEE Transactions on Medical Imaging, 10(2), 154–163. https://doi.org/10.1109/42.79473

Peters, A. M., Brookes, M. J., Hoogenraad, F. G., Gowland, P. A., Francis, S. T., Morris, P. G., & Bowtell, R. (2007). T2* measurements in human brain at 1.5, 3 and 7 T. Magnetic Resonance Imaging, 25(6), 748–753. https://doi.org/10.1016/j.mri.2007.02.014

Pipe, J. G., & Zwart, N. (2006). Turboprop: Improved PROPELLER imaging. Magnetic Resonance in Medicine, 55(2), 380–385. https://doi.org/10.1002/mrm.20768

Pohmann, R., Speck, O., & Scheffler, K. (2016). Signal-to-noise ratio and MR tissue parameters in human brain imaging at 3, 7, and 9.4 tesla using current receive coil arrays. Magnetic Resonance in Medicine, 75(2), 801–809. https://doi.org/10.1002/mrm.25677

Polders, D. L., Leemans, A., Hendrikse, J., Donahue, M. J., Luijten, P. R., & Hoogduin, J. M. (2011). Signal to noise ratio and uncertainty in diffusion tensor imaging at 1.5, 3.0, and 7.0 Tesla. Journal of Magnetic Resonance Imaging, 33(6), 1456–1463. https://doi.org/10.1002/jmri.22554

Polzehl, J., & Tabelow, K. (2016). Low SNR in Diffusion MRI Models. Journal of the American Statistical Association, 111(516), 1480–1490. https://doi.org/10.1080/01621459.2016.1222284

Porter, D. A., & Heidemann, R. M. (2009). High resolution diffusion-weighted imaging using readout-segmented echo-planar imaging, parallel imaging and a two-dimensional navigator-based reacquisition. Magnetic Resonance in Medicine, 62(2), 468–475. https://doi.org/10.1002/mrm.22024

Pruessmann, K. P., Weiger, M., Börnert, P., & Boesiger, P. (2001). Advances in sensitivity encoding with arbitrary k-space trajectories. Magnetic Resonance in Medicine, 46(4), 638–651. https://doi.org/10.1002/mrm.1241

Pruessmann, K. P., Weiger, M., Scheidegger, M. B., & Boesiger, P. (1999). SENSE: Sensitivity encoding for fast MRI. Magnetic Resonance in Medicine, 42(5), 952–962.

Qin, Q. (2012). Point spread functions of the T2 decay in k-space trajectories with long echo train. Magnetic Resonance Imaging, 30(8), 1134–1142. https://doi.org/10.1016/j.mri.2012.04.017

Ramos-Llordén, G., Bilgic, B., & Huang, S. Y. (2022). Rapid, high-spatial resolution in vivo diffusion MRI with joint subsampling and reconstruction in k-,q- and RF-space. ISMRM, London.

Ramos-Llordén, G., Ning, L., Liao, C., Mukhometzianov, R., Michailovich, O., Setsompop, K., & Rathi, Y. (2020). High-fidelity, accelerated whole-brain submillimeter in vivo diffusion MRI using gSlider-spherical ridgelets (gSlider-SR). Magnetic Resonance in Medicine, 84(4), 1781–1795. https://doi.org/10.1002/mrm.28232

Reischauer, C., Vorburger, R. S., Wilm, B. J., Jaermann, T., & Boesiger, P. (2012). Optimizing signal-to-noise ratio of high-resolution parallel single-shot diffusion-weighted echo-planar imaging at ultrahigh field strengths. Magnetic Resonance in Medicine, 67(3), 679–690. https://doi.org/10.1002/mrm.23057

Robson, M. D., Anderson, A. W., & Gore, J. C. (1997). Diffusion-weighted multiple shot echo planar imaging of humans without navigation. Magnetic Resonance in Medicine, 38(1), 82–88. https://doi.org/10.1002/mrm.1910380113

Robson, P. M., Grant, A. K., Madhuranthakam, A. J., Lattanzi, R., Sodickson, D. K., & McKenzie, C. A. (2008). Comprehensive quantification of signal-to-noise ratio and g-factor for image-based and k-space-based parallel imaging reconstructions. Magnetic Resonance in Medicine, 60(4), 895–907. https://doi.org/10.1002/mrm.21728

Rooney, W. D., Johnson, G., Li, X., Cohen, E. R., Kim, S.-G., Ugurbil, K., & Springer, C. S. (2007). Magnetic field and tissue dependencies of human brain longitudinal 1H2O relaxation in vivo. Magnetic Resonance in Medicine, 57(2), 308–318. https://doi.org/10.1002/mrm.21122

Saritas, E. U., Lee, D., Çukur, T., Shankaranarayanan, A., & Nishimura, D. G. (2014). Hadamard slice encoding for reduced-FOV diffusion-weighted imaging. Magnetic Resonance in Medicine, 72(5), 1277–1290. https://doi.org/10.1002/mrm.25044

Setsompop, K., Fan, Q., Stockmann, J., Bilgic, B., Huang, S., Cauley, S. F., Nummenmaa, A., Wang, F., Rathi, Y., Witzel, T., & Wald, L. L. (2018). High-resolution in vivo diffusion imaging of the human brain with generalized slice dithered enhanced resolution: Simultaneous multislice (gSlider-SMS). Magnetic Resonance in Medicine, 79(1), 141–151. https://doi.org/10.1002/mrm.26653

Setsompop, K., Kimmlingen, R., Eberlein, E., Witzel, T., Cohen-Adad, J., McNab, J. A., Keil, B., Tisdall, M. D., Hoecht, P., Dietz, P., Cauley, S. F., Tountcheva, V., Matschl, V., Lenz, V. H., Heberlein, K., Potthast, A., Thein, H., Van Horn, J., Toga, A., ... Wald, L. L. (2013). Pushing the limits of in vivo diffusion MRI for the Human Connectome Project. NeuroImage, 80, 220–233. https://doi.org/10.1016/j.neuroimage.2013.05.078

Tanner, J. E. (1979). Self diffusion of water in frog muscle. Biophysical Journal, 28(1), 107–116. https://doi.org/10.1016/S0006-3495(79)85162-0 Tournier, J.-D., Smith, R., Raffelt, D., Tabbara, R., Dhollander, T., Pietsch, M., Christiaens, D., Jeurissen, B., Yeh, C.-H., & Connelly, A. (2019). MRtrix3: A fast, flexible and open software framework for medical image processing and visualisation. NeuroImage, 202, 116137. https://doi.org/10.1016/j.neuroimage.2019.116137

Truong, T.-K., & Guidon, A. (2014). High-Resolution Multi-Shot Spiral Diffusion Tensor Imaging with Inherent Correction of Motion-Induced Phase Errors. Magnetic Resonance in Medicine: Official Journal of the Society of Magnetic Resonance in Medicine / Society of Magnetic Resonance in Medicine, 71(2), 790–796. https://doi.org/10.1002/mrm.24709

Uecker, M., Lai, P., Murphy, M. J., Virtue, P., Elad, M., Pauly, J. M., Vasanawala, S. S., & Lustig, M. (2014). ESPIRiT—an eigenvalue approach to autocalibrating parallel MRI: Where SENSE meets GRAPPA. Magnetic Resonance in Medicine, 71(3), 990–1001. https://doi.org/10.1002/mrm.24751

Uğurbil, K., Xu, J., Auerbach, E. J., Moeller, S., Vu, A. T., Duarte-Carvajalino, J. M., Lenglet, C., Wu, X., Schmitter, S., Van de Moortele, P. F., Strupp, J., Sapiro, G., De Martino, F., Wang, D., Harel, N., Garwood, M., Chen, L., Feinberg, D. A., Smith, S. M., ... Yacoub, E. (2013). Pushing spatial and temporal resolution for functional and diffusion MRI in the Human Connectome Project. NeuroImage, 80, 80–104. https://doi.org/10.1016/j.neuroimage.2013.05.012

Vaughan, J. T., Garwood, M., Collins, C. M., Liu, W., DelaBarre, L., Adriany, G., Andersen, P., Merkle, H., Goebel, R., Smith, M. B., & Ugurbil, K. (2001). 7 T vs. 4T: RF power, homogeneity, and signal-to-noise comparison in head images. Magnetic Resonance in Medicine, 46(1), 24–30. https://doi.org/10.1002/mrm.1156

Veraart, J., Novikov, D. S., & Fieremans, E. (2018). TE dependent Diffusion Imaging (TEdDI) distinguishes between compartmental T2 relaxation times. NeuroImage, 182, 360–369. https://doi.org/10.1016/j.neuroimage.2017.09.030

Veraart, J., Nunes, D., Rudrapatna, U., Fieremans, E., Jones, D. K., Novikov, D. S., & Shemesh, N. (2020). Noninvasive quantification of axon radii using diffusion MRI. eLife, 9, e49855. https://doi.org/10.7554/eLife.49855 Vu, A. T., Auerbach, E., Lenglet, C., Moeller, S., Sotiropoulos, S. N., Jbabdi, S., Andersson, J., Yacoub, E., & Ugurbil, K. (2015). High resolution whole brain diffusion imaging at 7 T for the Human Connectome Project. NeuroImage, 122, 318–331. https://doi.org/10.1016/j.neuroimage.2015.08.004

Wang, F., Dong, Z., Tian, Q., Liao, C., Fan, Q., Hoge, W. S., Keil, B., Polimeni, J. R., Wald, L. L., Huang, S. Y., & Setsompop, K. (2021). In vivo human whole-brain Connectom diffusion MRI dataset at 760 µm isotropic resolution. Scientific Data, 8(1), Article 1. https://doi.org/10.1038/s41597-021-00904-z

Wang, F.-N., Huang, T.-Y., Lin, F.-H., Chuang, T.-C., Chen, N.-K., Chung, H.-W., Chen, C.-Y., & Kwong, K. K. (2005). PROPELLER EPI: An MRI technique suitable for diffusion tensor imaging at high field strength with reduced geometric distortions. Magnetic Resonance in Medicine, 54(5), 1232–1240. https://doi.org/10.1002/mrm.20677

Wansapura, J. P., Holland, S. K., Dunn, R. S., & Ball, W. S. (1999). NMR relaxation times in the human brain at 3.0 tesla. Journal of Magnetic Resonance Imaging, 9(4), 531–538. https://doi.org/10.1002/(SICI)1522-2586(199904)9:4<531::AID-JMRI4>3.0.CO;2-L

Weiss, T., Senouf, O., Vedula, S., Michailovich, O., Zibulevsky, M., & Bronstein, A. (2021). PILOT: Physics-Informed Learned Optimized Trajectories for Accelerated MRI (No. arXiv:1909.05773). arXiv. https://doi.org/10.48550/arXiv.1909.05773

Westin, C.-F., Knutsson, H., Pasternak, O., Szczepankiewicz, F., Özarslan, E., van Westen, D., Mattisson, C., Bogren, M., O'Donnell, L. J., Kubicki, M., Topgaard, D., & Nilsson, M. (2016). Q-space trajectory imaging for multidimensional diffusion MRI of the human brain. NeuroImage, 135, 345–362. https://doi.org/10.1016/j.neuroimage.2016.02.039

Wilm, B. J., Barmet, C., Gross, S., Kasper, L., Vannesjo, S. J., Haeberlin, M., Dietrich, B. E., Brunner, D. O., Schmid, T., & Pruessmann, K. P. (2017). Single-shot spiral imaging enabled by an expanded encoding model: Demonstration in diffusion MRI. Magnetic Resonance in Medicine, 77(1), 83–91. https://doi.org/10.1002/mrm.26493

Wilm, B. J., Barmet, C., Pavan, M., & Pruessmann, K. P. (2011). Higher order reconstruction for MRI in the presence of spatiotemporal field perturbations. Magnetic Resonance in Medicine, 65(6), 1690–1701. https://doi.org/10.1002/mrm.22767

Chapter 3- High-resolution diffusion-weighted imaging at 7 T

Wilm, B. J., Nagy, Z., Barmet, C., Vannesjo, S. J., Kasper, L., Haeberlin, M., Gross, S., Dietrich, B. E., Brunner, D. O., Schmid, T., & Pruessmann, K. P. (2015). Diffusion MRI with concurrent magnetic field monitoring. Magnetic Resonance in Medicine, 74(4), 925–933. https://doi.org/10.1002/mrm.25827

Wilm, B. J., Roesler, M., Hennel, F., Weiger, M., & Pruessmann, K. P. (2020). Diffusion Imaging with Very High Resolution and Very Short Echo Time [Proceedings]. ISMRM.

Wu, W., Poser, B. A., Douaud, G., Frost, R., In, M.-H., Speck, O., Koopmans, P. J., & Miller, K. L. (2016). High-resolution diffusion MRI at 7 T using a three-dimensional multi-slab acquisition. NeuroImage, 143, 1–14. https://doi.org/10.1016/j.neuroimage.2016.08.054

Zhang, H., Schneider, T., Wheeler-Kingshott, C. A., & Alexander, D. C. (2012). NODDI: Practical in vivo neurite orientation dispersion and density imaging of the human brain. NeuroImage, 61(4), 1000–1016. https://doi.org/10.1016/j.neuroimage.2012.03.072

Chapter 4

3D MERMAID: 3D Multishot Enhanced Recovery Motion
Artifact Insensitive Diffusion for sub-millimeter, multi-shell,
and SNR efficient diffusion imaging

Sajjad Feizollah, Christine L Tardif

Submitted to Magnetic Resonance in Medicine in October 2024

Preface

The results from Chapter 3 demonstrate that the spiral readout trajectory is more SNR efficient than EPI for single-shot high-resolution dMRI at 7 T. But this single-shot 2D implementation is insufficient to achieve the goal of submillimeter effective resolution due to T_2^* blurring. Additionally, the resolution in the slice direction is limited by the quality of the RF excitation profile, slices are susceptible to recent motion due to spin history from previous

Chapter 4- 3D MERMAID sequence

excitations, and there are challenges of overcoming $B_1^{\scriptscriptstyle +}$ nonuniformity at ultra-high magnetic fields.

A 3D acquisition could potentially address these issues, but several challenges must first be addressed. Short TRs in 3D imaging cause signal saturation, leading to lower SNR. Additionally, acquiring a volume over multiple shots can result in significant motion artifacts, as discussed in Chapter 2. In this chapter, a novel 3D dMRI sequence will be introduced to tackle these two main challenges, demonstrating scans with effective submillimeter resolution. Due to challenges of diffusion imaging at 7 T, mostly related to RF stability and B₁⁺ nonuniformity, the novel sequence was first implemented at 3 T.

Abstract

Purpose: To enhance SNR per unit time of diffusion MRI to enable high spatial resolution and extensive q-sampling in a feasible scan time on clinical scanners.

Methods: 3D Multi-shot Enhanced Recovery Motion Insensitive Diffusion (MERMAID) consists of a whole brain non-selective 3D multi-shot spin-echo sequence with an inversion pulse immediately before the excitation pulse to enhance the recovery of longitudinal magnetization. The excitation flip angle is reduced to the Ernst angle. The sequence includes a TURBINE readout trajectory, where a 3D projection of the FOV is acquired at a different radial angle in every shot. An image-based phase correction method, combined with Compressed sensing image reconstruction, was developed to correct phase errors between shots. The performance of the 3D MERMAID sequence was investigated using Bloch simulations, as well as phantom and human scans at 3 T and compared to a typical multi-slice 2D spin-echo sequence.

Results: Improvements in SNR efficiency of 30-80% were observed in phantom and human scans when using 3D MERMAID compared to a multi-slice 2D spin-echo sequence. This SNR efficiency improvement allowed scans to be acquired at a nominal isotropic resolution of 0.74 mm and a total of 112 directions across 4 shells (b=150, 300, 1000, 2000 s/mm²) in 37 minutes on a clinical scanner.

Conclusion: The 3D MERMAID sequence was shown to significantly improve SNR per unit time compared to multi-slice 2D and 3D diffusion sequences. This SNR improvement allows for shorter scan times and higher spatial and angular resolutions on clinical scanners.

4.1. Introduction

High-resolution diffusion MRI (dMRI) is a powerful tool to map the microstructure of small structures across the entire brain. Ex-vivo dMRI studies of healthy human brains have been performed at isotropic resolutions of ~100-650 µm and validated using histology (Budde & Annese, 2013; Roebroeck et al., 2019; A. Seehaus et al., 2015; A. K. Seehaus et al., 2013). These studies have revealed the complex geometry and microstructure of crossing fibers in the white matter, the layered intracortical myeloarchitecture showing radial and tangential cortical projections, as well as short-range U-fibers (Aggarwal et al., 2015; Leuze et al., 2014; Ly et al., 2020). High-resolution post-mortem dMRI has also revealed microstructural alterations of cortical grey matter and small structures in patients such as the hippocampus in Alzheimer's (Zhao et al., 2023), seizures (Ke et al., 2020), and hippocampal sclerosis (Coras et al., 2014), the substantia nigra in Parkinson's (Knossalla et al., 2018), and the corpus callosum in Amyotrophic lateral sclerosis (ALS) (Cardenas et al., 2017). In contrast, the in-vivo spatial resolution is limited due to the inherently low signal-to-noise ratio (SNR) of dMRI, resulting in nominal resolutions of ~2.5-1.5 mm for scans performed in a reasonable scan time for most clinical and research scans. These high-resolution ex-vivo and in-vivo dMRI studies have motivated the development of MRI techniques to enhance SNR efficiency of in-vivo dMRI to achieve high-resolution imaging in clinical scan times.

Conventional dMRI employs a 2D single-shot acquisition of a spin-echo (SE) sequence with an echo-planar imaging (EPI) readout. Using this sequence, whole brain spatial resolutions of 2.5-1.5 mm are achievable at 3 Tesla (T), benefiting from techniques such as partial Fourier (Koopmans & Pfaffenrot, 2021; Noll et al., 1991) and parallel imaging (Griswold et al., 2002; Lustig et al., 2007; Pruessmann et al., 1999) to shorten the EPI train. Furthermore, simultaneous

multi-slice imaging (SMS) (Engel et al., 2024; Setsompop et al., 2012) significantly shortens the repetition time (TR), allowing for the acquisition of more volumes with different diffusion encodings (e.g., directions, b-values, diffusion times, etc.) within a reasonable scan time. While these methods are used to reconstruct white matter tracts and obtain valuable microstructural details through multi-compartment tissue models (Jelescu et al., 2016; Novikov et al., 2019; H. Zhang et al., 2012), the tissue within the achievable voxel size is highly complex due to partial volume effects with different fibre populations, grey matter structures, and CSF, highlighting the need for further improvement in resolution.

Most proposed methods for high-resolution dMRI have relied on multi-shot SE acquisitions at the cost of scan time. The main challenge in multi-shot acquisitions is phase differences between shots due to high sensitivity to unwanted motion such as bulk motion and nonlinear brain motion due to the pulsatile cardiac cycle. They often require the integrated acquisition of a navigator to correct phase errors between shots caused by microscopic and macroscopic motion (Butts et al., 1996). The navigator can be acquired by adding a refocusing pulse at the end of the image readout (Bammer et al., 1999; Holdsworth et al., 2008b; Porter & Heidemann, 2009b). Alternatively, a self-navigating readout trajectory such as variable density spirals and keyhole trajectories can be used (C. Liu et al., 2004b; Tang et al., 2024). Recent multishot acquisition techniques use navigator-free approaches such as MUSE and MUSSELS (N.-K. Chen et al., 2013; Mani et al., 2017b) that take advantage of the smoothness of the phase of each shot. Low-rank Hankel matrix techniques have also been used to solve for a smoothly varying phase assuming the magnitude of each shot is consistent (Z. Li et al., 2024a). Other multi-shot acquisition approaches based on the PROPELLER readout (Z. Li et al., 2011b; Pipe, 1999b; Pipe & Zwart, 2006b) eliminate the need for an additional navigator scan. This fast spin-echo (FSE)

sequence provides a robust artifact-free solution suitable for clinical settings where the specificabsorption-rate (SAR) and low number of diffusion directions are not limiting. Super-resolution techniques are another category of multi-shot imaging techniques that reconstruct high-resolution images from a series of lower resolution scans with translation or rotation (Scherrer et al., 2011; Vis et al., 2021). Most recently, rotating-view motion-robust super-resolution (ROMER) is combined with Echo Planar Time-resolved Imaging (EPTI) to achieve images at 3 T with an isotropic resolution of 500 µm, b-value of 1000 s/mm², and 25 diffusion directions in 80 minutes (an effective TR per volume of 3.2 minutes)(Dong et al., 2024). In addition to the multi-shot 2D dMRI techniques described above, 3D multi-slab approaches, where a slab of brain is excited and acquired in multiple shots, have been proposed to enhance resolution (Bruce et al., 2017b; Engström & Skare, 2013a). These methods use multiple slabs to lengthen the TR to avoid signal saturation, and use the same 2D navigator-based methods with the assumption that phase changes in the slice direction are small for slab thickness≤ 2 mm (Engström & Skare, 2013a; Frost et al., 2014). Alternatively, multiple RF pulse profiles can be used to differently encode slice information in a thick slab acquired in multiple shots as in g-Slider (Ramos-Llordén et al., 2020; Setsompop et al., 2018).

There are few 3D acquisition techniques for dMRI that use a whole brain excitation. As for anatomical imaging, these 3D techniques use steady-state sequences with a short TR (E.-K. Jeong et al., 2003b; Q. Zhang et al., 2019). A 3D steady-state free precession (SSFP) sequence was proposed by McNab et al. for high SNR in-vivo and ex-vivo imaging using the Trajectory Using Radially Batched Internal Navigator Echoes (TURBINE) readout (McNab et al., 2010). The main disadvantages of this technique are the complex T₁/T₂ and diffusion contrast, and high sensitivity to motion which limits its application in vivo. A 3D GRASE sequence that uses a 3D navigator to

correct for phase errors was also recently proposed (H. Li et al., 2023). Instead of estimating and correcting for phase errors between shots, some 3D dMRI sequence implementations use motion-compensated diffusion encoding gradients to minimize phase errors (Stoeck et al., 2016b; Szczepankiewicz et al., 2021). This type of diffusion encoding requires longer encoding times resulting in longer echo times and lower SNR. The echo times can be shortened by using high-performance gradient systems when available (Michael et al., 2024b).

Overall, most of the multi-shot 2D and 3D dMRI techniques reviewed above achieve high-resolution images but have a long effective TR (~40 seconds to 3.5 minutes per volume for resolutions ranging from ~1 to ~0.5 mm isotropic). This limits the number of diffusion encodings that can be acquired within a scanning session. Microstructure models, in particular of the grey matter, require extensive q-space sampling, and/or multi-echo, and multi-diffusion time experiments (Jelescu et al., 2022b; Palombo et al., 2020b; Uhl et al., 2024). Therefore, even though anatomical specificity is enhanced using these high-resolution techniques, the microstructural interpretation of the data remains limited. More efficient sequences are needed to fully utilize the potential of high-resolution dMRI for in-vivo applications.

We developed a whole brain 3D Multi-shot Enhanced Recovery Motion Insensitive Diffusion-weighted (MERMAID) sequence that improves SNR per unit time compared to a 2D SE-EPI sequence and keeps the scan time per volume short (Feizollah & Tardif, 2024). Going from 2D to 3D for high-resolution imaging improves SNR, spin history, and B₁⁺ uniformity, and eliminates slab/slice profile artifacts. However, several challenges need to be addressed. First, the available steady state signal is low due to saturation of the longitudinal magnetization caused by the short TR in a SE sequence. This was addressed by adding an inversion pulse before the excitation and reducing the excitation flip angle. The second challenge is phase errors between

shots caused by macroscopic motion and cardiac cycles. A TURBINE readout with a new image reconstruction pipeline was developed to correct for these errors. We demonstrate that this SNR efficient 3D dMRI technique can be used to acquire high spatial resolution images, up to 0.74 mm isotropic with an effective TR of 19 seconds, and advanced diffusion encoding schemes for high-resolution microstructural mapping.

4.2. Methods

4.2.1. 3D steady-state SE dMRI with enhanced longitudinal magnetization recovery

The simplest way of creating a 3D diffusion sequence is to change the excitation and refocusing pulses into 3D pulses, minimize TR, and add phase encoding along the slice direction to create a multi-shot 3D readout trajectory (henceforth referred to as the 3D SE sequence). Instead of lengthening the TR to improve the signal recovery, we propose a novel sequence referred to as 3D MERMAID, illustrated in Figure 4.1A. This sequence significantly enhances signal recovery in the 3D SE sequence by incorporating an inversion pulse immediately before excitation. To demonstrate the mechanism, we performed Bloch simulations comparing 3D MERMAID with a 3D SE sequence. These simulations used a TE of 64 ms and T₁/T₂ of 866/90 ms, consistent with the T₁ of white matter at 3 T (Cox & Gowland, 2010; Rooney et al., 2007). Figure 4.1B shows that in a traditional dMRI sequence with 90- and 180-degrees pulses, reducing the TR leads to prolonged recovery times for the longitudinal magnetization transitioning from negative to positive, resulting in a reduced steady-state signal. By inserting an inversion pulse just before the excitation, as depicted in Figure 4.1C, the longitudinal magnetization is flipped back to the positive side by the refocussing pulse, thereby enhancing signal recovery until the next TR.

According to the Bloch equations (Bloch, 1946b) and the sequence diagram in Figure 4.1A,

the normalized steady-state longitudinal magnetization $M_{z_{ss}}$ is described by Equation (27) assuming perfect spoiling and gradients:

$$M_{z_{SS}} = \frac{e^{\frac{TI}{T_1}}(\cos(\alpha) - 1) - e^{\frac{TR}{T_1}} + 2e^{\frac{TE}{2} + TI} - \cos(\alpha)}{-e^{\frac{TR}{T_1}} + \cos(\alpha)}$$
(27)

Here, TI represents the time between the inversion and excitation pulses, and α is the excitation flip angle. The normalized transverse magnetization at the echo time $M_{xy_{TE}}$ is calculated by Equation (28).

$$M_{xy_{TE}} = \frac{e^{\frac{TI}{T_1}}(\cos(\alpha) - 1) - e^{\frac{TR}{T_1}} + 2e^{\frac{TE}{\frac{2}{T_1}} - \cos(\alpha)}}{-e^{\frac{TR}{T_1}} + \cos(\alpha)} \cdot \sin(\alpha) \cdot e^{-\frac{TE}{T_2}}$$
(28)

To maximize the $M_{xy_{TE}}$, an optimal excitation flip angle must be employed. Determining this flip angle using Equations (27) and (28), yields the Ernst angle formula for gradient-echo sequences (Ernst & Anderson, 1966), shown in Equation (29).

$$\alpha_{Ernst} = \arccos(e^{\left(-\frac{TR}{T1}\right)}) \tag{29}$$

4.2.2. Image reconstruction and motion correction

Another challenge of multi-shot 3D SE imaging is sensitivity to inter-shot phase errors. We implemented the TURBINE (Graedel et al., 2022; McNab et al., 2010) strategy, as shown in Figure 4.1D. Each shot acquires a radial plane of k-space rotated around the anterior-posterior axis, such that each is individually reconstructed into a projection of the FOV. The acquisition is accelerated by undersampling each EPI plane, similar to a 2D EPI readout ($R_{in-plane}$), and undersampling in the projection dimension ($R_{projection}$), requiring $N\pi/2$ projections to meet the Nyquist criteria where N

is the matrix size. Partial Fourier is also applied within each radial plane in the EPI phase-encode direction as typically employed in 2D EPI readouts.

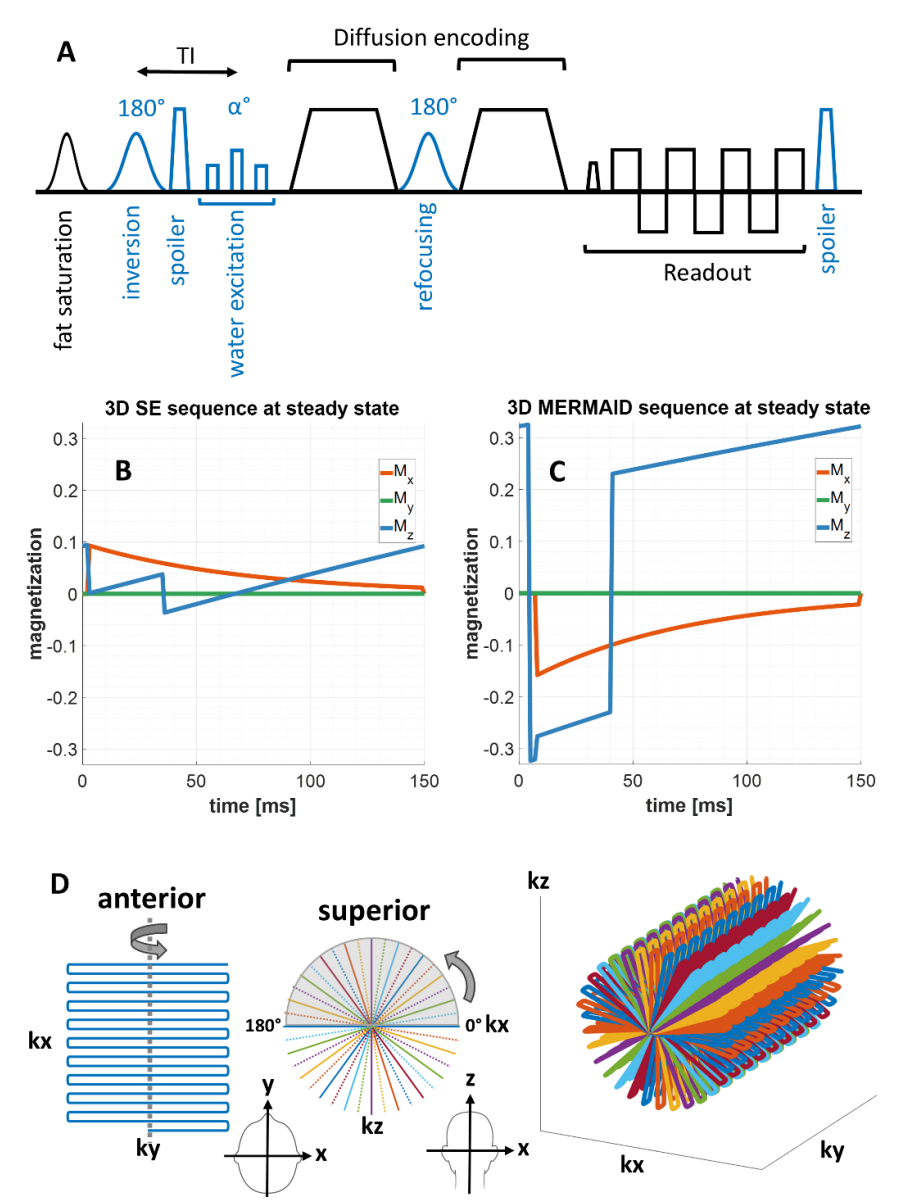


Figure 4.1. Sequence diagram, Bloch simulations, and the readout of the 3D MERMAID sequence. A: sequence diagram shows the new components added to/modified in a conventional SE sequence in blue: an inversion pulse, spoilers, and non-selective pulses. B: shows one TR of a 3D SE sequence at the steady state. C: shows Bloch simulation of the 3D MERMAID sequence at the steady state. D: TURBINE readout (undersampled due to better visualization) constructed from a 2D EPI plane rotating around anterior-posterior axis. Each color shows a shot, and projections specified by dotted line are skipped to accelerate the scan in the radial direction.

The 3D dMRI TURBINE image reconstruction pipeline is summarized in Figure 4.2. A GRAPPA kernel (Griswold et al., 2002) is estimated for in-plane (kx-ky) projection reconstruction, and coil sensitivity maps are estimated for a compressed sensing (CS) reconstruction (Lustig et al., 2007) of each phase-encode (PE) plane (kx-kz) with radial sampling as depicted in Figure 4.2A. The raw k-space data from the calibration scans are corrected for Nyquist ghosting using the method described by Heid (2000). From the corrected data, the in-plane GRAPPA kernel for each projection is estimated as for a typical 2D GRAPPA reconstruction. Before estimating coil sensitivity maps for each PE plane (Uecker et al., 2008), the phase of each projection is subtracted from a filtered image using a triangle window with a width of 0.25 as suggested in (Skare et al., 2009), similar to the method used by Pipe et al. (2002) and Wang et al. (2005) for removing motion-corrupted phase.

Once the GRAPPA kernel and coil sensitivity maps are calculated, scans are reconstructed using the pipeline shown in Figure 4.2B. Nyquist ghost correction and phase correction is done as previously described for the reference scans. Motion related to the cardiac cycle also corrupts the k-space data and introduces significant deviations in image magnitude. These artifacts appear as large hypointense areas in regions of significant motion, such as the ventricles and spine. To identify the corrupted projections, we compare the total image signal of each projection against the average across all projections of the same volume. The projections that deviate significantly from the average are removed. This method eliminates the need to record cardiac rhythm or make the acquisition cardiac gated. The motion-corrected k-space data are subsequently obtained by computing the inverse Fourier transformation of the corrected projections. To eliminate Gibbs ringing artifacts along the frequency-encode (FE) direction, a semi-Hanning filter is applied to the outer 20% of k-space representing high-frequency components in the FE direction. Lastly,

projections are combined using an inverse fast Fourier transformation along the PE direction, followed by CS reconstruction of each PE plane using the BART toolbox (Uecker et al., 2014b; X. Wang et al., 2020). Output of each step of the reconstruction pipeline is shown in Figure 4.10 of Supporting Information.

The reconstructed images can be post-processed using the tools developed for 2D EPI scans. Due to the long readout duration of each shot of the TURBINE trajectory, B_0 field inhomogeneities cause artifacts in the images that appear similar to EPI distortion artifacts. An image with an opposite PE direction is acquired and used to correct these artifacts (Andersson et al., 2003) using *topup* and *eddy* implemented in FSL (Smith et al., 2004). To achieve optimal denoising results, the image reconstruction pipeline was modified to include a denoising step right after the reconstruction of projections, as shown in Figure 4.11 of the Supporting Information.

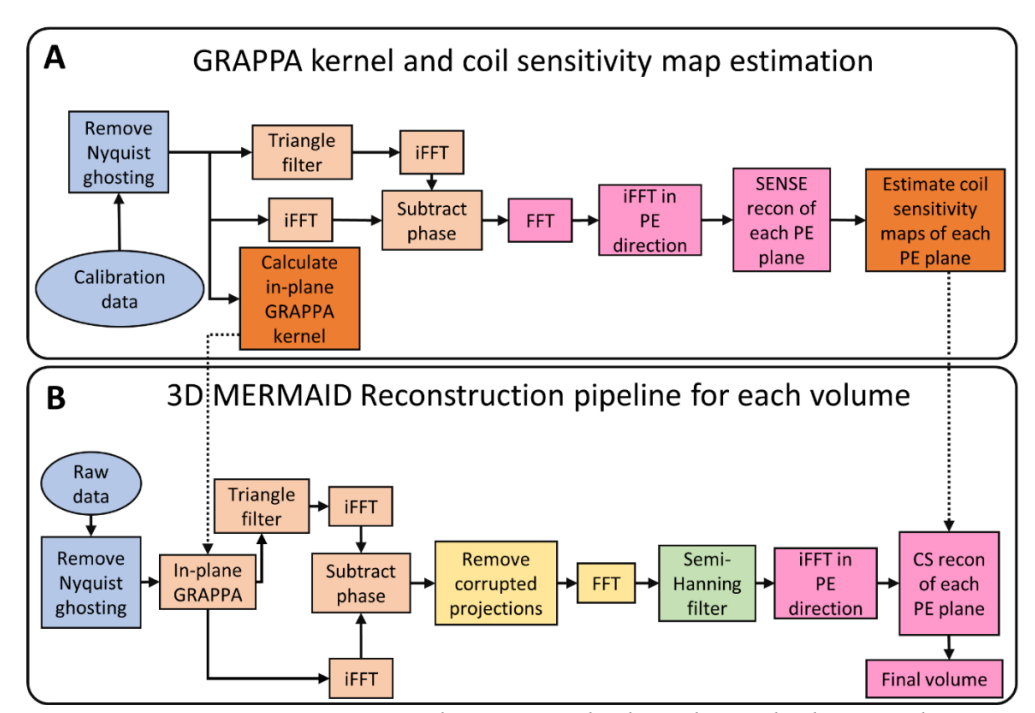


Figure 4.2. Image reconstruction pipeline. A: method used to calculate in-plane GRAPPA kernels and coil sensitivity of each PE plane. B: pipeline used to reconstruct each volume with motion correction.

4.2.3. Bloch Simulations to optimize the 3D MERMAID sequence

The SNR efficiency of the 3D MERMAID sequence is affected by various factors, including TR, flip angle, and B_1^+ uniformity. To explore the impact of these parameters on the sequence's efficiency, four Bloch simulations were conducted.

The first simulation aimed to compare the signal recovery enhancement using the 3D MERMAID sequence versus the 3D SE sequence across various b-values and resolutions. This simulation was performed with TEs and TRs adjusted to b-values of 1000, 2000, and 3000 s/mm², and a T₁ of 866 ms, alongside readouts matching the nominal resolution range of 0.8 to 1.5 mm achievable by the standard Siemens diffusion sequence. The excitation flip angle was adjusted to the Ernst angle for the corresponding TR. The analysis focused on the steady-state transverse magnetization of the 3D MERMAID sequence and the conventional 3D SE sequence, highlighting the signal recovery improvements.

The steady-state signal is sensitive to the flip angle of the inversion and refocusing pulses. A second Bloch simulation was performed to assess the impact of B_1^+ field variations, ranging from 0.4 to 1.4 times the nominal value, on the 3D SE and 3D MERMAID signals, and a T_1 of 866 ms.

A third Bloch simulation was performed to study the effect of TR on the steady-state transverse magnetization at the echo time. This was done for the white matter (WM), grey matter (GM), and CSF with T₁s/T₂s of 866/71 ms, 1300/72 ms, and 4160/1700 ms, respectively (Cox & Gowland, 2010; Rooney et al., 2007) for a range of TRs from 100 to 300 ms.

Lastly, the effect of varying flip angle between 1 and 90 degrees on the steady-state transverse magnetization at TE was simulated with the same relaxation times above and a TR of

150 ms.

4.2.4. Phantom scans to compare relative SNR of 3D MERMAID with 2D SE-EPI sequence

All scans were performed on a 3 T Prisma-Fit Siemens scanner running VE11C software (Siemens, Erlangen, Germany). The 3D MERMAID sequence was developed by modifying the Siemens diffusion sequence (henceforth referred to as the 2D SE-EPI sequence). An amplitude-modulated hyperbolic secant adiabatic pulse of 5120 µs was implemented for inversion and refocusing. To ensure complete fat signal suppression, a fat saturation pulse was applied before the inversion pulse and a non-selective water excitation pulse was implemented, as illustrated in Figure 4.1A. To prevent stimulated echoes, gradient spoiling was applied immediately following the inversion pulse and the readout, and RF spoiling was applied to the inversion and excitation pulses.

For the readout, a TURBINE trajectory was implemented as in Figure 4.1D, in which each shot is a rotated version of the single-shot 2D EPI trajectory around the anterior-posterior axis, chosen for minimum peripheral nerve stimulation (PNS).

To compare the SNR of the 3D MERMAID sequence with that of the 2D SE-EPI sequence, we prepared a spherical phantom with T_1/T_2 relaxation times of ~868/90 ms to model the white matter. To compute the SNR, 15 repetitions at nominal resolutions of 0.86, 1.0, 1.2, and 1.5 mm were acquired using the scan parameters specified in Table 4.1. Additionally, scans across a range of TEs and TRs corresponding to b-values of 0, 1000, 2000, and 3000 s/mm² were performed without employing diffusion-encoding gradients to avoid a signal loss due to the high diffusivity of the phantom. The 3D MERMAID scans were retrospectively undersampled in the projection dimensions ($R_{projection}$ =1, 2, 3, 4) to investigate the impact of undersampling on the relative SNR.

128 slices were acquired using 2D SE-EPI for all resolutions due to a limitation in the VE11C version of the Siemens diffusion sequence. The SNR was assessed in the center of the spherical phantom within a FOV of 100×100×100 mm by dividing the magnitude of the first scan by the standard deviation of the noise, derived from the 15 repetitions. No denoising or compressed sensing reconstruction was used for phantom scans.

4.2.5. Removal of motion artifacts in reconstruction of 3D images

All human scans received approval from the Research Ethics Board of the Montreal Neurological Institute, and informed consent was obtained from all participants.

The following scans were performed to test the motion correction strategy, and compare the resulting diffusion metrics in brain tissue with the standard Siemens 2D SE-EPI sequence. A participant (male, 25 years old) was scanned using both the 2D SE-EPI and 3D MERMAID sequences at an isotropic nominal resolution of 1.2 mm, b-values of 1000 and 2000 s/mm² with 12 diffusion directions each. Remaining acquisition parameters are detailed in Table 4.1. For the 3D MERMAID sequence, all projections were acquired to meet the Nyquist criteria and retrospectively undersampled by a factor of 3 to match the scan time of the 2D SE-EPI sequence. The subject's pulse was recorded and subsequently used to study the effects of the cardiac cycle on the diffusion images.

Scans acquired with the 2D SE-EPI sequence were processed using *mrdegibbs* to minimize Gibbs ringing artifacts. The fractional anisotropy (FA), direction encoded color (DEC), and apparent diffusion coefficient (ADC) maps were generated using MRtrix3 (Basser et al., 1994a; Tournier et al., 2019; Veraart et al., 2013).

4.2.6. 2D SE-EPI and 3D MERMAID comparison at sub-millimetre resolution

To demonstrate the performance of the 3D MERMAID compared to the 2D SE-EPI sequence in acquiring high spatial and angular resolution scans, a second participant (female, 27 years old) was scanned. A multi-shell protocol was used for microstructural modeling with matching acquisition parameters: a nominal isotropic resolution of 0.9 mm, b-values of 0, 150, 300, 1000, and 2000 s/mm² in 1, 7, 10, 30, 64 directions, respectively, totaling 112 directions. The b=0 s/mm² image was only used for motion correction using eddy. To reduce the impact of pulsatile CSF signal close to the cerebellum which causes strong streaking artifacts in the 3D MERMAID. a low b-value of 150 s/mm² was used for subsequent estimation of diffusion metrics. To calculate SNR maps, 20 averages of a b-value of 150 s/mm² were acquired using both sequences. Other scan parameters are listed in Table 4.1. A T1-weighted CS MPRAGE sequence (Mussard et al., 2020) with a nominal resolution of 1 mm was acquired for anatomical reference. The 2D SE-EPI scans were reconstructed using the scanner's image reconstruction pipeline which included POCS to recover resolution due to partial Fourier. Magnitude and phase images were used for denoising using the noise reduction with distribution corrected (NORDIC) method (Moeller et al., 2021). The 3D MERMAID scans were reconstructed using the image reconstruction pipeline in Figure 4.11 of Supporting Information including POCS and NORDIC.

Reconstructed scans from both dMRI sequences were post processed and analysed as described in Section 4.2.5. Additionally, fiber orientation distribution functions (fODFs) were estimated using all shells in MRTrix3 (Dhollander et al., 2019, 2021; Jeurissen et al., 2014; Raffelt et al., 2017; Tournier et al., 2004, 2019). The MPRAGE scan was then non-linearly registered to each diffusion sequence separately using Advanced Normalization Tools (ANTs) (Avants et al., 2009; Tardif et al., 2015). GM and WM were then segmented using FSL's *fast* function (Smith et

al., 2004; Y. Zhang et al., 2001).

4.2.7. Pushing the spatial resolution of 3D MERMAID

To demonstrate the capability of the 3D MERMAID sequence in acquiring high spatial and angular resolution scans within a reasonable scan time, a third participant (male, 24 years old) was scanned using the same multi-shell diffusion encoding protocol (112 volumes in total) as the previous scan, with a nominal isotropic resolution of 0.74 mm. The TR was set to 280 ms to improve the SNR, resulting in a total scan time of 37 minutes. Other scan parameters are listed in Table 4.1. The same image reconstruction, post processing, and analysis was performed as in the previous scan.

Table 4.1- Parameters of phantom and human scans. Phantom and human scans acquired to compare the 3D MERMAID and 2D SE-EPI sequences, and optimize 3D MERMAID sequence.

Phantom scans														ince.		
	Scan	2D EPI 3D MERMAID														
b-value				0 10		1000 2		3000			0 1000		20	00	3000	
			0.86	79/ 19500	79/ 2 19500 20		92/ 21200		97/ 23300		78/ 160	85/ 166	91 17	-	96/ 188	
TE/TR (ms)	Isotro	•	1.0	65/ 16000		74/ .7100	8	30/ 3400	85/ 23400		64/ 144	73/ 144	79 16	9/	84/ 187	
	resolut (mm		1.2	52/ 12500		62/ .6200	E	59/ 1700	75/ 23300		51/ 144	61/ 144	68	3/	73/ 192	
			1.5	45/ 10700		56/ .5000	6	63/ 1800	69/ 22600		44/ 144	56/ 144	63	3/	69/ 181	
F	240×240															
		0.86	402													
Number of			1.0	345							45					
slices/ resoluti projections (mm		1 1 2		128							314					
		.,	1.5	232												
	3															
R _{slie}		1/1														
F		6/8														
Echo spacing (ms)	_		0.86	1.32												
	Isotro resolut	•	1.0	1.16												
	(mm)		1.2	0.97												
		1.5		0.93												
In-vivo scans																
	Initial				Comparing 2D				2D a	D and 3D				High- solution		
Scan		2D SE-EPI		3D MERMAID		Multi-shell protocol			ocol	SNR calculation			3D			
						2D SE-I	EPI		BD MAID	2D	SE-EPI	3D MERMA	AID.	MI	ERMAID	
Nominal isot resolution (1	2		0.9					0.9				0.74		
FOV (mm	240		×240		198×198		×198	.98		198	×198		19	98×198		
Total number of slices*/projections		126		314		126		345			126	345		420		
R _{in-plane}		2		2		3				3					3	
$R_{\text{slice}}/R_{\text{projection}}$		2		1		2			4		2	4		6		
PF factor			5	/8		5/8				5/8					5/8	
TE/TR (ms)		71/10700		69/174		70/9700		68/	68/170		70/9700 68/170		0	74/280		
b-value (s/mm²)			0, 100	0, 2000		0, 150, 300, 1000, 2000			2000	150				100	150, 300, 00, 2000	
Number of directions (t		2, 12,	12 (26)		1, 7, 10, 30, 64 (112)			20 (same direction))		7, 10, 30, 4 (112)			
Echo spacing (ms)			0	98			1	.26	26		1	.26			1.26	
Scan time (min)**		8		24		26		2	26		6	6			37	

^{*} Maximum available number of slices in the standard Siemens diffusion sequence in VE11C.

^{**} Total scan time for 2D SE-EPI was adjusted for a FOV of 160 mm in the slice direction

4.3. Results

4.3.1. Bloch simulations to evaluate the performance of the 3D MERMAID sequence

Figure 4.3A illustrates the ratio between the steady-state transverse magnetization of the 3D MERMAID sequence and the 3D SE sequence. By employing the Ernst angle for excitation, the 3D MERMAID sequence enhances signal recovery by ~64% and ~96% at resolutions of 0.8 and 1.5 mm, respectively. However, as TE and TR increase at higher b-values, this enhancement in signal recovery diminishes slightly.

The sensitivity of the 3D MERMAID sequence to B₁⁺ non-uniformity is shown in Figure 4.3B. When the relative B₁⁺ field varies from 0.4 to 1.4, the transverse magnetization at steady state experiences a nonlinear change of approximately 80% in the 3D MERMAID, compared to about 38% in the 3D SE sequence. These results underscore the importance of achieving uniform RF pulse profiles across the volume to maintain the signal recovery enhancement of the 3D MERMAID sequence in all regions.

The transverse magnetization at TE for three tissues (WM, GM, and CSF) as a function of TR is plotted in Figure 4.3C. When the TR is increased from 100 to 300 ms, the available signal rises from \sim 0.02 for all tissues, to \sim 0.1, \sim 0.12, and \sim 0.13 for GM, WM, and CSF, respectively. This represents a \sim 6-fold increase in the available signal when the TR is tripled.

Figure 4.3D illustrates changes in the steady-state transverse magnetization as a function of the excitation flip angle. It shows a nonlinear change in the available signal at TE with a maximum occurring at the Ernst angle for each tissue as described above.

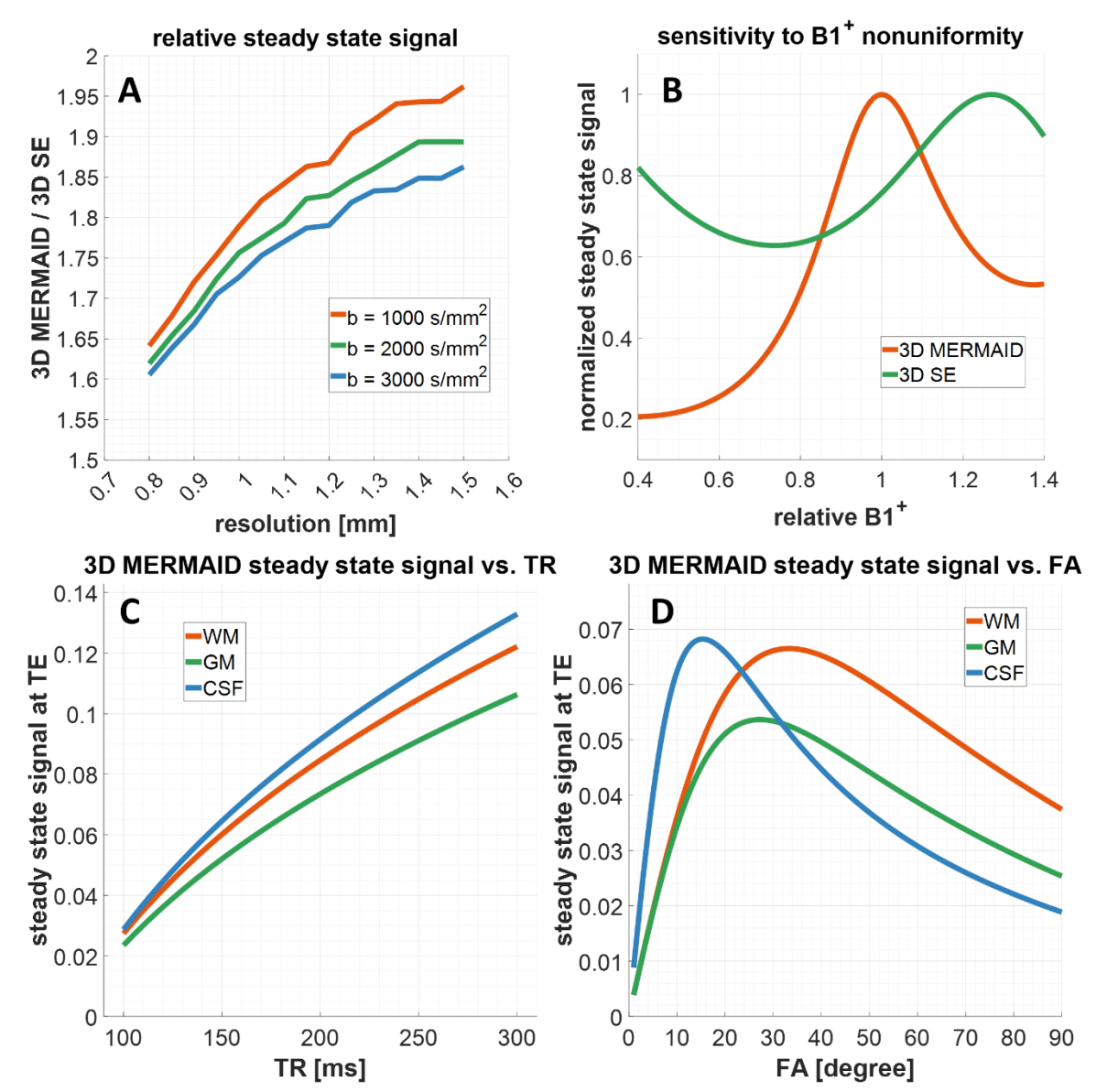


Figure 4.3. Bloch simulations to determine the performance of the 3D MERMAID sequence. A: ratio of the available transverse magnetization of the 3D MERMAID sequence and a 3D SE sequence at different TEs/TRs corresponding to b-values of 1000, 2000, and 3000 s/mm2. B: sensitivity of the 3D MERMAID sequence to B1+ nonuniformity compared to a 3D SE sequence. C: the transverse magnetization at steady state as a function of TR for three tissues. D: changes in transverse magnetization of GM, WM, and CSF with flip angle (FA).

4.3.2. Phantom scans show improved SNR for 3D MERMAID compared to 2D SE-EPI sequence

Figure 4.4A showcases the higher SNR of the 3D MERMAID sequence in comparison to

the conventional 2D SE-EPI sequence in the phantom at 1 mm resolution. Both sequences have approximately the same scan time per volume of 12 seconds and use the same in-plane acceleration factor of 3. Although there was no slice acceleration applied in 2D SE-EPI sequence, an acceleration factor of 2 is required to achieve this scan time which does not affect the SNR significantly. The 3D MERMAID sequence employs a projection acceleration factor of 4 to reduce the scan time per volume.

The SNR of the 3D MERMAID sequence relative to the 2D SE-EPI sequence for the TEs and TRs associated with b-values of 0, 1000, 2000, and 3000 s/mm² is depicted in Figure 4.4B-E. The relative SNR across different resolutions ranges between \sim 1.4 and 3 depending on the acceleration factor, with a notable exception at the resolution of 0.86 mm where the relative SNR is lower (in particular at higher b-values). This exception is attributed to the increased duration between the inversion and refocusing pulses during which magnetization decreases. At higher b-values, longer TRs contribute to improved magnetization recovery and, consequently, higher SNR. The SNR decreases approximately as a function of the square root of the projection acceleration ($\sqrt{R_{projection}}$). In contrast, the slice acceleration in the 2D SE-EPI sequence has a minimal effect on SNR for multi-band factors of 1 to 3 (results not shown).

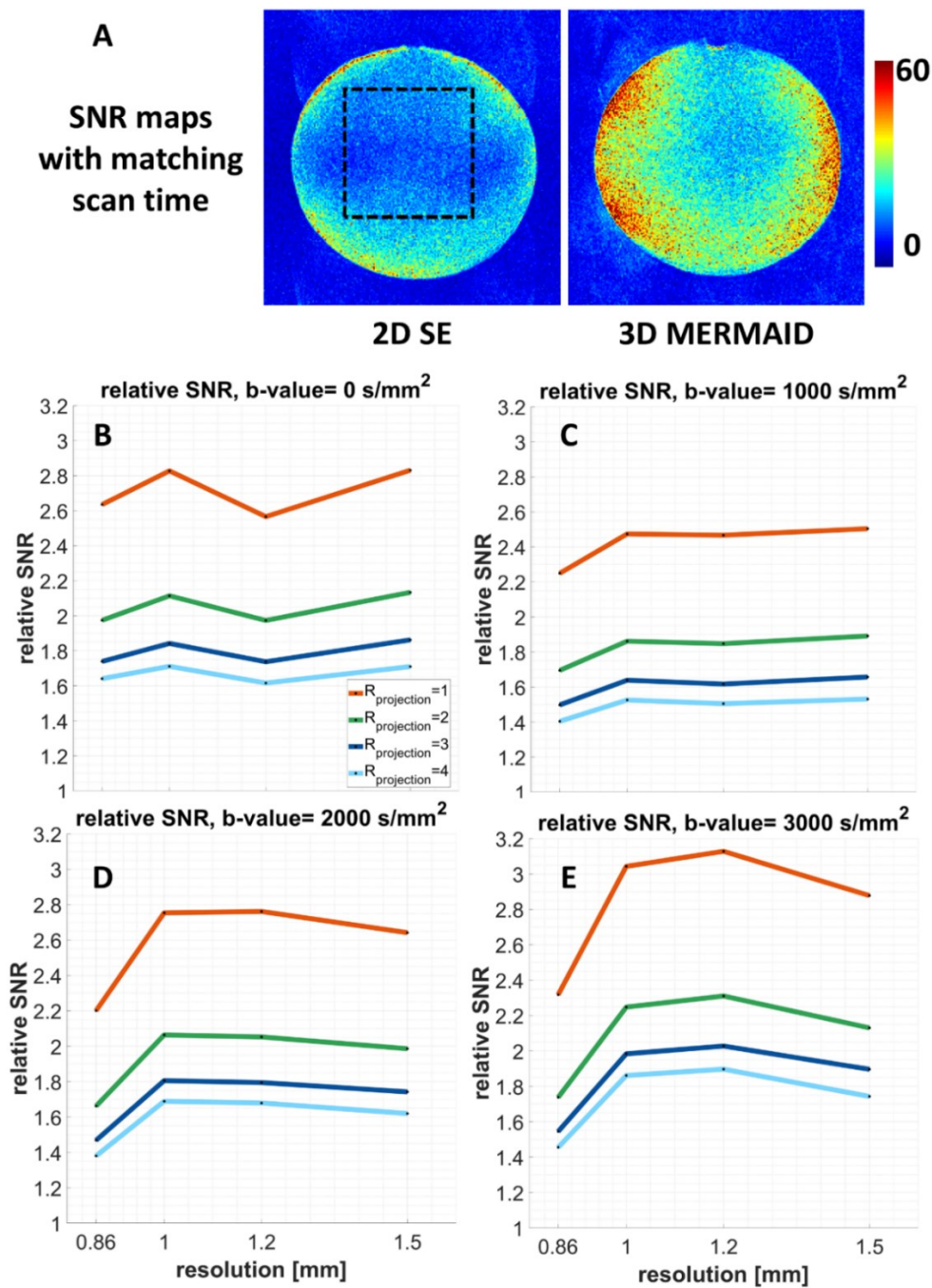


Figure 4.4. SNR map and relative SNR of the 3D MERMAID sequence compared to 2D SE-EPI sequence at different TEs/TRs. A: SNR maps of a 2D SE-EPI and 3D MERMAID sequence at nominal isotropic resolution of 1 mm. The scan times for both scans are matched to show the SNR efficiency of the 3D MERMAID sequence. The area at the center of the phantom used to calculate the relative SNR is specified as dotted line. B, C, D, and E are the SNR of the 3D MERMAID sequence relative to the 2D SE-EPI sequence at the center of the phantom for different timings corresponding to b-values of 0, 1000, 2000, and 3000 s/mm2, respectively.

4.3.3. Removal of motion artifacts in reconstructed 3D images

Reconstructed projections at 0, 45, and 90 degrees, acquired across different shots and b-values, are shown in Figure 4.5. Each shot is independently reconstructed showing projections of the brain from different angles in a 2D image. Signal accumulation occurs in regions with high ΔB_0 , such as the frontal lobe (indicated by a yellow arrow) and around the ear canal (blue arrow), as seen in a 2D SE-EPI with an EPI trajectory.

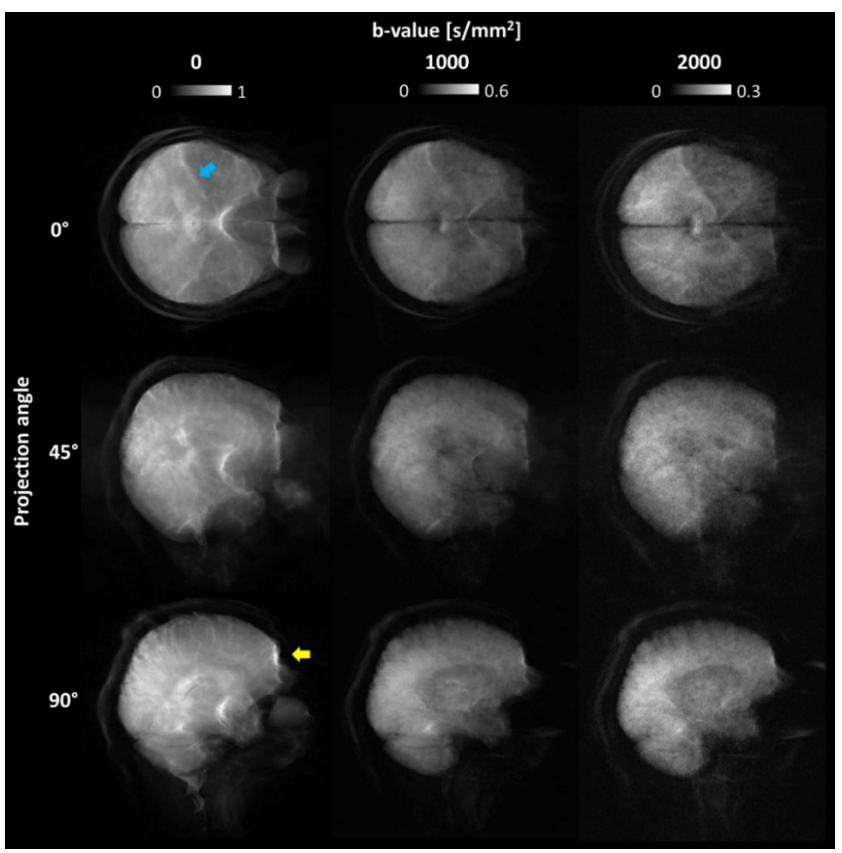


Figure 4.5. Raw projections acquired at b-values of 0, 1000, and 2000 s/mm2 in 0-, 45-, and 90-degrees angles. Each projection is independently reconstructed showing the brain overlaying on a single image. Blue and yellow arrows show artifacts due to $\Delta B0$ nonuniformities.

Figure 4.6A illustrates the impact of the cardiac cycle on the magnitude of the projection images acquired with a b-value of 1000 s/mm². It displays 10 consecutive projections corresponding to the duration of two cardiac cycles (I and II), with colors specifying the time range

at which the projections are acquired. At the third projection of both cycles, synchronized immediately after the peak of the cardiac signal, there is a visible signal drop at the center of the brain where the ventricles exhibit the greatest motion. This effect was consistently observed across all projections. For a healthy adult with a heart rate of 60-90 bpm, up to 20% of shots for the TRs used here were affected by this type of motion.

The effectiveness of the motion correction strategy on raw diffusion images is demonstrated in Figure 4.6B. The first column to the left presents images reconstructed without motion correction, highlighting signal drops and image artifacts. The second column shows the impact of removing the phase of each projection using a triangle filter (PC), which significantly reduces artifacts and recovers signal. The third column illustrates the results of the full motion correction method, where corrupted projections were also removed (MC), leading to further enhanced signal at the center, where motion is most pronounced. The percentage difference calculated between PC and PC+MC in the last column shows up to 10% increase in signal.

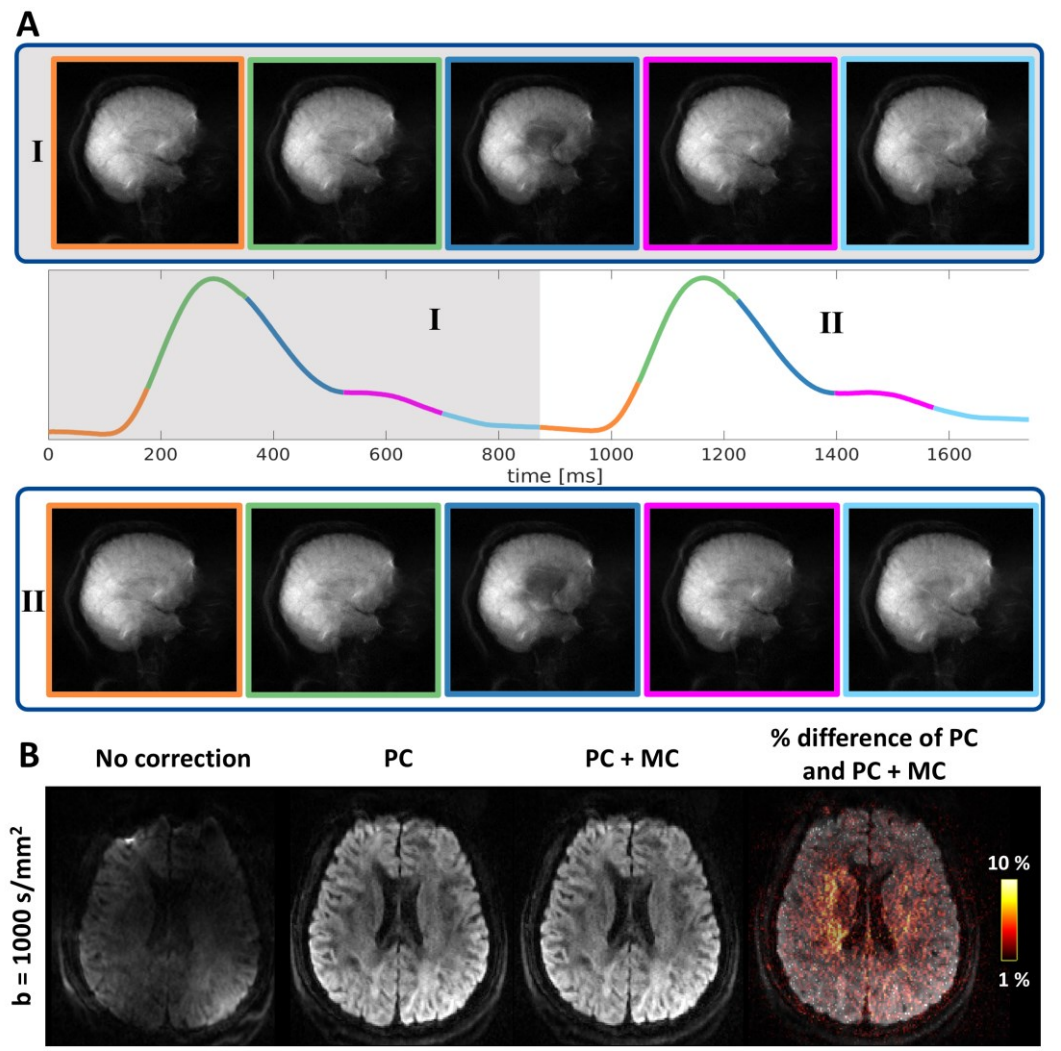


Figure 4.6. Effects of the cardiac cycle on the magnitude images of the projections and performance of the motion correction method. A: shows 10 consecutive sagittal projections for two cardiac cycles. Colors of the pulse signal correspond to a phase in the cardiac cycle a projection is acquired. Signal drop at the center of the brain is obvious in the third projection of each cycle. B: performance of the motion correction when there is no correction, only phase correction (PC), phase and magnitude correction (PC + MC), and the difference map between PC, and PC+MC images overlayed to the image.

The image contrast of the 3D MERMAID sequence differs from that of a typical 2D SE-EPI sequence, it has an enhanced T₁ weighting due to the shorter TR, as demonstrated in the b=0 images in Figure 4.7A. The scans acquired using 3D MERMAID exhibit less WM-GM contrast compared to those from the 2D SE-EPI sequence.

Post-processed images from 12 diffusion encoding directions were used to calculate mean diffusion-weighted images (MDWI), FA, and ADC maps for both sequences at two b-values of 1000 and 2000 s/mm² (Figure 4.7B). The SNR gain of the 3D MERMAID, matched for scan time with the 2D SE-EPI sequence, is clear in all diffusion maps, particularly at the center of the brain where B_1^+ nonuniformity is higher. The FA, DEC, and ADC maps are consistent across both sequences.

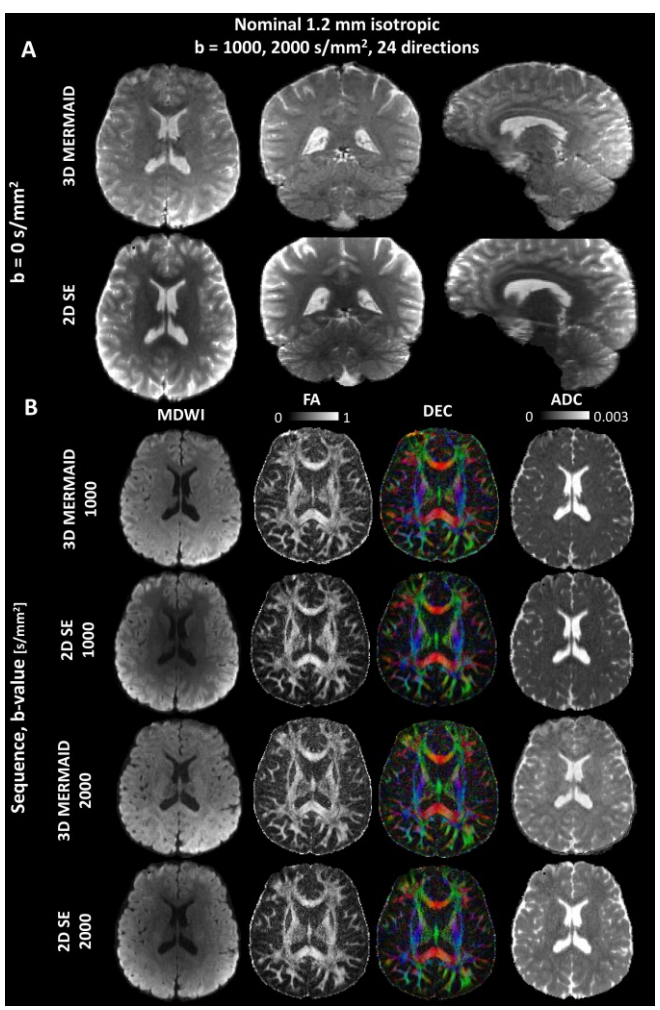


Figure 4.7. Comparison between diffusion measures calculated from a 2D SE-EPI and 3D MERMAID sequence with a matching scan time. A: shows different contrast between tissues in scans with no diffusion weighting. B: shows calculated diffusion parameters from 12 diffusion directions using the 3D MERMAID sequence compared to a standard 2D SE-EPI sequence.

4.3.4. 2D SE-EPI and 3D MERMAID comparison at sub-millimetre resolution

Figure 4.8 compares the 2D SE-EPI and 3D MERMAID sequences at high spatial and angular resolution. SNR maps calculated from 20 averages show an approximate 36% improvement in SNR across the entire volume with the 3D MERMAID sequence. This enhancement results in higher quality FA and ADC maps, and more significantly, less noisy fODFs derived from high b-values. Zoomed-in areas in the temporal lobe (A and B) and anterior commissure (C and D) clearly demonstrate improved fODFs with reduced noise contamination. The crossing fibers of the fornix and anterior commissure, shown in E and F, are more accurately detected using the 3D MERMAID sequence. Multiple slices and views of the SNR map, MDWI, DEC, ADC maps, and fODFs are presented in Figure 4.12-Figure 4.18 of the Supporting Information.

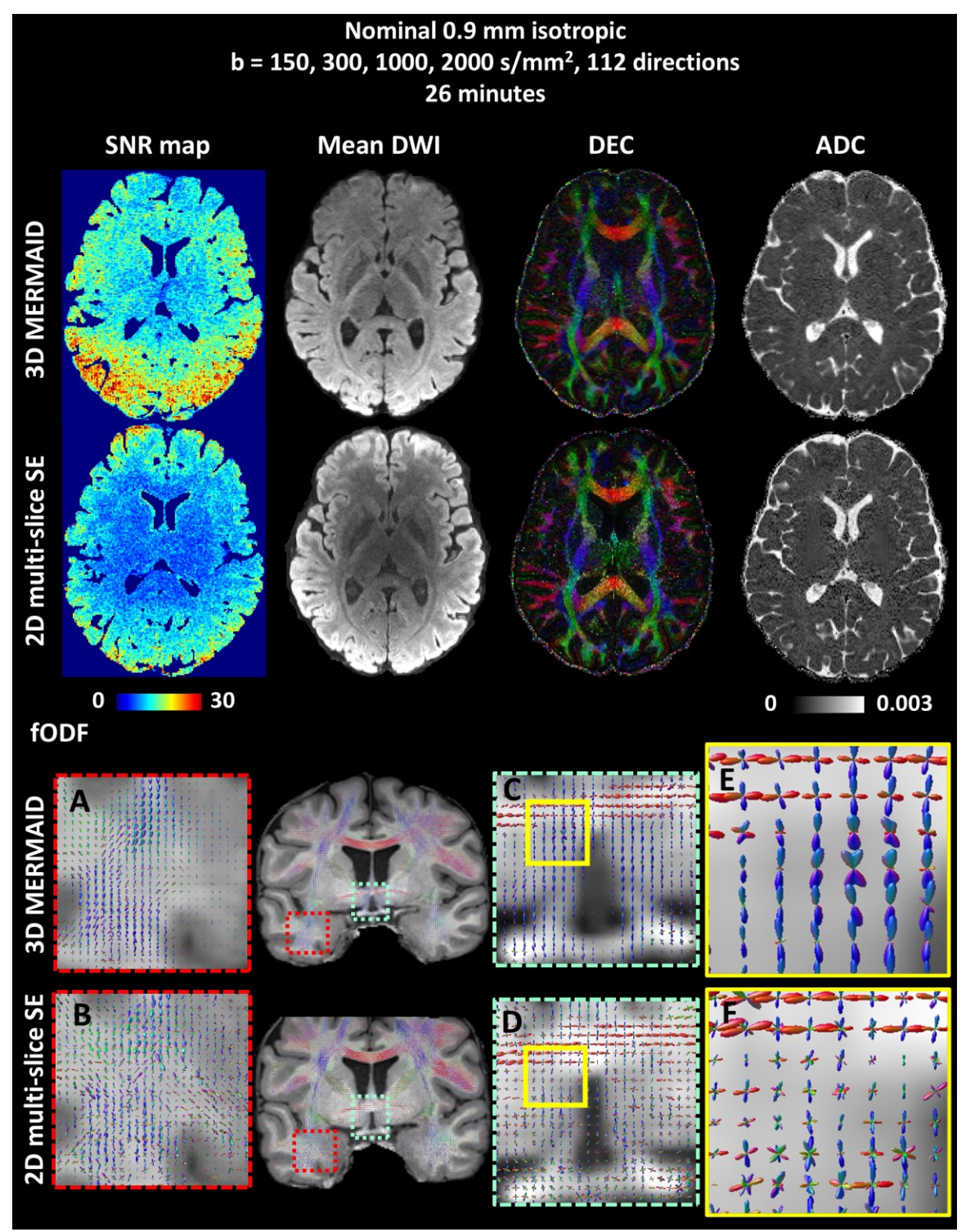


Figure 4.8. Comparison between high spatial- and angular-resolution scans of the 2D SE-EPI and 3D MERMAID sequences- SNR, MDWI, DEC, and ADC maps are shown in the top two rows. fODFs overlayed on the anatomical scan and their zoomed-in images are shown below.

4.3.5. Pushing the spatial resolution of 3D MERMAID

High-resolution diffusion maps and fODFs derived from the nominal 0.74 mm isotropic scan are presented in Figure 4.9. The diffusion maps in the first row show small anatomical features such as blood vessels that are not visible at lower resolutions. Additional views of this data can be found in Supporting Information Figure 4.19-Figure 4.22.

Zoomed-in areas of the fODFs overlayed on the anatomical scan show intricate details of various regions within the GM and WM. In Figure 4.9A, subcortical U-fibers connecting intracortical areas in the anterior-posterior direction are visible. In Figure 4.9B, orientations of tangential and radial intra-cortical fibers in different layers, and the projections of the WM into the cortex are displayed. The complex structure of crossing fibers in the WM is also shown in Figure 4.9C, and the small curvature of the hippocampus is detectable in Figure 4.9D.

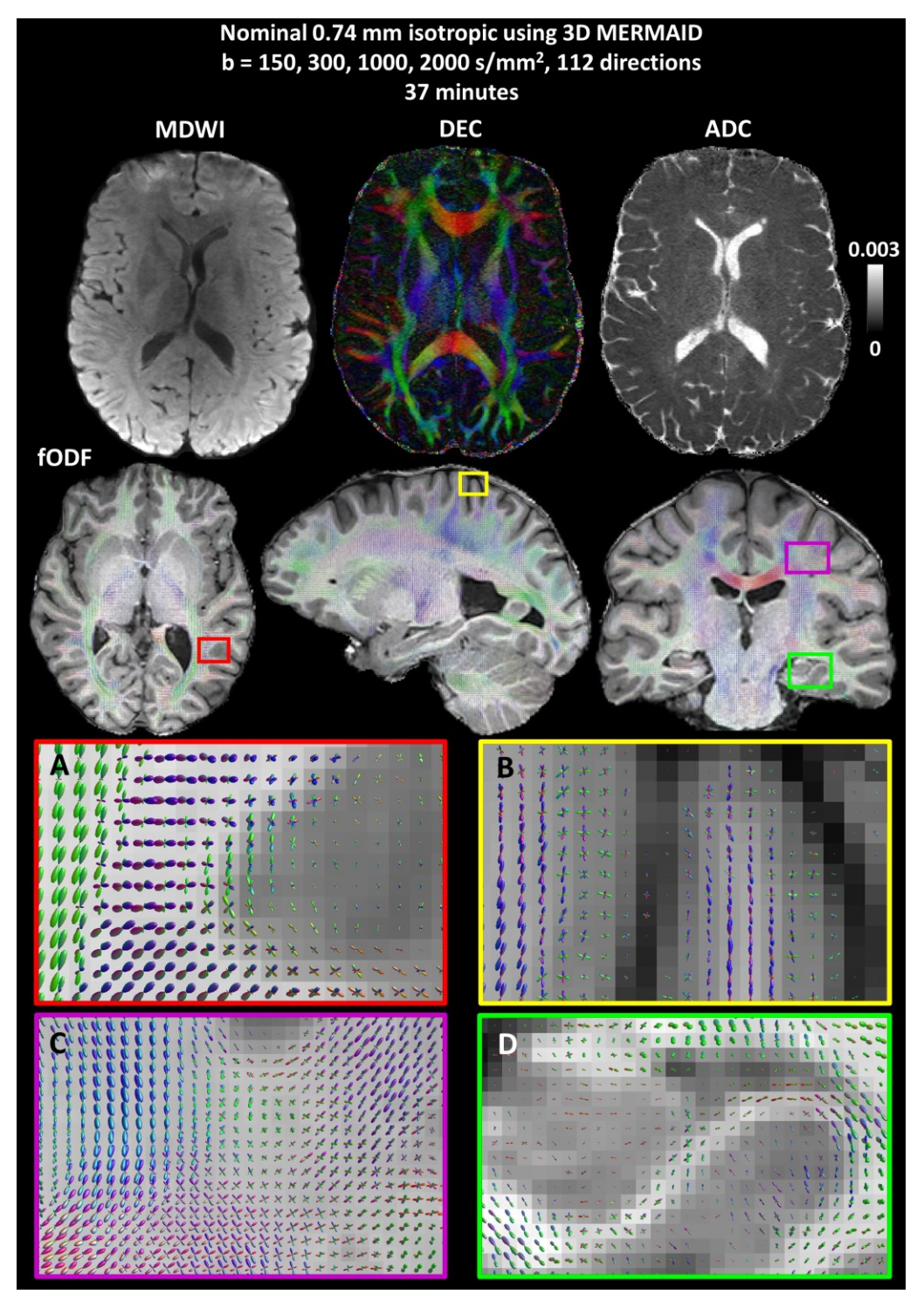


Figure 4.9. High-resolution diffusion maps and fODFs calculated from the nominal 0.74 mm isotropic scan acquired using the 3D MERMAID sequence- diffusion maps in the first row, and fODFs overlayed on the MPRAGE scan in different orientations are shown in the second row. Zoomed-in areas, delineated by different box colors, reveal exquisite details of the intra-cortical fibers, WM crossing fibers, and the curvature of the hippocampus.

4.4. Discussion

4.4.1. SNR advantage of 3D MERMAID sequence over other 2D and 3D sequences

The results of comparing multi-slice 2D SE-EPI and 3D MEMRAID sequences in Figure 4.4, Figure 4.7 and Figure 4.8 show that SNR is enhanced without increasing the scan time. This improvement can be used to increase the resolution of current multi-shell, high-b-value, and advanced diffusion-encoding protocols. Additionally, the increased SNR efficiency can be leveraged to reduce the scan time at resolutions currently achievable by 2D SE-EPI sequences by further accelerating the 3D MERMAID sequence.

As depicted in Figure 4.3C, the available signal, and therefore the SNR, increases with an exponential recovery as a function of TR. This presents a significant advantage compared to 2D SE-EPI and other 3D multi-slab sequences, where SNR is increased by averaging as a function of $\sqrt{N_{averages}}$. This makes 3D MERMAID sequence considerably more efficient for scans where longer acquisition times are permissible, as demonstrated in the 0.74 mm isotropic scan.

4.4.2. Effective resolution of 3D MERMAID

We previously demonstrated in (Feizollah & Tardif, 2023) that T_2^* decay causes blurring and lowers the effective image resolution, depending on the type of readout. In an EPI trajectory, the PE direction has the lowest bandwidth. Since the PE directions of the 2D EPI trajectory and TURBINE are the same, the resulting effective resolution in the PE direction is similar. For nominal resolutions of 1.5, 0.9, and 0.74 mm used, the effective resolutions are expected to be ~ 1.7 , ~ 1.2 , and ~ 0.9 mm, respectively, which are $\sim 30\%$ lower than the nominal values.

In the 2D SE-EPI case, the resolution along the slice direction depends on the quality of the slice profile, whereas in the 3D MERMAID sequence, effects of CS reconstruction and the semi-Hanning filter can slightly lower the effective resolution within the coronal plane, as seen in the coronal and sagittal views of Figure 4.12-Figure 4.18 of Supporting Information. This can be compensated by oversampling \sim 20% of the FE direction without a TE and readout time penalty.

4.4.3. Microstructure modeling using 3D MERMAID

The 3D MERMAID sequence provides a novel contrast that includes both T₁- and T₂-weighting. According to Eqs. (27) and (28), both longitudinal and transverse magnetizations at steady state are sensitive to TE. Tissue relaxation rates are not considered in several diffusion-based microstructure models that compute compartmental volume fractions (H. Zhang et al., 2012), which are in reality T₂-weighted signal fractions. To estimate true volume fractions, a coencoded diffusion-relaxometry acquisition is required (Frigo et al., 2020; Veraart et al., 2018b). Although the scans included in this work are suitable for microstructure modeling, the effect of the enhanced T₁-weighting on the compartmental signal fractions should be studied further in future work.

4.4.4. Limitations

The short scan time of 3D MERMAID and phase-correction approach developed was achieved by using a single-shot EPI acquisition for each projection. However, this approach is limiting for very high spatial resolutions where B₀ nonuniformities and higher eddy currents cause significant artifacts due to long readout times. Reducing echo-spacing shortens the readout time but also increases eddy-current induced artifacts due to higher gradient magnitudes. Techniques such as dual polarity GRAPPA (Hoge & Polimeni, 2016), better reference scans (Polimeni et al., 2016; Talagala et al., 2016), and using a field monitoring system (Feizollah & Tardif, 2023; Lee et al., 2021c; Ma et al., 2020; Veldmann et al., 2024) can help mitigate these artifacts, with an additional scan and/or image reconstruction time.

Imaging at ultra-high fields would enhance the SNR efficiency of the 3D MERMAID (Feizollah & Tardif, 2023). However, the higher B₁⁺ nonuniformity and increased SAR at ultra-high field are two limiting factors for the 3D MERMAID sequence due to its high sensitivity to B₁⁺ non-uniformity and added inversion pulse. Parallel transmit (pTX) approaches (Feizollah et al., 2024; Gras et al., 2017, 2018; Khaneja et al., 2005; Lowen et al., 2024) are needed to solve these limitations and achieve uniform high-resolution diffusion images at 7 T.

Motion sensitivity is a well-known challenge in dMRI, arising from the need to sensitize the MR signal to both desired and undesired motion, such as spin diffusion and non-linear brain motion during the cardiac cycle (Enzmann & Pelc, 1992; Poncelet et al., 1992; Bammer et al., 2010), respectively. Studies have shown that motion effects manifest as phase errors, leading to significant k-space shifts, particularly during systole, even in single-shot imaging approaches. As discussed in the Introduction, these artifacts are especially difficult to correct in multi-shot acquisitions.

The signal attenuation observed in the magnitude of some projections results from intravoxel incoherent motion during systole, which introduces a phase difference along the projection dimension. To address this, these affected projections were rejected during image reconstruction, enabling a more reliable reconstruction. This issue also exists in other 2D and 3D multi-slab approaches, as noted in prior studies (Pierpaoli et al., 2002; O'Halloran et al., 2011). However, due to the thinner thickness of individual slices/slabs, there is a lower probability of consistently falling within the affected region. In contrast, our approach, acquiring the full brain during each excitation, results in projections acquired during systole consistently containing these artifacts.

For correcting phase differences between shots, we employed a method to correct phase

errors with high-frequency components in two dimensions and at the k-space center along the projection dimension. Experiments (not included here) showed that this approach corrects these errors without causing a bias in a specific diffusion direction. The reason is that our method is less sensitive to shot-to-shot differences due to short interval between each shot, as opposed to most multi-shot approaches where each shot is acquired in a TR in a range of seconds.

Lastly, comparing the SNR plots of the phantom and human scans in Figure 4.4 and Figure 4.8 shows that the SNR gain of 3D MERMAID compared to 2D SE-EPI for the human scan was lower than for the phantom scan, decreasing from ~50% to ~30%. This was expected due to remaining small discrepancies between different projection magnitude images caused by the cardiac cycle. Using a cardiac-gated approach or motion-compensated gradients can potentially improve the SNR, but the trade-off between the SNR gain and longer TE and/or scan times should be considered.

4.5. Conclusion

The 3D MERMAID sequence offers several advantages over typically used 2D and 3D acquisitions: higher SNR per unit time, shorter TR per volume compared to 2D multi-slice acquisitions, no slice/slab profile artifacts, better spin history, and better B₁⁺ uniformity. These benefits become more pronounced in high- and ultra-high-resolution imaging. The 3D MERMAID sequence balances the trade-off between high-resolution k-space and q-space sampling. Preliminary results at 0.74 mm isotropic show the potential of this technique to study small and complex structures in vivo in a reasonable scan time on clinical scanners.

4.6. Acknowledgments

The authors would like to thank David Costa, Ronaldo Lopez, and Soheil Mollamohseni

Quchani, the MRI technicians at the McConnell Brain Imaging Center for their assistance with the human scans, Marcus Couch (Siemens Collaboration Scientist) for his technical support, Ilana Leppert for her technical suggestions and discussions on dMRI, Michael Ferreira for his help to make the phantom, Jennifer Campbell for her insights on microstructure modeling, Wen Da Lu for his suggestions and discussions on image registration, Mark Nelson for providing ANTs code for image registration, and all the volunteers who participated in the human scans.

This project was funded by the Natural Sciences and Engineering Research Council of Canada, the Fonds de recherche du Québec – Santé, and Healthy Brains for Healthy Lives. The data was acquired at the McConnell Brain Imaging center, which is supported by the Canadian Foundation for Innovation, Brain Canada, and Healthy Brains for Health Lives.

4.7. Data and Code Availability Statement

The MATLAB script Bloch simulations available used for is at (https://github.com/TardifLab/diffusion mermaid). The image reconstruction pipelines described Figure 4.2. and Figure 4.11 of Supporting Information are available (https://github.com/TardifLab/diffusion mermaid).

4.8. Supplementary materials

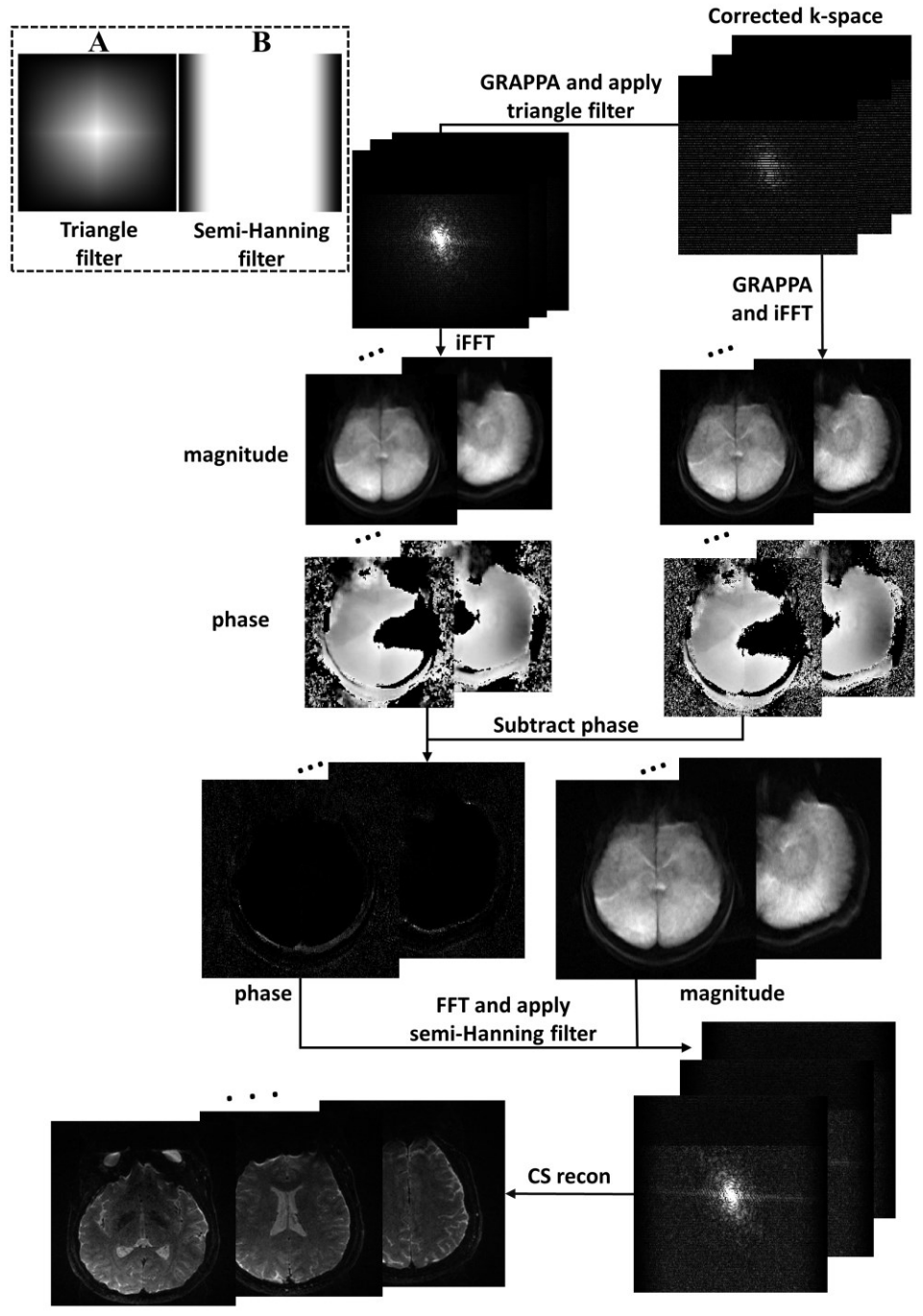


Figure 4.10. Output of each image reconstruction step described in Section 4.2.2. A and B are triangle and semi-Hanning filters, respectively.

Denoising integrated in 3D MERMAID reconstruction pipeline

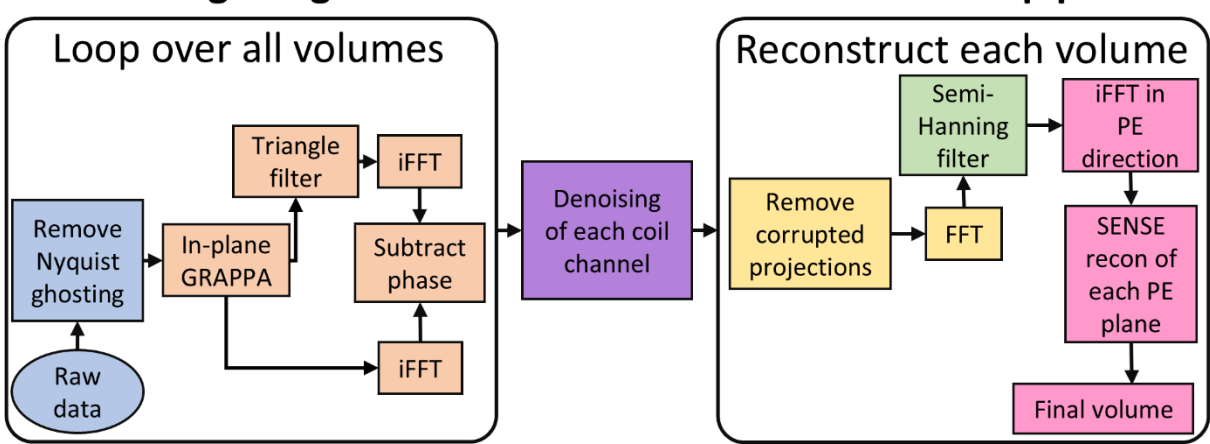


Figure 4.11. 3D MERMAID image reconstruction pipeline including denoising. First all projections of all volumes are reconstructed, then denoising (NORDIC) is performed for each coil channel individually. In the next step, denoised projections are used to reconstruct every volume as in the pipeline described in Figure 4.2.

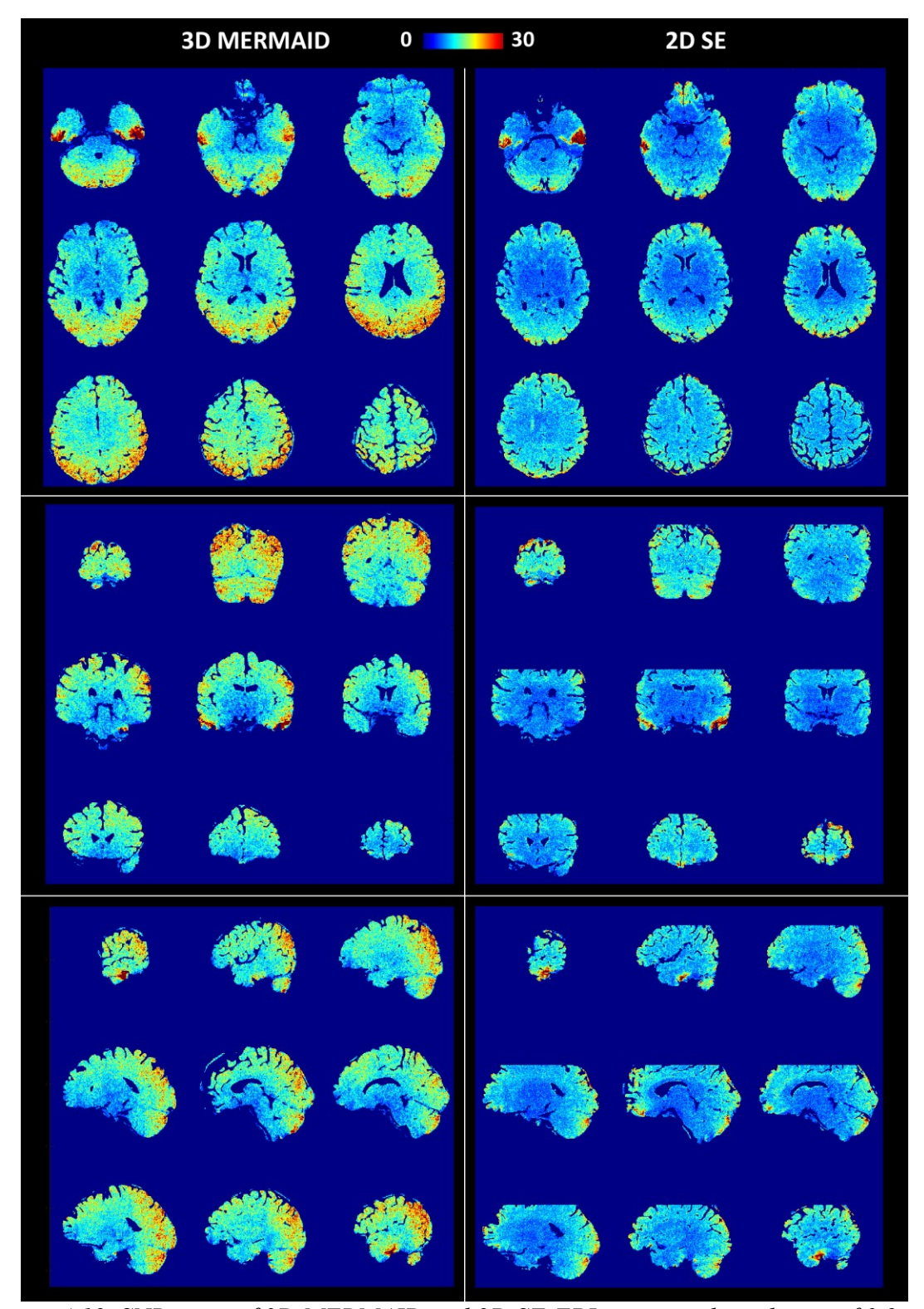


Figure 4.12. SNR maps of 3D MERMAID and 2D SE-EPI at nominal resolution of 0.9 mm.

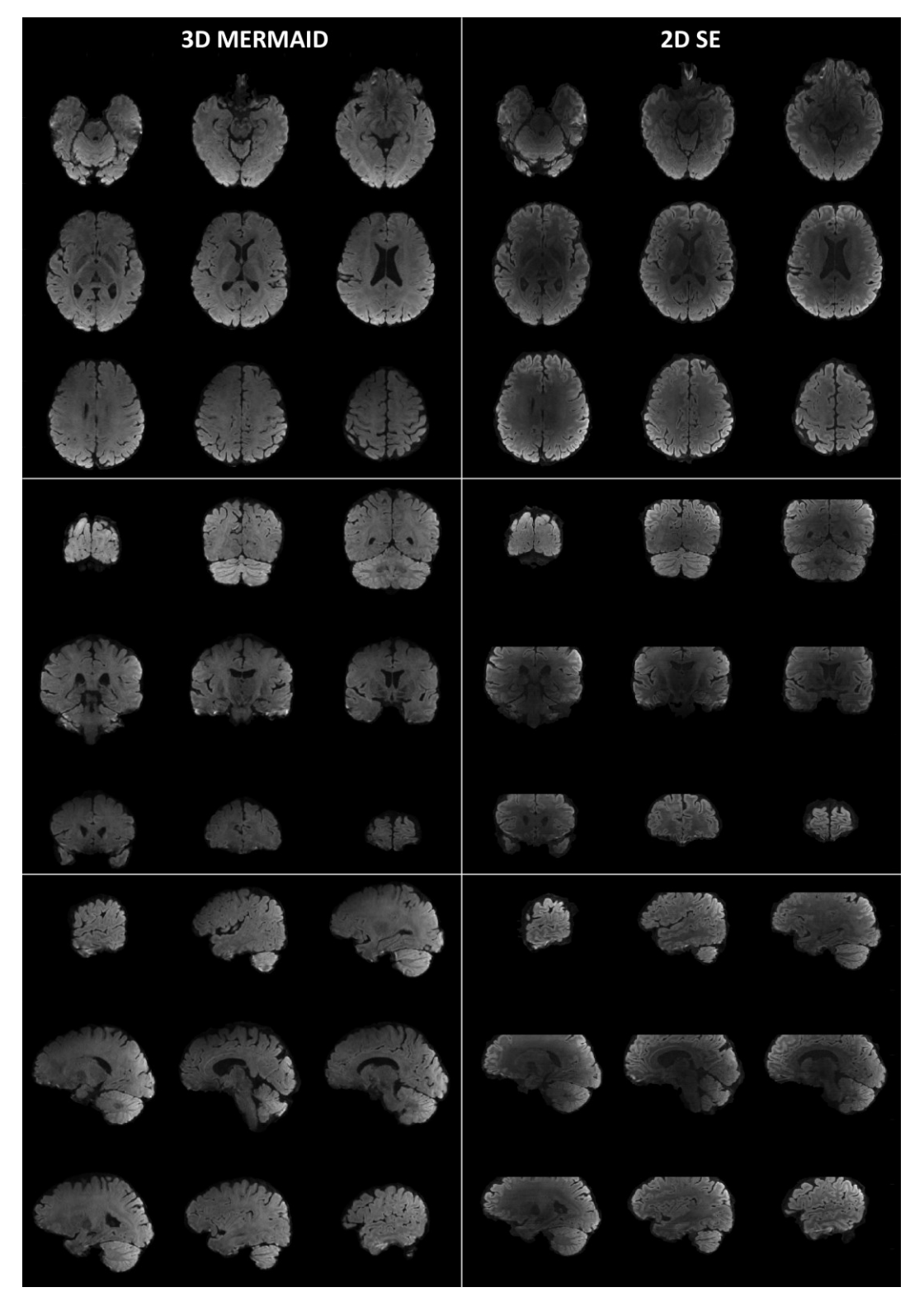


Figure 4.13. MDWI of 3D MERMAID and 2D SE-EPI at nominal resolution of 0.9 mm.

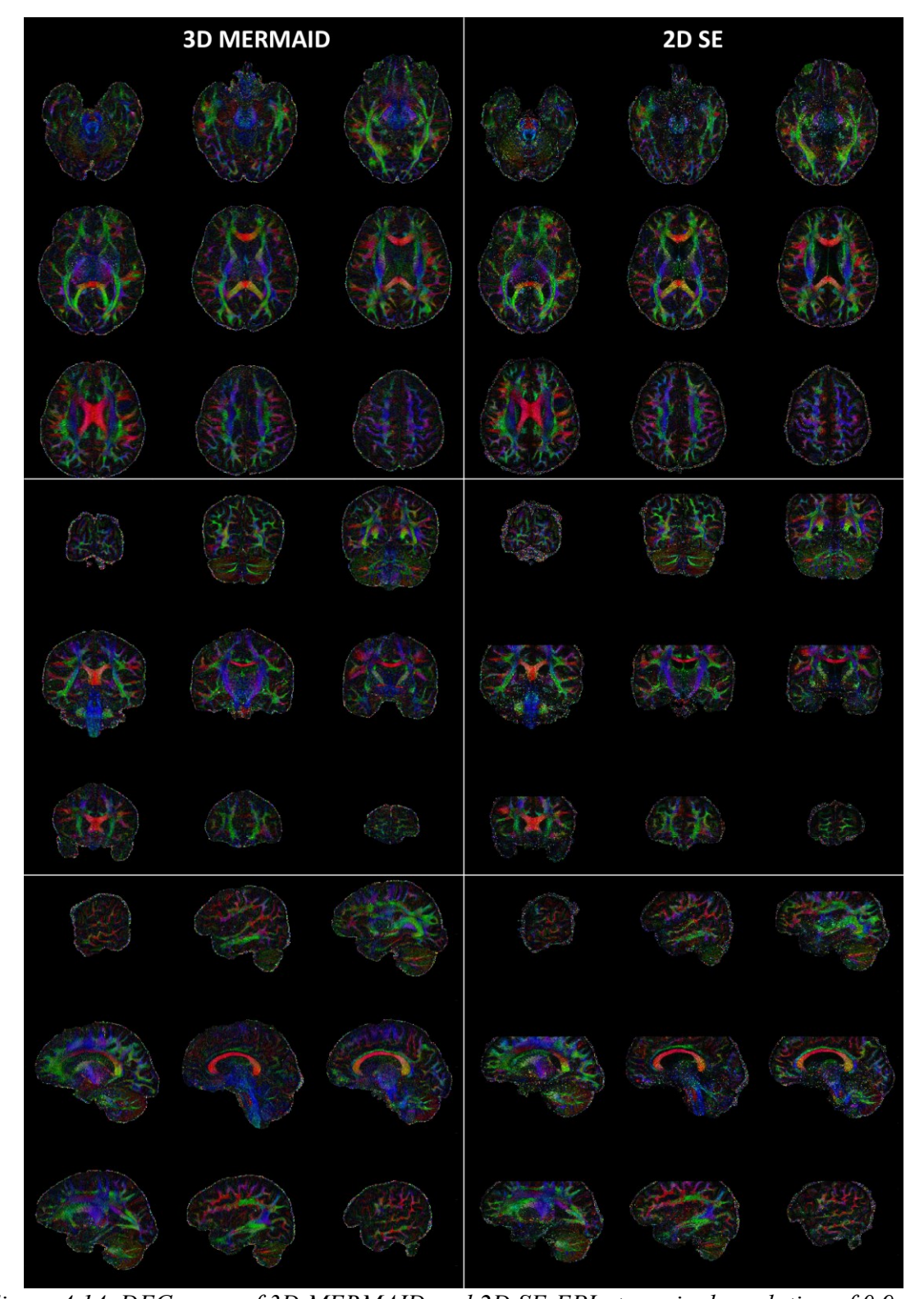


Figure 4.14. DEC maps of 3D MERMAID and 2D SE-EPI at nominal resolution of 0.9 mm.

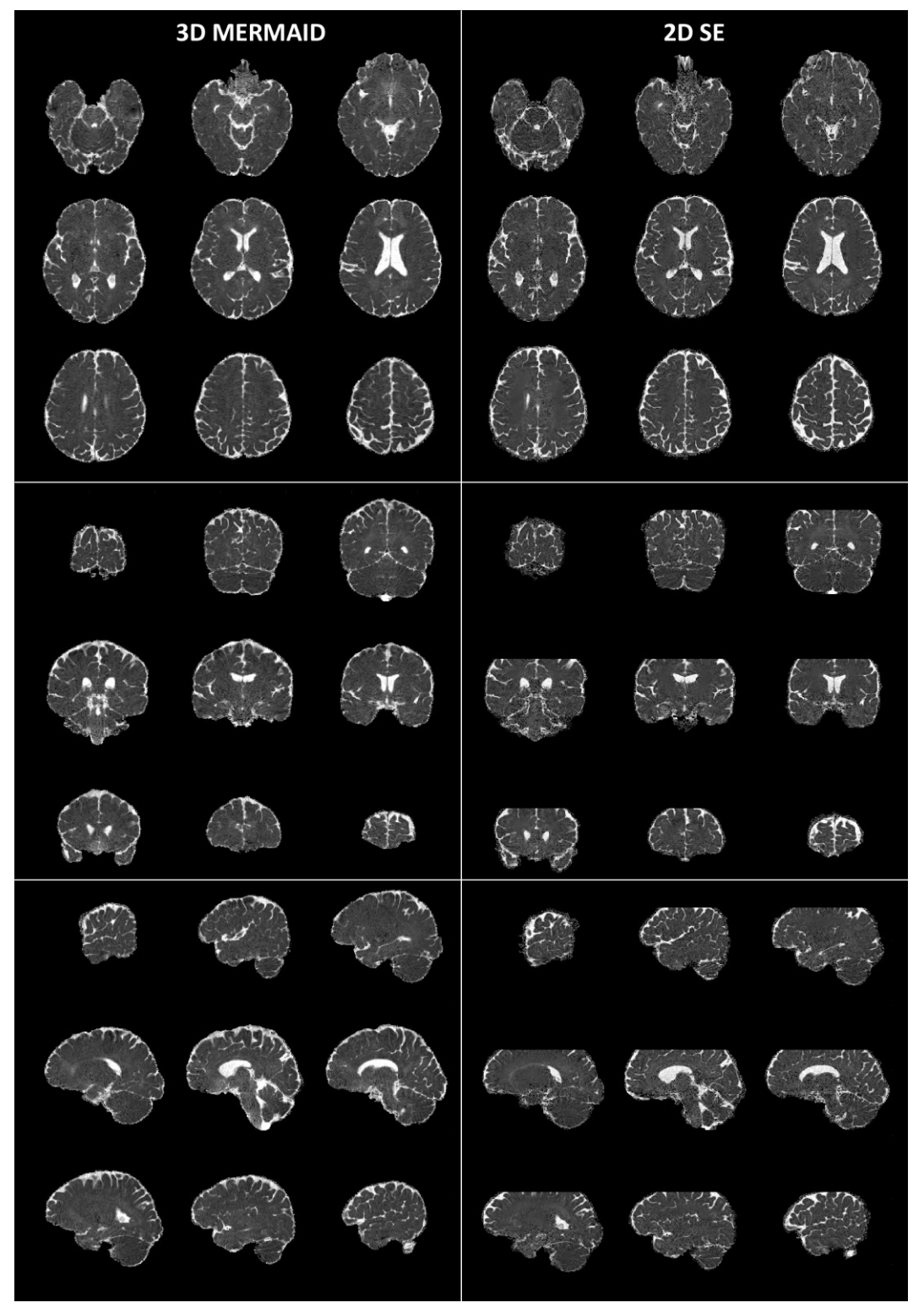


Figure 4.15. ADC maps of 3D MERMAID and 2D SE-EPI at nominal resolution of 0.9 mm.

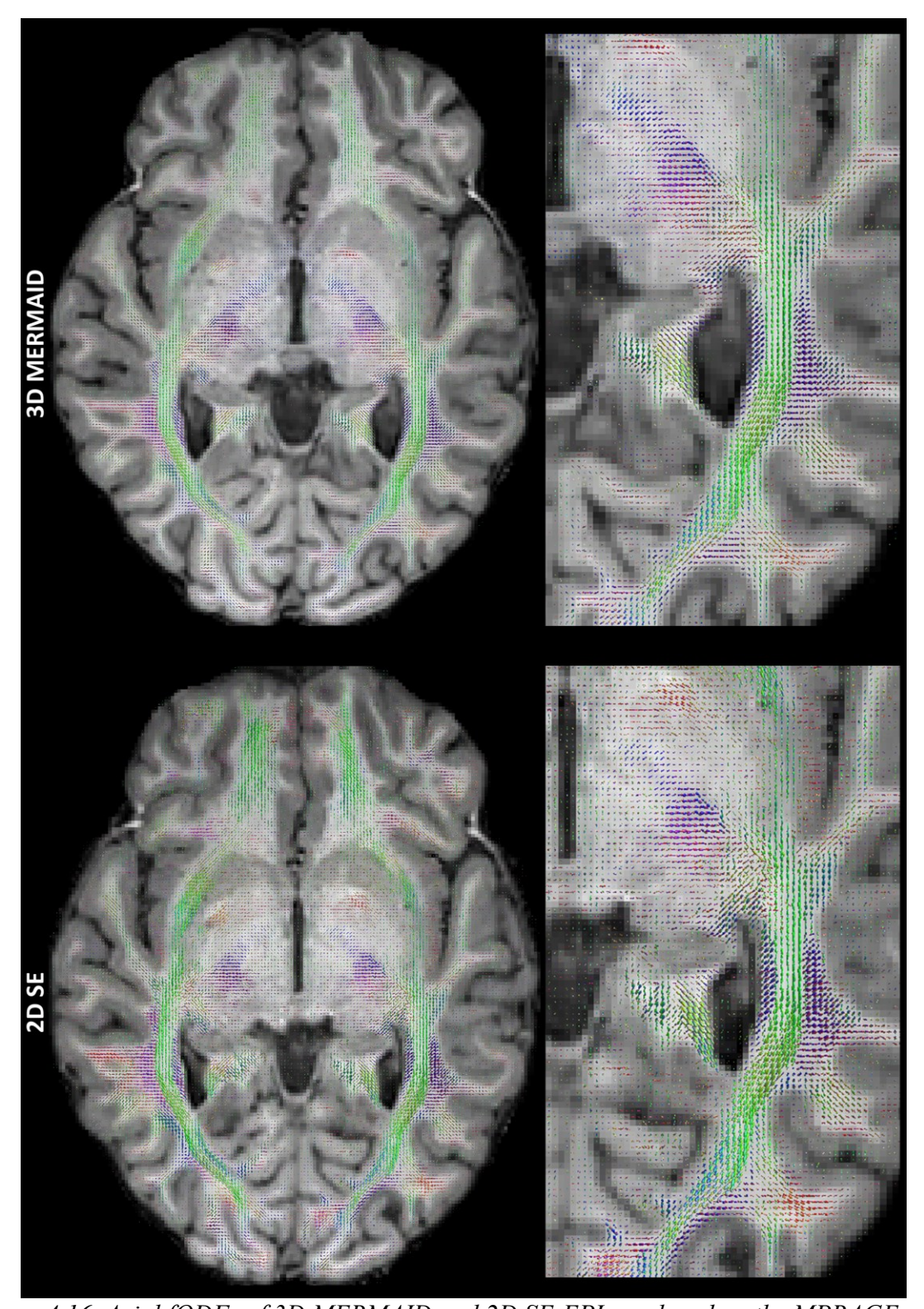


Figure 4.16. Axial fODFs of 3D MERMAID and 2D SE-EPI overlayed on the MPRAGE scan.

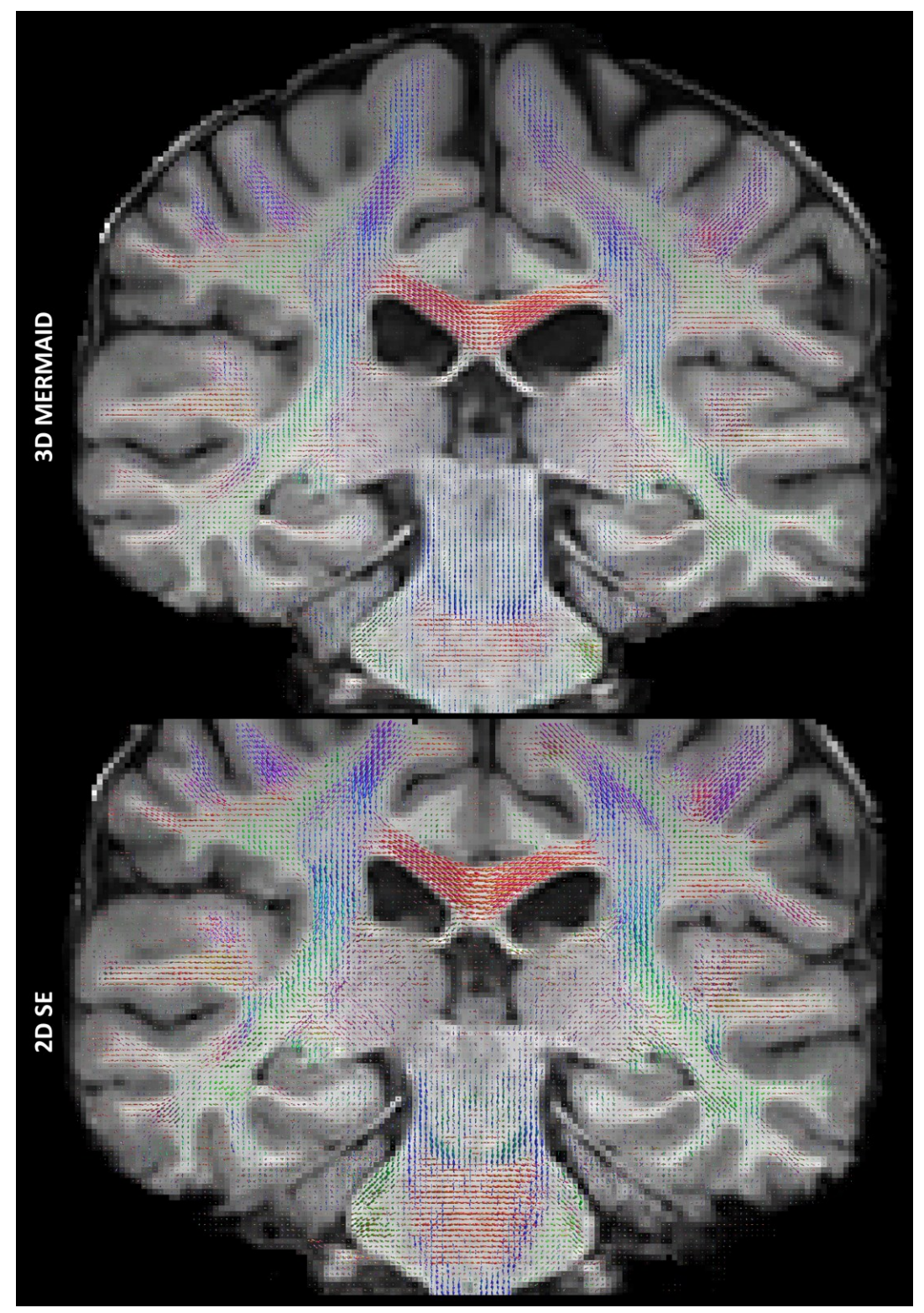


Figure 4.17. coronal fODFs of 3D MERMAID and 2D SE-EPI overlayed on the MPRAGE scan.

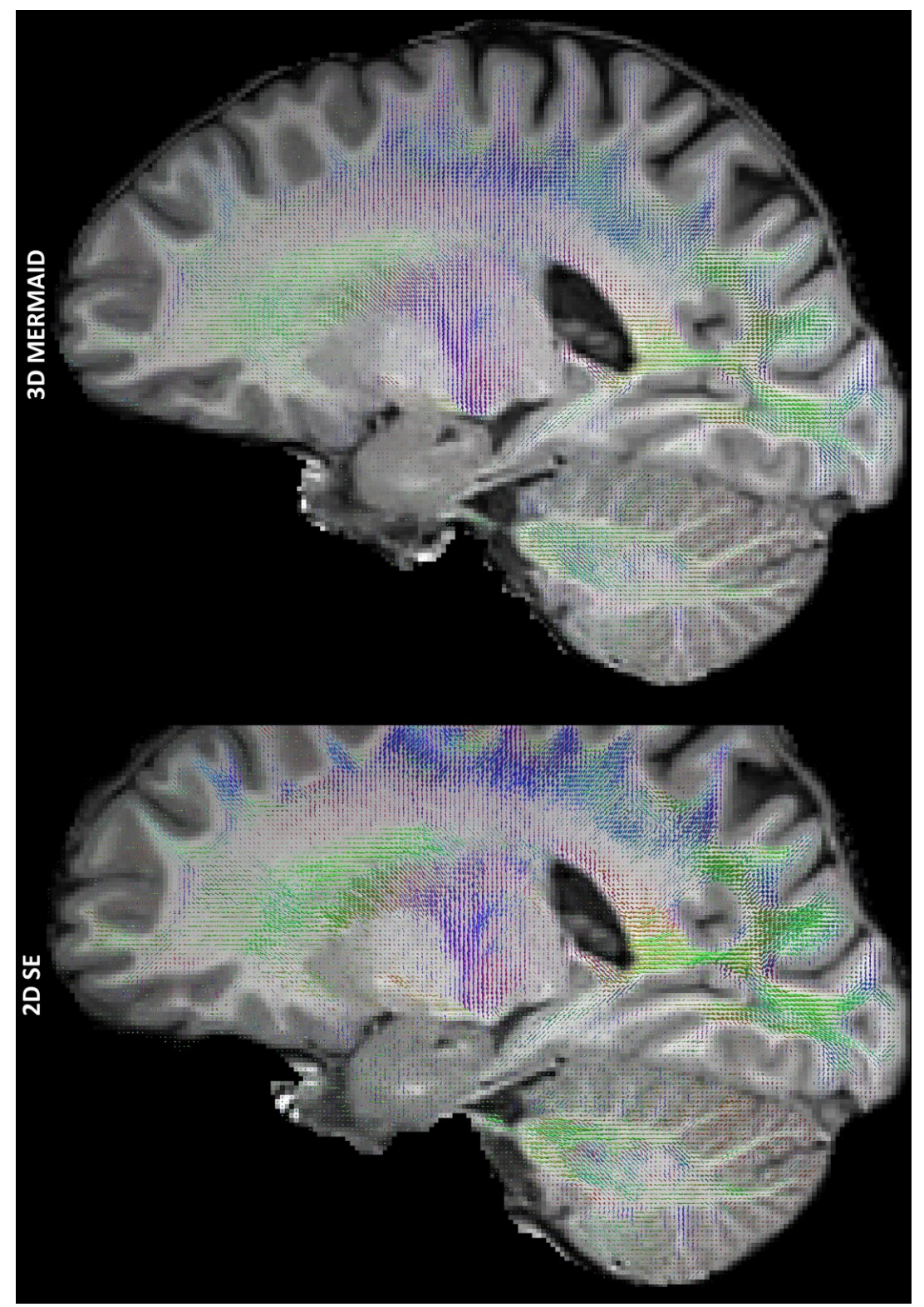


Figure 4.18. Sagittal fODFs of 3D MERMAID and 2D SE-EPI overlayed on the MPRAGE scan.

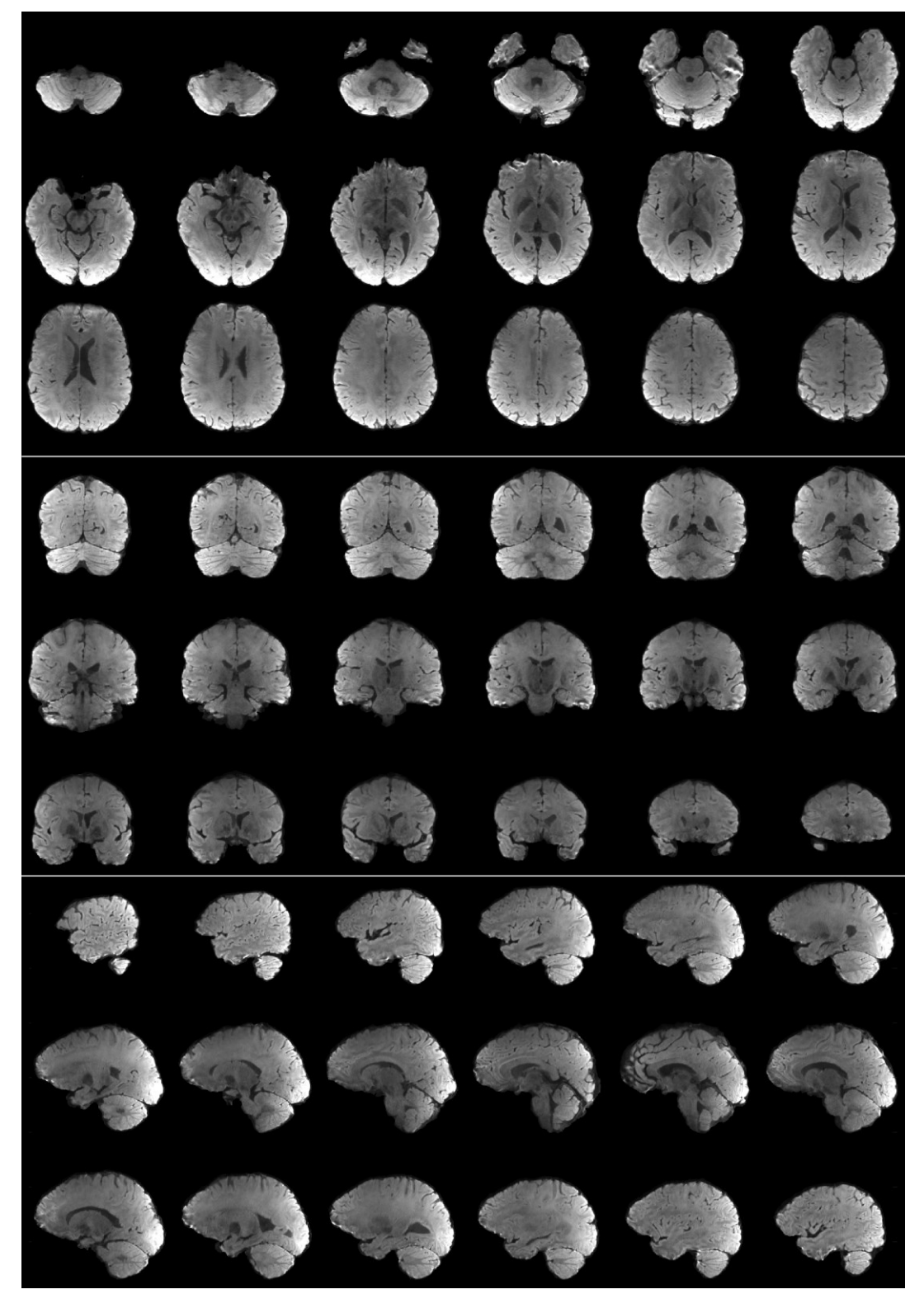


Figure 4.19. MDWI of nominal isotropic 0.74 scan.

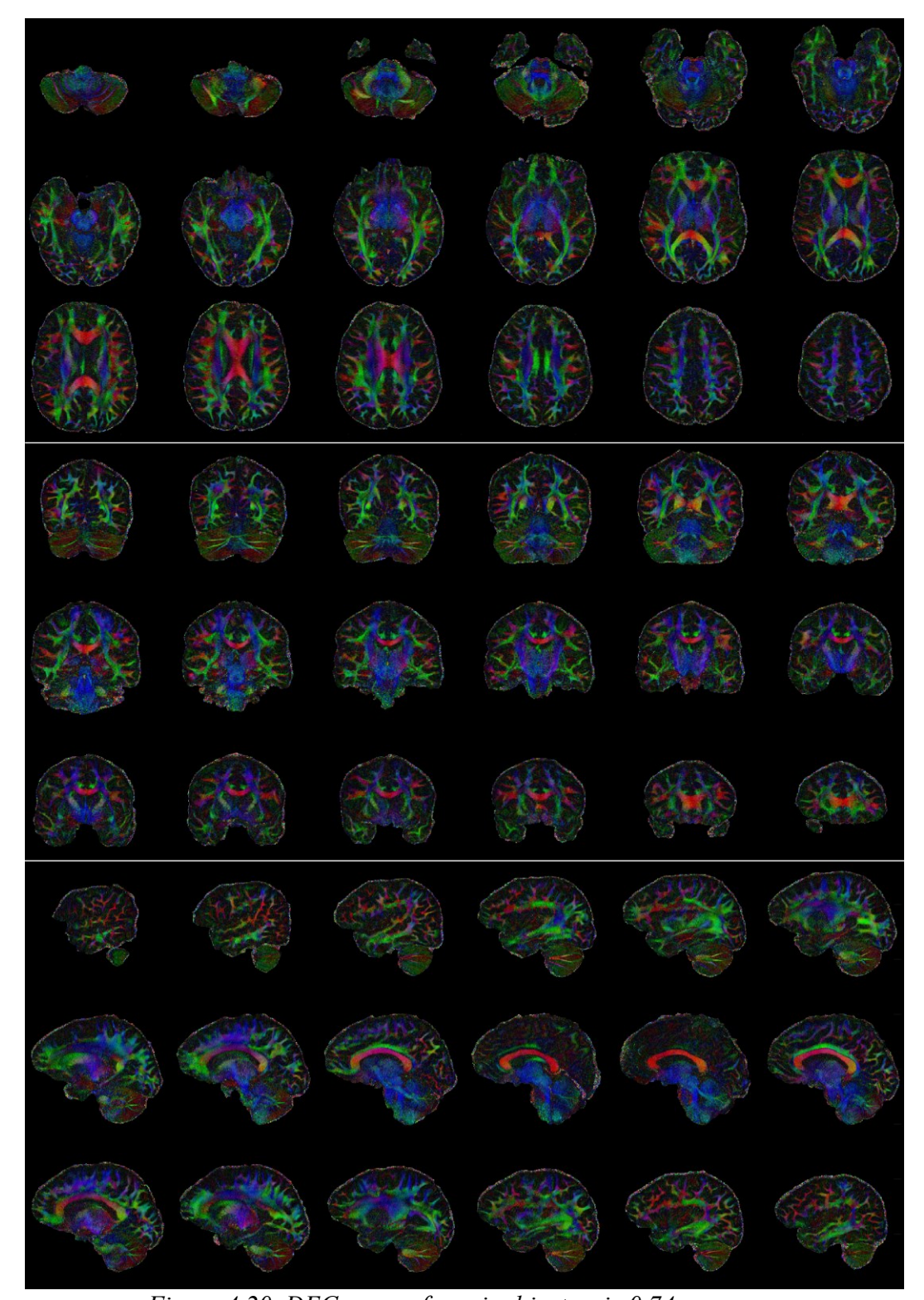


Figure 4.20. DEC maps of nominal isotropic 0.74 mm scan.

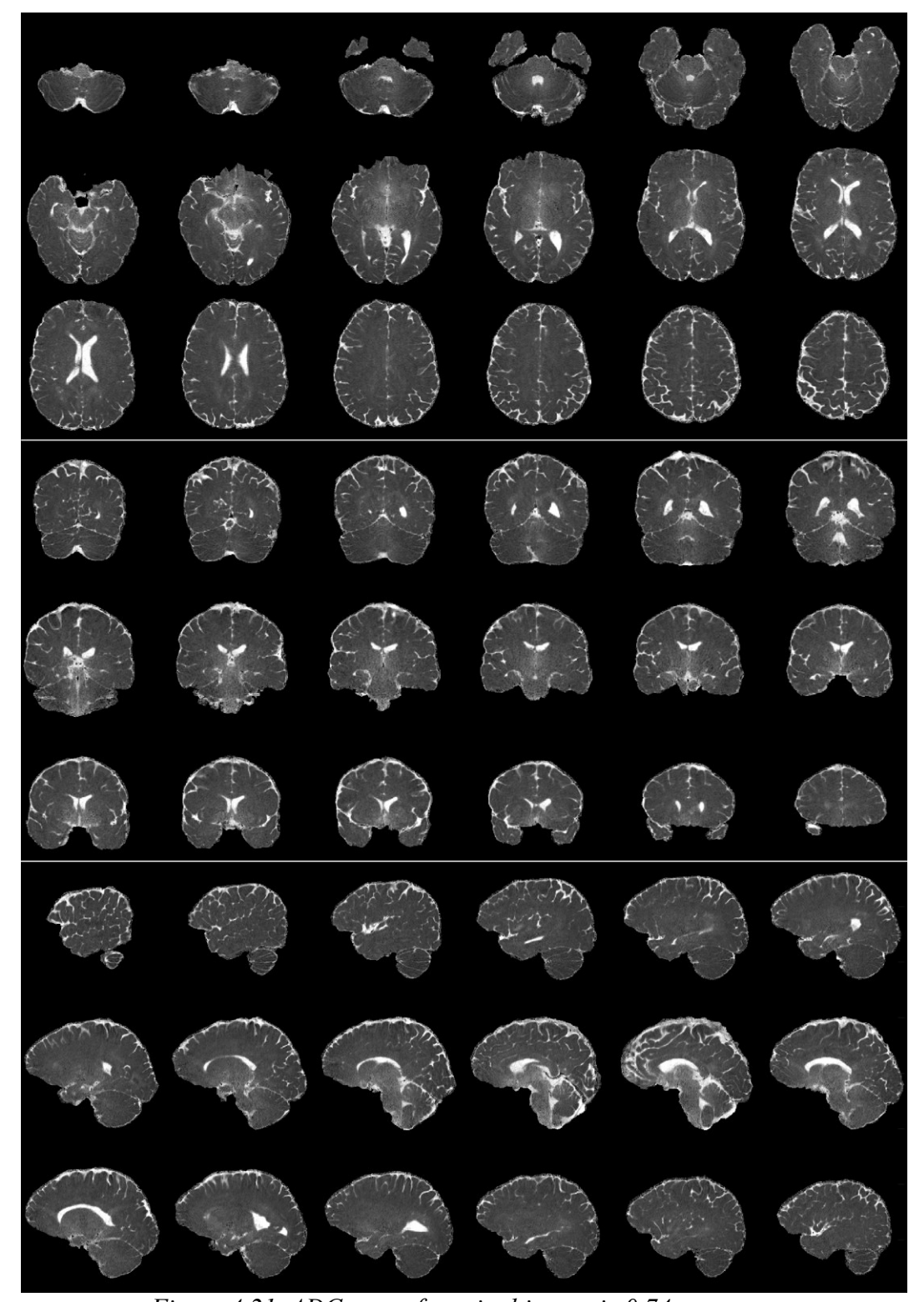


Figure 4.21. ADC map of nominal isotropic 0.74 mm scan.

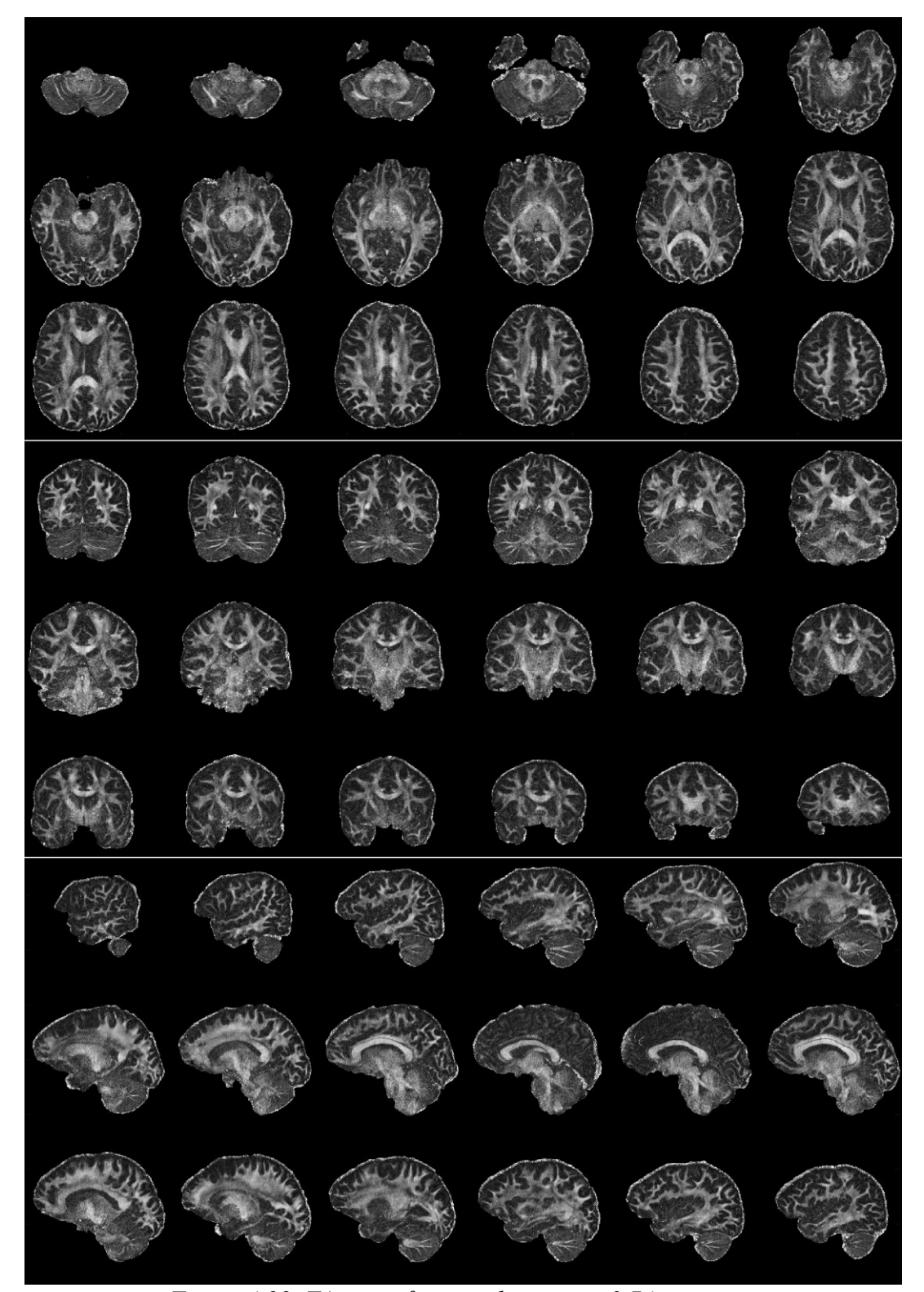


Figure 4.22. FA map of nominal isotropic 0.74 mm scan.

Postface

To implement the 3D MERMAID sequence, several practical challenges had to be addressed, which are not described in detail in the manuscript. The additional inversion pulse can cause unwanted stimulated echoes, causing spike artifacts in the image. To eliminate these echoes, the transverse magnetization needs to be spoiled at the end of each TR. Two spoiler gradients were added: one immediately after the EPI train and another between the inversion and excitation pulses. Additionally, the phase of the inversion and excitation pulses were incremented by 50 degrees each to ensure complete signal spoiling.

Fat tissue has a shorter T₁ compared to WM and GM, leading to faster recovery in short TRs. This results in a strong fat signal in 3D MERMAID, which can cause chemical shift artifacts in the PE direction due to the low bandwidth in this direction. Typically, either a fat suppression pulse or spectral-selective water excitation techniques are used to address this issue in dMRI. In the 3D MERMAID sequence, both fat suppression and water excitation were necessary to effectively eliminate the fat signal.

As shown in Figure 4.3, the SNR advantage of 3D MERMAID varies significantly as a function of the B_1^+ uniformity of the inversion and refocusing pulses. To achieve better uniformity, an amplitude-modulated hyperbolic secant adiabatic pulse was used. For the water excitation pulse, either a slab-selective or whole brain pulse can be implemented without significantly affecting the SNR advantage.

Lastly, microstructure modeling using the 3D MERMAID sequence was not investigated in this work. Future research should explore the effects of additional T₁ contrast on existing models that report signal fractions of the different microstructure compartments as an estimate of volume

Chapter 4- 3D MERMAID sequence

fractions. T_1 contrast could also be leveraged in multi-compartment modeling by adjusting parameters like the flip angle and/or TR to map the T_1 times of the different fibres or compartments within a voxel (Benjamini & Basser, 2020; Ning et al., 2020; Leppert et al., 2021).

References

Aggarwal, M., Nauen, D. W., Troncoso, J. C., & Mori, S. (2015). Probing region-specific microstructure of human cortical areas using high angular and spatial resolution diffusion MRI. NeuroImage, 105, 198–207. https://doi.org/10.1016/j.neuroimage.2014.10.053

Andersson, J. L. R., Skare, S., & Ashburner, J. (2003). How to correct susceptibility distortions in spin-echo echo-planar images: Application to diffusion tensor imaging. NeuroImage, 20(2), 870–888. https://doi.org/10.1016/S1053-8119(03)00336-7

Avants, B. B., Tustison, N., Song, G., & others. (2009). Advanced normalization tools (ANTS). Insight j, 2(365), 1–35.

Bammer, R., Stollberger, R., Augustin, M., Simbrunner, J., Offenbacher, H., Kooijman, H., Ropele, S., Kapeller, P., Wach, P., Ebner, F., & Fazekas, F. (1999). Diffusion-weighted Imaging with Navigated Interleaved Echo-planar Imaging and a Conventional Gradient System1. Radiology. https://doi.org/10.1148/radiology.211.3.r99jn15799

Basser, P. J., Mattiello, J., & LeBihan, D. (1994). Estimation of the effective self-diffusion tensor from the NMR spin echo. Journal of Magnetic Resonance. Series B, 103(3), 247–254. https://doi.org/10.1006/jmrb.1994.1037

Bloch, F. (1946). Nuclear Induction. Physical Review, 70(7–8), 460–474. https://doi.org/10.1103/PhysRev.70.460

Bruce, I. P., Chang, H.-C., Petty, C., Chen, N.-K., & Song, A. W. (2017). 3D-MB-MUSE: A robust 3D multi-slab, multi-band and multi-shot reconstruction approach for ultrahigh resolution diffusion MRI. NeuroImage, 159, 46–56. https://doi.org/10.1016/j.neuroimage.2017.07.035

Budde, M. D., & Annese, J. (2013). Quantification of anisotropy and fiber orientation in human brain histological sections. Frontiers in Integrative Neuroscience, 7.

https://www.frontiersin.org/journals/integrative-neuroscience/articles/10.3389/fnint.2013.00003

Butts, K., de Crespigny, A., Pauly, J. M., & Moseley, M. (1996). Diffusion-weighted interleaved echo-planar imaging with a pair of orthogonal navigator echoes. Magnetic Resonance in Medicine, 35(5), 763–770. https://doi.org/10.1002/mrm.1910350518

Cardenas, A. M., Sarlls, J. E., Kwan, J. Y., Bageac, D., Gala, Z. S., Danielian, L. E., Ray-Chaudhury, A., Wang, H.-W., Miller, K. L., Foxley, S., Jbabdi, S., Welsh, R. C., & Floeter, M. K. (2017). Pathology of callosal damage in ALS: An ex-vivo, 7 T diffusion tensor MRI study. NeuroImage: Clinical, 15, 200–208. https://doi.org/10.1016/j.nicl.2017.04.024

Chen, N.-K., Guidon, A., Chang, H.-C., & Song, A. W. (2013). A robust multi-shot scan strategy for high-resolution diffusion weighted MRI enabled by multiplexed sensitivity-encoding (MUSE). NeuroImage, 72, 41–47. https://doi.org/10.1016/j.neuroimage.2013.01.038

Coras, R., Milesi, G., Zucca, I., Mastropietro, A., Scotti, A., Figini, M., Mühlebner, A., Hess, A., Graf, W., Tringali, G., Blümcke, I., Villani, F., Didato, G., Frassoni, C., Spreafico, R., & Garbelli, R. (2014). 7 T MRI features in control human hippocampus and hippocampal sclerosis: An ex vivo study with histologic correlations. Epilepsia, 55(12), 2003–2016. https://doi.org/10.1111/epi.12828

Cox, E. F., & Gowland, P. A. (2010). Simultaneous quantification of T2 and T'2 using a combined gradient echo-spin echo sequence at ultrahigh field. Magnetic Resonance in Medicine, 64(5), 1440–1445. https://doi.org/10.1002/mrm.22522

Dhollander, T., Mito, R., Raffelt, D., & Connelly, A. (2019, May 11). Improved white matter response function estimation for 3-tissue constrained spherical deconvolution.

Dhollander, T., Tabbara, R., Rosnarho-Tornstrand, J., Tournier, J.-D., Raffelt, D., & Connelly, A. (2021, May 15). Multi-tissue log-domain intensity and inhomogeneity normalisation for quantitative apparent fibre density.

Dong, Z., Reese, T. G., Lee, H.-H., Huang, S. Y., Polimeni, J. R., Wald, L. L., & Wang, F. (2024). Romer-EPTI: Rotating-view motion-robust super-resolution EPTI for SNR-efficient distortion-free in-vivo mesoscale dMRI and microstructure imaging [Preprint]. Bioengineering. https://doi.org/10.1101/2024.01.26.577343

Engel, M., Mueller, L., Döring, A., Afzali, M., & Jones, D. K. (2024). Maximizing SNR per unit time in diffusion MRI with multiband T-Hex spirals. Magnetic Resonance in Medicine, 91(4), 1323–1336. https://doi.org/10.1002/mrm.29953

Chapter 4- 3D MERMAID sequence

Engström, M., & Skare, S. (2013). Diffusion-weighted 3D multislab echo planar imaging for high signal-to-noise ratio efficiency and isotropic image resolution. Magnetic Resonance in Medicine, 70(6), 1507–1514. https://doi.org/10.1002/mrm.24594

Ernst, R. R., & Anderson, W. A. (1966). Application of Fourier Transform Spectroscopy to Magnetic Resonance. Review of Scientific Instruments, 37(1), 93–102. https://doi.org/10.1063/1.1719961

Feizollah, S., Lowen, D., Couch, M., Pracht, E. D., Stöcker, T., & Tardif, C. (2024). 3D diffusion MRI at 7 T with Universal Pulses for improved image uniformity. Proceedings of the 32nd Annual Meeting of ISMRM.

Feizollah, S., & Tardif, C. (2024). Multi-shot 3D diffusion MRI sequence for a fast and high-resolution imaging at 3 T. Proceedings of the 32nd Annual Meeting of ISMRM.

Feizollah, S., & Tardif, C. L. (2023). High-resolution diffusion-weighted imaging at 7 Tesla: Single-shot readout trajectories and their impact on signal-to-noise ratio, spatial resolution and accuracy. NeuroImage, 274, 120159. https://doi.org/10.1016/j.neuroimage.2023.120159

Frigo, M., Fick, R. H. J., Zucchelli, M., Deslauriers-Gauthier, S., & Deriche, R. (2020). Multi Tissue Modelling of Diffusion MRI Signal Reveals Volume Fraction Bias. 2020 IEEE 17 Th International Symposium on Biomedical Imaging (ISBI), 991–994.

https://doi.org/10.1109/ISBI45749.2020.9098649

Frost, R., Miller, K. L., Tijssen, R. H. N., Porter, D. A., & Jezzard, P. (2014). 3D Multi-slab diffusion-weighted readout-segmented EPI with real-time cardiac-reordered k-space acquisition. Magnetic Resonance in Medicine, 72(6), 1565–1579. https://doi.org/10.1002/mrm.25062

Graedel, N. N., Miller, K. L., & Chiew, M. (2022). Ultrahigh Resolution fMRI at 7 T Using Radial-Cartesian TURBINE Sampling. Magnetic Resonance in Medicine, 88(5), 2058–2073. https://doi.org/10.1002/mrm.29359

Gras, V., Mauconduit, F., Vignaud, A., Amadon, A., Le Bihan, D., Stöcker, T., & Boulant, N. (2018). Design of universal parallel-transmit refocusing kT-point pulses and application to 3D T2-weighted imaging at 7 T. Magnetic Resonance in Medicine, 80(1), 53–65. https://doi.org/10.1002/mrm.27001

Chapter 4- 3D MERMAID sequence

Gras, V., Vignaud, A., Amadon, A., Le Bihan, D., & Boulant, N. (2017). Universal pulses: A new concept for calibration-free parallel transmission. Magnetic Resonance in Medicine, 77(2), 635–643. https://doi.org/10.1002/mrm.26148

Griswold, M. A., Jakob, P. M., Heidemann, R. M., Nittka, M., Jellus, V., Wang, J., Kiefer, B., & Haase, A. (2002). Generalized autocalibrating partially parallel acquisitions (GRAPPA).

Magnetic Resonance in Medicine, 47(6), 1202–1210. https://doi.org/10.1002/mrm.10171

Heid, O. (2000). Method for the phase correction of nuclear magnetic resonance signals (United States Patent No. US6043651A). https://patents.google.com/patent/US6043651A/en

Hoge, W. S., & Polimeni, J. R. (2016). Dual-Polarity GRAPPA for simultaneous reconstruction and ghost correction of EPI data. Magnetic Resonance in Medicine, 76(1), 32–44. https://doi.org/10.1002/mrm.25839

Holdsworth, S. J., Skare, S., Newbould, R. D., Guzmann, R., Blevins, N. H., & Bammer, R. (2008). Readout-segmented EPI for rapid high resolution diffusion imaging at 3 T. European Journal of Radiology, 65(1), 36–46. https://doi.org/10.1016/j.ejrad.2007.09.016

Jelescu, I. O., de Skowronski, A., Geffroy, F., Palombo, M., & Novikov, D. S. (2022). Neurite Exchange Imaging (NEXI): A minimal model of diffusion in gray matter with inter-compartment water exchange. NeuroImage, 256, 119277. https://doi.org/10.1016/j.neuroimage.2022.119277

Jelescu, I. O., Veraart, J., Fieremans, E., & Novikov, D. S. (2016). Degeneracy in model parameter estimation for multi-compartmental diffusion in neuronal tissue. NMR in Biomedicine, 29(1), 33–47. https://doi.org/10.1002/nbm.3450

Jeong, E.-K., Kim, S.-E., & Parker, D. L. (2003). High-resolution diffusion-weighted 3D MRI, using diffusion-weighted driven-equilibrium (DW-DE) and multishot segmented 3D-SSFP without navigator echoes. Magnetic Resonance in Medicine, 50(4), 821–829. https://doi.org/10.1002/mrm.10593

Jeurissen, B., Tournier, J.-D., Dhollander, T., Connelly, A., & Sijbers, J. (2014). Multi-tissue constrained spherical deconvolution for improved analysis of multi-shell diffusion MRI data. NeuroImage, 103, 411–426. https://doi.org/10.1016/j.neuroimage.2014.07.061

Ke, J., Foley, L. M., Hitchens, T. K., Richardson, R. M., & Modo, M. (2020). Ex vivo mesoscopic diffusion MRI correlates with seizure frequency in patients with uncontrolled mesial temporal lobe epilepsy. Human Brain Mapping, 41(16), 4529–4548. https://doi.org/10.1002/hbm.25139

Khaneja, N., Reiss, T., Kehlet, C., Schulte-Herbrüggen, T., & Glaser, S. J. (2005). Optimal control of coupled spin dynamics: Design of NMR pulse sequences by gradient ascent algorithms. Journal of Magnetic Resonance (San Diego, Calif.: 1997), 172(2), 296–305. https://doi.org/10.1016/j.jmr.2004.11.004

Knossalla, F., Kohl, Z., Winkler, J., Schwab, S., Schenk, T., Engelhorn, T., Doerfler, A., & Gölitz, P. (2018). High-resolution diffusion tensor-imaging indicates asymmetric microstructural disorganization within substantia nigra in early Parkinson's disease. Journal of Clinical Neuroscience, 50, 199–202. https://doi.org/10.1016/j.jocn.2018.01.023

Koopmans, P. J., & Pfaffenrot, V. (2021). Enhanced POCS reconstruction for partial Fourier imaging in multi-echo and time-series acquisitions. Magnetic Resonance in Medicine, 85(1), 140–151. https://doi.org/10.1002/mrm.28417

Lee, Y., Wilm, B. J., Brunner, D. O., Gross, S., Schmid, T., Nagy, Z., & Pruessmann, K. P. (2021). On the signal-to-noise ratio benefit of spiral acquisition in diffusion MRI. Magnetic Resonance in Medicine, 85(4), 1924–1937. https://doi.org/10.1002/mrm.28554

Leuze, C. W. U., Anwander, A., Bazin, P.-L., Dhital, B., Stüber, C., Reimann, K., Geyer, S., & Turner, R. (2014). Layer-Specific Intracortical Connectivity Revealed with Diffusion MRI. Cerebral Cortex, 24(2), 328–339. https://doi.org/10.1093/cercor/bhs311

Li, H., Zu, T., Chen, R., Ba, R., Hsu, Y.-C., Sun, Y., Zhang, Y., & Wu, D. (2023). 3D diffusion MRI with twin navigator-based GRASE and comparison with 2D EPI for tractography in the human brain. Magnetic Resonance in Medicine, 90(5), 1969–1978. https://doi.org/10.1002/mrm.29769

Li, Z., Miller, K. L., Chen, X., Chiew, M., & Wu, W. (2024). Self-navigated 3D diffusion MRI using an optimized CAIPI sampling and structured low-rank reconstruction (No. arXiv:2401.05844). arXiv. https://doi.org/10.48550/arXiv.2401.05844

Li, Z., Pipe, J. G., Lee, C.-Y., Debbins, J. P., Karis, J. P., & Huo, D. (2011). X-PROP: A fast and robust diffusion-weighted propeller technique. Magnetic Resonance in Medicine, 66(2), 341–347. https://doi.org/10.1002/mrm.23033

Liu, C., Bammer, R., Kim, D.-H., & Moseley, M. E. (2004). Self-navigated interleaved spiral (SNAILS): Application to high-resolution diffusion tensor imaging. Magnetic Resonance in Medicine, 52(6), 1388–1396. https://doi.org/10.1002/mrm.20288

Lowen, D., Pracht, E. D., Gras, V., Massire, A., Mauconduit, F., Stoecker, T., & Boulant, N. (2024). Design of calibration-free RF pulses for T-weighted single-slab 3D turbo-spin-echo sequences at 7 T utilizing parallel transmission. Magnetic Resonance in Medicine, 92(5), 2037–2050. https://doi.org/10.1002/mrm.30212

Lustig, M., Donoho, D., & Pauly, J. M. (2007). Sparse MRI: The application of compressed sensing for rapid MR imaging. Magnetic Resonance in Medicine, 58(6), 1182–1195. https://doi.org/10.1002/mrm.21391

Ly, M., Foley, L., Manivannan, A., Hitchens, T. K., Richardson, R. M., & Modo, M. (2020). Mesoscale diffusion magnetic resonance imaging of the ex vivo human hippocampus. Human Brain Mapping, 41(15), 4200–4218. https://doi.org/10.1002/hbm.25119

Ma, R., Akçakaya, M., Moeller, S., Auerbach, E., Uğurbil, K., & Van de Moortele, P.-F. (2020). A field-monitoring-based approach for correcting eddy-current-induced artifacts of up to the 2nd spatial order in human-connectome-project-style multiband diffusion MRI experiment at 7 T: A pilot study. NeuroImage, 216, 116861. https://doi.org/10.1016/j.neuroimage.2020.116861

Mani, M., Jacob, M., Kelley, D., & Magnotta, V. (2017). Multi-shot sensitivity-encoded diffusion data recovery using structured low-rank matrix completion (MUSSELS). Magnetic Resonance in Medicine, 78(2), 494–507. https://doi.org/10.1002/mrm.26382

McNab, J. A., Gallichan, D., & Miller, K. L. (2010). 3D steady-state diffusion-weighted imaging with trajectory using radially batched internal navigator echoes (TURBINE). Magnetic Resonance in Medicine, 63(1), 235–242. https://doi.org/10.1002/mrm.22183

Chapter 4- 3D MERMAID sequence

Michael, E. S., Hennel, F., & Pruessmann, K. P. (2024). Motion-compensated diffusion encoding in multi-shot human brain acquisitions: Insights using high-performance gradients. Magnetic Resonance in Medicine, 92(2), 556–572. https://doi.org/10.1002/mrm.30069

Moeller, S., Pisharady, P. K., Ramanna, S., Lenglet, C., Wu, X., Dowdle, L., Yacoub, E., Uğurbil, K., & Akçakaya, M. (2021). NOise reduction with Distribution Corrected (NORDIC) PCA in dMRI with complex-valued parameter-free locally low-rank processing. NeuroImage, 226, 117539. https://doi.org/10.1016/j.neuroimage.2020.117539

Mussard, E., Hilbert, T., Forman, C., Meuli, R., Thiran, J.-P., & Kober, T. (2020). Accelerated MP2RAGE imaging using Cartesian phyllotaxis readout and compressed sensing reconstruction. Magnetic Resonance in Medicine, 84(4), 1881–1894. https://doi.org/10.1002/mrm.28244

Noll, D. C., Nishimura, D. G., & Macovski, A. (1991). Homodyne detection in magnetic resonance imaging. IEEE Transactions on Medical Imaging, 10(2), 154–163. https://doi.org/10.1109/42.79473

Novikov, D. S., Fieremans, E., Jespersen, S. N., & Kiselev, V. G. (2019). Quantifying brain microstructure with diffusion MRI: Theory and parameter estimation. NMR in Biomedicine, 32(4), e3998. https://doi.org/10.1002/nbm.3998

Palombo, M., Ianus, A., Guerreri, M., Nunes, D., Alexander, D. C., Shemesh, N., & Zhang, H. (2020). SANDI: A compartment-based model for non-invasive apparent soma and neurite imaging by diffusion MRI. NeuroImage, 215, 116835. https://doi.org/10.1016/j.neuroimage.2020.116835

Pipe, J. G. (1999). Motion correction with PROPELLER MRI: Application to head motion and free-breathing cardiac imaging. Magnetic Resonance in Medicine, 42(5), 963–969. https://doi.org/10.1002/(sici)1522-2594(199911)42:5<963::aid-mrm17>3.0.co;2-1

Pipe, J. G., Farthing, V. G., & Forbes, K. P. (2002). Multishot diffusion-weighted FSE using PROPELLER MRI. Magnetic Resonance in Medicine, 47(1), 42–52. https://doi.org/10.1002/mrm.10014

Pipe, J. G., & Zwart, N. (2006). Turboprop: Improved PROPELLER imaging. Magnetic Resonance in Medicine, 55(2), 380–385. https://doi.org/10.1002/mrm.20768

Polimeni, J. R., Bhat, H., Witzel, T., Benner, T., Feiweier, T., Inati, S. J., Renvall, V., Heberlein, K., & Wald, L. L. (2016). Reducing sensitivity losses due to respiration and motion in accelerated echo planar imaging by reordering the autocalibration data acquisition. Magnetic Resonance in Medicine, 75(2), 665–679. https://doi.org/10.1002/mrm.25628

Porter, D. A., & Heidemann, R. M. (2009). High resolution diffusion-weighted imaging using readout-segmented echo-planar imaging, parallel imaging and a two-dimensional navigator-based reacquisition. Magnetic Resonance in Medicine, 62(2), 468–475. https://doi.org/10.1002/mrm.22024

Pruessmann, K. P., Weiger, M., Scheidegger, M. B., & Boesiger, P. (1999). SENSE: Sensitivity encoding for fast MRI. Magnetic Resonance in Medicine, 42(5), 952–962.

Raffelt, D., Dhollander, T., Tournier, J.-D., Tabbara, R., Smith, R., Pierre, E., & Connelly, A. (2017, April 22). Bias Field Correction and Intensity Normalisation for Quantitative Analysis of Apparent Fibre Density.

Ramos-Llordén, G., Ning, L., Liao, C., Mukhometzianov, R., Michailovich, O., Setsompop, K., & Rathi, Y. (2020). High-fidelity, accelerated whole-brain submillimeter in vivo diffusion MRI using gSlider-spherical ridgelets (gSlider-SR). Magnetic Resonance in Medicine, 84(4), 1781–1795. https://doi.org/10.1002/mrm.28232

Roebroeck, A., Miller, K. L., & Aggarwal, M. (2019). Ex vivo diffusion MRI of the human brain: Technical challenges and recent advances. NMR in Biomedicine, 32(4), e3941. https://doi.org/10.1002/nbm.3941

Rooney, W. D., Johnson, G., Li, X., Cohen, E. R., Kim, S.-G., Ugurbil, K., & Springer, C. S. (2007). Magnetic field and tissue dependencies of human brain longitudinal 1H2O relaxation in vivo. Magnetic Resonance in Medicine, 57(2), 308–318. https://doi.org/10.1002/mrm.21122

Scherrer, B., Gholipour, A., & Warfield, S. K. (2011). Super-Resolution in Diffusion-Weighted Imaging. Medical Image Computing and Computer-Assisted Intervention: MICCAI ... International Conference on Medical Image Computing and Computer-Assisted Intervention, 14(0 2), 124–132.

Chapter 4- 3D MERMAID sequence

Seehaus, A. K., Roebroeck, A., Chiry, O., Kim, D.-S., Ronen, I., Bratzke, H., Goebel, R., & Galuske, R. A. W. (2013). Histological Validation of DW-MRI Tractography in Human Postmortem Tissue. Cerebral Cortex, 23(2), 442–450. https://doi.org/10.1093/cercor/bhs036

Seehaus, A., Roebroeck, A., Bastiani, M., Fonseca, L., Bratzke, H., Lori, N., Vilanova, A., Goebel, R., & Galuske, R. (2015). Histological validation of high-resolution DTI in human post mortem tissue. Frontiers in Neuroanatomy, 9.

https://www.frontiersin.org/journals/neuroanatomy/articles/10.3389/fnana.2015.00098

Setsompop, K., Fan, Q., Stockmann, J., Bilgic, B., Huang, S., Cauley, S. F., Nummenmaa, A., Wang, F., Rathi, Y., Witzel, T., & Wald, L. L. (2018). High-resolution in vivo diffusion imaging of the human brain with generalized slice dithered enhanced resolution: Simultaneous multislice (gSlider-SMS). Magnetic Resonance in Medicine, 79(1), 141–151. https://doi.org/10.1002/mrm.26653

Setsompop, K., Gagoski, B. A., Polimeni, J. R., Witzel, T., Wedeen, V. J., & Wald, L. L. (2012). Blipped-controlled aliasing in parallel imaging for simultaneous multislice echo planar imaging with reduced g-factor penalty. Magnetic Resonance in Medicine, 67(5), 1210–1224. https://doi.org/10.1002/mrm.23097

Skare, S., Holdsworth, S., Newbould, R. D., & Bammer, R. (2009). On the battle between Rician noise and phase-interferences in DWI. Proceedings of the 17 Th Annual Meeting of ISMRM, 1409.

Smith, S. M., Jenkinson, M., Woolrich, M. W., Beckmann, C. F., Behrens, T. E. J., Johansen-Berg, H., Bannister, P. R., De Luca, M., Drobnjak, I., Flitney, D. E., Niazy, R. K., Saunders, J., Vickers, J., Zhang, Y., De Stefano, N., Brady, J. M., & Matthews, P. M. (2004). Advances in functional and structural MR image analysis and implementation as FSL. NeuroImage, 23 Suppl 1, S208-219. https://doi.org/10.1016/j.neuroimage.2004.07.051

Stoeck, C. T., von Deuster, C., Genet, M., Atkinson, D., & Kozerke, S. (2016). Second-order motion-compensated spin echo diffusion tensor imaging of the human heart. Magnetic Resonance in Medicine, 75(4), 1669–1676. https://doi.org/10.1002/mrm.25784

Szczepankiewicz, F., Sjölund, J., Dall'Armellina, E., Plein, S., Schneider, J. E., Teh, I., & Westin, C. (2021). Motion-compensated gradient waveforms for tensor-valued diffusion

encoding by constrained numerical optimization. Magnetic Resonance in Medicine, 85(4), 2117–2126. https://doi.org/10.1002/mrm.28551

Talagala, S. L., Sarlls, J. E., Liu, S., & Inati, S. J. (2016). Improvement of temporal signal-to-noise ratio of GRAPPA accelerated echo planar imaging using a FLASH based calibration scan. Magnetic Resonance in Medicine, 75(6), 2362–2371. https://doi.org/10.1002/mrm.25846

Tang, X., Gao, J., Aburas, A., Wu, D., Chen, Z., Chen, H., & Hu, C. (2024). Accelerated multi-b-value multi-shot diffusion-weighted imaging based on EPI with keyhole and a low-rank tensor constraint. Magnetic Resonance Imaging, 110, 138–148.

https://doi.org/10.1016/j.mri.2024.04.015

Tardif, C. L., Schäfer, A., Waehnert, M., Dinse, J., Turner, R., & Bazin, P.-L. (2015). Multi-contrast multi-scale surface registration for improved alignment of cortical areas. NeuroImage, 111, 107–122. https://doi.org/10.1016/j.neuroimage.2015.02.005

Tournier, J.-D., Calamante, F., Gadian, D. G., & Connelly, A. (2004). Direct estimation of the fiber orientation density function from diffusion-weighted MRI data using spherical deconvolution. NeuroImage, 23(3), 1176–1185.

https://doi.org/10.1016/j.neuroimage.2004.07.037

Tournier, J.-D., Smith, R., Raffelt, D., Tabbara, R., Dhollander, T., Pietsch, M., Christiaens, D., Jeurissen, B., Yeh, C.-H., & Connelly, A. (2019). MRtrix3: A fast, flexible and open software framework for medical image processing and visualisation. NeuroImage, 202, 116137. https://doi.org/10.1016/j.neuroimage.2019.116137

Uecker, M., Hohage, T., Block, K. T., & Frahm, J. (2008). Image reconstruction by regularized nonlinear inversion—Joint estimation of coil sensitivities and image content. Magnetic Resonance in Medicine, 60(3), 674–682. https://doi.org/10.1002/mrm.21691

Uecker, M., Lai, P., Murphy, M. J., Virtue, P., Elad, M., Pauly, J. M., Vasanawala, S. S., & Lustig, M. (2014). ESPIRiT — An Eigenvalue Approach to Autocalibrating Parallel MRI: Where SENSE meets GRAPPA. Magnetic Resonance in Medicine: Official Journal of the Society of Magnetic Resonance in Medicine, 71(3), 990–1001. https://doi.org/10.1002/mrm.24751

Uhl, Q., Pavan, T., Molendowska, M., Jones, D. K., Palombo, M., & Jelescu, I. O. (2024). Quantifying human gray matter microstructure using neurite exchange imaging (NEXI) and 300 mT/m gradients. Imaging Neuroscience, 2, 1–19. https://doi.org/10.1162/imag_a_00104

Veldmann, M., Edwards, L. J., Pine, K. J., Ehses, P., Ferreira, M., Weiskopf, N., & Stoecker, T. (2024). Improving MR axon radius estimation in human white matter using spiral acquisition and field monitoring. Magnetic Resonance in Medicine, 92(5), 1898–1912. https://doi.org/10.1002/mrm.30180

Veraart, J., Novikov, D. S., & Fieremans, E. (2018). TE dependent Diffusion Imaging (TEdDI) distinguishes between compartmental T2 relaxation times. NeuroImage, 182, 360–369. https://doi.org/10.1016/j.neuroimage.2017.09.030

Veraart, J., Sijbers, J., Sunaert, S., Leemans, A., & Jeurissen, B. (2013). Weighted linear least squares estimation of diffusion MRI parameters: Strengths, limitations, and pitfalls. NeuroImage, 81, 335–346. https://doi.org/10.1016/j.neuroimage.2013.05.028

Vis, G., Nilsson, M., Westin, C.-F., & Szczepankiewicz, F. (2021). Accuracy and precision in super-resolution MRI: Enabling spherical tensor diffusion encoding at ultra-high b-values and high resolution. NeuroImage, 245, 118673. https://doi.org/10.1016/j.neuroimage.2021.118673

Wang, F.-N., Huang, T.-Y., Lin, F.-H., Chuang, T.-C., Chen, N.-K., Chung, H.-W., Chen, C.-Y., & Kwong, K. K. (2005). PROPELLER EPI: An MRI technique suitable for diffusion tensor imaging at high field strength with reduced geometric distortions. Magnetic Resonance in Medicine, 54(5), 1232–1240. https://doi.org/10.1002/mrm.20677

Wang, X., Rosenzweig, S., Scholand, N., Holme, H. C. M., & Uecker, M. (2020). Data for: Model-Based Reconstruction for Simultaneous Multi-Slice T1 Mapping using Single-Shot Inversion-Recovery Radial FLASH [Dataset]. Zenodo. https://doi.org/10.5281/zenodo.3969809

Zhang, H., Schneider, T., Wheeler-Kingshott, C. A., & Alexander, D. C. (2012). NODDI: Practical in vivo neurite orientation dispersion and density imaging of the human brain. NeuroImage, 61(4), 1000–1016. https://doi.org/10.1016/j.neuroimage.2012.03.072

Chapter 4- 3D MERMAID sequence

Zhang, Q., Coolen, B. F., Nederveen, A. J., & Strijkers, G. J. (2019). Three-dimensional diffusion imaging with spiral encoded navigators from stimulated echoes (3D-DISPENSE). Magnetic Resonance in Medicine, 81(2), 1052–1065. https://doi.org/10.1002/mrm.27470

Zhang, Y., Brady, M., & Smith, S. (2001). Segmentation of brain MR images through a hidden Markov random field model and the expectation-maximization algorithm. IEEE Transactions on Medical Imaging, 20(1), 45–57. https://doi.org/10.1109/42.906424

Zhao, Z., Zhang, L., Luo, W., Cao, Z., Zhu, Q., Kong, X., Zhu, K., Zhang, J., & Wu, D. (2023). Layer-specific microstructural patterns of anterior hippocampus in Alzheimer's disease with ex vivo diffusion MRI at 14.1 T. Human Brain Mapping, 44(2), 458–471. https://doi.org/10.1002/hbm.26062

Chapter 5

Discussion

The goal of this work was to develop dMRI acquisition and reconstruction methods capable of achieving submillimeter resolutions for microstructure modeling within feasible scan times on clinical scanners. First, we characterized the effective resolution of dMRI using different readout trajectories through sequence simulations. We then implemented single-shot spiral trajectories at 7 T to maximize the SNR and investigated the achievable effective resolutions in short scan times. Spirals are more SNR efficient than EPI, producing high quality images at an effective resolution of 1.5 mm for a b-value of 2000 s/mm². Due to the limitations of 2D imaging and the higher SNR requirements of imaging at submillimeter resolutions, we introduced the novel 3D MERMAID sequence, which offers greater SNR efficiency compared to standard dMRI sequences. This sequence was implemented at 3 T, where we demonstrated that dMRI at nominal and effective resolutions of 0.74 mm and ~0.9 mm, respectively, in 112 diffusion directions with a maximum b-value of 2000 s/mm², can be achieved within 37 minutes on clinical scanners.

This chapter will discuss in more detail the practical challenges of implementing and using these advanced dMRI techniques. It will also explore potential improvements to the methods and conclude with a review of potential future research directions.

5.1. Practical considerations

In the first manuscript, Chapter 3, field monitoring probes were used to reconstruct highquality scans with minimal artifacts from spiral readout trajectories. This complicates the image acquisition and reconstruction process due to the lack of an integrated acquisition and reconstruction pipeline, mainly due to limitations imposed by different vendors. The raw data from the scanner, including multi-echo GRE and diffusion scans, as well as probe measurements, must be transferred separately to an image reconstruction system. These datasets then need to be synchronized, combined, and prepared before reconstruction, a process that usually takes several hours. Additionally, the non-cartesian image reconstruction itself can take a full day to complete for an entire 4D diffusion dataset. Integrated field probes in receive coils (Gilbert et al., 2022; Sprang, 2024) can accelerate the acquisition, but the lengthy process of transferring data and image reconstruction remains a challenge. This precludes quality control during the scan, increasing the risk of data loss due to issues such as subject motion during acquisition. This is particularly limiting for studies involving clinical populations and large cohorts. Furthermore, field monitoring systems are expensive and are not available at all MRI sites. As a result, the use of field probes is not currently very widespread. In contrast, the TURBINE trajectory in the 3D MERMAID sequence allows for image artifact correction using the methods established for EPI-based trajectories without the need for additional equipment. Furthermore, the proposed image reconstruction pipeline for 3D MERMAID can be implemented directly on the scanner for online quality control, as image reconstruction pipeline for PROPELLER imaging already exist. These features make the 3D MERMAID sequence well-suited for large and multi-site studies.

Moving from lower field strengths to 7 T for diffusion imaging, whether using 2D SE-EPI or 3D MERMAID sequences, may not offer the same advantages as it does with other contrasts. Assuming the gradient performance and reconstruction techniques are the same as at lower fields, higher resolutions typically require longer echo times when using an EPI-based trajectory. These long TEs result in SNR loss which is exacerbated by the faster T₂ decay at 7 T. Increasing the bandwidth can partially compensate for this, but it also reduces SNR further and amplifies ghosting and parallel imaging artifacts due to higher eddy currents. Efficient trajectories, such as spirals, could potentially recover the SNR lost to long TEs, but correcting distortions and artifacts without using field monitoring probes remains challenging. For efficient diffusion imaging at 7 T, advanced image reconstruction techniques that better correct these artifacts are essential to achieve superior image quality and SNR compared to lower field strengths.

For 2D imaging, addressing B₁⁺ nonuniformity is particularly difficult at 7 T, even with pTx pulses. This leads to signal loss in areas such as the cerebellum and temporal lobe. The 3D MERMAID sequence has the advantage of using 3D pulses, which are easier to design for uniform profiles at 7 T using parallel transmission (Gras et al., 2017; Feizollah et al., 2024; Lowen et al., 2024). Future work will focus on designing pTx pulses with high uniformity to fully utilize the SNR advantages of the sequence at 7 T (Feizollah et al., 2024).

5.2. Potential improvements to the sequences and reconstruction pipelines

There are several aspects of the MRI sequences and image reconstruction pipelines that could be improved in future work. The spiral sequence developed at 7 T could be further accelerated by incorporating SMS imaging. To reduce the g-factor penalty, blipped (Zahneisen et

al., 2014; Engel et al., 2021, 2024) or wave (Herbst et al., 2017) SMS approaches could be implemented. The image reconstruction pipeline could also be enhanced by introducing regularization into the forward model. Common approaches include phase-constrained methods that enforce partial Fourier symmetry, and sparsity constraints (Varela-Mattatall et al., 2023). Chapter 3 showed the impact of T_2^* decay on the effective resolution of spiral and EPI readouts. The T_2^* blurring could be corrected to improve the effective resolution of dMRI using PSF mapping (In et al., 2017) at the cost of scan time. Alternatively, a T_2^* map can be incorporated into the forward model to counteract these effects.

The 3D MERMAID sequence could benefit from incorporating different readout trajectories, such as rotating spirals (J. Zhang et al., 2009) to further improve the SNR by reducing the echo time. Similar to spiral trajectories, this will require field monitoring to correct distortions and artifacts. The current implementation has an isotropic 2D FOV in the radial plane. Other trajectories that have an anisotropic FOV can sample the k-space more efficiently, resulting in shorter scan times. Motion compensated diffusion-encoding gradients (Stoeck et al., 2016a; Szczepankiewicz et al., 2021; Michael et al., 2024b) could be incorporated into the 3D MERMAID sequence to provide greater flexibility in trajectory selection and improve SNR by using all acquired projections.

Both the 2D spiral trajectory at 7 T and the 3D TURBINE trajectory at 3 T can be segmented to reduce susceptibility artifacts and achieve ultra-high resolutions. Image reconstruction can be done through a navigation-free method reviewed in Section 2.5.3 such as MUSE (N.-K. Chen et al., 2013) or MUSSELS (Mani et al., 2017b). We did not investigate this further in this thesis as the objective was to keep scan time short.

5.3. Future research directions

Diffusion imaging greatly benefits from high-performance head-insert gradients. They provide significantly higher gradient amplitudes and slew rates that can be used due to lower PNS in a smaller FOV. They can also be used to shorten diffusion-encoding durations resulting in reduced echo time and higher SNR, and to shorten readout times and reduce susceptibility artifacts and distortions. Higher resolutions are also more easily obtained in a similar acquisition time. Application of field probes in combination with these gradients can improve the image quality further.

The 3D MERMAID sequence provides a novel contrast that includes both T₁- and T₂-weighting. Both longitudinal and transverse magnetizations at steady state are modulated by TE. Tissue relaxation rates are not considered in most diffusion-based microstructure models that compute compartmental volume fractions (H. Zhang et al., 2012), which are in reality T₂-weighted signal fractions. To estimate true volume fractions, a co-encoded diffusion-relaxometry acquisition is required (Frigo et al., 2020; Veraart et al., 2018b). Although the scans included in this work are suitable for microstructure modeling, the effect of the enhanced T₁-weighting on the compartmental signal fractions should be studied further. This new combined T₁ and T₂ contrast could also be used to extract multiple compartment features.

Chapter 6

Conclusion

The objective of this work was to develop dMRI acquisition and reconstruction methods capable of providing scans at submillimeter resolutions suitable for microstructure modeling, while maintaining feasibility on clinical scanners.

We began by exploring the effective resolutions achievable at 7 T using spiral trajectories, which are among the most SNR-efficient readout techniques, through sequence simulations and SNR measurements. To minimize distortions and artifacts caused by unwanted fields, a set of field monitoring probes were employed. Results showed an SNR increase of ~50% using spirals compared to EPI trajectories at a matching effective resolution in a shorter scan time. Our findings also showed a ~45% difference between nominal and effective resolutions, and insufficient SNR of spiral trajectories at 7 T for achieving submillimeter effective resolutions.

To address these limitations as well as the ones related to 2D and 3D multi-slab methods,

Chapter 6- Conclusion

we developed the novel 3D MERMAID sequence at 3 T, which provides significantly higher SNR efficiency than conventional dMRI sequences. Using this sequence, we demonstrated that submillimeter dMRI suitable for microstructure modeling can be achieved on clinical scanners with a nominal resolution of 0.74 mm in 112 directions in 37 minutes. This sequence has the potential to make a substantial impact on microstructure mapping using diffusion MRI, offering a more practical approach for studying brain structures in greater detail, even in large study cohorts, due to its high efficiency and simplicity. Furthermore, the 3D MERMAID sequence enables the examination of brain microstructure in both healthy and pathological conditions, even in settings where access to high-end scanners with a high-performance gradient system is limited.

References

The references for Chapter 1, Chapter 2, and Chapter 5.

Aboussouan, E., & Pipe, J. (2009). 3D PROPELLER-based diffusion weighted imaging. Proc Int Soc Magn Reson Med, 17, 2632.

Aggarwal, M., Nauen, D. W., Troncoso, J. C., & Mori, S. (2015). Probing region-specific microstructure of human cortical areas using high angular and spatial resolution diffusion MRI. NeuroImage, 105, 198–207. https://doi.org/10.1016/j.neuroimage.2014.10.053

Ahn, C. B., & Cho, Z. H. (1991). Analysis of the eddy-current induced artifacts and the temporal compensation in nuclear magnetic resonance imaging. IEEE Transactions on Medical Imaging, 10(1), 47–52. https://doi.org/10.1109/42.75610

Ahn, C. B., Kim, J. H., & Cho, Z. H. (1986). High-speed spiral-scan echo planar NMR imaging-I. IEEE Transactions on Medical Imaging, 5(1), 2–7. https://doi.org/10.1109/TMI.1986.4307732

Aksoy, M., Liu, C., Moseley, M. E., & Bammer, R. (2008). Single-step nonlinear diffusion tensor estimation in the presence of microscopic and macroscopic motion. Magnetic Resonance in Medicine, 59(5), 1138–1150. https://doi.org/10.1002/mrm.21558

Alexander, D. C., Hubbard, P. L., Hall, M. G., Moore, E. A., Ptito, M., Parker, G. J. M., & Dyrby, T. B. (2010). Orientationally invariant indices of axon diameter and density from diffusion MRI. NeuroImage, 52(4), 1374–1389.

https://doi.org/10.1016/j.neuroimage.2010.05.043

Anderson, A. W., & Gore, J. C. (1994). Analysis and correction of motion artifacts in diffusion weighted imaging. Magnetic Resonance in Medicine, 32(3), 379–387.

https://doi.org/10.1002/mrm.1910320313

Atkinson, D., Counsell, S., Hajnal, J. V., Batchelor, P. G., Hill, D. L. G., & Larkman, D. J. (2006). Nonlinear phase correction of navigated multi-coil diffusion images. Magnetic Resonance in Medicine, 56(5), 1135–1139. https://doi.org/10.1002/mrm.21046

Atkinson, D., Hill, D. L. G., Stoyle, P. N. R., Summers, P. E., & Keevil, S. F. (1997). Automatic correction of motion artifacts in magnetic resonance images using an entropy focus criterion. IEEE Transactions on Medical Imaging, 16(6), 903–910. IEEE Transactions on Medical Imaging. https://doi.org/10.1109/42.650886

Avram, A. V., Guidon, A., Truong, T.-K., Liu, C., & Song, A. W. (2014). Dynamic and inherent B0 correction for DTI using stimulated echo spiral imaging. Magnetic Resonance in Medicine, 71(3), 1044–1053. https://doi.org/10.1002/mrm.24767

Bai, R., Li, Z., Sun, C., Hsu, Y.-C., Liang, H., & Basser, P. (2020). Feasibility of filter-exchange imaging (FEXI) in measuring different exchange processes in human brain. NeuroImage, 219, 117039. https://doi.org/10.1016/j.neuroimage.2020.117039

Bammer, R., Stollberger, R., Augustin, M., Simbrunner, J., Offenbacher, H., Kooijman, H., Ropele, S., Kapeller, P., Wach, P., Ebner, F., & Fazekas, F. (1999). Diffusion-weighted Imaging with Navigated Interleaved Echo-planar Imaging and a Conventional Gradient System1. Radiology. https://doi.org/10.1148/radiology.211.3.r99jn15799

Basser, P. J., Mattiello, J., & LeBihan, D. (1994). MR diffusion tensor spectroscopy and imaging. Biophysical Journal, 66(1), 259–267. https://doi.org/10.1016/S0006-3495(94)80775-1

Basser, P. J., & Pierpaoli, C. (1996). Microstructural and physiological features of tissues elucidated by quantitative-diffusion-tensor MRI. Journal of Magnetic Resonance. Series B, 111(3), 209–219. https://doi.org/10.1006/jmrb.1996.0086

Blaimer, M., Gutberlet, M., Kellman, P., Breuer, F. A., Köstler, H., & Griswold, M. A. (2009). Virtual coil concept for improved parallel MRI employing conjugate symmetric signals. Magnetic Resonance in Medicine, 61(1), 93–102. https://doi.org/10.1002/mrm.21652

Bloch, F. (1946). Nuclear Induction. Physical Review, 70(7–8), 460–474. https://doi.org/10.1103/PhysRev.70.460

Bosak, E., & Harvey, P. R. (2001). Navigator motion correction of diffusion weighted 3D SSFP imaging. Magma (New York, N.Y.), 12(2–3), 167–176. https://doi.org/10.1007/BF02668098

Brockstedt, S., Thomsen, C., Wirestam, R., De Poorter, J., De Wagter, C., Salford, L. G., Holtås, S., & Ståhlberg, F. (1995). Use of an enhanced gradient system for diffusion MR imaging with motion-artifact reduction. Acta Radiologica (Stockholm, Sweden: 1987), 36(6), 662–670.

Bruce, I. P., Chang, H.-C., Petty, C., Chen, N.-K., & Song, A. W. (2017a). 3D-MB-MUSE: A robust 3D multi-slab, multi-band and multi-shot reconstruction approach for ultrahigh resolution diffusion MRI. NeuroImage, 159, 46–56. https://doi.org/10.1016/j.neuroimage.2017.07.035

Bruce, I. P., Chang, H.-C., Petty, C., Chen, N.-K., & Song, A. W. (2017b). 3D-MB-MUSE: A robust 3D multi-slab, multi-band and multi-shot reconstruction approach for ultrahigh resolution diffusion MRI. NeuroImage, 159, 46–56. https://doi.org/10.1016/j.neuroimage.2017.07.035

Budde, M. D., & Annese, J. (2013). Quantification of anisotropy and fiber orientation in human brain histological sections. Frontiers in Integrative Neuroscience, 7.

https://www.frontiersin.org/journals/integrative-neuroscience/articles/10.3389/fnint.2013.00003

Cardenas, A. M., Sarlls, J. E., Kwan, J. Y., Bageac, D., Gala, Z. S., Danielian, L. E., Ray-Chaudhury, A., Wang, H.-W., Miller, K. L., Foxley, S., Jbabdi, S., Welsh, R. C., & Floeter, M. K. (2017). Pathology of callosal damage in ALS: An ex-vivo, 7 T diffusion tensor MRI study. NeuroImage: Clinical, 15, 200–208. https://doi.org/10.1016/j.nicl.2017.04.024

Carr, H. Y., & Purcell, E. M. (1954). Effects of Diffusion on Free Precession in Nuclear Magnetic Resonance Experiments. Physical Review, 94(3), 630–638. https://doi.org/10.1103/PhysRev.94.630

Chang, H.-C., Sundman, M., Petit, L., Guhaniyogi, S., Chu, M.-L., Petty, C., Song, A. W., & Chen, N. (2015). Human brain diffusion tensor imaging at submillimeter isotropic resolution on a 3 Tesla clinical MRI scanner. NeuroImage, 118, 667–675. https://doi.org/10.1016/j.neuroimage.2015.06.016

Chen, L., Beckett, A., Verma, A., & Feinberg, D. A. (2015). Dynamics of respiratory and cardiac CSF motion revealed with real-time simultaneous multi-slice EPI velocity phase contrast imaging. NeuroImage, 122, 281–287. https://doi.org/10.1016/j.neuroimage.2015.07.073

Chen, N.-K., Guidon, A., Chang, H.-C., & Song, A. W. (2013). A robust multi-shot scan strategy for high-resolution diffusion weighted MRI enabled by multiplexed sensitivity-encoding (MUSE). NeuroImage, 72, 41–47. https://doi.org/10.1016/j.neuroimage.2013.01.038

Cheryauka, A. B., Lee, J. N., Samsonov, A. A., Defrise, M., & Gullberg, G. T. (2004). MRI diffusion tensor reconstruction with PROPELLER data acquisition. Magnetic Resonance Imaging, 22(2), 139–148. https://doi.org/10.1016/j.mri.2003.08.001

Clark, C. A., Barker, G. J., & Tofts, P. S. (2000). Improved Reduction of Motion Artifacts in Diffusion Imaging Using Navigator Echoes and Velocity Compensation. Journal of Magnetic Resonance, 142(2), 358–363. https://doi.org/10.1006/jmre.1999.1955

Coras, R., Milesi, G., Zucca, I., Mastropietro, A., Scotti, A., Figini, M., Mühlebner, A., Hess, A., Graf, W., Tringali, G., Blümcke, I., Villani, F., Didato, G., Frassoni, C., Spreafico, R., & Garbelli, R. (2014). 7 T MRI features in control human hippocampus and hippocampal sclerosis: An ex vivo study with histologic correlations. Epilepsia, 55(12), 2003–2016. https://doi.org/10.1111/epi.12828

Dai, E., Liu, S., & Guo, H. (2021). High-Resolution Whole-Brain Diffusion MRI at 3 T Using Simultaneous Multi-slab (SMSlab) Acquisition. NeuroImage, 118099. https://doi.org/10.1016/j.neuroimage.2021.118099

De Zanche, N., Barmet, C., Nordmeyer-Massner, J. A., & Pruessmann, K. P. (2008). NMR probes for measuring magnetic fields and field dynamics in MR systems. Magnetic Resonance in Medicine, 60(1), 176–186. https://doi.org/10.1002/mrm.21624

Deshmane, A., Gulani, V., Griswold, M. A., & Seiberlich, N. (2012). Parallel MR imaging. Journal of Magnetic Resonance Imaging, 36(1), 55–72. https://doi.org/10.1002/jmri.23639

Dietrich, O., Heiland, S., Benner, T., & Sartor, K. (2000). Reducing motion artefacts in diffusion-weighted MRI of the brain: Efficacy of navigator echo correction and pulse triggering. Neuroradiology, 42(2), 85–91. https://doi.org/10.1007/s002340050020

Dong, Z., Reese, T. G., Lee, H.-H., Huang, S. Y., Polimeni, J. R., Wald, L. L., & Wang, F. (2024). Romer-EPTI: Rotating-view motion-robust super-resolution EPTI for SNR-efficient

distortion-free in-vivo mesoscale dMRI and microstructure imaging [Preprint]. Bioengineering. https://doi.org/10.1101/2024.01.26.577343

Dong, Z., Wang, F., Reese, T. G., Manhard, M. K., Bilgic, B., Wald, L. L., Guo, H., & Setsompop, K. (2019). Tilted-CAIPI for highly accelerated distortion-free EPI with point spread function (PSF) encoding. Magnetic Resonance in Medicine, 81(1), 377–392. https://doi.org/10.1002/mrm.27413

Dubovan, P. I., Gilbert, K. M., & Baron, C. A. (2023). A correction algorithm for improved magnetic field monitoring with distal field probes. Magnetic Resonance in Medicine, 90(6), 2242–2260. https://doi.org/10.1002/mrm.29781

Engel, M., Kasper, L., Wilm, B., Dietrich, B., Vionnet, L., Hennel, F., Reber, J., & Pruessmann, K. P. (2021). T-Hex: Tilted hexagonal grids for rapid 3D imaging. Magnetic Resonance in Medicine, 85(5), 2507–2523. https://doi.org/10.1002/mrm.28600

Engel, M., Mueller, L., Döring, A., Afzali, M., & Jones, D. K. (2024). Maximizing SNR per unit time in diffusion MRI with multiband T-Hex spirals. Magnetic Resonance in Medicine, 91(4), 1323–1336. https://doi.org/10.1002/mrm.29953

Engström, M., Nordell, A., Nordell, B., & Skare, S. (2008). Fast Diffusion Imaging using Undersampled Propeller EPI.

Engström, M., & Skare, S. (2013a). Diffusion-weighted 3D multislab echo planar imaging for high signal-to-noise ratio efficiency and isotropic image resolution. Magnetic Resonance in Medicine, 70(6), 1507–1514. https://doi.org/10.1002/mrm.24594

Engström, M., & Skare, S. (2013b). Diffusion-weighted 3D multislab echo planar imaging for high signal-to-noise ratio efficiency and isotropic image resolution. Magnetic Resonance in Medicine, 70(6), 1507–1514. https://doi.org/10.1002/mrm.24594

Fa, B., M, B., Rm, H., Mf, M., Ma, G., & Pm, J. (2005). Controlled aliasing in parallel imaging results in higher acceleration (CAIPIRINHA) for multi-slice imaging. Magnetic Resonance in Medicine, 53(3). https://doi.org/10.1002/mrm.20401

Feinberg, D. A., Hoenninger, J. C., Crooks, L. E., Kaufman, L., Watts, J. C., & Arakawa, M. (1985). Inner volume MR imaging: Technical concepts and their application. Radiology, 156(3), 743–747. https://doi.org/10.1148/radiology.156.3.4023236

Feinberg, D. A., & Jakab, P. D. (1990). Tissue perfusion in humans studied by Fourier velocity distribution, line scan, and echo-planar imaging. Magnetic Resonance in Medicine, 16(2), 280–293. https://doi.org/10.1002/mrm.1910160209

Feinberg, D. A., & Mark, A. S. (1987). Human brain motion and cerebrospinal fluid circulation demonstrated with MR velocity imaging. Radiology, 163(3), 793–799. https://doi.org/10.1148/radiology.163.3.3575734

Feinberg, D. A., Moeller, S., Smith, S. M., Auerbach, E., Ramanna, S., Gunther, M., Glasser, M. F., Miller, K. L., Ugurbil, K., & Yacoub, E. (2010). Multiplexed echo planar imaging for subsecond whole brain FMRI and fast diffusion imaging. PloS One, 5(12), e15710. https://doi.org/10.1371/journal.pone.0015710

Feizollah, S., Lowen, D., Couch, M., Pracht, E. D., Stöcker, T., & Tardif, C. (2024). 3D diffusion MRI at 7 T with Universal Pulses for improved image uniformity. Proceedings of the 32nd Annual Meeting of ISMRM.

Feizollah, S., & Tardif, C. (2021). Toward high-resolution mapping of microscopic anisotropy in the cortex using b-tensor diffusion imaging with a spiral readout at 7 Tesla [Presentation]. Proceedings International Society of Magnetic Resonance in Medicine.

Feizollah, S., & Tardif, C. L. (2023). High-resolution diffusion-weighted imaging at 7 Tesla: Single-shot readout trajectories and their impact on signal-to-noise ratio, spatial resolution and accuracy. NeuroImage, 274, 120159. https://doi.org/10.1016/j.neuroimage.2023.120159

Fieremans, E., Novikov, D. S., Jensen, J. H., & Helpern, J. A. (2010). Monte Carlo study of a two-compartment exchange model of diffusion. NMR in Biomedicine, 23(7), 711–724. https://doi.org/10.1002/nbm.1577

Finsterbusch, J. (2009). High-resolution diffusion tensor imaging with inner field-of-view EPI. Journal of Magnetic Resonance Imaging: JMRI, 29(4), 987–993.

https://doi.org/10.1002/jmri.21717

Finsterbusch, J. (2010). Double-spin-echo diffusion weighting with a modified eddy current adjustment. Magnetic Resonance Imaging, 28(3), 434–440. https://doi.org/10.1016/j.mri.2009.12.004

Frank, L. R., Jung, Y., Inati, S., Tyszka, J. M., & Wong, E. C. (2010). High efficiency, low distortion 3D diffusion tensor imaging with variable density spiral fast spin echoes (3D DW VDS RARE). NeuroImage, 49(2), 1510–1523. https://doi.org/10.1016/j.neuroimage.2009.09.010

Frigo, M., Fick, R. H. J., Zucchelli, M., Deslauriers-Gauthier, S., & Deriche, R. (2020). Multi Tissue Modelling of Diffusion MRI Signal Reveals Volume Fraction Bias. 2020 IEEE 17 Th International Symposium on Biomedical Imaging (ISBI), 991–994.

https://doi.org/10.1109/ISBI45749.2020.9098649

Frost, R., Jezzard, P., Douaud, G., Clare, S., Porter, D. A., & Miller, K. L. (2015). Scan time reduction for readout-segmented EPI using simultaneous multislice acceleration: Diffusion-weighted imaging at 3 and 7 Tesla. Magnetic Resonance in Medicine, 74(1), 136–149. https://doi.org/10.1002/mrm.25391

Frost, R., Miller, K. L., Tijssen, R. H. N., Porter, D. A., & Jezzard, P. (2014). 3D Multi-slab diffusion-weighted readout-segmented EPI with real-time cardiac-reordered k-space acquisition. Magnetic Resonance in Medicine, 72(6), 1565–1579. https://doi.org/10.1002/mrm.25062

Gallichan, D. (2018). Diffusion MRI of the human brain at ultra-high field (UHF): A review. NeuroImage, 168, 172–180. https://doi.org/10.1016/j.neuroimage.2017.04.037

Geng, R., Zhang, Y., Starekova, J., Rutkowski, D. R., Estkowski, L., Roldán-Alzate, A., & Hernando, D. (2021). Characterization and correction of cardiovascular motion artifacts in diffusion-weighted imaging of the pancreas. Magnetic Resonance in Medicine, 86(4), 1956–1969. https://doi.org/10.1002/mrm.28846

Gerlach, W., & Stern, O. (1922). Der experimentelle Nachweis der Richtungsquantelung im Magnetfeld. Zeitschrift für Physik, 9(1), 349–352. https://doi.org/10.1007/BF01326983

Gilbert, K. M., Dubovan, P. I., Gati, J. S., Menon, R. S., & Baron, C. A. (2022). Integration of an RF coil and commercial field camera for ultrahigh-field MRI. Magnetic Resonance in Medicine, 87(5), 2551–2565. https://doi.org/10.1002/mrm.29130

Golay, X., Jiang, H., van Zijl, P. C. M., & Mori, S. (2002). High-resolution isotropic 3D diffusion tensor imaging of the human brain. Magnetic Resonance in Medicine, 47(5), 837–843. https://doi.org/10.1002/mrm.10143

Gras, V., Vignaud, A., Amadon, A., Le Bihan, D., & Boulant, N. (2017). Universal pulses: A new concept for calibration-free parallel transmission. Magnetic Resonance in Medicine, 77(2), 635–643. https://doi.org/10.1002/mrm.26148

Griswold, M. A., Jakob, P. M., Heidemann, R. M., Nittka, M., Jellus, V., Wang, J., Kiefer, B., & Haase, A. (2002). Generalized autocalibrating partially parallel acquisitions (GRAPPA).

Magnetic Resonance in Medicine, 47(6), 1202–1210. https://doi.org/10.1002/mrm.10171

Guhaniyogi, S., Chu, M.-L., Chang, H.-C., Song, A. W., & Chen, N. (2016a). Motion immune diffusion imaging using augmented MUSE for high-resolution multi-shot EPI. Magnetic Resonance in Medicine, 75(2), 639–652. https://doi.org/10.1002/mrm.25624

Guhaniyogi, S., Chu, M.-L., Chang, H.-C., Song, A. W., & Chen, N.-K. (2016b). Motion immune diffusion imaging using augmented MUSE for high-resolution multi-shot EPI. Magnetic Resonance in Medicine, 75(2), 639–652. https://doi.org/10.1002/mrm.25624

Guo, H., Ma, X., Zhang, Z., Zhang, B., Yuan, C., & Huang, F. (2016). POCS-enhanced inherent correction of motion-induced phase errors (POCS-ICE) for high-resolution multishot diffusion MRI. Magnetic Resonance in Medicine, 75(1), 169–180. https://doi.org/10.1002/mrm.25594

Haacke, E. M., Brown, R. W., Thompson, M. R., & Venkatesan, R. (1999). Magnetic Resonance Imaging: Physical Principles and Sequence Design. John Wiley & Sons.

Hahn, E. L. (1950). Spin Echoes. Physical Review, 80(4), 580–594. https://doi.org/10.1103/PhysRev.80.580

Heidemann, R. M., Anwander, A., Feiweier, T., Knösche, T. R., & Turner, R. (2012). k-space and q-space: Combining ultra-high spatial and angular resolution in diffusion imaging using ZOOPPA at 7 T. NeuroImage, 60(2), 967–978.

https://doi.org/10.1016/j.neuroimage.2011.12.081

Heidemann, R. M., Porter, D. A., Anwander, A., Feiweier, T., Heberlein, K., Knösche, T. R., & Turner, R. (2010). Diffusion imaging in humans at 7 T using readout-segmented EPI and GRAPPA. Magnetic Resonance in Medicine, 64(1), 9–14. https://doi.org/10.1002/mrm.22480

Herbst, M., Deng, W., Ernst, T., & Stenger, V. A. (2017). Segmented simultaneous multi-slice diffusion weighted imaging with generalized trajectories. Magnetic Resonance in Medicine, 78(4), 1476–1481. https://doi.org/10.1002/mrm.26545

Holdsworth, S. J., O'Halloran, R., & Setsompop, K. (2019). The quest for high spatial resolution diffusion-weighted imaging of the human brain in vivo. NMR in Biomedicine, 32(4), e4056. https://doi.org/10.1002/nbm.4056

Holdsworth, S. J., Skare, S., Newbould, R. D., & Bammer, R. (2009). Robust GRAPPA-accelerated diffusion-weighted readout-segmented (RS)-EPI. Magnetic Resonance in Medicine, 62(6), 1629–1640. https://doi.org/10.1002/mrm.22122

Holdsworth, S. J., Skare, S., Newbould, R. D., Guzmann, R., Blevins, N. H., & Bammer, R. (2008). Readout-segmented EPI for rapid high resolution diffusion imaging at 3 T. European Journal of Radiology, 65(1), 36–46. https://doi.org/10.1016/j.ejrad.2007.09.016

Hu, Y., Levine, E. G., Tian, Q., Moran, C. J., Wang, X., Taviani, V., Vasanawala, S. S., McNab, J. A., Daniel, B. A., & Hargreaves, B. L. (2019). Motion-robust reconstruction of multishot diffusion-weighted images without phase estimation through locally low-rank regularization. Magnetic Resonance in Medicine, 81(2), 1181–1190. https://doi.org/10.1002/mrm.27488

In, M.-H., Posnansky, O., & Speck, O. (2017). High-resolution distortion-free diffusion imaging using hybrid spin-warp and echo-planar PSF-encoding approach. NeuroImage, 148, 20–30. https://doi.org/10.1016/j.neuroimage.2017.01.008

Jelescu, I. O., de Skowronski, A., Geffroy, F., Palombo, M., & Novikov, D. S. (2022). Neurite Exchange Imaging (NEXI): A minimal model of diffusion in gray matter with inter-compartment water exchange. NeuroImage, 256, 119277. https://doi.org/10.1016/j.neuroimage.2022.119277

Jelescu, I. O., Veraart, J., Adisetiyo, V., Milla, S. S., Novikov, D. S., & Fieremans, E. (2015). One diffusion acquisition and different white matter models: How does microstructure change in

human early development based on WMTI and NODDI? NeuroImage, 107, 242–256. https://doi.org/10.1016/j.neuroimage.2014.12.009

Jeong, E.-K., Kim, S.-E., Guo, J., Kholmovski, E. G., & Parker, D. L. (2005). High-resolution DTI with 2D interleaved multislice reduced FOV single-shot diffusion-weighted EPI (2D ss-rFOV-DWEPI). Magnetic Resonance in Medicine, 54(6), 1575–1579. https://doi.org/10.1002/mrm.20711

Jeong, E.-K., Kim, S.-E., Kholmovski, E. G., & Parker, D. L. (2006). High-resolution DTI of a localized volume using 3D single-shot diffusion-weighted STimulated echo-planar imaging (3D ss-DWSTEPI). Magnetic Resonance in Medicine, 56(6), 1173–1181. https://doi.org/10.1002/mrm.21088

Jeong, E.-K., Kim, S.-E., & Parker, D. L. (2003). High-resolution diffusion-weighted 3D MRI, using diffusion-weighted driven-equilibrium (DW-DE) and multishot segmented 3D-SSFP without navigator echoes. Magnetic Resonance in Medicine, 50(4), 821–829. https://doi.org/10.1002/mrm.10593

Jeong, H.-K., Gore, J. C., & Anderson, A. W. (2013). High-resolution human diffusion tensor imaging using 2-D navigated multishot SENSE EPI at 7 T. Magnetic Resonance in Medicine, 69(3), 793–802. https://doi.org/10.1002/mrm.24320

Jiang, Y., Li, G., Shao, X., & Guo, H. (2024). Simultaneous Multi-Slice Diffusion Imaging using Navigator-free Multishot Spiral Acquisition (No. arXiv:2407.20904). arXiv. https://doi.org/10.48550/arXiv.2407.20904

Jones, D. K. (2010). Diffusion MRI: Theory, Methods, and Applications. In Diffusion MRI. Oxford University Press.

http://oxfordmedicine.com/view/10.1093/med/9780195369779.001.0001/med-9780195369779

Jung, Y., Samsonov, A. A., Block, W. F., Lazar, M., Lu, A., Liu, J., & Alexander, A. L. (2009). 3D diffusion tensor MRI with isotropic resolution using a steady-state radial acquisition. Journal of Magnetic Resonance Imaging: JMRI, 29(5), 1175–1184. https://doi.org/10.1002/jmri.21663

K, S., J, C.-A., Ba, G., T, R., A, Y., B, K., Vj, W., & Ll, W. (2012). Improving diffusion MRI using simultaneous multi-slice echo planar imaging. NeuroImage, 63(1). https://doi.org/10.1016/j.neuroimage.2012.06.033

Karampinos, D. C., Van, A. T., Olivero, W. C., Georgiadis, J. G., & Sutton, B. P. (2009). High-resolution diffusion tensor imaging of the human pons with a reduced field-of-view, multishot, variable-density, spiral acquisition at 3 T. Magnetic Resonance in Medicine, 62(4), 1007–1016. https://doi.org/10.1002/mrm.22105

Kärger, J. (1985). NMR self-diffusion studies in heterogeneous systems. Advances in Colloid and Interface Science, 23, 129–148. https://doi.org/10.1016/0001-8686(85)80018-X

Ke, J., Foley, L. M., Hitchens, T. K., Richardson, R. M., & Modo, M. (2020). Ex vivo mesoscopic diffusion MRI correlates with seizure frequency in patients with uncontrolled mesial temporal lobe epilepsy. Human Brain Mapping, 41(16), 4529–4548. https://doi.org/10.1002/hbm.25139

Knossalla, F., Kohl, Z., Winkler, J., Schwab, S., Schenk, T., Engelhorn, T., Doerfler, A., & Gölitz, P. (2018). High-resolution diffusion tensor-imaging indicates asymmetric microstructural disorganization within substantia nigra in early Parkinson's disease. Journal of Clinical Neuroscience, 50, 199–202. https://doi.org/10.1016/j.jocn.2018.01.023

Larkman, D. J., deSouza, N. M., Bydder, M., & Hajnal, J. V. (2001). An investigation into the use of sensitivity-encoded techniques to increase temporal resolution in dynamic contrast-enhanced breast imaging. Journal of Magnetic Resonance Imaging: JMRI, 14(3), 329–335. https://doi.org/10.1002/jmri.1190

Larmor, J. (1897). A Dynamical Theory of the Electric and Luminiferous Medium. Part III. Relations with Material Media. Philosophical Transactions of the Royal Society of London Series A, 190, 205-300+493. https://doi.org/10.1098/rsta.1897.0020

Le Bihan, D., Breton, E., Lallemand, D., Grenier, P., Cabanis, E., & Laval-Jeantet, M. (1986). MR imaging of intravoxel incoherent motions: Application to diffusion and perfusion in neurologic disorders. Radiology, 161(2), 401–407. https://doi.org/10.1148/radiology.161.2.3763909

Le Bihan, D., Turner, R., & MacFall, J. R. (1989). Effects of intravoxel incoherent motions (IVIM) in steady-state free precession (SSFP) imaging: Application to molecular diffusion imaging. Magnetic Resonance in Medicine, 10(3), 324–337. https://doi.org/10.1002/mrm.1910100305

Lee, Y., Wilm, B. J., Brunner, D. O., Gross, S., Schmid, T., Nagy, Z., & Pruessmann, K. P. (2021). On the signal-to-noise ratio benefit of spiral acquisition in diffusion MRI. Magnetic Resonance in Medicine, 85(4), 1924–1937. https://doi.org/10.1002/mrm.28554

Leuze, C. W. U., Anwander, A., Bazin, P.-L., Dhital, B., Stüber, C., Reimann, K., Geyer, S., & Turner, R. (2014). Layer-Specific Intracortical Connectivity Revealed with Diffusion MRI. Cerebral Cortex, 24(2), 328–339. https://doi.org/10.1093/cercor/bhs311

Li, H., Zu, T., Chen, R., Ba, R., Hsu, Y.-C., Sun, Y., Zhang, Y., & Wu, D. (2023). 3D diffusion MRI with twin navigator-based GRASE and comparison with 2D EPI for tractography in the human brain. Magnetic Resonance in Medicine, 90(5), 1969–1978. https://doi.org/10.1002/mrm.29769

Li, T.-Q., Kim, D.-H., & Moseley, M. E. (2005). High-resolution diffusion-weighted imaging with interleaved variable-density spiral acquisitions. Journal of Magnetic Resonance Imaging, 21(4), 468–475. https://doi.org/10.1002/jmri.20287

Li, Z., Miller, K. L., Chen, X., Chiew, M., & Wu, W. (2024). Self-navigated 3D diffusion MRI using an optimized CAIPI sampling and structured low-rank reconstruction estimated navigator. IEEE Transactions on Medical Imaging, 1–1. IEEE Transactions on Medical Imaging. https://doi.org/10.1109/TMI.2024.3454994

Li, Z., Pipe, J. G., Lee, C.-Y., Debbins, J. P., Karis, J. P., & Huo, D. (2011). X-PROP: A fast and robust diffusion-weighted propeller technique. Magnetic Resonance in Medicine, 66(2), 341–347. https://doi.org/10.1002/mrm.23033

Liao, C., Bilgic, B., Tian, Q., Stockmann, J. P., Cao, X., Fan, Q., Iyer, S. S., Wang, F., Ngamsombat, C., Lo, W.-C., Manhard, M. K., Huang, S. Y., Wald, L. L., & Setsompop, K. (2021). Distortion-free, high-isotropic-resolution diffusion MRI with gSlider BUDA-EPI and multicoil dynamic B0 shimming. Magnetic Resonance in Medicine, 86(2), 791–803. https://doi.org/10.1002/mrm.28748

Liu, C., Bammer, R., Kim, D., & Moseley, M. E. (2004). Self-navigated interleaved spiral (SNAILS): Application to high-resolution diffusion tensor imaging. Magnetic Resonance in Medicine, 52(6), 1388–1396. https://doi.org/10.1002/mrm.20288

Liu, G., van Gelderen, P., Duyn, J., & Moonen, C. T. (1996a). Single-shot diffusion MRI of human brain on a conventional clinical instrument. Magnetic Resonance in Medicine, 35(5), 671–677. https://doi.org/10.1002/mrm.1910350508

Liu, G., van Gelderen, P., Duyn, J., & Moonen, C. T. (1996b). Single-shot diffusion MRI of human brain on a conventional clinical instrument. Magnetic Resonance in Medicine, 35(5), 671–677. https://doi.org/10.1002/mrm.1910350508

Liu, S., Zhang, J., Shi, D., & Guo, H. (2023). Three-dimensional diffusion MRI using simultaneous multislab with blipped-CAIPI in a 4D k-space framework. Magnetic Resonance in Medicine, 90(3), 978–994. https://doi.org/10.1002/mrm.29685

Lowen, D., Pracht, E. D., Gras, V., Massire, A., Mauconduit, F., Stoecker, T., & Boulant, N. (2024). Design of calibration-free RF pulses for T-weighted single-slab 3D turbo-spin-echo sequences at 7 T utilizing parallel transmission. Magnetic Resonance in Medicine, 92(5), 2037–2050. https://doi.org/10.1002/mrm.30212

Lu, L., Erokwu, B., Lee, G., Gulani, V., Griswold, M. A., Dell, K. M., & Flask, C. A. (2012). Diffusion-prepared fast imaging with steady-state free precession (DP-FISP): A rapid diffusion MRI technique at 7 T. Magnetic Resonance in Medicine, 68(3), 868–873. https://doi.org/10.1002/mrm.23287

Lundell, H., Alexander, D. C., & Dyrby, T. B. (2014). High angular resolution diffusion imaging with stimulated echoes: Compensation and correction in experiment design and analysis. NMR in Biomedicine, 27(8), 918–925. https://doi.org/10.1002/nbm.3137

Lustig, M., Donoho, D., & Pauly, J. M. (2007). Sparse MRI: The application of compressed sensing for rapid MR imaging. Magnetic Resonance in Medicine, 58(6), 1182–1195. https://doi.org/10.1002/mrm.21391 Lustig, M., & Pauly, J. M. (2010). SPIRiT: Iterative self-consistent parallel imaging reconstruction from arbitrary k-space. Magnetic Resonance in Medicine, 64(2), 457–471. https://doi.org/10.1002/mrm.22428

Ly, M., Foley, L., Manivannan, A., Hitchens, T. K., Richardson, R. M., & Modo, M. (2020). Mesoscale diffusion magnetic resonance imaging of the ex vivo human hippocampus. Human Brain Mapping, 41(15), 4200–4218. https://doi.org/10.1002/hbm.25119

Mani, M., Aggarwal, H. K., Magnotta, V., & Jacob, M. (2020). Improved MUSSELS reconstruction for high-resolution multi-shot diffusion weighted imaging. Magnetic Resonance in Medicine, 83(6), 2253–2263. https://doi.org/10.1002/mrm.28090

Mani, M., Jacob, M., Kelley, D., & Magnotta, V. (2017a). Multi-shot sensitivity-encoded diffusion data recovery using structured low-rank matrix completion (MUSSELS). Magnetic Resonance in Medicine, 78(2), 494–507. https://doi.org/10.1002/mrm.26382

Mani, M., Jacob, M., Kelley, D., & Magnotta, V. (2017b). Multi-shot sensitivity-encoded diffusion data recovery using structured low-rank matrix completion (MUSSELS). Magnetic Resonance in Medicine, 78(2), 494–507. https://doi.org/10.1002/mrm.26382

Mani, M., Jacob, M., McKinnon, G., Yang, B., Rutt, B., Kerr, A., & Magnotta, V. (2020). SMS MUSSELS: A navigator-free reconstruction for simultaneous multi-slice-accelerated multi-shot diffusion weighted imaging. Magnetic Resonance in Medicine, 83(1), 154–169. https://doi.org/10.1002/mrm.27924

McNab, J. A., Edlow, B. L., Witzel, T., Huang, S. Y., Bhat, H., Heberlein, K., Feiweier, T., Liu, K., Keil, B., Cohen-Adad, J., Tisdall, M. D., Folkerth, R. D., Kinney, H. C., & Wald, L. L. (2013). The Human Connectome Project and beyond: Initial applications of 300 mT/m gradients. NeuroImage, 80, 234–245. https://doi.org/10.1016/j.neuroimage.2013.05.074

McNab, J. A., Gallichan, D., & Miller, K. L. (2010). 3D steady-state diffusion-weighted imaging with trajectory using radially batched internal navigator echoes (TURBINE). Magnetic Resonance in Medicine, 63(1), 235–242. https://doi.org/10.1002/mrm.22183

McNab, J. A., Jbabdi, S., Deoni, S. C. L., Douaud, G., Behrens, T. E. J., & Miller, K. L. (2009). High resolution diffusion-weighted imaging in fixed human brain using diffusion-weighted

steady state free precession. NeuroImage, 46(3), 775–785.

https://doi.org/10.1016/j.neuroimage.2009.01.008

McNab, J. A., & Miller, K. L. (2010). Steady-state diffusion-weighted imaging: Theory, acquisition and analysis. NMR in Biomedicine, 23(7), 781–793.

https://doi.org/10.1002/nbm.1509

Merboldt, K.-D., Hanicke, W., & Frahm, J. (1985). Self-diffusion NMR imaging using stimulated echoes. Journal of Magnetic Resonance (1969), 64(3), 479–486. https://doi.org/10.1016/0022-2364(85)90111-8

Meyer, C. H., Hu, B. S., Nishimura, D. G., & Macovski, A. (1992). Fast spiral coronary artery imaging. Magnetic Resonance in Medicine, 28(2), 202–213.

https://doi.org/10.1002/mrm.1910280204

Michael, E. S., Hennel, F., & Pruessmann, K. P. (2024a). Motion-compensated diffusion encoding in multi-shot human brain acquisitions: Insights using high-performance gradients. Magnetic Resonance in Medicine, 92(2), 556–572. https://doi.org/10.1002/mrm.30069

Michael, E. S., Hennel, F., & Pruessmann, K. P. (2024b). Motion-compensated diffusion encoding in multi-shot human brain acquisitions: Insights using high-performance gradients. Magnetic Resonance in Medicine, 92(2), 556–572. https://doi.org/10.1002/mrm.30069

Nguyen, C., Fan, Z., Sharif, B., He, Y., Dharmakumar, R., Berman, D. S., & Li, D. (2014). In vivo three-dimensional high resolution cardiac diffusion-weighted MRI: A motion compensated diffusion-prepared balanced steady-state free precession approach. Magnetic Resonance in Medicine, 72(5), 1257–1267. https://doi.org/10.1002/mrm.25038

Nishimura, D. G. (1996). Principles of Magnetic Resonance Imaging. Stanford University.

Noll, D. C., Nishimura, D. G., & Macovski, A. (1991). Homodyne detection in magnetic resonance imaging. IEEE Transactions on Medical Imaging, 10(2), 154–163. https://doi.org/10.1109/42.79473

Novikov, D. S., Kiselev, V. G., & Jespersen, S. N. (2018). On modeling. Magnetic Resonance in Medicine, 79(6), 3172–3193. https://doi.org/10.1002/mrm.27101

Novikov, D. S., Veraart, J., Jelescu, I. O., & Fieremans, E. (2018). Rotationally-invariant mapping of scalar and orientational metrics of neuronal microstructure with diffusion MRI. NeuroImage, 174, 518–538. https://doi.org/10.1016/j.neuroimage.2018.03.006

Nunes, R., Hajnal, J., Golay, X., & Larkman, D. J. (2006). Simultaneous slice excitation and reconstruction for single shot EPI. Proceedings of the 14th Annual Meeting of ISMRM.

O'Halloran, R. L., Aksoy, M., Van, A. T., & Bammer, R. (2013). 3D isotropic high-resolution diffusion-weighted MRI of the whole brain with a motion-corrected steady-state free precession sequence. Magnetic Resonance in Medicine, 70(2), 466–478. https://doi.org/10.1002/mrm.24489

Oshio, K., & Feinberg, D. A. (1991). GRASE (Gradient- and spin-echo) imaging: A novel fast MRI technique. Magnetic Resonance in Medicine, 20(2), 344–349.

https://doi.org/10.1002/mrm.1910200219

Ozaki, M., Inoue, Y., Miyati, T., Hata, H., Mizukami, S., Komi, S., Matsunaga, K., & Woodhams, R. (2013). Motion artifact reduction of diffusion-weighted MRI of the liver: Use of velocity-compensated diffusion gradients combined with tetrahedral gradients. Journal of Magnetic Resonance Imaging, 37(1), 172–178. https://doi.org/10.1002/jmri.23796

Palombo, M., Ianus, A., Guerreri, M., Nunes, D., Alexander, D. C., Shemesh, N., & Zhang, H. (2020a). SANDI: A compartment-based model for non-invasive apparent soma and neurite imaging by diffusion MRI. NeuroImage, 215, 116835.

https://doi.org/10.1016/j.neuroimage.2020.116835

Palombo, M., Ianus, A., Guerreri, M., Nunes, D., Alexander, D. C., Shemesh, N., & Zhang, H. (2020b). SANDI: A compartment-based model for non-invasive apparent soma and neurite imaging by diffusion MRI. NeuroImage, 215, 116835.

https://doi.org/10.1016/j.neuroimage.2020.116835

Pipe, J. G. (1999). Motion correction with PROPELLER MRI: Application to head motion and free-breathing cardiac imaging. Magnetic Resonance in Medicine, 42(5), 963–969. https://doi.org/10.1002/(sici)1522-2594(199911)42:5<963::aid-mrm17>3.0.co;2-1

Pipe, J. G., & Zwart, N. (2006). Turboprop: Improved PROPELLER imaging. Magnetic Resonance in Medicine, 55(2), 380–385. https://doi.org/10.1002/mrm.20768

Porter, D. A., & Heidemann, R. M. (2009). High resolution diffusion-weighted imaging using readout-segmented echo-planar imaging, parallel imaging and a two-dimensional navigator-based reacquisition. Magnetic Resonance in Medicine, 62(2), 468–475. https://doi.org/10.1002/mrm.22024

Prasad, P. V., & Nalcioglu, O. (1991). A modified pulse sequence for in vivo diffusion imaging with reduced motion artifacts. Magnetic Resonance in Medicine, 18(1), 116–131. https://doi.org/10.1002/mrm.1910180113

Pruessmann, K. P., Weiger, M., Scheidegger, M. B., & Boesiger, P. (1999). SENSE: Sensitivity encoding for fast MRI. Magnetic Resonance in Medicine, 42(5), 952–962.

Purcell, E. M., Torrey, H. C., & Pound, R. V. (1946). Resonance Absorption by Nuclear Magnetic Moments in a Solid. Physical Review, 69(1–2), 37–38. https://doi.org/10.1103/PhysRev.69.37

Ramos-Llordén, G., Ning, L., Liao, C., Mukhometzianov, R., Michailovich, O., Setsompop, K., & Rathi, Y. (2020). High-fidelity, accelerated whole-brain submillimeter in vivo diffusion MRI using gSlider-spherical ridgelets (gSlider-SR). Magnetic Resonance in Medicine, 84(4), 1781–1795. https://doi.org/10.1002/mrm.28232

Reese, T. G., Heid, O., Weisskoff, R. M., & Wedeen, V. J. (2003). Reduction of eddy-current-induced distortion in diffusion MRI using a twice-refocused spin echo. Magnetic Resonance in Medicine, 49(1), 177–182. https://doi.org/10.1002/mrm.10308

Reischauer, C., Vorburger, R. S., Wilm, B. J., Jaermann, T., & Boesiger, P. (2012). Optimizing signal-to-noise ratio of high-resolution parallel single-shot diffusion-weighted echo-planar imaging at ultrahigh field strengths. Magnetic Resonance in Medicine, 67(3), 679–690. https://doi.org/10.1002/mrm.23057

Rieseberg, S., Frahm, J., & Finsterbusch, J. (2002). Two-dimensional spatially-selective RF excitation pulses in echo-planar imaging. Magnetic Resonance in Medicine, 47(6), 1186–1193. https://doi.org/10.1002/mrm.10157

Robson, M. D., Gore, J. C., & Constable, R. T. (1997). Measurement of the point spread function in MRI using constant time imaging. Magnetic Resonance in Medicine, 38(5), 733–740. https://doi.org/10.1002/mrm.1910380509

Roebroeck, A., Miller, K. L., & Aggarwal, M. (2019). Ex vivo diffusion MRI of the human brain: Technical challenges and recent advances. NMR in Biomedicine, 32(4), e3941. https://doi.org/10.1002/nbm.3941

S, M., E, Y., Ca, O., E, A., J, S., N, H., & K, U. (2010). Multiband multislice GE-EPI at 7 tesla, with 16-fold acceleration using partial parallel imaging with application to high spatial and temporal whole-brain fMRI. Magnetic Resonance in Medicine, 63(5). https://doi.org/10.1002/mrm.22361

Saritas, E. U., Lee, D., Çukur, T., Shankaranarayanan, A., & Nishimura, D. G. (2014). Hadamard slice encoding for reduced-FOV diffusion-weighted imaging. Magnetic Resonance in Medicine, 72(5), 1277–1290. https://doi.org/10.1002/mrm.25044

Sarlls, J. E., Newbould, R. D., Altbach, M. I., Gmitro, A. F., Seeger, J., & Trouard, T. P. (2005). Isotropic diffusion weighting in radial fast spin-echo magnetic resonance imaging. Magnetic Resonance in Medicine, 53(6), 1347–1354. https://doi.org/10.1002/mrm.20493

Sarlls, J. E., & Pierpaoli, C. (2008). Diffusion-weighted radial fast spin-echo for high-resolution diffusion tensor imaging at 3 T. Magnetic Resonance in Medicine, 60(2), 270–276. https://doi.org/10.1002/mrm.21639

Scherrer, B., Gholipour, A., & Warfield, S. K. (2011). Super-Resolution in Diffusion-Weighted Imaging. Medical Image Computing and Computer-Assisted Intervention: MICCAI ... International Conference on Medical Image Computing and Computer-Assisted Intervention, 14(0 2), 124–132.

Schneider, J. T., Kalayciyan, R., Haas, M., Herrmann, S. R., Ruhm, W., Hennig, J., & Ullmann, P. (2013). Inner-volume imaging in vivo using three-dimensional parallel spatially selective excitation. Magnetic Resonance in Medicine, 69(5), 1367–1378. https://doi.org/10.1002/mrm.24381

Schomberg, H., & Timmer, J. (1995). The gridding method for image reconstruction by Fourier transformation. IEEE Transactions on Medical Imaging, 14(3), 596–607. IEEE Transactions on Medical Imaging. https://doi.org/10.1109/42.414625

Seehaus, A. K., Roebroeck, A., Chiry, O., Kim, D.-S., Ronen, I., Bratzke, H., Goebel, R., & Galuske, R. A. W. (2013). Histological Validation of DW-MRI Tractography in Human Postmortem Tissue. Cerebral Cortex, 23(2), 442–450. https://doi.org/10.1093/cercor/bhs036

Seehaus, A., Roebroeck, A., Bastiani, M., Fonseca, L., Bratzke, H., Lori, N., Vilanova, A., Goebel, R., & Galuske, R. (2015). Histological validation of high-resolution DTI in human post mortem tissue. Frontiers in Neuroanatomy, 9.

https://www.frontiersin.org/journals/neuroanatomy/articles/10.3389/fnana.2015.00098

Setsompop, K., Fan, Q., Stockmann, J., Bilgic, B., Huang, S., Cauley, S. F., Nummenmaa, A., Wang, F., Rathi, Y., Witzel, T., & Wald, L. L. (2018). High-resolution in vivo diffusion imaging of the human brain with generalized slice dithered enhanced resolution: Simultaneous multislice (gSlider-SMS). Magnetic Resonance in Medicine, 79(1), 141–151.

https://doi.org/10.1002/mrm.26653

Setsompop, K., Kimmlingen, R., Eberlein, E., Witzel, T., Cohen-Adad, J., McNab, J. A., Keil, B., Tisdall, M. D., Hoecht, P., Dietz, P., Cauley, S. F., Tountcheva, V., Matschl, V., Lenz, V. H., Heberlein, K., Potthast, A., Thein, H., Van Horn, J., Toga, A., ... Wald, L. L. (2013). Pushing the limits of in vivo diffusion MRI for the Human Connectome Project. NeuroImage, 80, 220–233. https://doi.org/10.1016/j.neuroimage.2013.05.078

Seunarine, K. K., & Alexander, D. C. (2009). Chapter 4 - Multiple Fibers: Beyond the Diffusion Tensor. In H. Johansen-Berg & T. E. J. Behrens (Eds.), Diffusion MRI (pp. 55–72). Academic Press. https://doi.org/10.1016/B978-0-12-374709-9.00004-3

Skare, S., Holdsworth, S. J., Lilja, A., & Bammer, R. (2013). Image domain propeller fast spin echo. Magnetic Resonance Imaging, 31(3), 385–395. https://doi.org/10.1016/j.mri.2012.08.010

Skare, S., Newbould, R. D., Clayton, D. B., & Bammer, R. (2006). Propeller EPI in the other direction. Magnetic Resonance in Medicine, 55(6), 1298–1307.

https://doi.org/10.1002/mrm.20890

Skare, S., Newbould, R. D., Nordell, A., Holdsworth, S. J., & Bammer, R. (2008). An auto-calibrated, angularly continuous, two-dimensional GRAPPA kernel for propeller trajectories. Magnetic Resonance in Medicine, 60(6), 1457–1465. https://doi.org/10.1002/mrm.21788

Sodickson, D. K., & Manning, W. J. (1997). Simultaneous acquisition of spatial harmonics (SMASH): Fast imaging with radiofrequency coil arrays. Magnetic Resonance in Medicine, 38(4), 591–603. https://doi.org/10.1002/mrm.1910380414

Sprang, C. (2024). A size-adaptive radiofrequency coil with integrated NMR field probes for magnetic resonance imaging of the pediatric human brain at 7 T [McGill University]. http://oatd.org/oatd/record?record=oai%5C%3Aescholarship.mcgill.ca%5C%3Ah415ph23f

Srinivasan, G., Rangwala, N., & Zhou, X. J. (2018). Steer-PROP: A GRASE-PROPELLER sequence with interecho steering gradient pulses. Magnetic Resonance in Medicine, 79(5), 2533–2541. https://doi.org/10.1002/mrm.26898

Stejskal, E. O., & Tanner, J. E. (1965a). Spin Diffusion Measurements: Spin Echoes in the Presence of a Time-Dependent Field Gradient. The Journal of Chemical Physics, 42(1), 288–292. https://doi.org/10.1063/1.1695690

Stejskal, E. O., & Tanner, J. E. (1965b). Spin Diffusion Measurements: Spin Echoes in the Presence of a Time-Dependent Field Gradient. The Journal of Chemical Physics, 42(1), 288–292. https://doi.org/10.1063/1.1695690

Stoeck, C. T., von Deuster, C., Genet, M., Atkinson, D., & Kozerke, S. (2016). Second-order motion-compensated spin echo diffusion tensor imaging of the human heart. Magnetic Resonance in Medicine, 75(4), 1669–1676. https://doi.org/10.1002/mrm.25784

Szczepankiewicz, F., Sjölund, J., Dall'Armellina, E., Plein, S., Schneider, J. E., Teh, I., & Westin, C. (2021). Motion-compensated gradient waveforms for tensor-valued diffusion encoding by constrained numerical optimization. Magnetic Resonance in Medicine, 85(4), 2117–2126. https://doi.org/10.1002/mrm.28551

Tanner, J. E. (1972). Erratum: Use of the Stimulated Echo in NMR Diffusion Studies. The Journal of Chemical Physics, 57(8), 3586. https://doi.org/10.1063/1.1678810

Terem, I., Dang, L., Champagne, A., Abderezaei, J., Pionteck, A., Almadan, Z., Lydon, A.-M., Kurt, M., Scadeng, M., & Holdsworth, S. J. (2021). 3D amplified MRI (aMRI). Magnetic Resonance in Medicine, 86(3), 1674–1686. https://doi.org/10.1002/mrm.28797

Tournier, J.-D., Calamante, F., Gadian, D. G., & Connelly, A. (2004). Direct estimation of the fiber orientation density function from diffusion-weighted MRI data using spherical deconvolution. NeuroImage, 23(3), 1176–1185.

https://doi.org/10.1016/j.neuroimage.2004.07.037

Trouard, T. P., Theilmann, R. J., Altbach, M. I., & Gmitro, A. F. (1999). High-resolution diffusion imaging with DIFRAD-FSE (diffusion-weighted radial acquisition of data with fast spin-echo) MRI. Magnetic Resonance in Medicine, 42(1), 11–18.

https://doi.org/10.1002/(sici)1522-2594(199907)42:1<11::aid-mrm3>3.0.co;2-j

Truong, T.-K., Chen, N., & Song, A. W. (2012a). Inherent correction of motion-induced phase errors in multishot spiral diffusion-weighted imaging. Magnetic Resonance in Medicine, 68(4), 1255–1261. https://doi.org/10.1002/mrm.24124

Truong, T.-K., Chen, N., & Song, A. W. (2012b). Inherent correction of motion-induced phase errors in multishot spiral diffusion-weighted imaging. Magnetic Resonance in Medicine, 68(4), 1255–1261. https://doi.org/10.1002/mrm.24124

Truong, T.-K., & Guidon, A. (2014a). High-resolution multishot spiral diffusion tensor imaging with inherent correction of motion-induced phase errors. Magnetic Resonance in Medicine, 71(2), 790–796. https://doi.org/10.1002/mrm.24709

Truong, T.-K., & Guidon, A. (2014b). High-resolution multishot spiral diffusion tensor imaging with inherent correction of motion-induced phase errors. Magnetic Resonance in Medicine, 71(2), 790–796. https://doi.org/10.1002/mrm.24709

Uecker, M., Lai, P., Murphy, M. J., Virtue, P., Elad, M., Pauly, J. M., Vasanawala, S. S., & Lustig, M. (2014). ESPIRiT — An Eigenvalue Approach to Autocalibrating Parallel MRI: Where SENSE meets GRAPPA. Magnetic Resonance in Medicine: Official Journal of the Society of Magnetic Resonance in Medicine, 71(3), 990–1001. https://doi.org/10.1002/mrm.24751

Uğurbil, K., Xu, J., Auerbach, E. J., Moeller, S., Vu, A. T., Duarte-Carvajalino, J. M., Lenglet, C., Wu, X., Schmitter, S., Van de Moortele, P. F., Strupp, J., Sapiro, G., De Martino, F., Wang, D., Harel, N., Garwood, M., Chen, L., Feinberg, D. A., Smith, S. M., ... Yacoub, E. (2013). Pushing spatial and temporal resolution for functional and diffusion MRI in the Human Connectome Project. NeuroImage, 80, 80–104. https://doi.org/10.1016/j.neuroimage.2013.05.012

Van, A. T., Aksoy, M., Holdsworth, S. J., Kopeinigg, D., Vos, S. B., & Bammer, R. (2015). Slab profile encoding (PEN) for minimizing slab boundary artifact in three-dimensional diffusion-weighted multislab acquisition. Magnetic Resonance in Medicine, 73(2), 605–613. https://doi.org/10.1002/mrm.25169

Van, A. T., Karampinos, D. C., Georgiadis, J. G., & Sutton, B. P. (2009). K -Space and Image-Space Combination for Motion-Induced Phase-Error Correction in Self-Navigated Multicoil Multishot DWI. IEEE Transactions on Medical Imaging, 28(11), 1770–1780. IEEE Transactions on Medical Imaging. https://doi.org/10.1109/TMI.2009.2023212

Varela-Mattatall, G., Dubovan, P. I., Santini, T., Gilbert, K. M., Menon, R. S., & Baron, C. A. (2023). Single-shot spiral diffusion-weighted imaging at 7 T using expanded encoding with compressed sensing. Magnetic Resonance in Medicine, 90(2), 615–623. https://doi.org/10.1002/mrm.29666

Veraart, J., Novikov, D. S., & Fieremans, E. (2018). TE dependent Diffusion Imaging (TEdDI) distinguishes between compartmental T2 relaxation times. NeuroImage, 182, 360–369. https://doi.org/10.1016/j.neuroimage.2017.09.030

Vis, G., Nilsson, M., Westin, C.-F., & Szczepankiewicz, F. (2021). Accuracy and precision in super-resolution MRI: Enabling spherical tensor diffusion encoding at ultra-high b-values and high resolution. NeuroImage, 245, 118673. https://doi.org/10.1016/j.neuroimage.2021.118673

von Morze, C., Kelley, D. A. C., Shepherd, T. M., Banerjee, S., Xu, D., & Hess, C. P. (2010). Reduced field-of-view diffusion-weighted imaging of the brain at 7 T. Magnetic Resonance Imaging, 28(10), 1541–1545. https://doi.org/10.1016/j.mri.2010.06.025

Vu, A., Auerbach, E., Lenglet, C., Moeller, S., Sotiropoulos, S., Jbabdi, S., Andersson, J., Yacoub, E., & Ugurbil, K. (2015). High resolution whole brain diffusion imaging at 7 T for the

Human Connectome Project. NeuroImage, 122, 318–331.

https://doi.org/10.1016/j.neuroimage.2015.08.004

Vu, A. T., Auerbach, E., Lenglet, C., Moeller, S., Sotiropoulos, S. N., Jbabdi, S., Andersson, J., Yacoub, E., & Ugurbil, K. (2015). High resolution whole brain diffusion imaging at 7 T for the Human Connectome Project. NeuroImage, 122, 318–331.

https://doi.org/10.1016/j.neuroimage.2015.08.004

Wald, L. L. (2019). Ultimate MRI. Journal of Magnetic Resonance, 306, 139–144. https://doi.org/10.1016/j.jmr.2019.07.016

Wen, Q., Kodiweera, C., Dale, B. M., Shivraman, G., & Wu, Y.-C. (2018). Rotating single-shot acquisition (RoSA) with composite reconstruction for fast high-resolution diffusion imaging. Magnetic Resonance in Medicine, 79(1), 264–275. https://doi.org/10.1002/mrm.26671

Wheeler-Kingshott, C. A. M., Parker, G. J. M., Symms, M. R., Hickman, S. J., Tofts, P. S., Miller, D. H., & Barker, G. J. (2002). ADC mapping of the human optic nerve: Increased resolution, coverage, and reliability with CSF-suppressed ZOOM-EPI. Magnetic Resonance in Medicine, 47(1), 24–31. https://doi.org/10.1002/mrm.10016

Wider, G., Dotsch, V., & Wuthrich, K. (1994). Self-Compensating Pulsed Magnetic-Field Gradients for Short Recovery Times. Journal of Magnetic Resonance, Series A, 108(2), 255–258. https://doi.org/10.1006/jmra.1994.1120

Willig-Onwuachi, J. D., Yeh, E. N., Grant, A. K., Ohliger, M. A., McKenzie, C. A., & Sodickson, D. K. (2005). Phase-constrained parallel MR image reconstruction. Journal of Magnetic Resonance (San Diego, Calif.: 1997), 176(2), 187–198. https://doi.org/10.1016/j.jmr.2005.06.004

Wilm, B. J., Barmet, C., Gross, S., Kasper, L., Vannesjo, S. J., Haeberlin, M., Dietrich, B. E., Brunner, D. O., Schmid, T., & Pruessmann, K. P. (2017). Single-shot spiral imaging enabled by an expanded encoding model: Demonstration in diffusion MRI. Magnetic Resonance in Medicine, 77(1), 83–91. https://doi.org/10.1002/mrm.26493

Wilm, B. J., Barmet, C., Pavan, M., & Pruessmann, K. P. (2011). Higher order reconstruction for MRI in the presence of spatiotemporal field perturbations. Magnetic Resonance in Medicine, 65(6), 1690–1701. https://doi.org/10.1002/mrm.22767

Wilm, B. J., Nagy, Z., Barmet, C., Vannesjo, S. J., Kasper, L., Haeberlin, M., Gross, S., Dietrich, B. E., Brunner, D. O., Schmid, T., & Pruessmann, K. P. (2015). Diffusion MRI with concurrent magnetic field monitoring. Magnetic Resonance in Medicine, 74(4), 925–933. https://doi.org/10.1002/mrm.25827

Wu, W., Koopmans, P. J., Frost, R., & Miller, K. L. (2016). Reducing slab boundary artifacts in three-dimensional multislab diffusion MRI using nonlinear inversion for slab profile encoding (NPEN). Magnetic Resonance in Medicine, 76(4), 1183–1195. https://doi.org/10.1002/mrm.26027

Wu, W., & Miller, K. L. (2017). Image formation in diffusion MRI: A review of recent technical developments. Journal of Magnetic Resonance Imaging: JMRI, 46(3), 646–662. https://doi.org/10.1002/jmri.25664

Wu, W., Poser, B. A., Douaud, G., Frost, R., In, M.-H., Speck, O., Koopmans, P. J., & Miller, K. L. (2016). High-resolution diffusion MRI at 7 T using a three-dimensional multi-slab acquisition. NeuroImage, 143, 1–14. https://doi.org/10.1016/j.neuroimage.2016.08.054

Xie, Y., Yu, W., Fan, Z., Nguyen, C., Bi, X., An, J., Zhang, T., Zhang, Z., & Li, D. (2014). High resolution 3D diffusion cardiovascular magnetic resonance of carotid vessel wall to detect lipid core without contrast media. Journal of Cardiovascular Magnetic Resonance, 16(1), 67. https://doi.org/10.1186/s12968-014-0067-z

Zahneisen, B., Poser, B. A., Ernst, T., & Stenger, V. A. (2014). Simultaneous Multi-Slice fMRI using Spiral Trajectories. NeuroImage, 92, 8–18. https://doi.org/10.1016/j.neuroimage.2014.01.056

Zeng, H., & Constable, R. T. (2002). Image distortion correction

Zeng, H., & Constable, R. T. (2002). Image distortion correction in EPI: Comparison of field mapping with point spread function mapping. Magnetic Resonance in Medicine, 48(1), 137–146. https://doi.org/10.1002/mrm.10200 Zhang, H., Hubbard, P. L., Parker, G. J. M., & Alexander, D. C. (2011). Axon diameter mapping in the presence of orientation dispersion with diffusion MRI. NeuroImage, 56(3), 1301–1315. https://doi.org/10.1016/j.neuroimage.2011.01.084

Zhang, H., Schneider, T., Wheeler-Kingshott, C. A., & Alexander, D. C. (2012). NODDI: Practical in vivo neurite orientation dispersion and density imaging of the human brain. NeuroImage, 61(4), 1000–1016. https://doi.org/10.1016/j.neuroimage.2012.03.072

Zhang, J., Liu, C., & Moseley, M. (2009). Steady-State Free Precession (SSFP) Diffusion Imaging Using 3D Rotating Spirals (3DRS). Proc. Intl. Soc. Mag. Reson. Med. 17.

Zhao, Z., Zhang, L., Luo, W., Cao, Z., Zhu, Q., Kong, X., Zhu, K., Zhang, J., & Wu, D. (2023). Layer-specific microstructural patterns of anterior hippocampus in Alzheimer's disease with ex vivo diffusion MRI at 14.1 T. Human Brain Mapping, 44(2), 458–471. https://doi.org/10.1002/hbm.26062

Copyright

Copyright approval has been obtained from the publisher for using the following figures:

Figure 2.5, Figure 2.6, Figure 2.7, Figure 2.10, Figure 2.12, Figure 2.14, Figure 2.15, Figure 2.17, Figure 2.18, Figure 2.19, Figure 2.20, Figure 2.21, Figure 2.22, Figure 2.23, Figure 2.24.